e-ISSN: 2602-277X
https://dergipark.org.tr/tr/pub/ijct

IJCT

International Journal of Chemistry and Technology

Editor-in-Chief

Prof. Dr. İbrahim Demirtaş

Editor

Assist. Prof. Dr. Oğuzhan KOÇER
Lecturer Rabia ACEMİOĞLU

Advisory Editorial Board

Prof. Harun Parlar (Technical University of Munich, München, Germany)
Prof. Shaobin Wang (Curtin University, Perth, Australia)
Prof. Dr. Ana Beatriz Rodriguez Moratinos (Univesity of Exramadura, Badajoz, Spain)
Prof. Dr. Gelu Bouceanu (Alexandru Ioan Cuza University, Romania)
Prof. Jon-Bae Kim (College of Health Sciences, South Korea)
Prof. Rashid Ahmad (University of Malakand, Chakdara, Pakistan)
Prof. Guang-Jie Zhao (Beijing Forestry University, Beijing, China)
Prof. Dr. Jaine H. Hortlan Luiz (Federal University of Alfenas, Unıfal-MG, Brazil)
Prof. Papita Das (Jadavpur University, Jadavpur, India)
Prof. Vagıf Abbasov (Nef-Kimya Prosesleri Institutu, Baku, Azerbaijan)
Prof. Atiqur Rahman (Islamic University, Kushita, Bangladesh)
Prof. Dr. Mika Silanpaa (LUT Lappeenranta University of Technology, Lappeenranta, Finland)
Prof. Salah Akkal (University of Mentouri Consatntine, Consatntine, Algeria)
Prof. Gilbert Kapche Deccaux (The University of Yaounde I, Yaounde, Cameroon)
Prof. Dr. Anatoli Dimoglu (Düzce University, Düzce, Turkey)
Prof. Dr. Inderbir Singh (Chitkara University, Rajpura, India)
Prof. Dr. Ramazan Erenler (Gaziosmanpaşa University, Tokat, Turkey)
Prof. Dr. Ahmet Çakır (Kilis 7 Aralik University, Kilis, Turkey)
Prof. Dr. M. Salih Ağırtaş (Yüzünücü Yıl University, Van, Turkey)
Prof. Dr. Rahmi Kasımoğulları (Dumlupınar University, Kütahya, Turkey)
Prof. Dr. Ahmet Baysar (Inonu University, Malatya, Turkey)
Prof. Dr. Hamdi Temel (Dicle University, Diyarbakır, Turkey)
Prof. Dr. Ö. İrfan Küfrevioğlu (Atatürk University, Erzurum, Turkey)
Prof. Dr. Ömer Şahin (Siirt University, Siirt, Turkey)
Prof. Dr. Mehmet Uğurlu (Sıtkı Kocman university, Muğla, Turkey)
Prof. Dr. Şükrü Beydemir (Anadolu University, Eskişehir, Turkey)
Prof. Dr. Ramazan Solmaz (Bingol University, Bingöl, Turkey)
Prof. Dr. Mahfuz Elmastaş (Health Sciences University, İstanbul, Turkey)
Prof. Dr. Murat Sadıkoğlu (Gaziosman Paşa University, Tokat, Turkey)
Prof. Dr. Mehmet Doğan (Balıkesir University, Balıkesir, Turkey)
Prof. Dr. Giray Topal (Dicle University, Diyarbakır, Turkey)
Prof. Dr. Birgül Yazıcı (Cukurova University, Adana, Turkey)
Prof. Dr. Ahmet Yartaşı (Çankırı University, Çankırı, Turkey)

e-ISSN: 2602-277X
https://dergipark.org.tr/tr/pub/ijct

IJCT

International Journal of Chemistry and Technology

Prof. Dr. Murat Alanyalıoğlu (Atatürk University, Erzurum, Turkey)
Prof. Dr. T. Abdulkadir Çoban (Erzincan University, Erzincan, Turkey)
Prof. Dr. İsmet Kaya (18 Mart University, Çanakklae, Turkey)
Prof. Dr. Barbaros Nalbantoğlu (Yıldız Technical University, İstanbul, Turkey)
Prof. Dr. Ömer Işıldak (Gaziosmanpaşa University, Tokat, Turkey)
Prof. Dr. Nurullah Saraçoğlu (Atatürk University, Erzurum, Turkey)
Prof. Dr. Ahmet Tutar (Sakarya University, Sakarya, Turkey)
Prof. Dr. Duygu Ekinci (Atatürk University, Erzurum, Turkey)
Prof. Dr. Metin Bülbül (Dumlupınar University, Kütahya, Turkey)
Prof. Dr. Ali Kara (Uludağ University, Bursa, Turkey)
Prof. Dr. Murat Saraçoğlu (Erciyes University, Kayseri, Turkey)
Prof. Dr. Halim Avcı (Kilis 7 Aralik University, Kilis, Turkey)
Prof. Dr. Mustafa Karataş (Aksaray University, Aksaray, Turkey)
Prof. Dr. Serhan Uruş (Sütçü İmam University, K.Maraş, Turkey)
Assoc. Prof. Dr. Şenay Şimşek (North Dakota State Unıversıty, Fargo, USA)
Assoc. Prof. Chin-Hung Lai (Chung Shan Medical University, Taiwan)
Assoc. Prof. Mahjoub Jabli (University of Monastir, Monastir , Tunisia)
Assoc. Prof. Niyaz M. Mahmoodi (Institute for Color Science and Technology, Tehran, Iran)
Assoc. Prof. Dr. Metin Açıkyıldız (Kilis 7 Aralik University, Kilis, Turkey)
Assoc. Prof. Dr. Muhammet Köse (Sütçü İmam University, K.Maraş, Turkey)
Assoc. Prof. Dr. Mustafa Özdemir (Süleyman Demirel University, Isparta, Turkey)
Assist. Prof. Mtasem Z. Bani-Fwaz (King Khalid University, Asir-Abha, Saudi Arabia
Assist. Prof. Bakhtiyor Rasulev (North Dakota State Unıversıty, Fargo, USA)
Assist. Prof. Masood Ayoub Kaloo (Govt. Degree College Shopian, J &K, INDIA)
Assist. Prof. Viyaj Tangde (Rashtrasant Tukadoji Maharaj Nagpur University, India)
Assit. Prof. Safa Majeed Hameed (University of Kufa, Iraq)
Dr. Zineb Tribak (Sidi Mohammad Ben Abdellah University, Fez Morocco)
Dr. Sameer Ahmed Awad (University of Anbar, Iraq)
Dr. Ramadan E. Ashery (Damanhour University, Egypt)

Language Editor

Assist. Prof. Dr. Muhittin Kulak
Assist. Prof. Dr. İbrahim Ertekin
Dr. Emrah Şavran

Spelling Editor

Dr. Ali AÇIKGÖZ

Technical Editor

MSc. İbrahim Halil DOĞRUER

Layout Editor

Research Assistant Uğur YİĞİT

e-ISSN: 2602-277X
https://dergipark.org.tr/tr/pub/ijct

IJCT
International Journal of Chemistry and Technology

Table of Contents

DOI: http://dx.doi.org/10.32571/ijct.1199967 **E-ISSN: 2602-277X**

International Journal of Chemistry and Technology

http://dergipark.org.tr/ijct

Research Article

Hydrogen production via water electrolysis on an active electrocatalyst: rGO/Ni nanocomposite

Didem BALUN KAYAN*

Aksaray University, Faculty of Arts & Sciences, Department of Chemistry, Aksaray 68000, Türkiye

Received: 6 November 2022; Revised: 2 December 2022; Accepted: 5 December 2022

*Corresponding author e-mail: didembalun@gmail.com

Citation: Balun Kayan, D. *Int. J. Chem. Technol.* **2023**, 7 (1), 1-5.

ABSTRACT

The development of inexpensive and effective electrocatalyses are all-important for hydrogen production from water electrolysis. In this study, a facile design of a reduced graphene oxide (rGO) based electrocatalyst decorated with nickel nanoparticles is described. The voltammetric results and the hydrogen evolution reaction (HER) kinetics showed that the as-prepared nanocomposite is an effective and stable electrocatalyst for hydrogen production with a small Tafel slope of 152 mVdec-1 and long-term continuous durability (over 24 h) in 0.5 M H2SO4 solution. Also, the enhanced HER activity was confirmed by characterization results with the porous/greater electroactive surface area. The remarkable increase in electrocatalytic activity was due to the surface roughness and the synergetic chemical coupling effects between rGO and Ni nanoparticles.

Keywords: Hydrogen energy, water electrolysis, reduced graphene oxide, nickel nanoparticles.

Aktif bir elektrokatalizör üzerinde suyun elektroliziyle hidrojen üretimi: rGO/Ni nanokompozit

ÖZ

Suyun elektroliziyle hidrojen üretiminde ekonomik ve etkin elektrokatalizlerin geliştirilmesi oldukça önemlidir. Bu çalışmada, nikel nanoparçacıklarla dekore edilmiş indirgenmiş grafen oksit (rGO) bazlı bir elektrokatalizörün basit bir tasarımı anlatılmaktadır. Voltametrik çalışmaların ve hidrojen oluşumu reaksiyonu (HER) kinetiğinin sonuçları, 152 mVdec-1'lık düşük Tafel eğimi ve 0,5 M H2SO4 çözeltisi içinde uzun süreli gösterdiği dayanıklılıkla (24 saatin üzerinde), hazırlanan nanokompozitin hidrojen üretimi için etkili ve kararlı bir elektrokatalizör olduğunu göstermiştir. Ayrıca gözenekli/daha yüksek elektroaktif yüzey alanıyla HER aktivitesinin arttığını karakterizasyon sonuçları doğrulamıştır. Elektrokatalitik aktivitedeki dikkate değer artış, yüzey pürüzlülüğünden ve rGO ile Ni nanopartiküller arasındaki kimyasal etkileşmelerin sinerjik etkilerinden kaynaklanmaktadır.

Anahtar kelimeler: Hidrojen enerjisi, suyun elektrolizi, indirgenmiş grafen oksit, nikel nanopartikül.

1. INTRODUCTION

Energy demand and consequently environmental pollution increasing day by day. Hydrogen energy is viewed as a clean energy, alternative to the traditional fossil energy sources.[1-6] Although there are many production methods, water electrolysis is the most featured method because it is a cheap, sustainable and clean process.[7-10] So far, commercially available Pt/C is the most efficient electrocatalyst for the hydrogen evolution reaction (HER) but the use of these expensive catalysts does not allow viable operation of such processes on an industrial scale.[11,12] Inexpensive non-noble metal electrocatalysts are essential for successful hydrogen production.[13-16] As such, researchers have shifted their focus to base metals such as nickel (Ni), which are cheap yet exhibit high catalytic performance.[17-20] Trasatti plotted the logarithm of the exchange current density to the metal-hydrogen bond strength for various metals for hydrogen evolution reaction in acidic media. This diagram is known as a volcano diagram and allows us to compare the electrocatalytic activity of different metals on HER.[21] In this volcano plot, Ni is close to Pt, as an efficient catalyst for HER.[22] Besides, the use of metals in nanoscale not only provides to develop a cost-effective material, but also provides a more effective electrocatalyst with a high surface/volume ratio.[23] At

DOI: http://dx.doi.org/10.32571/ijct.1199967 **E-ISSN: 2602-277X**

the same time, an appropriate support material plays a significant role for homogenous distribution of the metal catalyst and to demonstrate the effectiveness of it. As is known, the electrocatalytic activity of Ni can be increased with support materials or co-catalysts.[24,25] The reduced graphene oxide (rGO) is regarded as the catalyst support of choice due to its excellent properties of high specific surface area and superior electrical conductivity.[26-29] Furthermore, the effectual interaction between metal rGO increases the catalytic activity by increasing the active sites of the electrocatalyst.[30] Although there are many studies in the literature in which rGO is used as a supporting material for metal catalysts and numerous reduction methods for the preparation of rGO have been described,[31-33] developing a facile, low-cost and one-step method is still accepted as a challenge.

In this work, the surface of the glassy carbon electrode modified by reduced graphene oxide layer and then decorated with Ni nanoparticles, as an effective electrocatalyst for hydrogen evolution reaction in acidic media. As an alternative to the electrodes obtained by using many complex and expensive methods in the literature, the goal of this study is to obtain a new electrode surface for hydrogen evolution reaction by a simple, low cost and eco-friendly method. Linear sweep voltammetry (LSV) was used to get an idea about the electrocatalytic activity of rGO/Ni nanocomposite electrode for hydrogen evolution reaction. Then the Tafel polarization curves and electrochemical impedance spectroscopy (EIS) techniques were used to identify the electrode kinetics for HER. The morphology and elemental analysis of the electrode surface were carried out by scanning electron microscopy (SEM) and energy dispersive X-ray spectroscopy (EDS). Furthermore, the stability test of the rGO/Ni nanocomposite electrode was performed by chronopotentiometry technique.

2. MATERIALS AND METHODS

2.1. Materials

The chemicals and reagents of aqueous suspension of graphene oxide (GO), nickel sulphate (Ni_2SO_4), sulfuric acid (H_2SO_4), disodium hydrogen phosphate (Na_2HPO_4) were purchased from Sigma-Aldrich and were used without further purification. Deionized water was used for all experiments.

2.2. Methods

The electrochemical measurements were performed by potentiostat (Gamry Interface 1000) in a classical three-electrode system in 0.5 M H_2SO_4. The electrochemical cell system consisted of a Pt wire (counter electrode), Ag/AgCl/Cl^- reference electrode and a modified GCE as an indicator electrode. The modified electrodes and the bare electrode (for the comparison), tested for HER performance by LSV, EIS and Tafel polarization curves. The LSV tests were conducted in 0.5 M H_2SO_4 at a sweep rate of 10 mV s^{-1}. The electrochemical impedance spectroscopy analysis was measured in the same electrochemical cell overpotential of -0.55V using frequency range between 10^6 and 0.1 Hz with 5 mV of AC amplitude voltage.

First the surface of the glassy carbon electrode (3 mm diameter) was mechanically polished with a solution of alumina powder (0.3 µm). Then, the electrode was kept in ethanol for 5 minutes and then in an ultrasonic bath in distilled water for 5 minutes. 7µL of 0.5 mg. mL^{-1} graphene oxide solution was dropped onto the electrode surface and dried in an oven at 70^{o}C for 15 minutes. The reduction of graphene oxide (rGO) was carried out by electrochemical reduction at a constant potential of -0.9 V [Ag/AgCl] for 900 s in 0.1 M phosphate buffer solution (pH=7). Also, the reduced graphene oxide surface decorated with nickel nanoparticles to achieve rGO/Ni surface.

In this case, the reduction of graphene oxide and nickel ions on the glassy carbon electrode surface was carried out simultaneously. After dropping 7µL of graphene oxide on the glassy carbon electrode it was dried as described above, then it was immersed in 0.1 M Na_2HPO_4 solution (pH=4) containing 0.05 M $NiSO_4$ and the reduction was performed at -0.9 V for 900s, so that the graphene oxide and Ni^{2+} ions were reduced simultaneously (rGO/Ni). All prepared electrodes were washed with distilled water and made ready for electrochemical measurements.

3. RESULTS AND DISCUSSION

3.1. Characterization Studies

The morphological properties of the electrode surfaces were analysed by SEM. Figure 1a shows the surface of the electrode coated with rGO, verifying the typical crumpled morphology. Figure 1b demonstrates the successful decoration of Ni nanoparticles onto rGO surface which is a major advantage for high electrocatalytic activity. Figure 1b, 1c and 1d are the different magnification images of rGO/Ni surface, which reveal the uniform distribution of Ni nanoparticles with multiple pores. The high magnification image shows distinctly the rough surface of the electrocatalyst. The size of the particles are in the range of 100-200 nm. It is well known that this bumpy surface provides more active sites which increases the accessibility of the H^+ ions, consequently the electrochemical performance of the catalyst.[34] Such a surface also facilitates the evolution of hydrogen gas bubbles. The chemical composition of the rGO/Ni composite film was evaluated by EDS and obtained spectrum is shown in Figure 2. The presence of carbon,

DOI: http://dx.doi.org/10.32571/ijct.1199967 **E-ISSN: 2602-277X**

oxygen and nickel peaks with mass and atomic percentage ratios are indicated in the EDS spectrum.

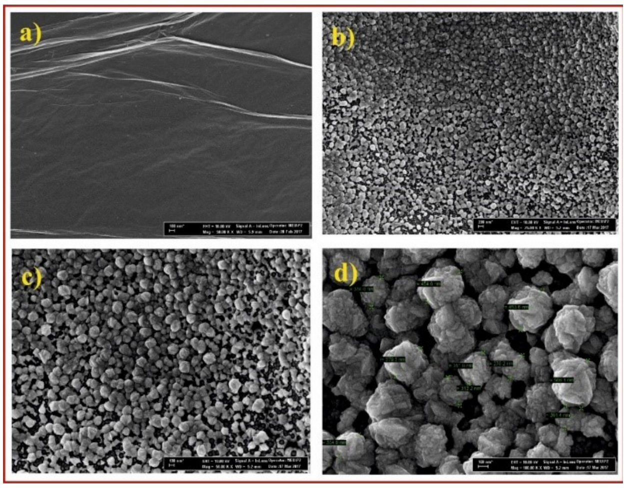

Figure 1. SEM images of rGO (a) and rGO/Ni surface with different magnifications (b-d).

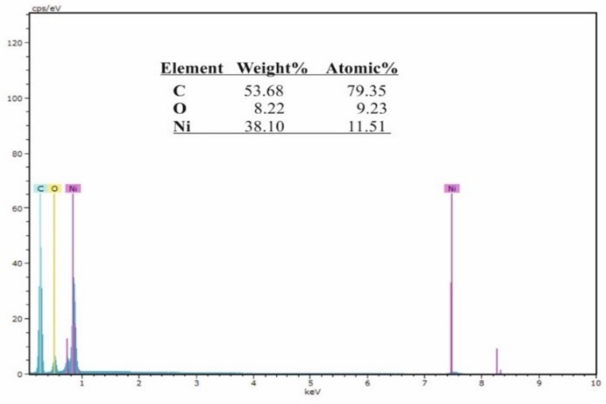

Figure 2. The EDS spectrum of rGO/Ni composite film.

3.2. Electrochemical Studies

The HER performances of the rGO and rGO/Ni nanoparticles coated electrodes first investigated with linear sweep voltammetry (Figure 3) in the potential range of -0.2 V and -0.8V. The polarization curve for GCE also obtained, for comparison. Data from LSV have demonstrated that the electron transfer rate in the Ni decorated composite film is fast, compatible with the high catalytic activity of the Ni particles. The catalytic performance of the rGO/Ni electrode was based upon to the structuration of the composite, which caused a homogenous distribution of the Ni nanoparticles on the rGO, as shown by SEM micrograph. Well dispersion of Ni nanoparticles on the rGO surface provides a large active surface area for H^+ adsorption, and it leads the higher current density, as expected.

After LSV studies, Tafel polarization curves (current-potential diagrams) of the electrodes were evaluated and the results given in the Figure 4.

From the Tafel polarization curves, it is seen that the highest current density is obtained on the GCE/rGO/Ni electrode. The calculated Tafel slopes were 249, 178 and 152 mV dec^{-1}, respectively. The Tafel slope denoted by *b*, derived from Tafel equation (η=a+*b*logi), provides important information about electrode kinetics and expresses as mV per decade (mV.$decade^{-1}$) of current.[35] The smaller slope, requires lower overpotential to get higher current densities. It seems clearly that, the calculated Tafel slopes are reduced when the electrode surface modified with rGO and then Ni nanoparticles. The decrease in Tafel slopes is an evidence of the enhancing the electrocatalytic activity for HER.[36,37]

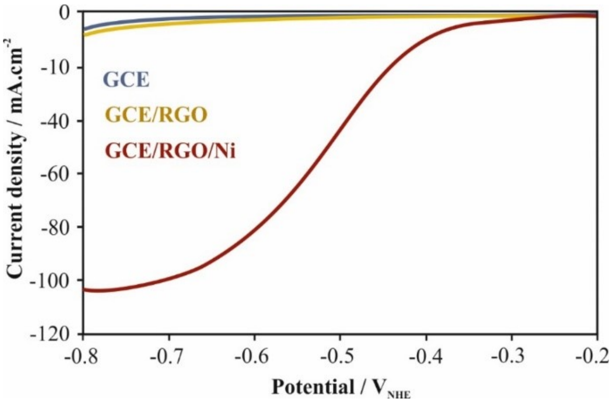

Figure 3. LSV of bare GCE, GCE/rGO and GCE/rGO/Ni electrodes recorded in 0.5 M H2SO4 solution (ν =10 mV s-1).

Another important parameter obtained for HER kinetics from Tafel plots is the required overpotential (η_{10}) to achieve 10 mA.cm^{-2} current density.[6,38] A smaller η_{10} indicates a higher catalytic performance. It can be seen from Figure 4 that the GCE/rGO/Ni exhibited the best HER activity with the smallest overpotential (0.475 V) required at 10 mA.cm^{-2}.

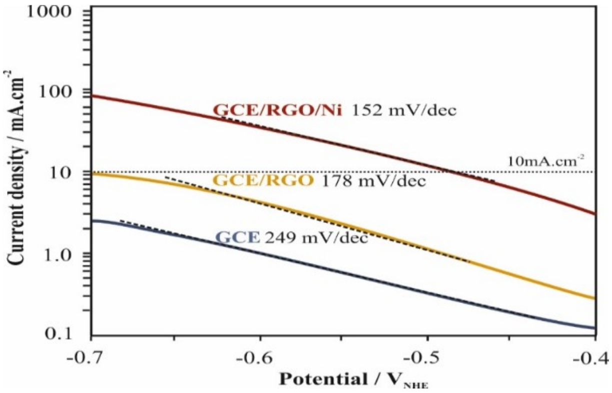

Figure 4. Current-potential diagrams (Tafel curves) of bare GCE, GCE/rGO and GCE/rGO/Ni electrodes recorded in 0.5 M H_2SO_4 electrolyte medium (v:1 mVs^{-1}).

The HER performances of the electrode surfaces also examined by electrochemical impedance spectroscopy measurements. The EIS results are shown as Nyquist diagrams in Figure 5 to better understand the electrochemical behaviour of rGO and rGO/Ni coated electrodes. The semi-circle obtained from Nyquist plots have been simulated with the Randles equivalent circuit which shown as inset in Figure 5, consisted of electrolyte resistance (R_e), a constant phase element (CPE) used instead of a double layer capacitance (C_{dl}), in order to give a more accurate fit to the experimental results. The calculated double layer capacitance values were 9.03 and 1.22 mF.cm^{-2} for rGO/Ni coated and rGO coated electrodes respectively. This result confirms the higher hydrogen adsorption of the porous structure which leads the higher electrocatalytic performance for hydrogen evolution.

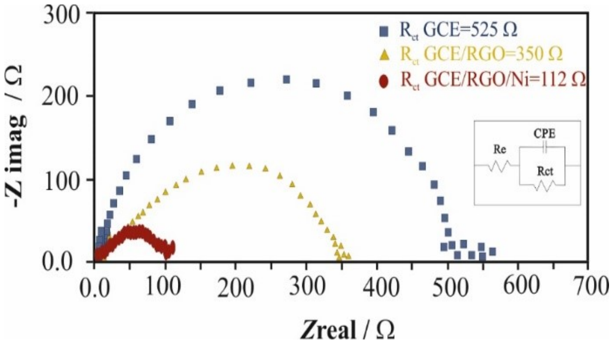

Figure 5. Nyquist diagrams of bare GCE, GCE/rGO and GCE/rGO/Ni electrodes recorded in 0.5 M H_2SO_4 at-0.55V.

The real and the imaginary impedance of the rGO/Ni coated electrode are significantly lower than that of the rGO coated electrode. The charge transfer resistance for hydrogen formation was calculated for bare GCE as 525Ω, it decreases to 350 Ω on the rGO coated electrode and to 112 Ω on the rGO/Ni coated electrode. The values of R_{ct} can be represented for the total reaction resistance, and lower reaction resistance means higher electrocatalytic performance for HER.[39-40]

3.3. Stability Studies

We also investigated the HER performance of the as-prepared electrode by stability tests. The long-term stability of rGO/Ni nanocomposite was tested at -0.7 V, the result shown in Figure 6 revealed that the as-prepared electrode can work continuously for ≥24 h with a slight decrease.

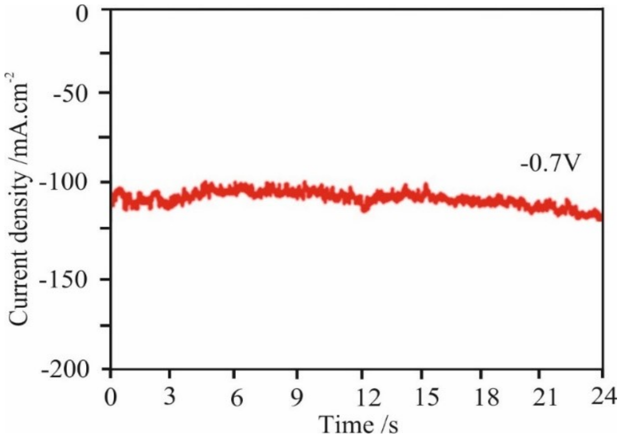

Figure 6. Long-term stability test of rGO/Ni coated electrode in 0.5 M H_2SO_4 at-0.7V.

CONCLUSIONS

An efficient electrocatalyst, based on reduced graphene oxide (rGO) decorated with Ni nanoparticles was synthesized by a facile method in this study. The synthesized nanocomposite was characterized by SEM and EDS techniques. The Ni nanoparticles were found to be uniformly distributed on the rGO sheets which had high surface area. The electrocatalytic activity of the nanocomposite investigated for hydrogen production, by electrochemical measurements; by LSV, Tafel extrapolation curves and EIS. High electrocatalytic activity was observed for the rGO/Ni nanocomposite, with a Tafel plot slope of 152 mV dec^{-1}, a low charge transfer resistance of 112 Ω and a long-term stability over 24 h at -0.7V. These results demonstrate that this nanocomposite which synthesized by a facile and cost-effective way, is a promising catalyst for applications water electrolysis to produce hydrogen.

ACKNOWLEDGEMENTS

The author is grateful to Aksaray University Scientific Research Projects Coordination Unit (ASU-BAP, 2016-034) for financial support.

Conflict of interest

I declare that there is no a conflict of interest with any person, institute, company, etc.

REFERENCES

1. Razi, F.; Dincer, I. *Renew. Sustain. Energy Rev*. **2022**, 168, 112763- 112775.

2. Qureshi, F.; Yusuf, M.; Kamyab H.; Zaidi, S. Khalil M. J.; Khan, M. A.; Alam, M.A.; Masood F.; Bazli, L.; Chelliapan.; Abdullah, B. *Sustain. Energy Technol. Assess.* **2022**, 53, 102677-102694.

3. Wang, S.; Wu, X.; Jafarmadar S.; Singh, P.K.; Khorasani, S.; Marefati, M.; Alizadeh, A. *J. Energy Storage* 2022, 54, 105274- 105290.

4. Zahedi, R.; Ghodusinejad, M. H.; Aslani, A.; Hachem-Vermette, C. *Energy Strategy Rev.* **2022**, 43, 100930-100946.

5. Ang, T-Z.; Salem, M.; Kamarol, M.; Das, H.S.; Nazari, M.A.; Prabaharan, N. *Energy Strategy Rev.* 43, **2022**, 100939-100964.

6. Balun Kayan, D.; Baran, T.; Menteş, A. *Electrochim. Acta*, **2022**, 422, 140513-140520.

DOI: http://dx.doi.org/10.32571/ijct.1199967 **E-ISSN: 2602-277X**

7. Yu, Z-Y.; Duan, Y.; Feng, X-Y.; Yu, X.; Gao, M-R.; Yu, S-H. *Adv. Mater.* **2021**, 33, 2007100-20071034.
8. Ahmed, S. F.; Mofijur, M.; Nuzhat, S.; Rafa, N.; Musharrat, A.; Lam, S.S.; Boretti, A. *Int. J. Hydrog. Energy,* **2022**, 47(88), 37227-37255

9. Vıdas, Leonardo; Castro, Rui. *Applied Sciences*, **2021**, 11(23), 11363-11389.
10. Kamaroddin, M.F.A.; Sabli, N.; Abdullah T.A.T.; Siajam, S.I.; Abdullah, L.C.; Jalil A.A.; Ahmad, A. *Membranes*, **2021**, *11(*810), 1-28.

11. Yao, R-Q.; Zhou, Y-T.; Shi, H.; Wan, W-B.; Zhang, Q-H.; Gu, L.; Zhu, Y-F.; Wen, Z.; Lang, X-Y.; Jiang, Q. *Adv. Func. Mat.* **2021,** *31*(10), 2009613-2009621.

12. Liu, C.; Song, H.; Dai, Z.; Xiong, Y. *Ionics*, **2022**, *28*(3), 1311-1321.

13. Cao, Z.; Song, H.; Liu, C.; Tang, W.; Liu J.; Yang, B.; Xie, W.; Yu, Z. *Electrocatalysis*, **2022**, 13, 807–817.

14. Kumar, S.S.; Lim, H. *Energy Reports*, **2022**, *8*, 13793-13813.

15. Theerthagiri, J.; Lee, S. J.; Murthy, A.P.; Madhavan, J.; Choi, M.Y. *Curr. Opin. Solid State Mater. Sci.* **2020,** *24*(1), 100805-100826.

16. Wu, T.; Sun, M.Z.; Huang, B.L. *Rare Metals*, **2022**, 41, 2169-2183

17. Ji, L.; Lv, C.; Chen, Z.; Huang, Z.; Zhang, C. *Adv. Mater.* **2018**, *30*(17), 1705653-1705659.

18. Chen, Z.; Wei, W.; Ni, B.J. *Curr. Opin. Green Sustain. Chem.* **2021**, *27*, 100398-100405.

19. Wu, H.; Feng, C.; Zhang, L.; Zhang, J.; Wilkinson, D.P. *Electrochem. Energy Reviews* **2021**, *4*(3), 473-507.

20. Guo, M.; Song, S.; Zhang, S.; Yan, Y.; Zhan, K.; Yang, J.; Zhao, B. *ACS Sustain. Chem. Eng.* **2020**, *8*(19), 7436-7444.

21. Trasatti, S. *J. Electroanal. Chem.* **1972**, 39, 163-184.

22. Jin, H.; Liu, X.; Chen, S.; Vasileff, A.; Li, L.; Jiao, Y.; Song, L.; Zheng, Y.; Qiao, S-Z.; ACS Energy Lett. **2019**, 4, 4, 805-810

23. Chang, H.; Shi, L.N.; Chen, Y.H.; Wang, P.F.; Yi, T.F. *Coord. Chem. Rev.* **2022**, *473*, 214839-214870.

24. Zaher, A.; El Rouby, W.M.; Barakat, N.A. *Fuel*, **2020**, *280*, 118654.

25. Liu, G.; Hou, F.; Peng, S.; Wang, X.; Fang, B. *Nanomaterials* **2022**, *12(17),* 2935-2947.

26. Askari, M.B.; Rozati, S.M.; Salarizadeh, P.; Azizi, S. *Ceramics International*, **2022** *48*(11), 16123-16130.

27. Karimi, A.; Kazeminezhad, I.; Naderi, L.; Shahrokhian, S. *J. Phys. Chem.* C., **2020**, *124*(8), 4393-4407.

28. Wan, Z., Bai, X., Mo, H., Yang, J., Wang, Z., Zhou, L. *Colloids Surf A Physicochem Eng Asp.* **2021**, 614, 126048-126059.

29. Zhao, X.; Luo, D.; Wang, Y.; Liu, Z.H. *Nano Res.* **2019**, *12*(11), 2872-2880.

30. Xu, Q.; Zang L.; Li, Z.; Shen, F.; Zhang, Y.; Sun, L.; *Int. J. Hydrog. Energy,* 2**022***,* 47(91), 38571-38582.

31. Wu, J.; Wang, J.; Huang, X.; Bai, H. *Energy Environ. Sci.* **2018**, 11(5), 1280-1286.

32. Rafiee, M.; Nitzsche, F.; Laliberte, J.; Hind, S.; Robitaille, F.; Labrosse, M.R. *Compos. B: Eng.* **2019,** *164*, 1-9.

33. Qian, H.; Wang, J.; Yan, L. *J. Bioresour. Bioprod.* **2020**, *5*(3), 204-210.

34. Nairan, A.; Liang, C.; Chiang, S.W.; Wu, Y.; Zou, P.; Khan, U.; Liu, W.; Kang F.; Guo S.; Wu, J.; Yang, C. *Energy Environ. Sci.* **2021**, *14*(3), 1594-1601.

35. Murthy, A.P.; Theerthagiri, J.; Madhavan, J. *J. Phys. Chem. C.* **2018**, *122*(42), 23943-23949.

36. Wu, L.; Hoof, A. J. F.; Dzade N.Y.; Gao L.; Richard M-I.; Friedrich H.; Leeuw N.H.D.; Hensen E.J.M.; Hofmann J. P. *Phys. Chem. Chem. Phys.* **2019**, 21, 6071-6079.

37. Najafi, L.;, Bellani, S.; Oropesa-Nuñez, R.; Ansaldo, A.; Prato M.; Castillo, A. E. D.R.; Bonaccorso F. *Adv. Energy Mater.* **2018**, 8, 1703212-1703227.

38. Zeng M.; Li, Y. ***J. Mater. Chem. A*, 2015**,**3**, 14942-14962

39. Balun Kayan, D.; İlhan, M.; Koçak, D. *Ionics*, **2018**, *24*(2), 563-569.

40. Wang, X.; Zhou, H.; Zhang, D.; Pi, M.; Feng, J.; Chen, S. *J. Power Sources*. **2018**, *387*, 1-8.

DOI: http://dx.doi.org/10.32571/ijct.1105415 **E-ISSN: 2602-277X**

International Journal of Chemistry and Technology

http://dergipark.org.tr/ijct

Research Article

Chemical extraction of Biodiesel and Parametric analysis of DI-Diesel Engine using Algae esterified Oil-Gasoline Blends

Panduranga MURTHY[1*] Rajesh KUMAR[2]

[1]*Ranchi University, University Department of Chemistry, Ranchi-834 001, India.*

Received: 18 April 2022; Revised: 11 September 2022; Accepted: 22 September 2022

*Corresponding author e-mail: drgpmurthy2467@gmail.com

Citation: Murthy, P.; Kumar, R. *Int. J. Chem. Technol.* **2023**, 7(1), 6-24.

ABSTRACT

Of late, the automobiles of all categories are massively increasing which aggravates the dependency on fossil fuel thus, the accessibility of petro-fuel decreases relentlessly. Under these circumstances, the investigations are taking new dimensions to find alternative, renewable with cost-effective fuel exclusively biofuels. However, a newer approach has been attempted for the production of biodiesel from wild stuff of Spirulina algae which is explored directly in its aquatic systems of the natural environment. The chemical extraction process was attempted with wild biomass of algae via pre-treatment for obtaining promising lipid content then; the algal oil (lipid) was subjected to the production of biodiesel through sequential transesterification reactions. The obtained biodiesel was measured as 94.65% produced from 0.920kg of algal oil extracted out of 1.6kg of algal biomass in a stipulated duration of time (2.50hr) taken for attaining maximum temperature. Further, the produced biodiesel was evaluated for its distinctive properties and the outcomes were compared with ASTM standard specifications. All the results appeared to be within the standards limit thereby, the methodical analysis was done for the performance and emission parameters via interacting algal biodiesel in the experimental (DI) diesel engine test-rig configured with a variable injection pressure of 210, 220 & 230 respectively. The blending ratio of algal diesel and gasoline (AB10 & AB 20v/v) were prepared based on volume and the results were correlated with petro-diesel. The physico-chemical parameters like color, odour, viscosity, density, total acid number, initial boiling point, flash point, calorific value, cetane number etc. were found to be significant when compared with petro-fuel. Correspondingly, the interactive parameters like flash point, pour point, cloud point, carbon residue, sulfur, ash, and water contents were correlated with the standard specifications. The substantial approach was observed in emission characteristics such as hydrocarbon (HC), carbon monoxide (CO), oxides of nitrogen (NOX) respectively in engine-algal fuel interactions. Whereas, a slight increase than petro-diesel with respect to sulfur oxide (SOX) emission and smoke opacity were also recorded. However, the marginal increase in Brake specific fuel consumption (BSFC) and Brake thermal efficiency (BTE) was noticed and the brake power (BP) was found slightly lower than petro-diesel. In conclusion, the protocol of producing biodiesel from wild stuff biomass of Spirulina maxima was found to be techno-economically feasible and this potential algal biodiesel can be recommended for the current engine applications without any alterations.

Keywords: Microalgae, wild stuff of Spirulina maxima, Biodiesel production, Direct injection (DI) Engine, Performance-Emission analysis, Algae Oil-Gasoline blends.

1. INTRODUCTION

The limitations of exploiting non-renewable fossil fuels are a center of attention in the world with respect to environmental protection from global warming in terms of the release of greenhouse gases, climatic fluctuations, a decline in economic growth, and steadiness followed by rapid depletion of oil reserves[1,2]. Therefore, the development of potential and alternative fuel resources is very essential for monitoring the present global energy state of affairs. The search is already scheduled for one of the promising unconventional fuel sources called biofuels which is a renewable and real-time approach [3,4]. The most recurrent biofuels comprising biodiesel, bioethanol, bio-butanol, and biogas respectively are in line with production with less expensive methods. The production of these biofuels is derived mainly from vegetable sources like soybean, Sesame, Niger, sunflower, groundnut, etc. and non-edible sources such as Pongamia, Jatropha, Simaruba, Neem, Mahuva followed by non-food biomasses, agricultural wastes, and animal wastes respectively. Despite these resources available for the production of biofuels, the factor of cost-effectiveness is needed for the hour consequently; the research community formed with scientists and technologists is, therefore, motivated to think about a range of most effective alternative sources for boosting the energy sector[5-7]. However,

DOI: http://dx.doi.org/10.32571/ijct.1105415 **E-ISSN: 2602-277X**

algae have been demonstrated as the best efficient resource for biodiesel at optimum level, thus algae furnished with modified protocols are of great importance in the present scenario.

However, algal biodiesel has emerged as the most practical resolution in India to corroborate the deficient components that occurred due to the scarcity of petroleum fuels. The statistics on the exploitation of petroleum products is about 125 million tons per annum as projected in the country. Interestingly, the feedstock of microalgae has been identified as it is the only source which can operate precisely to minimize the burden on petro-fuels and also cutback of the oil imports[8,9]. Besides, the obligation on the need of a very large land area can be reduced, if the algal feedstock has opted. The algae can give a good amount of oil yield per acre of cultivation even with extremely less input. It has been estimated that less than 3-4 percent of total cultivating land is adequate to produce sufficient algae biodiesel for substituting all petro-fuels being used in the country[10]. However, microalgae have been justified as a reliable source of feedstock and defined alternative to fossil-fuel by facilitating large-scale biodiesel production.

1.1. Algae: A glance on biofuel research

As a result of incessant investigations accomplished by illustrious researchers, algae are found to be the most prospective sources for mitigating the substitution of fossil fuels[11]. The higher photosynthetic competence is the predominant factor as compared to other terrestrial feedstock which is also a discrete benefit of the algal community[12]. The substantial production of algal biomass in natural habitation has already proven by its significant yields of biomass per day and per unit cropping area without placing any input and no agricultural land with a large area is required.
Furthermore, the sustainability of biodiesel production is well in line with micro-algae which are demonstrated in the process of biodiesel production, where the algae can consume carbon dioxide in the environment, where algae can captivate carbon dioxide from the air for the process of photosynthesis and replacing it with oxygen[13]. As a result, algae biodiesel plants have become very close to energy manufacturing plants that produce lots of carbon dioxide and the reprocessing of carbon dioxide by the algae community can reduce environmental pollution. Besides, the imperative approach of algae which can also generate some beneficial byproducts such as bio-manure and processed feed-stock without depleting other food sources. Further, the differential approach of algal strains with respect to appearance, color, biomass texture, cultural conditions, and chemical compositions can strongly facilitate a variable significant amount of biodiesel which can trigger efficient engine performance and exhaust gas emission while retaining superficial energy dynamics[14, 15].
The algal biofuels will have lesser impact on the environment as compared with the biodiesel derived from food producing typical crop plants. The selection of strain, method of cultivation, culturing conditions, and the chemical profile are strongly facilitating the cost effectiveness and also significantly exciting engine's performance and exhaust gas emissions[16]. The importance of the proposed study was to make an attentive analysis of the impact of the use of biodiesel produced from microalgae to the diesel engine system. There is a huge divergence in the number of papers reported on collection of algae, culturing process, oil extraction, and biodiesel production followed by overall engine performance[17]. The analytical works relating to the blending phenomenon of both biodiesel and petro-diesel is also considerably untouched as it is the most requisite approach in the automobile industry[18].

The thorough analysis of literature indicated that only a few attempts were made on different blending ratios (B5 to B50) of biodiesel and gasoline. Whereas, the tested clean biodiesel characteristics were found to be analogous with petro-diesel at B20 proportions[19]. The results also showed that some serious noxious pollutants can be reduced if the produced bio-fuels are from appropriate sources with diverse strains. Although, there was a non-significant increase of NOx which may possibly be associated with higher temperatures in the combustion chamber. Besides, the usage of additives/emulsions as a supplement to the mixture of blends or neat biodiesel exhibited a promising impact on reductions of CO2 and NOx[20]. However, few reports on testing engine efficiency with the blends of clean biodiesel and gasoline displayed some ambiguity results where the well-defined essential statistics on all the experiments is seriously lacking. However, the evaluation of biodiesel produced from algae conceivably is a field almost not explored accurately as the available research papers encompassing contrary results or perhaps the specific objectives are not explicitly deliberated with respect to the biofuel-engine interactive performances as this review makes evident[21].

1.2. The need for Research Intercession

The studies linking to the production of algal biodiesel, fuel mechanical properties in comparison with ASTM specifications are certainly lacking thus, this gap has to be bridged by framing the appropriate objectives[22,23]. Hence, the core objective of the current study was to analyze the efficiency of algal oil in association with blending performance in the experimental engine system. The physico-chemical characteristics of the algal esterified oil were decisively assessed and the promising blends were subjected to parameterize the virtual enactment of a diesel engine for performance and emission characteristics and were also critically evaluated through a comparative approach in the engine system running on algal biodiesel. Some of the previous research works on algae source concerning their types, growth attributes, processing for biodiesel production, optimization parameters followed by engine interactions were prominently discussed in the following review studies.

Therefore, in the recent scenario, the effectiveness of Biodiesel derived from algae source has been considered as a substitute to the other renewable fuels which are based on their diverse characteristics such as performance, emission, and combustion coupled with steadiness in the engine interaction with the fuel. Initially, combustion is a crucial process which helps in evaluating the feasibility of the tested biofuel as well as overall competency of the engine. Further, the crucial factor is validating performance characteristics like, thermal efficiency, engine power, specific fuel consumption, torque, brake power, respectively. Finally, the emission properties are concerned, environmental approval is a strategic aspect for selection of fuel and gratification of environmental regulatory norms which are deliberated exclusively for exhaust gases[23].

Hence, the review of literature consistently reveals that many researchers have experimented on diverse range of engine system using different blending ratios (5% to 100%) of biodiesel by weight/mass and this has molded some unpredictable outcomes that are difficult to compare the overall performance of the engine system. Consequently, the literature analysis on engine performance has been represented in a tabular format for having critical analysis and also for better understanding on the engines of variable configuration. Thus, the previous studies carried-out on the production of Bio-fuels from different bio-resources followed by biofuel-engine interactions are analytically deliberated hereunder.

1.3. Recent investigations on the production of Bio-fuels from different bio-resource samples

Feedstock	Objectives focused	Major findings	Ref.
Microalgae *Spirulina platensis*	To assess fuel properties for microalgae biodiesel and its blends with Egyptian petro-diesel were analysed.	All the characteristics were closer to the standard range with competence. The outcome was significant.	[24]
Green algae (*Chlorophyceae*)	To appraise the performance and emission characteristics of Algae Bio-fuel supplemented with additives using blends of biodiesel & diesel fuel.	The Performance was accelerated admitting with low emission. Biodiesel- diesel blends with nanoparticles were attempted to get a little modified fuel. Results on performance and Emission tests are compared for both fuels.	[25]
Sunflower oil	To achieve production & optimization of Biodiesel by RSM approach. CI engine was interacted with blends of biodiesel & diesel fuels for assessing its performance and its emission characteristics.	The blending of B5, B10, B15 (biodiesel with diesel fuel) were found to be significant in decreasing harmful gas emissions while maintaining equivalent performance output and efficiency.	[26]
	To evaluate performance of Algae oil using Diesel Engine system configured with different Injection pressure.	The superior performance in the diesel engine as well as reduced emission characteristics was noticed with change in injection pressure of AME20.	[27]
	To know how the performance and exhaust emissions in the Diesel Engine adopted to interact with blends of algal biodiesel-diesel *i.e.,* B10, B20 respectively.	Similar approach of physico-chemical properties in blends of biodiesel (B10 and B20) was observed. B20 blend displayed a considerable decrease in specific fuel consumption & exhaust gas temperature, similarly, a substantial increase in B20 than B10 blending was noticed in thermal efficiency. The emission gas was reduced considerably at B20 compared to B10 blending ratios of both fuels. The superior grade of biodiesel can be achieved from microalgae *S. obliquus* and may recommend the same with eco-friendly approach in the conventional diesel engine system.	[28]

Spirulina maxima algae	To Optimize Biodiesel production from *Spirulina maxima* microalgae and testing of performance in a diesel engine.	The physico-chemical properties of the optimized biodiesel were equated with the ASTM D6751 standard specification and found to be justified as it is closer to petro-diesel. The unmodified diesel engine interacted with biodiesel blends of both 20 % and 40 % (v/v) for its performance and emission tests which showed significant as a whole when compared with Diesel fuel outcomes. But, the amount Nox found to be little higher in biodiesel than petro-diesel which is due to presence of more oxygen within it. This may leads to complete combustion of the fuel and inturn raises the temperature of products.	[29]
Microalgae	To cultivate microalgae for the production of biodiesel by employing both upstream and downstream techniques.	Microalgae require less land as compare to other feedstock. The cultivation practice of algae found to be more economical compared to other feedstock.	[30]
Non-edible Oils	To appraise the efficacy of additives supplementing with biodiesel fuel to enhance the combustion and performance followed by reducing the emission using direct injection diesel engine.	The employing of selected additives with variable specifications *i.e.,* metal-based, cetane number, antioxidant, & oxygenation facilitated the improved characteristics of biodiesel. But, the use of additives will affect the cost effectiveness of the biodiesel.	[31]
Microalgae, fossil diesel, and Soybean Methyl Ester	To analyse performance & emission characteristics of microalgae fuel using combustion engine system. The esterified oils of microalgae, soybean methyl ester and blends with fossil diesel are used.	Lower power & torque to some extent, More SFC, reduced NOx & PM at lower blending ratio. İn all, it was compatible with petro-diesel	[32]
Microalgae	To assess the efficiency of microalgae biodiesel and biodiesel from vegetable oils is also attempted.	Comparatively, algae displayed more economical than other feedstocks.	[33]
Vegetable oil and animal oil	To understand the efficacy of vegetable oils supplemented with new solid catalyst for enhancing the Biodiesel production *via* transesterification.	Increase BSFC & BTE and reduction in HC & CO and the other related parameters are within the acceptance range. But, the economics of the biodiesel derived from animal oil has to be viable	[34]
Algal biomass	Production of Biodiesel from algae and suggesting it as an alternative fuel for Diesel	The characteristics analysed were within the range of ASTM standards and were comparatively analogous. The cultural segment has to be reformed.	[35]
Algae Oil	To analyse the characteristics of performance, emissions, sound and combustion in Algae oil Biofuel.	The increased oxides of carbon and decrease of nitrogen, hydrocarbons were noticed at lower fuel blends.	[36]
Soybean, Rapeseed, Cottonseed, Palm oil, Peanut + sun-flower, Mineral Diesel	To evaluate spray, combustion, performance, and emissions characteristics of Biodiesel fuelled engines by Computational approach.	The results are found to be within the genuine range except some differential approach in emission properties. İn addition, the edible oils are not viable as these sources have food cum medicinal value. So, non edible oils are suggested.	[37]
FAEE, FFA, Glycerol, Triglyceride	To know-how the consequences of producing biodiesel from acidic oil using sulfuric acid and calcium oxide as catalysts with techno-economic feasibility.	Acidic oil using sulfuric acid and calcium oxide are used as catalysts are employed. The Catalysts showed improved performance of the engine. Additives needs to be stndardized.	[38]
PME RME SME TME	To study the parameters such as cetane number, density, kinematic viscosity, and heating values from their respective fatty acid compositions to attain biodiesel.	The data was found to be compatible in line with cetane number and density. But, heating values and kinematic viscosity were found to be Poor.	[39]
ALGAE Methyl Esters	To study the characteristics of algae biodiesel by experimental engine test rig.	BTE & SEC were comparable, but CO_2 was increased and both CO & NOx reduced. The rate of heat release was also found to be compatible with respect to engine efficiency.	[40]

DOI: http://dx.doi.org/10.32571/ijct.1105415 E-ISSN: 2602-277X

Algal feedstock	To investigate the blends of Algae oil-Gasoline for its performance at variable compression ratio (VCR) Spark Ignition Engine.	Algal-fuel blends showed increase in BSFC and reduction in BTE thereby engine peroformance was found to be significant.	[41]
Algal biomass (Unused)	To study the magnitude of biodiesel production from unused algae and analysis of fuel & emission characteristics.	The results were found to be within the ASTM standards with respect to fuel performance and emission properties. CO, CO_2 & HC were reduced and higher Nox was noticed.	[42]
Algae Oil	To analyse the characteristics of Performance and Emission in VCR Diesel Engine interacted with Algae Oil.	Algae-20 has showed better engine performance and the exhaust characteristics were found to be marginally reduced.	[43]
Biodiesel from Freshwater Algae	To study the performance of CI Engine at different compression ratio fuelled with freshwater algae biodiesel.	The blends of both B10 and B20 fuel are recommended as ideal proportions for CI Engine system. The results of both B10 and B20 algal blends were found to be closer to that of petro-diesel relating to overall performance characteristics.	[44]
Rubber seed oil	To produce of biodiesel using rubber seed oil by catalysed transesterification processes	By varying the reaction mixture, biodiesel has been achieved to a significant level.	[45]
Vegetable oils	To determine the response in vegetable oils added with a new solid catalyst for enhancing Biodiesel *via* transesterification.	Cracking and hydrocracking approach by the role of heterogeneous catalysis is noticed, thus, the process can be employed to exercise vegetable oils into fuels with deoxygenated hydrocarbon	[46]
Bio-fuels (Nine varieties) and pure diesel.	To study the characteristics like, performance, combustion, and emission of various biofuels through numerical investigation.	Nine different alternative biofuels along with petro-diesel were employed. The efficacy of biofuels has been justified for exploring as alternative fuels.	[47]
Microalgae	Assessment of combustion characteristics of engine fuelled with sustainable biodiesel with respect to magnitudes of injection timing and pressure.	Injection timing and pressure on CI Engine was recorded and the results are quite closer to petrodiesel	[48]
Microalgae	To review the prospective approach of microalgae to bio-fuels: Objective of Promising alternative and renewable energy	Review substantiated that; the algae will be a better option for alternative fuel.	[49]
Microalgae	To evaluate the effect combustion, performance, and emission characteristics of Microalgae Biodiesel using a Diesel Power Generator.	The algae oil can be used as fuel in Diesel Power Generator. Combustion, Performance and Emission Characteristics were found to be significant.	[50]
Microalgae	To know the performance and emission properties using a compression ignition engine. To analyse the effect of antioxidant additives with biodiesels for refining the parameters.	Treating biodiesel with antioxidant additive was found to be a promising approach for reducing NOx emission. In conclusion, performance is improved and emissions are reduced.	[51]

On account literature survey, it was apparent that the number of research investigations demonstrating the use of algal oil with engine interaction and its performance appear to be scarce and abridged to know-how the mechanism of fuel competence with the existing engine system. The exercise of algae esterified oil may conquer the difficulties relating to the practice of overpriced chemicals and laborious processes during the reaction of the transesterification process are of the most considerable factors for having sustainable production of biodiesel.

1.4. About Spirulina algal wild stuff

The search is on for documentation on diversified algae and their respective species at their natural origin and also monitoring of the conservation of algal diversity at their natural habitat. This database will make it possible to obtain desired algal types for biodiesel production[52].

The algal wild stuff collected in the study area was Spirulina is explicit biomass belongs to the group Cyanobacteria (blue-green algae). For a long time, Spirulina was regarded as algae. However, it is now known that it is a bacterium, thereby it can be able to perform photosynthesis; subsequently, it is classified as Cyanobacteria. This alga is found in ponds, lakes with increased pH. Therefore, it can only survive in alkaline waters, with a pH between 10 and 11. The algae Spirulina was found to be most viable for biodiesel production as it is having significant lipid contents in its biological organization[53,54].

The contemporary use of this biological resource has three patterns: traditional, scientific, and technological development, and the so-called green tendency. Spirulina is being cultured in vitro under controlled conditions. But, it has been focused to maintain and motor the wild stuff culture at its natural habitat

DOI: http://dx.doi.org/10.32571/ijct.1105415 **E-ISSN: 2602-277X**

followed by attempts with the cultural approach in large at its natural environment such as outdoor ponds, lakes, streams, trough/gully; other desired waterway channels under moderate-controlled conditions[55,56]. On the other hand, it is now widely cultured throughout the globe as a most stabilizing component with health benefits in a variety of human foods and animal feeds. Currently, the production of *Spirulina* worldwide is projected to be about 3000 metric tons. Besides, the market value of *Spirulina* is considerably high (70%) which is exclusively for human consumption in terms of healthy food supplemented with rich content of protein followed by essential amino acids, vitamins, essential fatty acids and minerals[57, 58].

In the Open System of Natural habitation (OSNH), it was found that the of S. maxima algae was most abundant in its natural ecosystem with respect to its production with the minimum technical strategies which can facilitate the significant production of *S. maxima* in its natural region like, controlling the culture temperature, minimizing production cost and displaying climatic data-based Habitation information modelling (HIM) cluster in their natural environment[59,60,61]. Hence, the proposed approach would be distinctive with significant objectives that can reduce the burden on culturing constraints of algae *in vitro*. However, the main focus of the current study is to produce biodiesel from algae wild stuff via chemical extraction methods and to analyse the efficacy of the algal oil with respect to performance and emission characteristics using a diesel engine experimental test rig at variable fuel blends.

2. MATERIALS AND METHODS

The wild stuff of *Spirulina maxima* algal material was collected productively in its natural origin at different locations of Devarayana Durga, Tumakuru district, Karnataka during 2019-2020 (Fig. A & B). The variability of algal samples in their growth expressions, were compared between two geographical regions *i.e.,* Ranchi, Jharkhand state and the Tumakuru & Mysuru (southern part) of Karnataka, India.

2.1. Materials

Pure sodium hydroxide as an alkaline catalyst, anhydrous sodium sulfate, chloroform, and methanol was procured from Merck Co. (Mumbai). All other chemicals used for the preparation of cultivation medium were of analytical grade. A commercial Gasoline/petro-diesel sample was obtained from a local fueling station. Besides, highly pure analytical grade chemicals were selected for this investigation: 99.8 % pure CH_3OH (methanol), 96 % pure H_2SO_4 (sulphuric acid), 86 % pure KOH (potassium hydroxide), diethyl ether, methylene chloride, n-hexane.

2.2. Classification of collected Microalgae

The collected algal sample was thoroughly analyzed using a light microscope and the characteristic features were assessed by means of standard references. Besides, the quantifiable observation of algal mass was done with plankton-counting cell method (Sedgwick rafter). Later, citation of algae was accomplished in accordance with the distinctive methods for ensuring its taxonomy[62,63].

2.3 Collection of Algal feedstock & pretreatment

The water samples with a visible micro-algal population of *Spirulina maxima* were collected from ponds, lakes, temple tanks, and rivers that are located in and around Devarayana durga a divine hill station of Tumakuru district (Karnataka), India. The wild stuff of *Spirulina maxima* was obtained openly from its natural habitat and the sample was then subjected to pretreatment. Primarily; the algal sample was properly washed with fresh water, dehydrated under shade, and subjected for heating in the oven at 70°C for complete removal of moisture. Subsequently, the dried algal biomass was made into fine powder using a mechanical grinder and the sample was mixed with water in 1:3 (v/v) ratios. Later, the cell destruction of the algae biomass was facilitated using an ultra-sonication process unit adjusted with 24 kHz frequency and 50°C temperature were monitored for 5-8 minutes. Then the sample was made ready for extraction of oil proceeding in line with biodiesel production (Figure 5A-F).

METHODS

2.4. Extraction of Oil from Algal sample

The pre-processed biomass of *Spirulina maxima* wild stuff was ground into a homogenous fine powder using a mechanical grinder and the dried cells of algae were mixed with the solvent system comprising of Hexane and Iso-propanol (3:2 v/v ratio). Then, the homogenate mixture was put into a soxhlet apparatus fitted to a round bottom flask and together with a magnetic stirrer. The cell residue was detached by the filtering process at 30°C for 2hr and the filtrate was transmitted into a separating funnel and sufficient water was added to induce the formation of a biphasic layer. The solvent mixture was partitioned soon after settling into two distinct phases, the top dark green hexane layer having most of the extracted lipids and the bottom light green layer containing most of the co-extracted non-lipids. Finally, the hexane layer was collected in a pre-weighted flask and subjected for evaporation using a rotary evaporator[64,65].

DOI: http://dx.doi.org/10.32571/ijct.1105415 **E-ISSN: 2602-277X**

2.5. Algal oils to Biodiesel production

The production of biodiesel was performed through time and temperature based receptive reactions called esterification and transesterification processes. The esterification reaction was carried-out using 98% acid catalyst, (H_2SO_4) and 100% lipid-derived from algal mass (wild feedstock), in the meantime, methanol (CH_3OH) was added and the ratio of alcohol/lipid was 50:2 (vol./wt.). Methanol (50% of the consigned volume) was added earlier to facilitate the dissolution of oil and the remaining 50% of the methanol was mixed with an acid catalyst followed by a total reaction component. The reaction was carried out at 60°C for 3 hours duration in continuous stirring using a water bath equipped with reflux system. The surplus alcohol was removed after the completion of reaction by evaporation using a rotary evaporator. Further, the esterified oil was subjected to a transesterification reaction with a base catalyst (NaOH/KOH) using methanol, and the rest of the reaction will be performed with the algal feed-stock as explained above.

2.6. Esterification of *S. maxima* algae crude Oil

Theoretically, it comprises two-step reaction processes, where, the esterification was performed at the initial stage with an acid catalyst (H_2SO_4), using a suitable glass reactor for the production of biodiesel. This has been explicitly recommended when the algal oil consists of a high content of Free Fatty Acid (FFA) which is above 2%. The esterification process facilitates the reduction of FFA in algal Oil which will be preventing the formation of emulsified soap as it will be inhibiting the yield of biodiesel at the end. Hence, the two-step process for the production of biodiesel has been carry out. Therefore, in the esterification reaction, H_2SO_4 (1.5%v/v) and 12:1 methanol to oil molar ratio with 500rpm stirring speed at 60^0C temperature for about 90 min duration were monitored [66, 67]. Finally, the esterified oil was separated through a separating funnel and the FFA (%) was found to be reduced from 5.9% to 0.450% (Fig. 1). Further, the esterified oil will be subjected to a transesterification process using an alkali catalyst (NaOH/KOH).

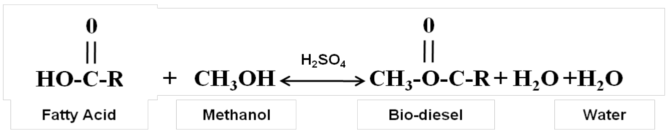

$$\mathrm{HO\text{-}\overset{O}{\overset{\|}{C}}\text{-}R} + CH_3OH \xleftrightarrow{H_2SO_4} \mathrm{CH_3\text{-}O\text{-}\overset{O}{\overset{\|}{C}}\text{-}R} + H_2O + H_2O$$

Figure 1. Esterification reaction with an acid catalyst

2.7. Transesterification of *S. maxima* algae Oil

Subsequently, the second stage of reaction is the transesterification process which is performed as a major step of biodiesel production. The esterified oil was transferred into the glass reactor and subjected for heating at 60°C. The base catalyst, KOH was prepared in a separate flask with methanol at different concentrations and the molar ratio was taken (Fig.2).

Subsequently, the methanolic KOH was subjected to heating up to 60°C and this was mixed with the algal oil. The reaction mixture was set aside for the period of 90 min to carry on the reaction and allow settling for 2 h in a distinctive funnel to separate the layer of biodiesel (top layer) and glycerol (bottom layer). Meanwhile, the optimizing reaction parameters like, biodiesel yield, molar ratio, amount of catalyst, temperature, reaction time coupled with a stirring speed were recorded at variable settings[68, 69,70]. At last, the upper layer containing biodiesel and a lower layer having glycerol was successfully divided. The Biodiesel was then subjected to the purification process and the glycerine was stored in a suitable container as it is having a value addition in soap industries.

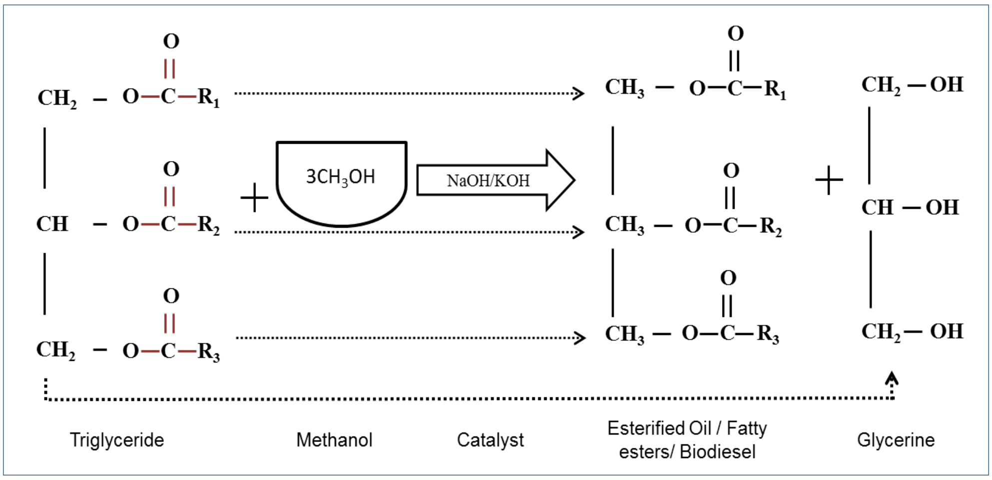

Figure 2. Transesterification reaction (R1, R2, and R3 are long-chain hydrocarbons/fatty acid) with the base catalyst

2.8. Determination of Biodiesel Yield (%)

The yield of Biodiesel (% w/w) was measured by the following standard formula (69).

$$\text{Biodiesel Yield (\%)} = \frac{\text{Weight of the biodiesel produced (g)}}{\text{Weight of the algal oil used (g)}} \times 100\%$$

2.9. Designing of Experimental Engine Test rig

The biodiesel from the Microalgae sample was subjected to interaction using a Diesel Engine having requisite configuration[71]. The engine test rig was designed based on the parametric objectives projected in the experiment. The specification consisted of a direct injection (DI engine) diesel engine provided by Kirloskar TV-I (Table 4). The experimental engine test rig was accomplished with a single-cylinder and 4-stroke water-cooled system having 3.4 kW brake power at a constant of 1600 rpm. In addition, the engine was further connected to an eddy current dynamometer provided with a well-acquainted controlling system. The engine test rig was compatible with elegant sensors for piezo-type cylinder pressure, crank angle, thermocouples to measure the temperature of the water, air, and exhaust gas respectively. Besides, a di-gas analyzer was affixed to measure the emissions from the exhaust gas. Besides, the smoke density from the engine exhaust gas was analyzed using AVL smoke meter[72,73]. The graphic diagram of the engine test rig has been represented (Fig. 3).

The DI-engine test rig was interacted with the clean algae oil-gasoline using a set proportion of fuel blends at a constant speed of 1600 rpm and the engine was allowed to run for 25 minutes till attaining a steady-state condition. The efficiency of the engine test rig for its objectives connected with range at variable loads and at each load, rate of airflow & fuel flow was measured. The exhausts gas temperature; oxides of nitrogen, carbon monoxide, unburnt hydrocarbon and smoke density were systematically recorded[74].

The tangible experiment with all the equipped configurations of engine test rig was performed to examine the efficacy of algae oil-gasoline blends of AB10 and AB20 respectively. The parametric analysis relating to the performance and exhaust emissions of the diesel engine was evaluated and the results were compared with diesel fuel. Further, observations were recorded after the engine reached its steady-state condition and then, the engine was re-stabilized before the operations at each trial. The trials were repeated and systematically monitored to ascertain the readings generated from experimental investigations.

The engine speed was constantly maintained at a speed of 1600 rpm at each engine load. The performance oriented parameters such as engine power, thermal efficiency, specific fuel consumption, air-fuel ratio followed by exhaust gas temperature and volumetric efficiency were evaluated. The analysis on emission parameters such as CO, CO_2, NOx, and HC were executed and the results were systematically recorded[75].

All the data were analyzed with ANOVA two way interaction test for the parameters and the features found to be significant ($p \leq 0.05$).

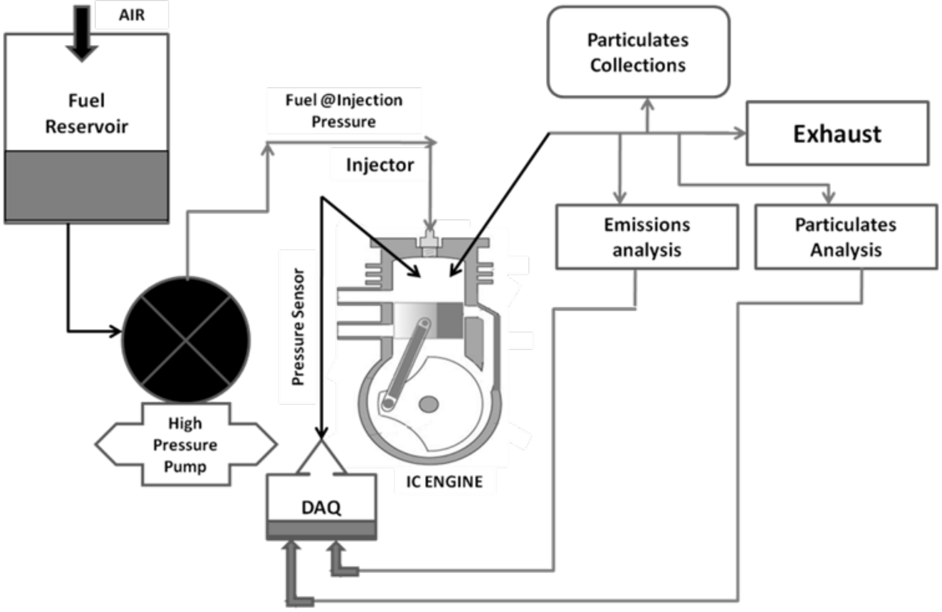

Figure 3. Schematic showing engine testing experimental layout

DOI: http://dx.doi.org/10.32571/ijct.1105415 E-ISSN: 2602-277X

3. RESULTS AND DISCUSSION

The analytical study was carried out in association with the Bio-energy Research division of Hamsa Research Foundation, Tumakuru during 2019-2020 in association with Azyme Biotechnologies, Bengaluru. The qualitative parameters were analyzed at Chemistry Research Laboratory, University department of Chemistry, Ranchi University, Ranchi, Jharkhand State, India.

3.1. Collection and Classification of Microalgae

The algal feedstock collected as wild stuff of algal biomass directly in the natural habitat during the baseline survey was identified as Spirulina maxima in its natural habitat (water bodies located near Devrayana Durga, Tumakuru district, Karnataka). The identification of algal species normally necessitates a concoction of both morphological and genetic description. The onsite morphological identification was done for the wild culture sample using a dissection microscope followed by a compound light microscope which was done using the standard method[76,77]. The collected sample was intact mass with lush green and found to a significant algal wild stuff material presented in Figure 4A-F.

3.2. Production of Biodiesel via Transesterification reaction

3.2.1. Algal biomass yield

The collected huge mass of *Spirulina maxima* wild stuff was processed as per the standard procedure and after drying, a substantial reduction in the weight of algal feedstock was noticed. The estimated dry weight of the *S. maxima* algae was 1.25 to 1.60 kg for every 10 kg of wet algal biomass (Table 1). The algal mass after processes looks sizably thin & slightly dark green liquid and the quantity oil obtained was 0.920 kg and the final recovery of biodiesel was found to be 94.65 (%) (Figure 4C and Table 1).

3.2.2. Oil generation form Algal biomass

The fine-tuned and weighed algal biomass was subjected for oil extraction and the generated oil in weight per kilogram of dried biomass was calculated using the standard formula (Table 1).

$$\text{Oil yield} = \frac{\text{Oil extracted}}{\text{Algal dried biomass taken}} \times 100$$

The oil from algal biomass was obtained through solvent extraction (hexane-9%) where the volume of hexane was higher out of two solvents used in the extraction process. In addition, acetone was preferred to extract algal oil (8.5%) as it is economically viable compared to hexane (Table 1).

3.3. Transesterification and Biodiesel production

The algae oil accomplished through chemical extraction was subjected for transesterification processes to achieve biodiesel. When the algal biomass was processed into the pre-esterification method, the significant reduction of free fatty acid (FFA) was observed. Subsequently, the transesterification process was employed to enhance the quantum of biodiesel where all FFA will be converted into esterified oil *i.e.,* biodiesel. As per the protocol, the yield of biodiesel along with crude glycerol was measured by their weight corresponding to the weight of algal biomass which was found to be around 16% and 3.45% (wt%), respectively. The FAME composition of the algal diesel achieved and its profile was compared with the common fatty acid outline that has been compared with other biodiesel. The produced algal biodiesel was analyzed based on its distillation approach as well as its fuel properties and compared with petro-diesel as per the ASTM standards. The data of algal diesel characteristics are found to be significant and are most acceptable as the statistics meet most of the specifications. Hence, the biodiesel resulting from algae wild stuff can be graded as a most reliable fuel and the same can be recommended for its use in automobiles as a potential alternative to petroleum-diesel (Table 2).

3.4. Blending of Algal Biodiesel with Petro-diesel

The algal biodiesel was then subjected to blending with petroleum diesel to test the efficacy of the engine, so the algae esterified oil with petro-fuel in the ratio of AB10, and AB20 were prepared respectively. The Kinematic viscosity for fuel blends of AB10 and AB20 was found to be 4.26 and 4.87 CST @ 40° C. subsequently, the Net Calorific value of AB10 and AB20 blend was 41019 and 45787 kJ / kg recorded. However, it is evident from the experimental investigations, the properties of the biodiesel and their blends are found to be very close to the petro-diesel therefore, it can be used in the existing engine system (Table 3).

3.5. Chemical and Mechanical properties of Biodiesel

In all, the obtained data on physico-chemical properties by means of viscosity, density, flash point, cetane index and heating values of algal biodiesel with their blending proportions of AB10 and AB20 were analogous to the diesel fuel. The crucial parameters were very close to ASTM standard values. The viscosity of algae diesel blends of AB10 and AB20 were found to be higher than diesel fuel; nevertheless, it was meeting with ASTM standards values. The higher viscosity in fuel is generally unsuitable for use in diesel engines due to inefficient atomization. However, the heating values of AB10 and AB20 biodiesel blends were within the acceptable limit of diesel fuel. In addition, the flashpoint values of biodiesel blend AB10 and AB20 were higher (80.50 and 89.6) than diesel fuel respectively. This facilitates the safer handling and storage of biodiesel than petroleum-fuel. Further, the blends of AB10 and AB20 showed the Cetane Index of 52.6 and 64.24 respectively and were significant to touch the minimum prerequisite of diesel fuel (Table 3).

Therefore, it is appraised that combustion efficiency and fuel quality parameters were higher than that of diesel fuel. It could be concluded that the fuel properties of S. maxima algae biodiesel are placed almost within the suitable range and commended limits[61]. This is in accordance with the previous report made on Chlorella biodiesel with respect to its physico-chemical characteristics. In comparison, the biodiesel derived from both algae exhibited analogous properties with considerable variations. But, the properties of S. maxima biodiesel justified with ASTM standards were found to be clean with superior quality and sustainable biodiesel.

3.6. Analysis of diesel and biodiesel

The production of biodiesel with a maximum yield was explored from the algae oil obtained from algal biomass collected directly in the natural habitations (Table 1). The blends of algal diesel exhibited a higher viscosity than diesel fuel and the higher calorific value (43.23 MJ/kg) of the algal biodiesel was recorded as compared to petroleum-diesel. The Cetane number (CN) of the biodiesel and its blends was comparatively higher than diesel fuel. The acid value of the algae diesel was found to be significant and the higher oxygen content of algae-oil is more attractive for the production of automobile fuels. The moisture and carbon residue content was 0.04 % and 0.045 %wt., respectively. The analyzed properties of biodiesel and diesel were found within ASTM standard limits (Table 3).

Further, the experimental engine test rig was designed and the required specification has been given in Table 4.

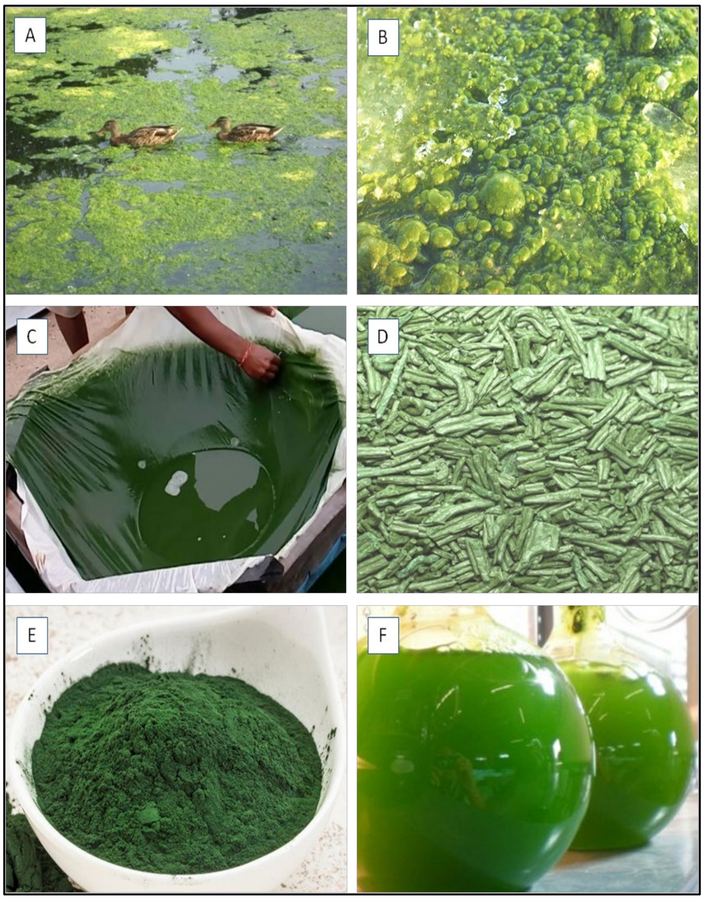

Figure 4. **(A-F).** ***Spirulina maxima*- the stages of wild stuff to biodiesel**

A. The feedstock of *S. maxima* at Lake,
B. Closer view of *S. maxima* wild stuff Sample in its habitat,
C. Extraction of Algal sample,
D. Algal sample air dried,
E. Powder sample of *S. maxima* and
F. Algae Oil

Table 4. Specifications of Experimental Engine Test Rig

SL. No.	Engine parameters	Specifications
1.	Production Industry	Kirloskar
2.	Cylinders number	Single cylinder
3.	Cycle	Four-stroke
4.	Cooling system	Water-cooled
5.	Cylinder diameter (mm)	90
6.	Piston stroke (mm)	120
7.	Compression ratio	17:1
8.	Rated speed	1600 rpm
9.	Maximum output	7.5 hp

DOI: http://dx.doi.org/10.32571/ijct.1105415 **E-ISSN: 2602-277X**

Table 1. Preliminary Physico-chemical analysis of *S. maxima* algae Oil and Biodiesel production

Algae type	Sample Type	Appearance	Moisture (Wt %)	Temperature (^{O}C)	Biomass of Algae (Kg)	Time engaged for max Temp.(hr)	Quantity of Oil (Kg)	Biodiesel Recovery (%)
Spirulina maxima	Wild-stuff	Thin & slightly dark green liquid	0.062	60-90	1.6	2.50	0.920	94.65

Table 2. Analysis of characteristics of Biodiesel derived from *S. maxima* algae

SL. No.	Properties	Crude Oil	Algal diesel	Limits (ASTM)
1.	Density (kg/m3) at 15^{0}C	1.026	0.882	0.87-0.89
2.	Higher heating value (MJ/kg)	46.5	40.8	--
3.	Kinematic Viscosity (mm^{2}/s) @40^{0}C	37.45	4.82	1.9-6.2
4.	Carbon (wt%)	78	86	--
5.	Hydrogen (wt%)	≤10,5	≤12,6	--
6.	Oxygen (wt%)	≥10,3	≥11,4	--
7.	Sulphur (wt%)	0	0	<10 max. 0,03
8.	Higher calorific value (MJ/kg)	nd	43.23	46.56
9.	Cetane Number (CN)	nd	47	na
10.	Acid value (mg KOH/g)	11.435	0.524	0.50 max.
11.	Iodine value (IV)	84.24	nd	na
12.	Saponification Value (mgKOH/g)	188.92	nd	na
13.	Flash Point (0C)	nd	189	130 max.
14.	Pour point (°C)	-14	-13	--
15.	Cloud point (°C)	-	1	3 (maximum)
16.	Carbon Residues (wt%)	nd	0.0412	0.050 max.

Table 3. Analysis of chemical & mechanical properties of Algal diesel (*S.maxima*) blends AB10 and AB20 comparing with diesel fuel and ASTM standards

SL . No	Properties	Method	ASTM D-6751-02 Standard	Diesel oil	Blend of Algal diesel (*S.maxima*) (AB10)	(AB20)
1.	Density @ 15 °C	ASTM D-4052	0.880	0.838	0.869	0.886
2.	Kinematic viscosity, CST @ 40° C	ASTM D-4450	1.9-6.0	1.97	4.26	4.87
3.	Heating value (kJ g^{-1})	ASTM-D975	-------	--------	38.51	41.45
4.	Flash point, °C	ASTM D-93	>125	75	80.5	89.6
5.	Cetane Index	ASTM D-976	> 47	69.75	52.66	64.24
6.	Gross Calorific value GCV (kJ / kg)	ASTM D-225	--------	45401	43224	46454
7.	Net Calorific value NCV (kJ / kg)	ASTM D-225	--------	42670	41019	45787

Table 5. Emission properties of algal Biodiesel in comparison with Petroleum diesel

SL. No	Fuel Type	Emission Characteristics				
		CO (%)	CO$_2$ (%)	NOx (ppm)	HC (ppm)	O$_2$ (%)
1.	Algal diesel *(S. maxima)*	0.076±0.002	3.942±0.024	20.70±1.266	12.76±0.44	15.6±0.000
2.	Petro-diesel	0.103±0.02	4.245±0.00	22.80±1.71	27.65±0.01	16.4±0.02

The outcomes of the previous literature review and the results of present study both indicate that algal biodiesel has enormous potential as a future fuel source. The data on emission parameters were documented from a diesel ngine in operation at about 3000 rpm for the time duration of 10min. The standard average data was recorded at 60 seconds of interval where the exhaust emissions were at a steady state and was revealed together with the standard deviation (±). However, the

DOI: http://dx.doi.org/10.32571/ijct.1105415 **E-ISSN: 2602-277X**

emissions data was corresponding to a percentage of the total gas followed by parts per million (ppm). **3.7.**

ANALYSIS OF ENGINE PERFORMANCE

The experimental investigation was carried out with the picture-perfect configuration. The testing was executed for a blending proportion of AB20% with neat diesel fuel using various injection pressures (210 bar, 220 bar, and 230 bar) respectively.

3.7.1. Brake Thermal Efficiency (BTE)

In this parameter, the idiosyncratic curve of brake power against the brake thermal efficiency was observed and it was also noticed that, more or less all the parameter were lies with the same trend. Whereas, the brake thermal efficiency was pronounced a slight increase for AB20 at 210 bar injection pressure up to part load. Subsequently, the increase in brake thermal efficiency for AB20 fuel along with the varied injection pressure was noticed (Fig. 5).

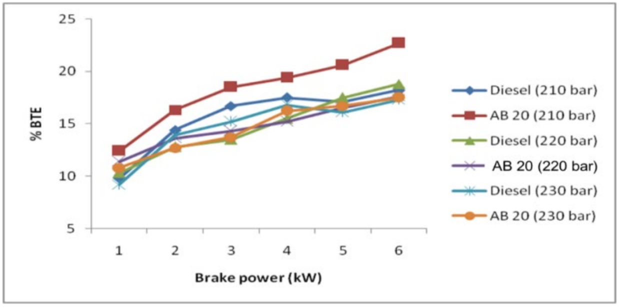

Figure 5. Brake Power v/s Brake Thermal Efficiency in Fuel blend of Algal diesel-petro-diesel at variable injection pressure

3.7.2. Engine Power (EP)

The algal oil exhibited lower engine power compared to petro-diesel; this is due to the lower heating value of the algal diesel when it is subjected alone. When the algal diesel is subjected to an experimental engine test rig with different blending proportions of petro-diesel then, the engine power can be monitored significantly at required level (Fig. 6).

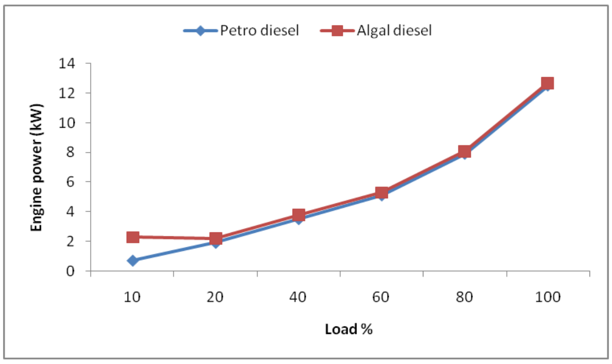

Figure 6. Engine power in Fuel blend of Algal diesel-petro-diesel at variable loads

3.7.3. Brake Specific Fuel Consumption (BSFC)

The higher brake fuel consumption (BSFC) at lower loads was recorded for algal fuel, whereas; the difference was lesser at higher loads which were also treated as significant. This may be due to the slightly higher energy density of algae diesel compared to petrol-diesel which entitles an increase in the volume of injected fuel to maintain the same power output, thereby; increase in BSFC for algal diesel compared to petro-diesel was observed. The causal phenomenon also ratifying the high kinematic viscosity and density of fuels can cause a decrease in the fuel atomization and vaporization which leads to high BSFC[78]. Later, there was a low-temperature rise at 10% engine load, which affects a lean combustion mixture; as a result it can trigger even higher fuel consumption in low energy containing fuels, compared to fuels with higher heating values (Fig. 7).

However, the higher oxygen index of algal oil compared to diesel oil facilitates the complete combustion of the fuel blend which can certainly reduce the BSFC at higher loads, wherein there is a rise in temperature compared to low loads[79].

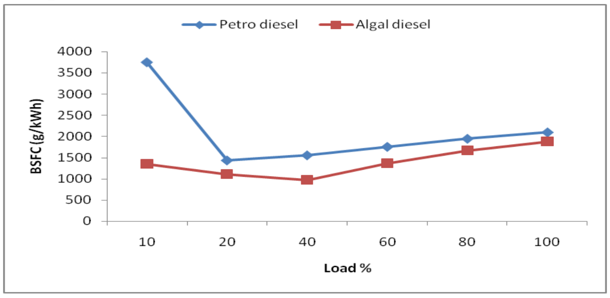

Figure 7. Brake Specific Fuel Consumption (BSFC) in Fuel blend of Algal diesel-petro-diesel at variable loads

3.8.1. Smoke Density (SD)

The brake power against smoke density of both algal diesel and diesel fuel with standard injection pressure displayed the lesser smoke density and reflected as significant to the engine system (Fig 8). It was evident in the previous reports as the parameter almost lies on the similar trend[80].

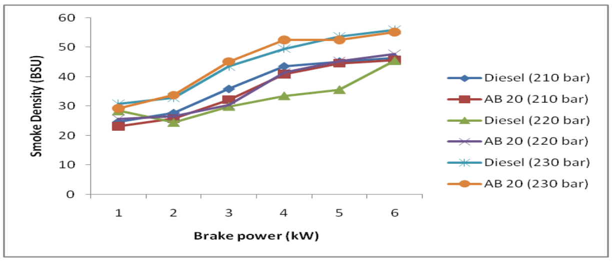

Figure 8. Brake power against smoke density in Fuel blend of Algal diesel-petro-diesel at variable injection pressure

3.8.2. Carbon Monoxide (CO)

The graph specifying the brake power against carbon monoxide has been observed and it was apparent that

DOI: http://dx.doi.org/10.32571/ijct.1105415 **E-ISSN: 2602-277X**

carbon monoxide emission increases as the load increases (Fig 9). When it is equated to the injection pressure, less carbon monoxide emission was noticed at the standard injection pressure than detained approach thus, the standard injection pressure was significant when it is associated with algae fuel and clean diesel fuel[81].

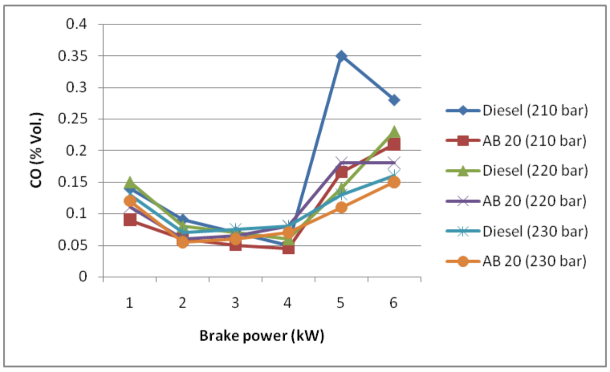

Figure 9. Brake power against carbon monoxide emission in Fuel blend of Algal diesel-petro-diesel at a variable injection pressure

3.8.3. Hydrocarbon (HC)

The considerable variation in the emission of hydrocarbon versus brake power was observed for the algae fuel and diesel fuel at various injection pressures (Fig 10). In the comparative approach, at the standard injection pressure of neat diesel fuel, the reduction in the amount of hydrocarbon was noticed. Specifically, AB20 with standard injection pressure showed the maximum reduction in the hydrocarbon emission[82].

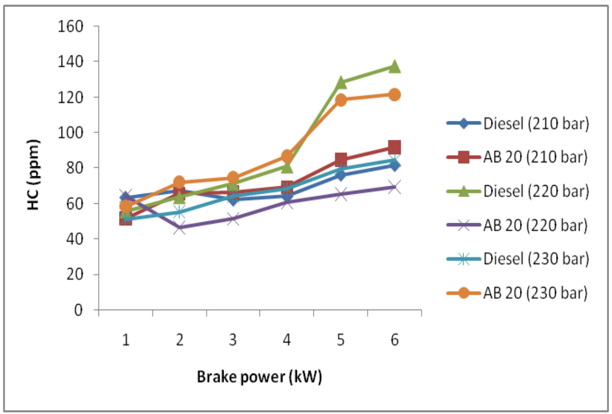

Fuel blend of Algal diesel-petro-diesel at a variable injection pressure

3.8.4. Oxides of Nitrogen (NOx)

The graph obtained for brake power against oxides of nitrogen was critically analyzed for its expression

wherein, the oxides of nitrogen emission at the injection pressure of 210 bars was found to be average followed by varied injection pressures (Fig 11). The algae fuel at AB20 exhibited maximum reduction compared to that of all other factors[83].

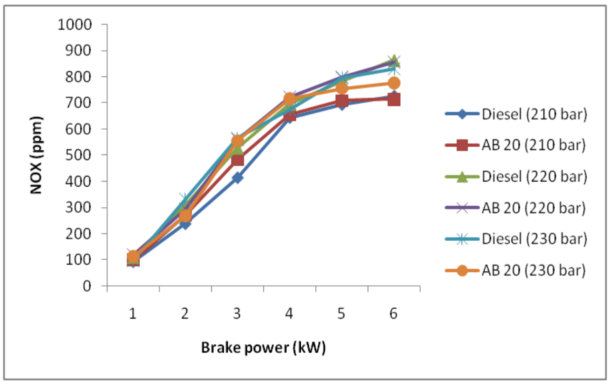

Figure 11. Brake power against oxides of nitrogen in Fuel blend of Algal diesel-petro-diesel at a variable injection pressure

3.8.5. Emission of CO_2 vs. Load

Initially, the deviance of the emission of CO2 with algal diesel blends at constant speeds of the engine was recorded. Further, the algal biodiesel blend exhibited lower CO2 emission compared to Petro-diesel. Theoretically, the emission of CO2 is due to the unfinished combustion particularly at low temperature and non-supply of oxygen into the combustion chamber.

In view of the fact that algal biodiesel blends contain a surplus amount of oxygen, which facilitates the combustion of fuel at a superior level and imparts the generation of higher temperature in the cylinder. This high temperature further makes possible the oxidation reaction for having conversion into CO2 towards the end[84]. The tendency of CO2 emission declined with the increase of loads in the engine (Fig 12).

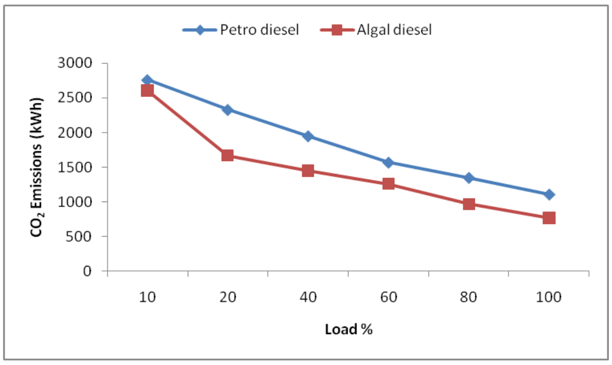

Figure 12. CO_2 Emissions (Kwh) Vs. Load (%) in Fuel blend of Algal diesel-petro-diesel

The capping and significant parameter is NOX when it comes to the interaction of the engine system with emission characteristics.

The differential approach in the emission of nitric oxide (NOX) with variable loads for both algal diesel and petro-diesel is represented in Figure 13.

DOI: http://dx.doi.org/10.32571/ijct.1105415 **E-ISSN: 2602-277X**

The NOX emission gradually increased with an increase in load at both algal diesel and petro-diesel blends respectively. Hypothetically, the emission of NOX is depending on the concentration of oxygen and higher temperatures in the combustion chamber. The emission of NOX was found to be higher at all the different loads, which may be due to a higher cetane number, which leads to enhanced combustion of the algal diesel. The increasing trend of temperature during the reaction of engine interaction will facilitate improved combustion of fuels, which ultimately increases the NOX formation. The NOX emission was considered as significant at algal diesel blend as compared to Petro-diesel at full load conditions[85, 86].

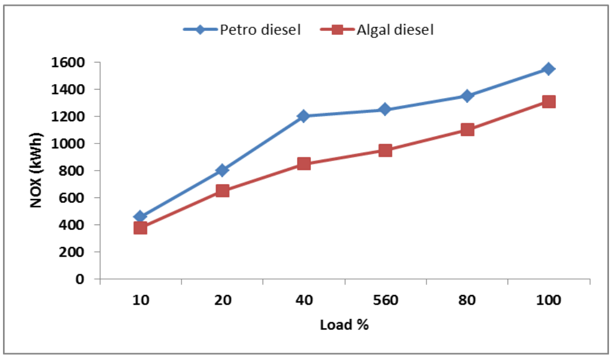

Figure 13. NOx Emissions (Kwh) Vs. Load (%) in Fuel blend of Algal diesel-petro-diesel

4. DISCUSSION

The only potential sources of alternative renewable fuel in the future are Microalgae which are available even in diversified ecological conditions. The microalgae are very minute aquatic organisms that transform sunlight into dynamic energy and hence these algal communities will have a stockpile of energy in the form of natural oils called 'Algae Fatty Acid Methyl ester' (AFME). Under reliable conditions, algae can further construct a lot of oil stack which can be converted later into biofuels. In addition, algae need carbon dioxide to grow and that is commendable for the environment, where it takes CO2 out of the atmosphere, establishing it an essentially carbon-neutral fuel source[87].

4.1. Algae Wild biomass to Biodiesel

Consequently, the algae are deliberated to be as the wildest rising primitive plant and theoretically, authenticated that their functional properties are effectual to produce a significant amount of oil as compared to other oil yielding crop plants. However, the ratio with respect to energy efficiency and carbon along with water footprint for algae-based biofuels are evaluated as the potential fuel sources that can replace the petroleum diesel. The algal lipids would be a superlative feedstock for generating transportation fuels with high energy density such as biodiesel, green jet fuel, and green gasoline, etc. This is in view of the fact that algae are not inclusive with food products, agricultural land and it exhibits the extreme ability to sequester large quantities of carbon dioxide in the environment. In addition, the practical analysis indicated that biodiesel is more focused on its power output due to higher oxygen content over the petro-diesel[88].

Hypothetically, multifarious fatty acids of different stretches esterified with alcohol, reliably methanol finally constitutes a Biodiesel. The theory reveals that the algae oil consisting of high free fatty acid content will be converted into Biodiesel by employing two phase chemical reactions *i.e.,* pre-esterification and transesterification processes. The biomass of microalgae is compelled by the higher growth rates and the lipid content of several species of algae is also superior when compared to other conventional plant crops. The competency of algal biomass is materialized as a valid biofuel feedstock which is directly proportional to the degree of saturation of its fatty acids validated with iodine value, oxidation stability, cetane number, etc. This has been categorically justified through its physical properties comprising viscosity, density, heating value, and melting temperature, etc.[89].

4.2. Engine performance with Algal Biodiesel

The parametric evaluation on performance and exhaust emissions of the experimental diesel engine fueled with blends of algal diesel and diesel fuels were remarkably deliberated. Prior to this, the analysis on fatty acid derived from microalgae, S. maxima showed fuel properties which were exceedingly significant and subsidized by fatty acid composition. In addition, the physico-chemical properties of biodiesel blends AB10 and AB20 were found to be close to diesel fuel. Subsequently, the heating value for each unit mass of algal diesel was found to be substantially more constructive than that of gasoline fuel. Therefore, the variation in the volumetric energy density of algal diesel compared to petro-diesel displayed lessening the difference of energy density on per unit volume basis respectively. The reduced difference in energy density was evident in the power and torque outputs generated by petro-diesel and algal diesel. In comparison, the algae biodiesel fuels had considerable power outputs as compared to petro-diesel that was also much closer to the expected power production based on the difference in volumetric energy density (kJ cm^{-3}). Eventually, the power produced by each fuel is directly interrelated to the volumetric energy density of the fuel[90, 91].

The torque output was observed for algal diesel wherein, analogous tendency coupled with most energy dense fuels attaining the maximum torque output similarly, the least energy-dense fuels generating the minimum amount of torque output. With this capacious background, the effectiveness of BSFC of algal diesel was correlated and was found to be considerably better

DOI: http://dx.doi.org/10.32571/ijct.1105415 **E-ISSN: 2602-277X**

than that of petro-diesel. On a serious note, the BSFC curve for algal biodiesel fuel was similarly shaped and no clear difference is evident in blends of biodiesel fuel studied [92,93].

In particular, the evaluation of brake specific fuel consumption is a crucial tool in assessing the consumption of fuel for every power output which is justified in the present study, where the power output of biodiesel was compared to petro-fuel. Besides, the higher oxygen content of algal diesel relating to fossil fuels is immensely accountable which may further contribute to significant energy density with well-balanced BSFC[94, 95, 96].

4.3. Emission characteristics of Algal Biodiesel

The imperative and vital aspect of using algal diesel as a supplement with petro-diesel is enhanced performance with improved characteristic features. Although the algal diesel was shown to reduce a number of emissions, including CO and hydrocarbons (HC) with unfinished combustion, the blending proportion of both algal diesel and petrol-diesel showed significant performance on most of the parameters. In general, it has been also noticed that algal diesel is attributed with substantial leading hold on all emission parameters. The obtained data on emission characteristics were critically analysed for both algal diesel and petrol-diesel covering CO_2, CO, and O_2 in percentage of total gas and HC and NOx as parts per million (ppm) respectively[97,98]. The increase in emission of CO_2 for algal diesel in relation to petroleum-diesel indicating improved combustion due to the presence of oxygen content in biodiesel has been substantiated. Besides, the CO emission was considerably reduced in the algal diesel compared to petro-diesel. Besides, the similar trend was also observed in Hydrocarbon emissions which were significantly higher in algal diesel fuel compared to petro-diesel. Subsequently, the convincing factor on the emission of NOx in algae biodiesel was noticeably lower than petro-diesel[99,100]. As a whole, the emission results are in agreement with the other studies on the potential of algal fuel technology. One such example is ‘Commercialization potential of microalgae for biofuels production’ where three crucial steps to the success of algal biofuel are listed: selection of the most desirable species, development of low cost production technology and production and marketing of other products derived from algae. Since these steps are being addressed, these authors also predict that, the algal biofuel will become commercially available in the near future [101].

5. CONCLUSION

The data obtained from the present investigation showed that biodiesel derived from wild stuff of algal biomass performed better on all the parameters. The approach of collecting the algal biomass directly in its natural ecosystem can be the most competent biofuel resources producing sustainable biodiesel as a substitute to the petroleum diesel. The production of algal biodiesel is found to be very cost-effective compared to the biodiesel produced from other plant oils. The characteristics of algal diesel were very much closer to petro-diesel when it is subjected for ASTM validation. Therefore, the algal diesel was able to exhibit similar potential of engine power and torque when compared to petro-diesel and the well-balanced approach in BSFC and BTE which was found to be significantly superior. The well-finished Hydrocarbon during combustion process and reduction of CO emissions was observed in algal diesel which may possibly trigger the optimized performance with respect to energy output. The reduction in NOx emissions in algal biodiesel than petro-diesel was recorded. Further, the findings of the present investigations validate that, microalga producing biodiesel explicitly showed analogous properties relating to engine parameters. In conclusion, the dynamic exploration of microalgae oils from its natural habitation can be a potential resource for biodiesel production which practically requires expansions in large scale cultivation, optimized processing followed by complete recovery of oils to achieve the sustainable biodiesel production.

Therefore, the results of the current study electrifies the equations on efficient biodiesel production from wild biomass of algae which is a preferential and well-organized approach as it is the most potential feedstock source that belongs to the non-edible oil category. Finally, the data of experimental investigations on the overall performance of the diesel engine test rig in tandem with all the specification fuelled by neat algae fuel (AB20) and diesel fuel was analysed with various injection pressure such as 210 bar, 220 bar, and 230 bar respectively, hence, the following conclusions are convoluted.

- ✓ The significant approach of brake thermal factor in AB20 blending at 210 bar compared to petro-fuel was noticed.
- ✓ The lesser smoke density was recorded with standard injunction pressure of algal fuel as compared to petro-fuel.
- ✓ The algal fuel (AB20) showed the maximum reduction of Carbon dioxide followed by diesel fuel.
- ✓ The maximum reduction of hydrocarbon emission with standard injunction pressure at AB20 was observed
- ✓ The algal biodiesel (AB20) exhibited considerable reduction of oxides of nitrogen in parallel with neat diesel at an injunction pressure of 210 bar compared to all other parameters.
- ✓ On the whole, AB20 blend displayed reduction in the emission of HC and CO gases up to 20 and 25%, respectively with a marginal difference in

NOx up to 10–15% due to unsaturation moiety factor.

- ✓ The minimum exhaust emissions of pollutant gases were noticed for AB20 blending at 210 bar that adjacently followed the standard diesel. However, the significant results in all the parametric analysis at AB20 blending ratio which appeared to be cost effective, eco-friendly and technologically feasible.

Therefore, based on the generated results, it can be substantiated that the algae biodiesel derived from wild biomass of Spirulina maxima can be acclaimed as an alternative & prospective bio-fuel in the existing diesel engine system. The variation in the injection pressures particularly @ 210 bars displays a very significant change in the engine performance along with emission characteristics at AB20 blending fractions as compared to petro-fuel.

ACKNOWLEDGEMENT

The first authors acknowledge Ranchi University, Ranchi (Jharkhand State), INDIA for providing the opportunity to carry-out the Research study. The first author is indebted to 'Hamsageetha Research Foundation', Tumakuru (Karnataka) for helping to procure algal wild biomass in the natural ecosystem and sample processing. Further, biodiesel testing followed by preliminary analysis performed at University department of Chemistry, Ranchi University, Ranchi (Jharkhand State), India. The first author also acknowledges Dr. Rajesh Kumar (Professor & Research Supervisor), for facilitating to complete the methodical works and data compilation under his incessant guidance and motivation rendered during the course of investigations.

Conflict of interest

I declare that there is no a conflict of interest with any person, institute, company, etc.

REFERENCES

1. Balat, M. *Energy Sources, Part B Economics, Planning, and Policy*. 2007, 30, 2(2), 167-181.
2. Demirbas, A. *Progress in energy and combustion science*. 2007, 33(1), 1-8.
3. Demirbas, A. *Energy Policy*. 2007, 35(9), 4661–4670.
4. Jaichandar, S.; Annamalai, K. *Journal of Sustainable Energy & Environment*. 2011, 2(2), 71-5.
5. Schenk, PM.; Thomas-Hall, SR.; Stephens, E.; Marx, UC. *Bioenergy Res*. 2008, 1, 20-43.
6. Bajpai, D.; Tyagi, VK. *Journal of OLEo science*. 2006, 55(10), 487-502.
7. Carraretto, C.; Macor, A.; Mirandola, A.; Stoppato, A.; Tonon, S. *Energy*. 2004, 29, 2195-2211.
8. Sahoo, PK.; Das, LM.; Babu, MK.; Arora, P.; Singh, VP.; Kumar, NR.; Varyani, TS. *Fuel*. 2009, 1, 88(9), 1698-707.
9. Singh, SP.; Singh, D. *Renewable and sustainable energy reviews*. 2010, 1, 14(1), 200-216.
10. Scott, SA.; Davey, MP.; Dennis, JS.; Horst, I.; Howe, CJ.; Lea-Smith, DJ.; Smith, AG. *Current opinion in biotechnology*. 2010, 1, 21(3), 277-286.
11. Eloka-Eboka, AC.; Inambao, FL. *Energy Sources, Part A: Recovery, Utilization, and Environmental Effects*. 2016, 2, 38(11), 1495-502.
12. Zhang, X.; Rong, J.; Chen, H.; He, C.; Wang, Q. *Frontiers in Energy Research*. 2014, 19, 2, 32.
13. Wahlen, BD.; Morgan, MR.; McCurdy, AT.; Willis, RM.; Morgan, MD.; Dye, DJ.; Bugbee, B.; Wood, BD.; Seefeldt, LC. *Energy & Fuels*. 2013, 17, 27(1), 220-228.
14. Stephens, E.; Ross, IL.; Mussgnug, JH.; Wagner, LD.; Borowitzka, MA.; Posten, C.; Kruse, O.; Hankamer, B. *Trends in plant science*. 2010, 1, 15(10), 554-64.
15. Eloka-Eboka, AC.; Onunka, C. *African Journal of Science, Technology, Innovation and Development*. 2016, 1,8(2), 221-232.
16. Das, Debabrata, ed. Algal biorefinery: an integrated approach. Springer, 2015.
17. Ahmed, AS. *Journal of Energy and Environment*. 2010, 31, 2(1), 1-5.
18. Siwale, L.; Kristóf, L.; Adam, T.; Bereczky, A.; Mbarawa, M.; Penninger, A.; Kolesnikov, A. *Fuel*. 2013, 1, 107, 409-18.
19. Mostafa, SS.; El-Gendy, NS. *Arabian journal of chemistry*. 2017, 1, 10, S2040-50.
20. Hansen, AC.; Gratton, MR.; Yuan, W. *Transactions of the ASABE*. 2006, 49(3), 589-95.
21. Sanjay Singh, M.; Prabhahar, M. *International Journal of Engineering and Advanced Technology*. 2019, 9(2), 5609-5614.
22. Tüccar, G.; Aydın, K. *Fuel*. 2013, 1, 112:203-7.

DOI: http://dx.doi.org/10.32571/ijct.1105415 **E-ISSN: 2602-277X**

23. Knothe, G. *Fuel processing technology*. 2005, 25, 86(10), 1059-70.
24. Leung, DY.; Luo, Y.; Chan, TL. *Energy & fuels*. 2006, 17, 20(3), 1015-23.
25. Natarajan, S.; Trasy, KA.; Srihari, N.; Raja, S. *Energy Procedia*. 2017, 1, 105, 1043-50.
26. Varghese, T.; Raj, J.; Raja, E.; Thamotharan, C. *International Journal of Engineering and Advanced Technology*. 2015, 4(5), 28-33.
27. Abuhabaya, A.; Fieldhouse, J.; Brown, D. *Energy*, 201,3 15, 59, 56-62.
28. Velappan, R.; Sivaprakasam, S.; Kannan, M. *Int. Res. J. Eng. Technol*. 2015, 2(5), 1152-7.
29. El-Baza, FK.; Gadb, MS.; Abdoc, SM.; Abedd, KA.; Mattere, IA. *Fuel*. 2016, 10:11.
30. Rahman, MA.; Aziz, MA.; Ruhul, AM.; Rashid, MM. *Journal of Mechanical Science and Technology*. 2017, 31(6), 3025-33.
31. Tan, XB.; Lam, MK.; Uemura, Y.; Lim, JW.; Wong, CY.; Lee, KT. *Chinese Journal of Chemical Engineering*. 2018, 1, 26(1), 17-30.
32. Kumar, MV.; Babu, AV.; Kumar, PR. *Alexandria Engineering Journal*. 2018, 1, 57(1), 509-16.
33. Yadav, B.; Noguchi, R.; Soni, P.; Abah, E. *J. Pharmacogn. Phytochem*. 2018, 7(2), 2319-26.
34. Chen, J.; Li, J.; Dong, W.; Zhang, X.; Tyagi, RD.; Drogui, P.; Surampalli, RY. *Renewable and Sustainable Energy Reviews.* 2018, 90, 336-46.
35. Rajendra, P.; Kamalesh, J.; Pranali, G.; Vishal, B.; Bhushan, S.A. *Chemical Engineering Transactions*. 2018, 1, 65, 451-6.
36. Bellad, M.; Tevari, R.; Rakesh, BV.; Swamith, KB.; Avinash Patel, KL. *Journal of Innovative Research in Science, Engineering and Technology*. 2018, 7(4), 3896-902.
37. Naresh, V.; Prabhakar, S.; Annamalai, K.; & Naveenchandran, P. *International Journal of Pure and Applied Mathematics*, 2018, 119 (17), 123-130.
38. Agarwal, AK.; Park, S.; Dhar, A.; Lee, C.; Park, S.; Gupta, T.; Gupta, NK. *Journal of Energy Resources Technology*. 2018, 1, 140(12), 01-104.
39. Gebremariam, SN.; Marchetti, JM. *Energy Conversion and Management*. 2018, 1, 171, 1712-20.
40. Giakoumis, EG.; Sarakatsanis, CK. *Fuel*. 2018, 15, 222, 574-85.
41. Naresh, V.; Prabhakar, S.; Annamalai, K.; Naveenchandran, P. *International Journal of Engineering & Technology*. 2018;7(1.9):1-5.
42. Saraswat, M.; Chauhan, NR. *Journal of Scientific & Industrial Research*. 2018, 77, 723-727.
43. Karmakar, R.; Kundu, K.; Rajor, A. *Petroleum Science*. 2018, 15(2), 385-95.
44. Naresh, V.; Prabhakar, S. *J. Chem. Pharm. Res*. 2018, 10(4), 44-55.
45. Prabhu, A.; Venkata Ramanan, M.; Jayaprabakar, J. *International Journal of Ambient Energy*. 2020, 2, 41(1), 80-3.
46. Ikwuagwu, OE.; Ononogbu, IC.; Njoku, OU. *Industrial crops and products*. 2000, 1, 12(1), 57-62.
47. Delfort, B.; Hillion, G.; & Martino, G. *Trans. ASAE*.2004, 28-028.
48. Rajak, U.; Nashine, P.; Singh, TS.; Verma, TN. *Energy Conversion and Management*. 2018, 15, 156, 235-52.
49. Shameer, PM.; Ramesh, K. *Renewable and Sustainable Energy Reviews*. 2018, 1, 81, 45-61.
50. Shuba, ES.; Kifle, D. *Renewable and Sustainable Energy Reviews*. 2018, 1, 81, 743-55.
51. Yaşar, F.; Altun, Ş. *Thermal Science*, 2018, 22(3), 1481-1492.
52. Ramalingam, S.; Rajendran, S.; Ganesan, P.; Govindasamy, M. *Renewable and Sustainable Energy Reviews*. 2018, 1, 81, 775-88.
53. Miao, X.; Wu, Q. *Bioresource technology*. 2006, 1, 97(6), 841-6.
54. Unpaprom, Y.; Tipnee, S.; Ramaraj, R. *International Journal of Sustainable and Green Energy*. 2015, 11, 4(1), 1-6.
55. Topare, NS.; Renge, VC.; Khedkar, SV.; Chavan, YP.; Bhagat, SL. *Int J Chem Environ Pharm Res*. 2011, 2, 116-20.
56. Amin, S. *Energy conversion and management*. 2009, 50(7), 1834-40.

DOI: http://dx.doi.org/10.32571/ijct.1105415 E-ISSN: 2602-277X

57. Demirbas, A.; & Demirbas, M.F. *Energy Conversion and Management*. 2011, 52, 163-170.
58. Jones, CS.; Mayfield, SP. *Current opinion in biotechnology*. 2012,1, 23(3), 346-51.
59. Nagaraja, YP.; Chandrashekhar, B.; Manasa, KS.; Venkatesh, HS. *International Journal of Current Microbiology and Applied Sciences.* 2014, 3(4), 851-60.
60. Hossain, AS.; Salleh, A.; Boyce, AN.; Chowdhury, P.; Naqiuddin, M. *American journal of biochemistry and biotechnology*. 2008, 4(3), 250-4.
61. Chisti, Y. *Biotechnology advances*. 2007, 1, 25(3), 294-306.
62. Annam, RA. *Journal of Chemical and Pharmaceutical Research*. 2015, 7(2), 755-60.
63. Prescott, GW. *Algae of the Western great lakes area*, Publ. Otto. Kaetz, Science Publishers, W. Germany. 1998, pp 977.
64. Gandhi, HP. *Fresh water diatom of Central Gujarat*, Bishen Sing. Mahendra Pal Singh.1998; pp. (i-vi), 1-324.
65. Benkendorff, K.; Davis, AR.; Rogers, CN.; Bremner, JB. *Journal of Experimental Marine Biology and Ecology*. 2005, 9, 316(1), 29-44.
66. Bligh, E.G.; & Dyer, W.J. *Canadian Journal of . Biochemistry and Physiology*, 1959, 37, 911–917.
67. Jensen, G.S.; Wu, X.; Patterson, K.M.; Barnes, J.; Carter, S.G.; & Scherwitz, L. *Lipid technology*. 2008, 20(12), 280-1.
68. Levine, R.B.; Pinnarat, T.; Savage, P.E. *Energy & Fuels*. 2010, 16, 24(9), 5235-5243.
69. Thoai, D.N.; Photaworn, S.; Kumar, A.; Prasertsit, K.; Tongurai, C. *Energy Procedia*. 2017, 1, 138, 536-43.
70. Johnson, M.B.; Wen, Z. *Energy & Fuels*. 2009, 15, 23(10), 5179-83.
71. D'oca, M.G.; Viêgas, C.V.; Lemoes, J.S.; Miyasaki, EK.; Morón-Villarreyes, JA.; Primel, EG.; Abreu, PC. *Biomass and bioenergy*. 2011, 1,35(4), 1533-8.
72. Al-lwayzy, S.H.; Yusaf, T.; Al-Juboori, RA. *Energies*. 2014, 7(3), 1829-51.
73. Basha, S.A.; Gopal, K.R.; Jebaraj, S. *Renewable and sustainable energy reviews*. 2009, 13(6-7), 1628-34.
74. Topare, N.S.; Renge, V.C.; Khedkar, S.V.; Chavan, YP.; Bhagat, SL. *Int J Chem Environ Pharm Res*. 2011, 2, 116-20.
75. Demirbas, A. *Applied Energy*. 2011, 88(10), 3541-7.
76. Halim, R.; Gladman, B.; Danquah, MK.; Webley, PA. *Bioresource technology*. 2011, 102(1), 178-85.
77. Kumar, P.; Suseela, M.R.; Toppo, K. *Asian J Exp Biol Sci.* 2011, 2(3), 493-7.
78. Patel, J.S.; Kumar, N.; Deep, A.; Sharma, A.; Gupta, D. *SAE Technical Paper.* 2014, 01-1378.
79. Ganapathy, T.; Gakkhar, R.P.; Murugesan, K. *Applied energy*. 2011, 88(12), 4376-86.
80. Hellier, P.; Purton, S.; Ladommatos, N. *Frontiers in bioengineering and biotechnology*. 2015, 20, 3:49.
81. Rashid, U.; Anwar, F. *Fuel*. 2008, 1, 87(3), 265-73.
82. Vicente, G.; Martínez, M.; Aracil, J. *Journal of the American Oil Chemists' Society*. 2005, 82(12), 899-904.
83. Suganya, T.; Gandhi, NN.; Renganathan, S. *Bioresource technology*. 2013, 1, 128, 392-400.
84. Banerjee, A.; Sharma, R.; Chisti, Y.; Banerjee, UC. *Critical reviews in biotechnology*. 2002, 1, 22(3), 245-79.
85. Tang, D.; Han, W.; Li, P.; Miao, X.; Zhong, J. *Bioresource technology*. 2011, 1, 102(3), 3071-6.
86. Sathya, AB.; Thirunavukkarasu, A.; Nithya, R.; Nandan, A.; Sakthishobana, K.; Kola, AK.; Sivashankar, R.; Tuan, HA.; Deepanraj, B. *Fuel*. 2023, Jan, 15, 332, 126199.
87. Haik, Y.; Selim, MY.; Abdulrehman, T. *Energy*. 2011, 1, 36(3), 1827-35.
88. Shirvani, T.; Yan, X.; Inderwildi, OR.; Edwards, PP.; King, DA. *Energy & Environmental Science*. 2011, 4(10), 3773-8.
89. Kumar, A.; Tripathi, RK.; Ranjan, S.; Hasan, AS. *Int. J. Eng. Res. Technol.* 2020, 9(4), 378-92.

DOI: http://dx.doi.org/10.32571/ijct.1105415 E-ISSN: 2602-277X

90. Giakoumis, EG.; Sarakatsanis, CK. *Fuel*. 2018, 15, 222, 574-85.

91. Bhojraj, N.; Kale.; Patle, S. D.; Khawale, V.R.; Lutade, S.V. *International Journal of Control and Automation*. 2019, 12(4), 97-102.

92. Yahya, W.; Norhisyam, M. *Journal of Mechanics Engineering and Automation*. 2012, 2(4), 267-70.

93. Tsaousis, P.; Wang, Y.; Roskilly, AP.; Caldwell, GS. *Energy Procedia*. 2014, 1, 61, 656-9.

94. Sayin, C.; Ozsezen, AN.; Canakci, M. *Fuel*. 2010, 1, 89(7), 1407-14.

95. Makarevičienė, V.; Lebedevas, S.; Rapalis, P.; Gumbyte, M.; Skorupskaite, V.; Žaglinskis, J. *Fuel*. 2014, 15, 120, 233-9.

96. Nabi, MN.; Rahman, MM.; Akhter, MS. *Applied thermal engineering*. 2009, 1, 29(11-12), 2265-70.

97. Fisher, BC.; Marchese, AJ.; Volckens, J.; Lee, T.; Collett, JL. *SAE International Journal of Fuels and Lubricants*. 2010, 1, 3(2), 292-321.

98. Paul, G.; Datta, A.; Mandal, BK. *Energy Procedia*. 2014, 54:455-67.

99. Scragg, AH.; Morrison, J.; Shales, SW. *Enzyme and Microbial Technology*. 2003, 2, 33(7), 884-9.

100. Kumar, R.; Mishra, MK.; Singh, SK.; Kumar, A. *Journal of mechanical science and technology*. 2016, 30(10), 4781-9.

101. Singh, J.; Gu, S. *Renewable and sustainable energy reviews*. 2010, 1, 14(9), 2596-610.

DOI: http://dx.doi.org/10.32571/ijct.1194356 **E-ISSN: 2602-277X**

International Journal of Chemistry and Technology

http://dergipark.org.tr/ijct

Research Article

Antifungal activity and optimization procedure of microwave-synthesized silver nanoparticles using linden (*Tilia rubra* subsp. *caucasica*) flower extract

Uğur YİĞİT[1] Muharrem TÜRKKAN[1] *

[1]*Department of Plant Protection, Faculty of Agriculture, Ordu University, Ordu 52200, Türkiye*

Received: 25 October 2022; Revised: 28 November 2022; Accepted: 2 December 2022

*****Corresponding author e-mail: muharremturkkan@gmail.com

Citation: Yiğit, U.; Türkkan, M. *Int. J. Chem. Technol.* **2023**, 7(1), 25-37

ABSTRACT

The present study used linden [*Tilia rubra* DC. subsp. *caucasica* (Rupr.)] flower extract as a reducing and coating agent to create silver nanoparticles (AgNPs). The Face-Centered Central Composite Design (FCCD) of Response Surface Methodology (RSM) was used to investigate the combined effect of four different synthesis variables in order to obtain the maximum amount of AgNPs produced. Optimal AgNP production was achieved within the investigated range when the AgNO$_3$ concentration, plant extract amount, microwave power, and time were 10 mM, 2.5 ml, 800 watts, and 90 seconds, respectively. The Ultraviolet–Visible Spectroscopy (UV–Vis), Fourier Transform Infrared Spectroscopy (FT–IR), Scanning Electron Microscopy (SEM)–Energy Dispersive X-ray Spectroscopy (EDS), and Transmission Electron Microscopy (TEM) were utilized to characterize the synthesized AgNPs. In addition, *in vitro* experiments revealed that the EC$_{50}$, minimum inhibitory concentration (MIC), and minimum fungicidal concentration (MFC) values of synthesized AgNPs for seven *Phytophthora* (*P. cactorum*, *P. capsici*, *P. cinnamomi*, *P. citrophthora*, *P. megasperma*, *P. nicotianae*, and *P. palmivora*) species varied between 46.38 and 119.36 µg ml^{-1}, 225 and 450 µg ml^{-1}, and 225 and 900 µg ml^{-1}, respectively. The findings of this study suggest that AgNPs synthesized with linden flower extract should be investigated further for use in the treatment of *Phytophthora* spp.-caused diseases.

Keywords: Silver nanoparticles, *Tilia rubra* subsp. *caucasica*, face-centered central composite design, *Phytophthora* spp., toxicity

Ihlamur (*Tilia rubra* subsp. *caucasica*) çiçek ekstraktı kullanılarak mikrodalga aracılığıyla sentezlenen gümüş nanopartiküllerin antifungal aktivitesi ve optimizasyon prosedürü

ÖZ

Mevcut çalışmada gümüş nanopartiküller (AgNP'ler) oluşturmak için indirgeyici ve kaplayıcı etken olarak ıhlamur [*Tilia rubra* DC. subsp. *caucasica* (Rupr.)] çiçek ekstraktı kullanılmıştır. Üretilen AgNP'lerin maksimum miktarını elde etmek için dört farklı sentez değişkeninin birleşik etkisini araştırmak için Yanıt Yüzey Metodolojisi (RSM)'nin Yüz Merkezli Merkezi Kompozit Tasarım (FCCD)'ı kullanılmıştır. Optimum AgNP üretimi, AgNO$_3$ konsantrasyonu, bitki ekstrakt miktarı, mikrodalga gücü ve sürenin sırasıyla 10 mM, 2.5 ml, 800 watt ve 90 saniye olduğunda incelenen aralıkta elde edilmiştir. Sentezlenen AgNP'leri karakterize etmek için Ultraviyole Görünür Bölge Spektroskopisi (UV–Vis), Fourier Dönüşümü Kızılötesi Spektroskopisi (FT–IR), Taramalı Elektron Mikroskobu (SEM)–Enerji Dağıtıcı X-ışını Spektroskopisi (EDS) ve Geçirgen Elektron Mikroskobu (TEM) kullanılmıştır. Ayrıca *in vitro* deneyler, yedi *Phytophthora* (*P. cactorum*, *P. capsici*, *P. cinnamomi*, *P. citrophthora*, *P. megasperma*, *P. nicotianae*, and *P. palmivora*) türü için sentezlenen AgNP'lerin EC$_{50}$, minimum engelleyici konsantrasyon (MIC) ve minimum fungisidal konsantrasyon (MFC) değerlerinin sırasıyla 46.38 ve 119.36 µg ml^{-1}, 225 ve 450 µg ml^{-1}, ve 225 ve 900 µg ml^{-1} arasında değiştiğini ortaya koymuştur. Bu çalışmanın bulguları, ıhlamur çiçek ekstraktı ile sentezlenen AgNP'lerin, *Phytophthora* türlerinin neden olduğu hastalıkların mücadelesinde kullanılmak üzere daha fazla araştırılması gerektiğini önermektedir.

Anahtar Kelimeler: Gümüş nanopartiküller, *Tilia rubra* subsp. *caucasica*, yüz merkezli merkezi kompozit tasarım, *Phytophthora* spp., zehirlilik

---

This research was produced from the doctoral thesis of the first author.

DOI: http://dx.doi.org/10.32571/ijct.1194356 E-ISSN: 2602-277X

1. INTRODUCTION

Nanomaterials have unique physical and chemical properties that cannot be observed in bulk or molecular form.[1] Silver nanoparticles (AgNPs) in particular are gaining popularity due to their optical, catalytic, mechanical, electrical, and biosensing properties.[2-4] AgNPs have strong antimicrobial activity and are used as a component of human health drugs in the pharmaceutical industry.[5] Numerous studies have shown that AgNPs can be produced using physical and chemical methods, but due to the use of toxic chemicals in the synthesis process, an alternative method must be found.[6-12] In this regard, the biological approach, which is based on living organisms such as bacteria, fungi, lichens, and plants, provides a reliable, simple, quick, non-toxic, and environmentally friendly solution.[13-16] Plants are the most popular bio-resource because they are easily accessible, non-toxic, and easy to process. Plants also contain a large number of biologically active compounds, such as polyphenols, organic acids, and proteins, which act not only as reducing agents but also as stabilizing agents, making synthesis simple.[17-18] Gardea-Torresdey was the first to report on the green synthesis of nano-sized AgNPs using alfalfa sprouts (variety Mesa).[19] AgNPs have recently been reported to synthesize with leaf extracts of *Acalypha indica*[20], *Camellia japonica*[21], *Nigella arvensis*[22], *Malva parviflora*[23], and *Psidium guajava*[24]; flower extract of *Clitoria ternatea*[25]; fruit extracts of *Rubus glaucus*[26], and *Diospyros malabarica*[27]; bark extracts of *Cinnamon zeylanicum*[28], *Alstonia scholaris*[29], and *Prosopis juliflora*[30]; peel extract of *Musa paradisiaca*[31]; root extract of *Berberis vulgaris*[32]; rhizome extract of *Zingiber officinale*[33]; tuber extract of *Pueraria tuberosa*[34]; and seed extracts of *Jatropha curcas*[35] and *Macrotyloma uniflorum*[36]. Some of the AgNPs synthesized with these plant extracts had antibacterial and/or antifungal activity. For instance, Al-Otibi and co-workers[23] determined that AgNPs synthesized from *Malva parviflora* had a strong fungistatic effect on the mycelial growth of *Alternaria alternata*, *Helminthosporium rostratum*, *Fusarium solani*, and *F. oxysporum*. *Acalypha indica*-derived AgNPs, on the other hand, were found to be highly effective against some sclerotial fungi.[20]

Tilia is a genus of 25 species in the Tiliaceae family that is distributed in East Asia, Europe-West Siberia, and North America.[37] *Tilia rubra* DC. subsp. *caucasica* (Rupr.) is the dominant linden species in the flora extending from the Black Sea Region's eastern part (Melet river) to the Caucasus Mountains' southern slopes.[38] Linden flowers are used in Turkish traditional medicine to treat indigestion, headaches, cold flu, insomnia, high blood pressure, cholesterol, and atherosclerosis[39], as well as their diaphoretic, antispasmodic, and expectorant properties.[40] On the other hand, it has been documented that linden flowers have limited antifungal[41] and antibacterial[42] activity. Linden flowers contain various biologically active compounds such as flavonoids, mucilage, essential oil, phenolic acids, amino acids, and proanthocyanidins[43,40], which serve to produce AgNPs by mediating the reduction of Ag ions.[44]

A statistical and graphical technique, Response Surface Methodology (RSM), is a widely used methodology for designing models and analyzing various manufacturing issues.[45] RSM assists in identifying factors, investigating interactions, determining optimal conditions, computing the optimal level of variables, and ensuring maximum output in a fixed number of experiments.

The study aims to optimize the production of microwave-synthesized AgNPs using *T. rubra* subsp. *caucasica* extracts with RSM based on the face-centered central composite design (FCCD), characterize the synthesized nanoparticles by various spectroscopic and microscopic methods, and evaluate their antifungal effects on some *Phytophthora* species.

2. MATERIALS AND METHODS

2.1. Plant material, chemicals, and fungal cultures

Tilia rubra subsp. *caucasica* flowers were collected from Gülyalı county, Ordu province, Türkiye. Merck (Darmstadt, Germany) supplied the silver nitrate ($AgNO_3$), sodium hydroxide (NaOH), and agar agar medium.

Phytophthora (*P. cactorum*, *P. capsici*, *P. cinnamomi*, *P. citrophthora*, *P. megasperma*, *P. nicotianae*, and *P. palmivora*) isolates used in this study were provided by Dr. Ilker Kurbetli at Batı Akdeniz Agricultural Research Institute (BATEM).

2.2. Preparation of linden flower extract

Linden flowers were washed with distilled water and dried in an oven at 60 °C after being dehumidified with paper towels. Ten grams of the flowers were mixed with 100 ml of distilled water in a 500-ml flask and stirred continuously for 30 min at 80 °C using a heater stirrer. After cooling, the extracts were centrifuged and filtered through Whatman No. 1 filter paper and then kept in a refrigerator at 4 °C.

2.3. Green synthesis of AgNPs

For the green synthesis of AgNPs in this study, 2.5–7.5 ml of linden flower extract were added to 1–10 mM $AgNO_3$ solution, and the mixture (25 ml) was stirred

DOI: http://dx.doi.org/10.32571/ijct.1194356 **E-ISSN: 2602-277X**

using a magnetic stirrer. The final pH of the mixture was adjusted to 12 with 0.1 M NaOH. The mixture was heated in a microwave for 30 to 90 seconds at a power range of 400 to 800 watts. Silver ion reduction resulted in a color change from yellowish to brownish or dark brown depending on the reaction conditions. The synthesized AgNPs were centrifuged at 15000 rpm for 15 minutes, then washed twice with distilled water and dried at 80 °C. They were then stored in the refrigerator at 4 °C.

2.4. Statistical optimization of AgNPs synthesis

The face-centered central composite design (FCCD) from RSM was used to evaluate the effect of independent variables [$AgNO_3$ concentration (mM), linden flower extract (ml), power (watt), and time (sec.)] on AgNP synthesis and to identify an optimum condition. Each variable was coded at three levels of +1 (high), 0 (middle) and, -1 (low) (Table 1). An FCCD was designed, consisting of a total of 29 runs with five repetitions at the central point (Table 2). Response variables were fitted into the quadratic polynomial model, which is normally defined as a relationship between responses and independent variables: where Y is the absorbance of AgNPs (response), β_0 is the regression coefficient, β_i, β_{ii}, and β_{ij} are the linear, quadratic and interaction coefficients, X_i and X_j are the independent variables (factors), and ε is the error.

$$y = \beta_0 + \sum_{i=1}^{k} \beta_i X_i + \sum_{i=1}^{k} \beta_{ii} X_i^2 + \sum_{i=1}^{k-1} \sum_{j=1}^{k} \beta_{ij} X_i X_j + \varepsilon$$

Table 1. Level of variables chosen for the face-centered central composite design

Coded	Variables	Units	Min.	Max.	Coded		Mean	Std. Dev.
					Low	High		
A	$AgNO_3$ concentration	mM	1.0	10.0	1 ↔ 1.0	1 ↔ 10.0	5.5	3.61
B	Extract	ml	2.5	7.5	1 ↔ 2.5	1 ↔ 7.5	5.0	2.00
C	Power	watt	400.0	800.0	1 ↔ 400.0	1 ↔ 800.0	600.0	160.36
D	Time	sec	30.0	90.0	1 ↔ 30.0	1 ↔ 90.0	60.0	24.05

Table 2. Face-centered central composite design showing actual values along with the experimental and predicted responses

Std. order*	Run order	A-$AgNO_3$ concn. (mM)	B-Extract (ml)	C-Power (watt)	D-Time (sec)	Actual (Absorbance)	Square root transform	
							Actual	Predicted
8	1	10	7.5	800	30	0.2179	0.466798	0.472825
15	2	1	7.5	800	90	0.1257	0.354542	0.371875
21	3	5.5	5	400	60	0.1511	0.388716	0.400669
4	4	10	7.5	400	30	0.1852	0.430349	0.413638
18	5	10	5	600	60	0.3478	0.589746	0.593934
12	6	10	7.5	400	90	0.3198	0.565509	0.577405
6	7	10	2.5	800	30	0.2760	0.525357	0.569602
2	8	10	2.5	400	30	0.2840	0.532917	0.507788
1	9	1	2.5	400	30	0.0306	0.174929	0.208229
20	10	5.5	7.5	600	60	0.1483	0.385097	0.424879
25	11	5.5	5	600	60	0.1802	0.424500	0.440307
19	12	5.5	2.5	600	60	0.2372	0.487032	0.442635
28	13	5.5	5	600	60	0.2088	0.456946	0.440307
26	14	5.5	5	600	60	0.2018	0.449222	0.440307
10	15	10	2.5	400	90	0.3828	0.618708	0.639426
3	16	1	7.5	400	30	0.0503	0.224277	0.237366
16	17	10	7.5	800	90	0.6396	0.799750	0.775398
24	18	5.5	5	600	90	0.2507	0.500700	0.519448
9	19	1	2.5	400	90	0.0431	0.207605	0.193783
11	20	1	7.5	400	90	0.0843	0.290345	0.255049
5	21	1	2.5	800	30	0.0435	0.208567	0.188876
29	22	5.5	5	600	60	0.1761	0.419643	0.440307
22	23	5.5	5	800	60	0.2566	0.506557	0.489989
27	24	5.5	5	600	60	0.1913	0.437379	0.440307
7	25	1	7.5	800	30	0.0516	0.227156	0.215387
17	26	1	5	600	60	0.0631	0.251197	0.242393
13	27	1	2.5	800	90	0.0827	0.287576	0.313235
23	28	5.5	5	600	30	0.1590	0.398748	0.375385
14	29	10	2.5	800	90	0.7412	0.860930	0.840045

*Standard order

DOI: http://dx.doi.org/10.32571/ijct.1194356 **E-ISSN: 2602-277X**

All analyses were performed with version 13 of the Design Expert program (Stat-Ease, Inc., USA). The program was used for regression analysis of the obtained data and to estimate the regression equation coefficient. The fitted model was then plotted in the form of perturbation, 3D, and 2D contour plots to illustrate the relationship between responses. Finally, to validate the developed model, experimental sets were created using the suggested optimum combination.

2.5. Characterization of AgNPs

Preliminary characterization of the synthesized AgNPs was performed using UV–Vis Spectroscopy (Lambda 35, Perkin Elmer, Inc., MA, USA). A 200 µl solution containing AgNPs was diluted with 2 ml of distilled water. The spectra of AgNPs were obtained in the wavelength range of 200–700 nm at 1 nm resolution using a quartz cuvette. Baseline correction was done using distilled water as the blank.

Infrared spectra of the AgNPs were recorded using Fourier Transform Infrared (FT–IR) Spectroscopy (Spectrum 65, Perkin Elmer, Inc., MA, USA). 1 mg of the synthesized AgNPs was mixed with 200 mg KBr, then pressed into a pellet. The FT–IR spectra from the nanoparticles were collected in the transmittance mode at a wave number range of 4000-400 cm^{-1}.
Elemental and morphological analysis of the AgNPs were carried out with a Scanning Electron Microscope (SEM) (SU-1510, Hitachi High-Tech., Tokyo, Japan) coupled with Energy Dispersive X-ray Spectroscopy (EDS).

A Transmission Electron Microscope (TEM) (HighTech HT7700, Hitachi High-Tech., Tokyo, Japan) was used to confirm the particle size and structure of the AgNPs.

2.6. Antifungal effect of the synthesized AgNPs on *Phytophthora* species

Antifungal activities of the synthesized AgNPs on seven *Phytophthora* (*P. cactorum*, *P. capsici*, *P. cinnamomi*, *P. citrophthora*, *P. megasperma*, *P. nicotianae*, and *P. palmivora*) species were tested according to Türkkan[46] with a small modification. Different concentrations of AgNPs (28.125, 56.25, 112.5, 225, 450, and 900 µg ml^{-1}) were added to autoclaved and then cooled V8 agar medium at 50 °C. A 15-ml aliquot of modified V8 medium was aseptically dispensed into a Petri plate (7 cm in diameter) with an unmodified V8 agar plate used as a control. A 5 mm-diameter mycelial disc from 7-day-old fungal cultures was placed in the center of each plate and incubated at 25 °C in the dark after sealing the plates with Parafilm. When control growth covered plates (4–7 days), all fungal growth diameters were converted to percent inhibition compared to controls.

A probit analysis of the SPSS (Version 22; IBM Company, Chicago, USA) was used to compute the concentrations of the AgNPs that caused a 50% reduction (EC_{50}) in the fungal growth. The minimum inhibitory concentration (MIC) value, which completely stopped the fungal growth, was also found by parallel experiments.

The toxicity (fungistatic/fungicidal) of the AgNPs was evaluated according to Thompson[47] and Tripathi and co-workers[48]. V8 agar discs from modified plates that exhibited no fungal growth were re-inoculated with unmodified V8 agar plates and then monitored for 9 days at 25 °C for revivals of growth. The minimum fungicidal concentration (MFC) value was determined at the end of this period as the minimum AgNPs concentration required to completely and irreversibly stop fungal growth.

3. RESULTS AND DISCUSSION

Over the last two decades, numerous studies have demonstrated the use of various plant extracts for the green synthesis of AgNPs.[19,20,23,25,26,28,29,31-35] In this study, linden flower extract was used as a reducing and stabilizing agent in the green synthesis of AgNPs.

3.1. Optimization of process parameters by response surface methodology

In the study, we used the face-centered central composite design (FCCD) to determine the optimum experimental condition for the synthesis of AgNPs from linden flowers. Considering the peak intensity, four independent synthesis factors, including the concentration of $AgNO_3$ solution, linden flower extract (ml), power (watt), and time (sec.), were investigated to obtain the optimal SPR band of the synthesized AgNPs.

Previous studies have shown that pH is one of the most effective factors in the synthesis of AgNPs. For instance, Veerasamy and co-workers[49] reported that high pH values facilitate the binding of more AgNPs with many functional groups available for silver bonding. According to Vanaja and co-workers[50], the formation of nanoparticles increased with increasing pH. Khalil and co-workers[51] demonstrated that synthesis of AgNPs using olive leaf extract under alkaline conditions improved the antioxidants' reducing and stabilizing ability. As a result, the pH values of alkaline solutions (8, 10, and 12) were used in the current study (Figure 1). The FCCD for the four factors with a solution pH of 12 was constituted with a total of 29 runs. The SPR peak intensity of AgNPs was determined using responses resulting from the absorbance of 29 runs synthesized in the 372-401 nm range (Table 2).

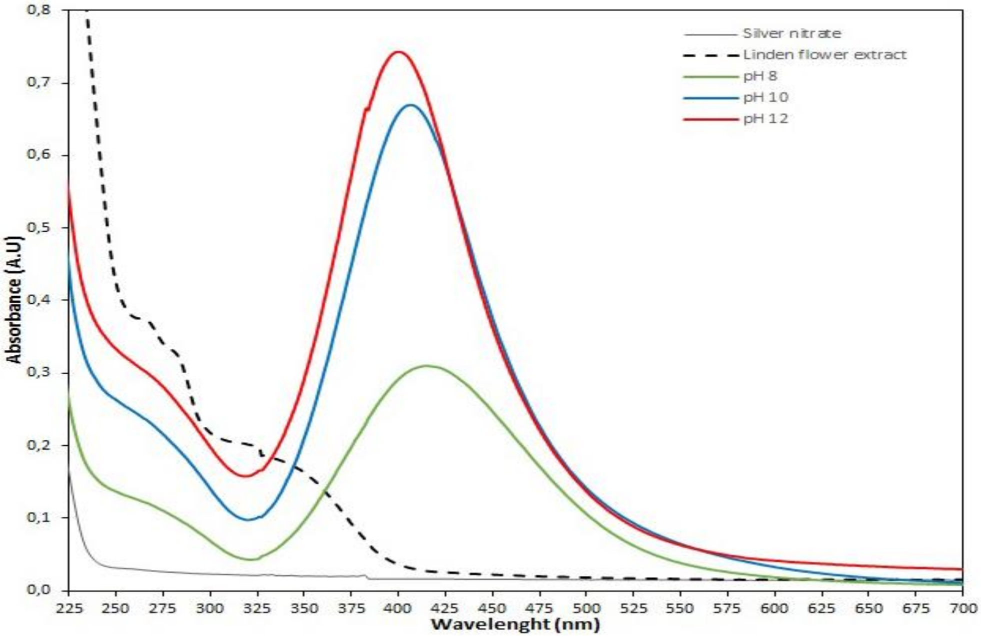

Figure 1. UV–Vis spectra of AgNPs synthesized with linden flower extract under alkaline conditions.

The model expressing the relationship between experimental factors and response to determine optimal values of AgNP synthesis is presented in Eq. (1) and Eq. (2):

$$Y(coded)=0.4403+0.1758A-0.0089B+0.0447C+0.0720D-0.0221A^2-0.0065B^2+0.0050C^2+0.0071D^2-0.0308AB+0.0203AC+0.0365AD-0.0007BC+0.0080BD+0.0347CD \quad (1)$$

$$Y(actual)=+0.304280+0.035028A+0.016359B-0.000392C-0.004040D-0.001093A^2-0.001048B^2+0.000000125551C^2+0.00000789931D^2-0.002740AB+0.000023AC+0.000271AD-0.0000013291BC+0.000107BD+0.00000578358CD \quad (2)$$

Where Y is the obtained absorbance (square root transformation, sqrt) as an indication of the SPR intensity; A is silver nitrate concentration; B is the linden flower extract; C is the power and D is the time. In the present study, data transformation is required since the ratio of maximum (0.7412) to minimum (0.0306) among responses is greater than 10. Therefore, before statistical analysis, the response was transformed to fit a normal distribution using sqrt. The significance of this quadratic model was assessed using analysis of variance (ANOVA) (Table 3).

Table 3. ANOVA for absorption response

Source	Sum of Squares	df	Mean Square	F-value	p-value	
Model	0.7528	14	0.0538	51.17	< 0.0001	significant
A-$AgNO_3$ concentration (mM)	0.5561	1	0.5561	529.2	< 0.0001	
B-Extract (ml)	0.0014	1	0.0014	1.35	0.2647	
C-Power (watt)	0.0359	1	0.0359	34.16	< 0.0001	
D-Time (sec.)	0.0934	1	0.0934	88.87	< 0.0001	
AB	0.0152	1	0.0152	14.46	0.0019	
AC	0.0066	1	0.0066	6.27	0.0253	
AD	0.0213	1	0.0213	20.31	0.0005	
BC	6.90E-06	1	6.90E-06	0.0066	0.9366	
BD	0.001	1	0.001	0.9823	0.3385	
CD	0.0193	1	0.0193	18.33	0.0008	
A^2	0.0013	1	0.0013	1.21	0.2906	
B^2	0.0001	1	0.0001	0.1056	0.7501	
C^2	0.0001	1	0.0001	0.0621	0.8069	
D^2	0.0001	1	0.0001	0.1244	0.7296	
Residual	0.0147	14	0.0011			
Lack of Fit	0.0137	10	0.0014	5.46	0.058	not significant
Pure Error	0.001	4	0.0003			
Cor Total	0.7675	28				

DOI: http://dx.doi.org/10.32571/ijct.1194356 **E-ISSN: 2602-277X**

The model F-value of 51.17 implies that the model is statistically significant. There is only a 0.01% chance that an F-value this large could occur due to noise, while p-values are 0.0001. P-values less than 0.05 indicate that the developed quadratic model and some terms are significant. A lack of fit of 5.46 (F-value) compared to pure error means it is negligible and is a good indicator for the model. In our study, the regression value (R^2 = 0.9808) means that 98.08% of both observed and predicted data can be explained by using this model (Figure 2a, Table 4). Moreover, the predicted R^2 of 0.8760 is in reasonable agreement with the adjusted R^2 of 0.9617, since the difference between the two is less than 0.2. It is reported that a suitable statistical model should result in R^2~1.[52] Adequate precision measures the signal-to-noise ratio, and a ratio greater than 4 is desirable. The ratio of 27.93 indicated an adequate signal; hence, this model can be used to continue the design process. In the developed model, the residuals show a random distribution between the predicted and actual (observed) values, which indicates that all the residual values lie along a straight line without large deviations, confirming the normality of the error distribution (Figure 2b). It is also shown in Figure 2(c) that not only is the residue randomly distributed on both sides of the zero line, but it is also within the acceptable range. Mondal and Purkait[53] stated that the residuals between predicted and actual values should be in the range of ±3%, demonstrating that the constructed model is adequate. The perturbation plot shows that $AgNO_3$ concentration (A) has a greater positive effect than the other three factors in increasing the amount of silver nanoparticle synthesis (Figure 2d).

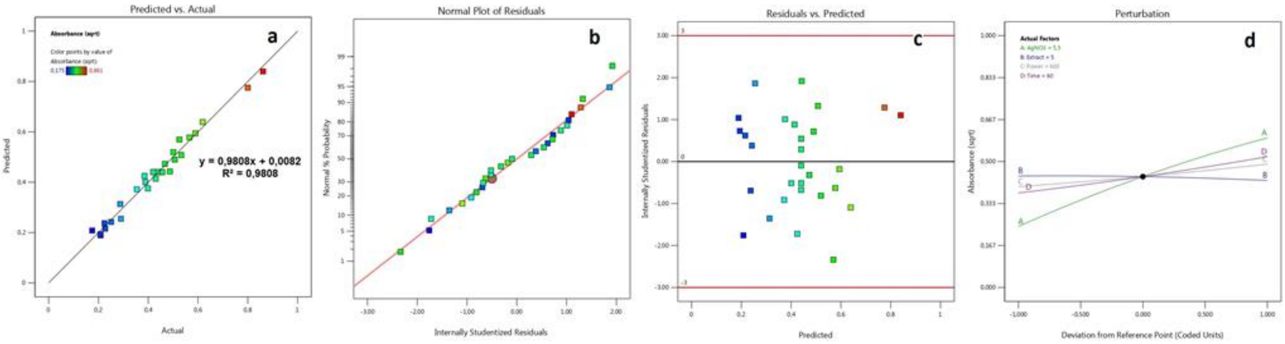

Figure 2. Diagnostic plots of AgNPs optimized using FCCD: (a) Predicted vs. Actual, (b) Normality, (c) Residual vs. Predicted, (d) Perturbation.

Table 4. Fit and model summary statistics

Std. Dev.	0.0324	R²	0.9808
Mean	0.43	Adjusted R²	0.9617
C.V. %	7.54	Predicted R²	0.876
		Adeq Precision	27.9303
PRESS	0.0952	-2 Log Likelihood	-137.71
BIC	-87.20	AICc	-70.78

In the study, 3D and 2D contour plots were used to show the interactions among variables and their mutual effects on the absorbance (Figure 3). The relationship between $AgNO_3$ concentration and the extract is depicted in Figure 3(a). AgNP synthesis tends to be higher, especially under conditions where the $AgNO_3$ concentration is 10 mM and the extract is between 2.5 and 3.5. On the contrary, the production of AgNPs is maximized when it comes to the same concentration of $AgNO_3$, the highest power level, and the longest duration of time (Figure 3b, 3c). Moreover, the relationship between $AgNO_3$ concentration and power was similar to that of $AgNO_3$ concentration and time. When the extract interacts with power or time, it appears to have a limited effect on the synthesis of AgNPs, as shown in Figures 3(d) and 3(e). The synthesis of AgNPs, on the other hand, reaches its peak when both power and time are at their peak (Figure 3f). These findings are consistent with those of Cai and co-workers[54], who reported that by adjusting power and time, total energy (power x time) is optimized over a specific range of 700-850 watts min 100 ml^{-1}, resulting in high-quality output. Furthermore, they discovered that if the total energy is less than 700 watts min, Ag ions cannot be fully reduced, resulting in low AgNP synthesis. Nikaeen and co-workers[55] found that the effects of $AgNO_3$ concentration and time on SPR intensity were similar, and that higher concentrations of both increased the quality of AgNPs. For the synthesis of AgNPs, Krishnaraj and co-workers[20] revealed that 50 ml of reaction medium containing 6 ml of *A. indica* leaf extract and 1 mM of $AgNO_3$ solution is optimum.

DOI: http://dx.doi.org/10.32571/ijct.1194356 **E-ISSN: 2602-277X**

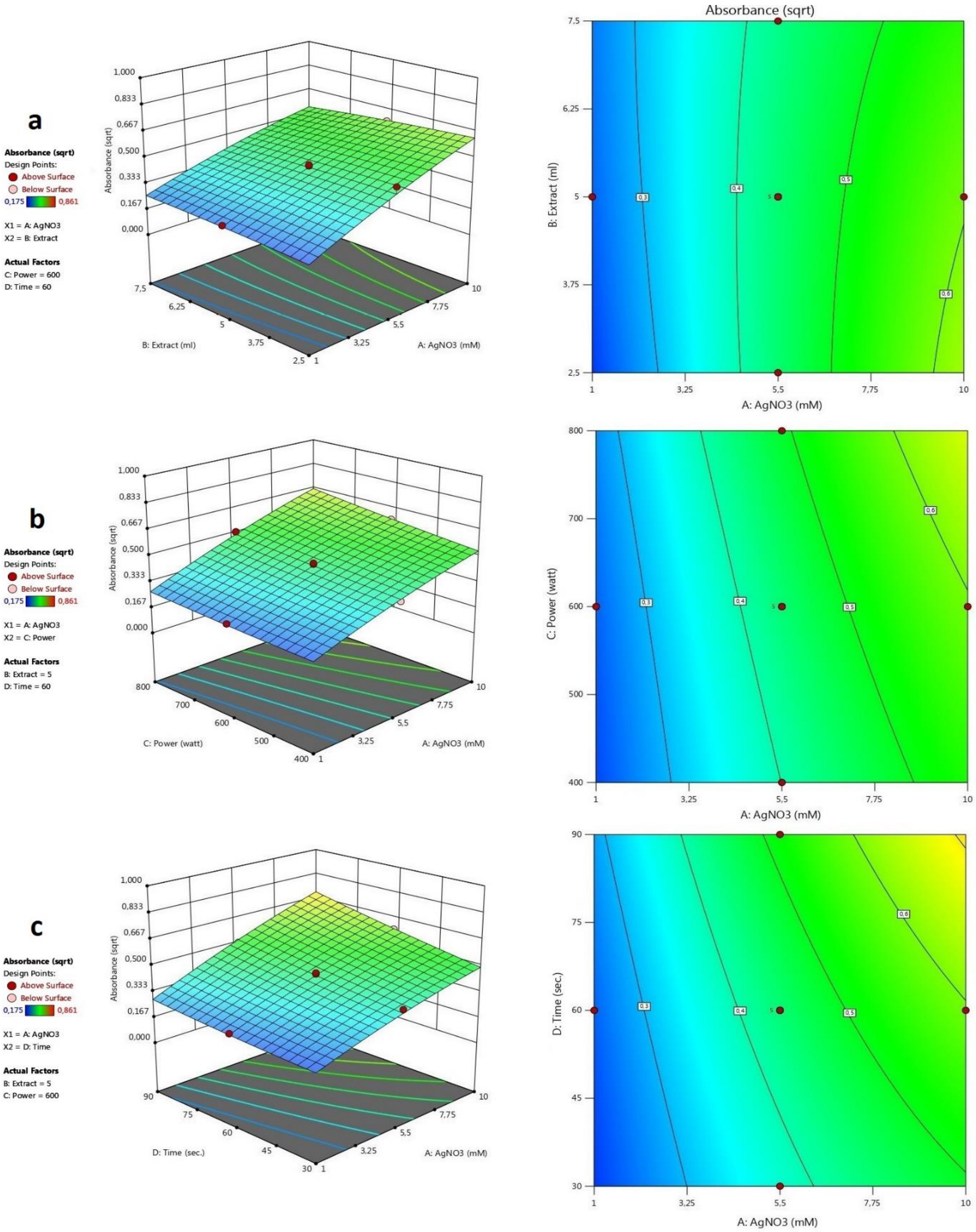

Figure 3. 3D and 2D plots showing the combined effects of factors affecting the synthesis of AgNPs:
(a) $AgNO_3$ concentration and linden flower extract, (b) $AgNO_3$ concentration and power, and (c) $AgNO_3$ concentration and time.

DOI: http://dx.doi.org/10.32571/ijct.1194356 **E-ISSN: 2602-277X**

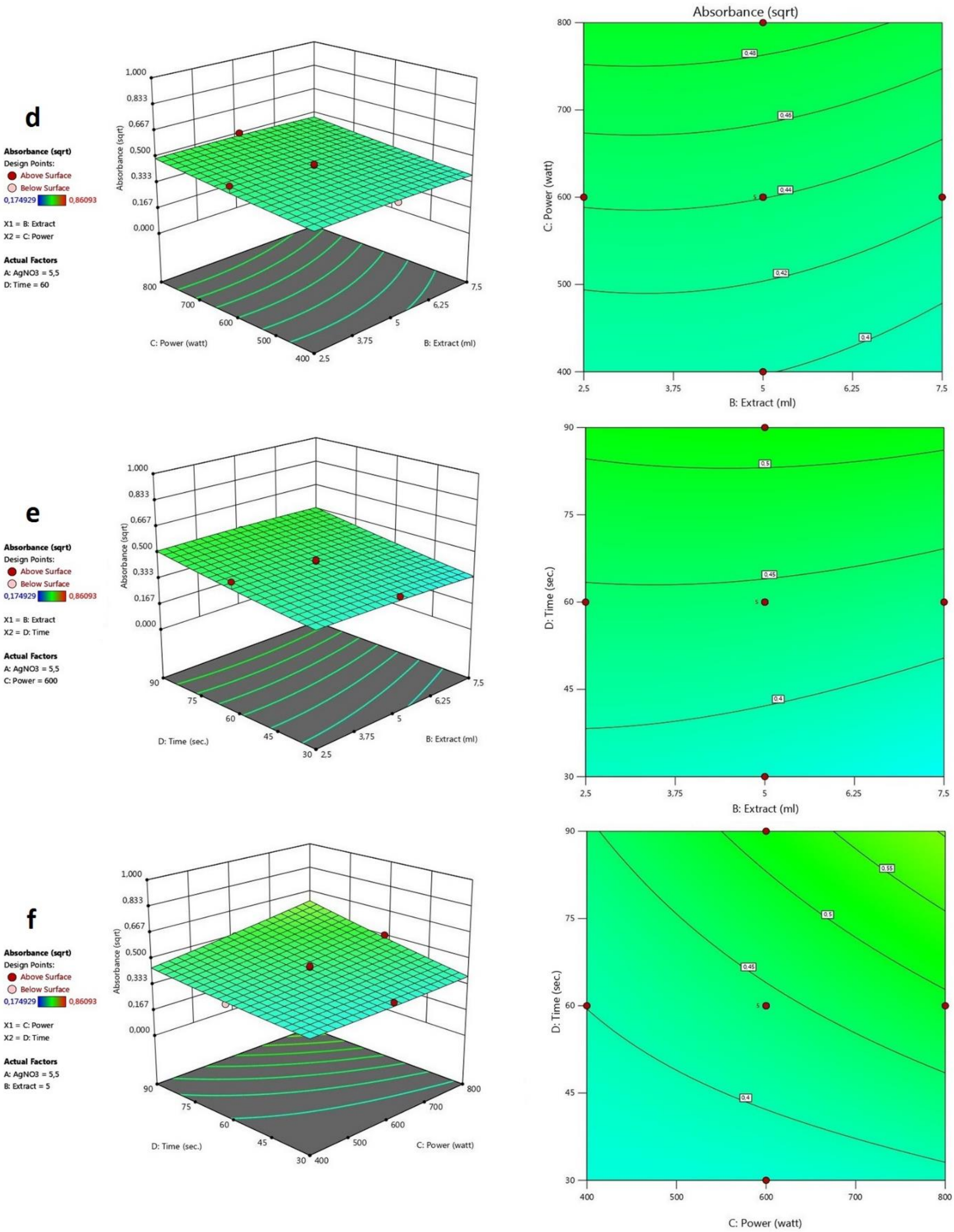

Figure 3. 3D and 2D plots showing the combined effects of factors affecting the synthesis of AgNPs: (d) linden flower extract and power, (e) linden flower extract and time, and (f) power and time.

DOI: http://dx.doi.org/10.32571/ijct.1194356 **E-ISSN: 2602-277X**

In our study, the optimum values of $AgNO_3$ concentration, extract volume, power, and time for the synthesis of AgNPs at 401 nm are 10mM, 2.5 ml, 800 watts, and 90 sec., respectively, and the the predicted absorbance value of the corresponding AgNPs is 0.840 (Table 5). We repeated the experimental synthesis of AgNPs using the parameters mentioned above and obtained an absorbance value of 0.896 with an error value of 3.2%, which is less than the 20% (0.2) error value. Because the error value is much lower than the standard value (0.2) of Design Expert software, it has been verified that it is sufficient for model parameter optimization.

Table 5. Validation of experimental model

Experiments	Absorbance (401 nm)	Absorbance (Sqrt)	Absorbance (Predicted)
1	0.8031	0.8962	-
2	0.7921	0.8900	-
3	0.8069	0.8983	-
4	0.7994	0.8941	-
5	0.8130	0.9017	-
Average	0.8029	0.8960	0.840

3.2. Characterization of AgNPs

3.2.1. UV–Vis spectral analysis

UV-Vis spectroscopy was used to determine the absorbance spectra of the synthesized AgNPs. AgNPs synthesized under optimum conditions caused a dark brown color change, which is a sign of reduction of silver ions in solution from Ag^{+1} to Ag^0. This is due to the excitation of the SPR of AgNPs.[56] Figure 4 shows the absorbance spectra of silver colloid as a function of the reactions of Ag ions with the linden flower extract. The characteristic absorbance peak of AgNPs in the study was observed at 401 nm (Figure 4), which is within the range previously reported for AgNPs. [57,58]

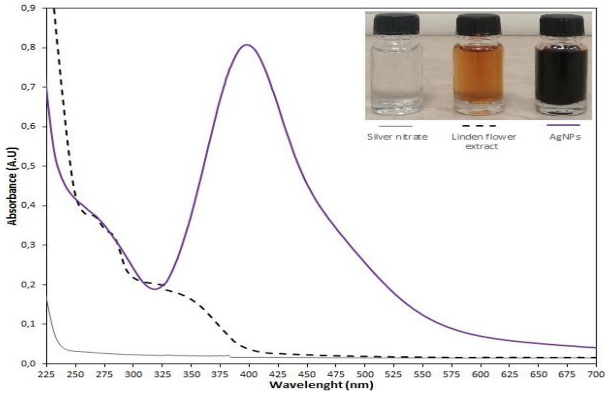

Figure 4. Visual observation and UV–Vis spectra of AgNPs synthesized with linden flower extract under optimum conditions.

3.2.2. FT–IR studies

The functional groups of both the linden flower extract and the synthesized AgNPs were determined by FT-IR analysis. FT-IR spectrum of the plant extract showed nine major peaks at 3248.13 (O–H stretching, alcoholic or phenolic), 2931.80 (C–H and CH_2; aliphatic hydrocarbons), 2322.29 (O=C=O stretching), 2129.41 (C≡C stretching, alkyne), 1589.34 (C=C), 1388.75 (C–O, ester group), 1234.44 (C–O, cyclic polyphenolics), 1049.28 (O–H deformation) and 663.51 (C–C bending) cm^{-1} (Figure 5a). Flavonoid and phenolic compounds could be adsorbed on the surface of AgNPs, possibly by the interaction through π-electrons interaction.[44] The carbonyl and hydroxyl linkages in the components of linden flower extract are responsible for the reduction of silver ions to AgNPs. On the other hand, in the FT-IR spectrum of AgNPs, different peaks were observed between 3556.74 cm and 1126.43 cm, originating from the O–H, N–H, C=C, C–N, and C–O groups (Figure 5b). It also reveals the possible interaction between Ag ions and linden flower extract during the bioreduction stage.

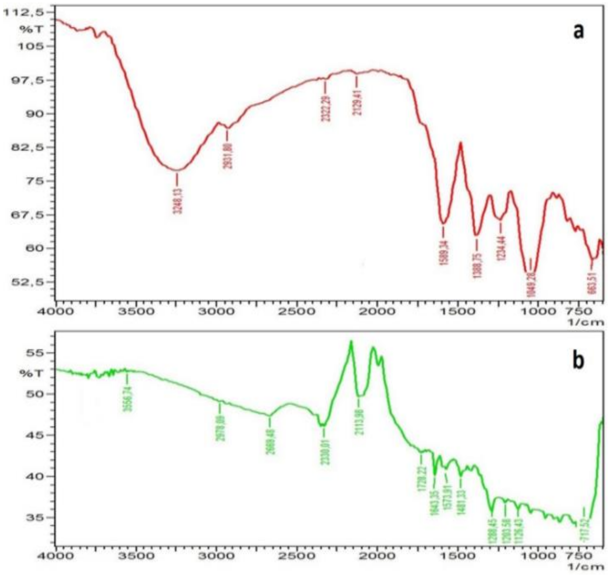

Figure 5. FT–IR spectra of (a) linden flower extract and (b) AgNPs synthesized with linden flower extract.

3.2.3. SEM–EDS and TEM analyzes

The size, shape, and morphologies of the synthesized AgNPs were characterized by SEM–EDS and TEM. SEM (Figure 6a) and TEM (Figure 6b) data revealed that the AgNPs were nearly spherical in shape and ranged in size from 9.92 to 87.34 nm, with an average particle size of 24.77 nm. Also, a few clusters were noticed in the SEM image. In EDS profiles, the AgNPs with crystalline character were determined to have a peak in the 3KeV area (Figure 6c), which is consistent with the results of previous studies. Vijayaraghavan and co-workers[59] observed an absorption spectrum at 3KeV with a strong peak at the silver region confirming the presence of AgNPs. It has also been reported that this may be due to the SPR property of AgNPs.[60] EDS spectral data revealed that the nanoparticles were composed primarily of silver, and the two prominent contaminants were phosphorus

DOI: http://dx.doi.org/10.32571/ijct.1194356 E-ISSN: 2602-277X

(P) and calcium (Ca), possibly from linden flower extract. In addition, carbon (C), and oxygen (O) were found in the residual materials surrounding the nanoparticles and the SEM grid used to prepare them. EDS mapping of the nanoparticles is shown in Figure 6(d), where Ag, C, O, and Ca are expressed as green, yellow, red, blue, and purple color, respectively.

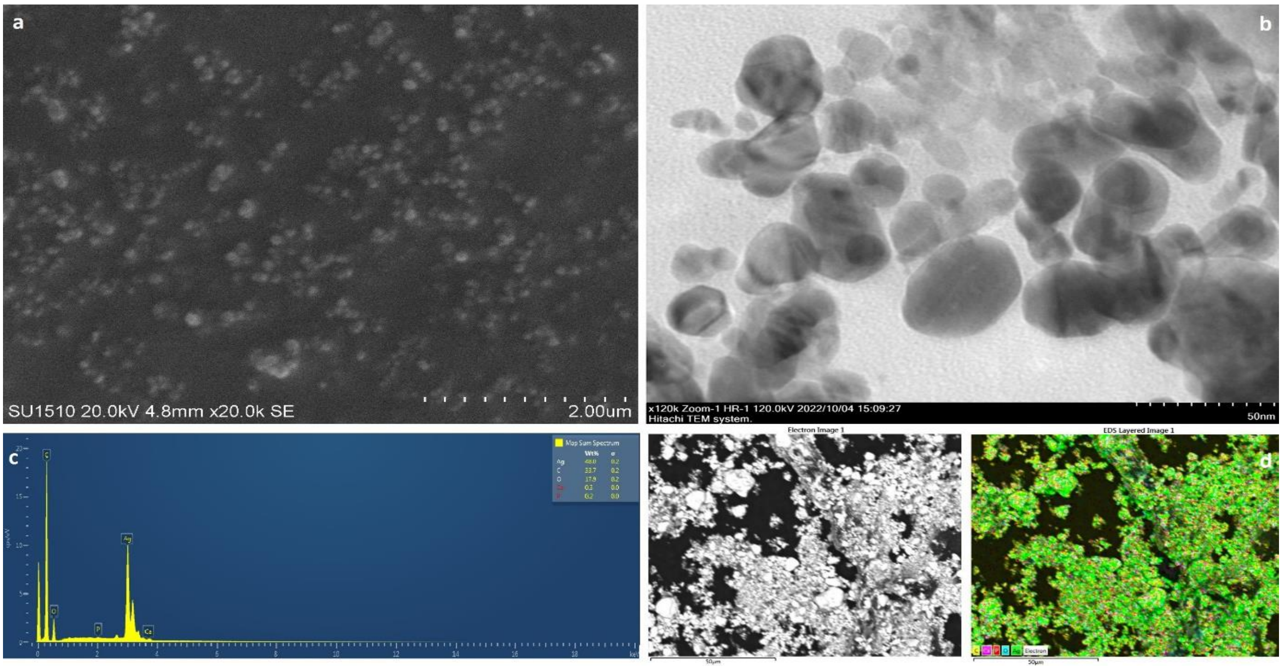

Figure 6. Microscopic and elemental analyses of synthesized AgNPs are based on (a) SEM image, (b) TEM image, (c) EDS spectrum, and (d) SEM–EDS mapping approach.

3.3. Antifungal activity of the synthesized AgNPs

Of the *Phytophthora* isolates tested in this study, *P. cactorum* and *P. palmivora* were more sensitive to the AgNPs than others (Table 6). EC_{50} values of AgNPs for *Phytophthora* isolates ranged from 46.38 to 119.36 µg ml^{-1}. At concentrations of 225 or 450 µg ml^{-1} AgNPs, mycelial growth of all 7 *Phytophthora* isolates was completely stopped (Figure 7). Furthermore, at 225 µg ml^{-1}, the inhibitory effect was fungicidal for *P. cactorum* and *P. palmivora* but fungistatic for *P. megasperma* and *P. cinnamomi*, whose inoculums began to grow when transferred to fresh V8 agar medium and then covered all Petri plates within a few days. The fungicidal effect of AgNPs was observed at 450 µg ml^{-1} for the remaining 4 *Phytophthora* species, with the exception of *P. cinnamomi*. In several previous studies, AgNPs synthesized by different plant extracts have been shown to have potent antifungal activity against various phytopathogenic fungi. Krishnaraj and co-workers[20] reported that the mycelial growth of some sclerotial fungi, including *Botrytis cinerea*, *Macrophomina phaseolina*, *Rhizoctonia solani*, and *Sclerotinia sclerotiorum*, was greatly suppressed by *Acalypha indica* AgNPs at a concentration of 1500 µg ml^{-1}. Al-Zahrani and Al-Garni[61] determined that the MIC values of AgNPs synthesized using *Allium ampeloprasum* ranged from 652 to 2500 µg ml^{-1} for different *Aspergillus* species. On the other hand, AgNPs synthesized using *Artemisia absinthium* were observed to have a much lower MIC value than 100 µg ml^{-1} against different *Phytophthora* species such as *P. capsici*, *P. cinnamomi*, *P. infestans*, *P. katsurae*, *P. palmivora*, *P. parasitica*, and *P. tropicalis*.[62] However, these differences may be due to the biochemical content of the plants that mediate the synthesis of AgNPs and the difference in target organisms. It is assumed that the toxicity of silver nanoparticles is related to their very small structure, shape, and form, and that silver nanoparticles act by disrupting the normal functions of cell organelles after penetrating the microbial cell.[63]

Table 6. Toxic effects of AgNPs synthesized with linden flower extract against some *Phytophthora* species

***Phytophthora* spp.**	**EC_{50}^{a} (µg ml^{-1})**	**MIC^{b} (µg ml^{-1})**	**MFC^{c} (µg ml^{-1})**
P. cactorum	50.66	225	225
P. capsici	110.38	450	450
P. cinnamomi	46.38	225	900
P. citrophthora	119.36	450	450
P. megasperma	96.37	225	450
P. nicotianae	77.27	450	450
P. palmivora	91.71	225	225

^{a}The concentration that caused 50% reduction.
^{b}Minimum inhibitory concentration.
^{c}Minimum fungicidalconcentration.

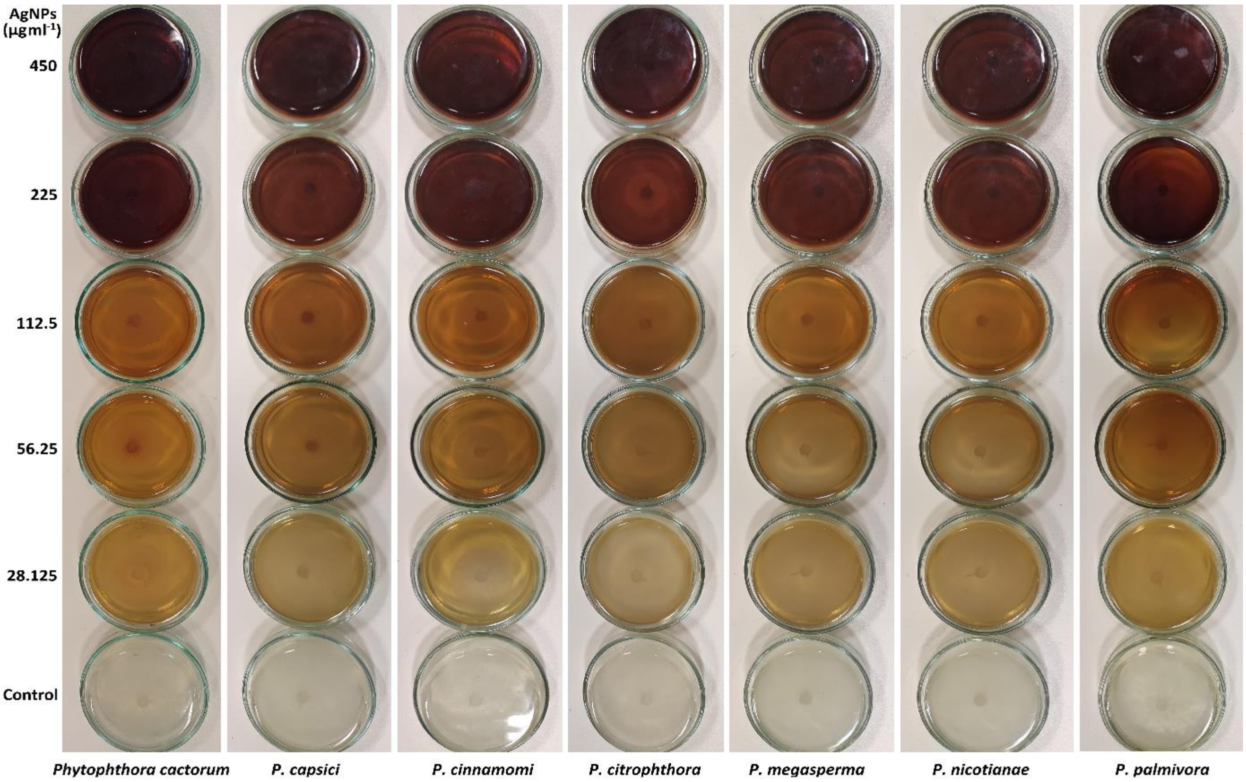

Figure 7. Effects of the different concentrations of synthesized AgNPs on *Phytophthora* species.

4. CONCLUSIONS

In this study, AgNPs were synthesized by a green method using linden (*Tilia rubra* subsp. *caucasica*) flower extract. Based on the RSM, the FCCD was used to optimize four important experimental parameters in the biosynthesis process of AgNPs, such as $AgNO_3$ concentration, extract volume, power, and time. Through a four-factor equation, the FCCD with 29 runs, the optimum conditions of the experimental parameters are computed as 10 mM, 2.5 ml, 800 watts, and 90 seconds, and this reaction condition was experimentally verified. The synthesized AgNPs were characterized by UV–Vis, FT–IR, SEM–EDS, and TEM. In addition, the synthesized AgNPs exhibited antifungal activity against some important *Phytophthora* species, such as *P. cactorum*, *P. capsici*, *P. cinnamomi*, *P. citrophthora*, *P. megasperma*, *P. nicotianae*, and *P. palmivora*.

ACKNOWLEDGEMENTS

This study, supported by Ordu University (The project no: B-2209), is part of the first author's doctoral thesis. We also thank Dr. İlker Kurbetli for providing *Phytophthora* isolates.

Conflict of interests

I declare that there is no conflict of interest with any person, institute, company, etc.

REFERENCES

1. Ahn, E.Y.; Park, Y. *Mater. Sci. Engin*. **2020**, C, 116, 111253.

2. Jain, R.K.; Huang, X.; El-Sayed, I.H.; El-Sayed, M.A. *Acc. Chem. Res.* **2008**, 41, 1578-1586.

3. Tran, Q.H.; Le, A.T. *Adv. Nat. Sci.: Nanosci. Nanotechnol. 4*. **2018.**

4. Wei, L.; Lu, J.; Xu, H.; Patel, A.; Chen, Z.S.; Chen, G. *Drug Disc. Tod*. **2015**. 20, 595.

5. Lansdown, A.B. *Advanc. Pharmacol. Sci.* **2010**. 2010, 16.

6. Goia D.V.; Matijević, E. *New Journ. Chem*. **1998**. 11, 1203-1208.

7. Taleb, A.; Petit, C.; Pileni, M.P. *Chem. Mater*. **1997**. 9, 950-959.

8. Esumi, K.; Tano, T.; Torigoe, K.; Meguro, K. *Chem. Mater*. **1990**. 2, 564-567.

9. Henglein, A. *Langmuir*. **2001**. 17, 2329-2333.

10. Rodríguez-Sánchez, L.; Blanco M.C.; López-Quintela, M.A. *J. Physc. Chem. B*. **2000.** 104, 9683-9688.

11. Zhu, J.; Liu, S.; Palchik, O.; Koltypin, Y.; Gedanken, A. *Langmuir*. **2000**. 16, 6396-6399.

12. Pastoriza-Santos, I.; Liz-Marzán, L.M. *Langmuir*.

DOI: http://dx.doi.org/10.32571/ijct.1194356 E-ISSN: 2602-277X

2002. 18, 2888-2895.

13. Kröger, N.; Deutzmann, R.; Sumper, M. *Sci*. **1999**. 286, 1129-1132.

14. Ahmad, A.; Mukherjee, P.; Senapati, S.; Mandal, D.; Khan, M.I.; Kumar, R.; Sastry, M. *Coll. Surf. B: Biointer*. **2003**. 28, 313-318.

15. Shahverdi, A.R.; Minaeian, S.; Shahverdi, H.R.; Jamalifar, H.; Nohi, A.A. *Proc. Biochem*. **2007**. 42, 919-923.

16. Siddiqi, K.S.; Rashid, M.; Rahman, A.; Husen, A.; Rehman, S. *Biomat. Res*. **2018**. 22, 1-9.

17. Nath, D.; Banerjee, P. *Enviro. Toxicol. Pharm*. **2013**. 36, 997-1014.

18. Ovais, M.; Khalil, A.T.; Islam, N.U.; Ahmad, I.; Ayaz, M.; Saravanan, M.; Shinwari, Z.K.; Mukherjee, S. *Appl. Micr. Biotech*. **2018**. 102, 6799-6814.

19. Gardea-Torresdey, J.L. Gomez, E.; Jose, R.; Peralta-Videa, J.R.; Parsons, J.G.; Horacio, T.H.; Jose-Yacaman, M. *Langmuir*. **2003**. 19, 1357-1361.

20. Krishnaraj, C.; Ramachandran, R.; Mohan, K.; Kalaichelvan, P.T. *Spectro.Acta Part A: Mol. Biomol. Spectro*. **2012**. 93, 95-99.

21. Karthik, R.; Govindasamy, M.; Shen-Ming, C.S.; Cheng, Y.; Muthukrishnan, P.; Padmavathy, S.; Elangovan, A. *Jour. Photochem. Photo. B: Bio*. **2017**. 170, 164-172.

22. Chahardoli, A.; Karimi, N.; Fattahi, A. *Advanc. Pow. Techn*. **2017**. 29, 202–210.

23. Al-Otibi, F.; Perveen, K.; Al-Saif, N.A.; Alharbi, R.I.; Bokhari, N.A.; Al-Otaibi, R.M.; Al-Mosa, M.A. *Saudi Journ. Biol. Sci*. **2021**. 28, 2229–2235.

24. Le, N.T.T.; Trinh, B.T.; Nguyen, D.H.; Tran, L.D.; Luu, C.H,; Hoang Thi, T.T. *Journ. Clus. Sci.* **2021**. 32, 601-611.

25. Fatimah, I.; Hidayata, H.; Nugrohob, B.H.; Huseinc, S. *South Afr. Journ. Chem. Engin.* **2020**. 34, 97–106.

26. Kumar, B.; Smita, K.; Cumbal, L.; Debut, A. *Saudi Journ. Biol. Sci.* **2017**. 24, 45-50.

27. Bharadwaj, K.K.; Rabha, B.; Pati, S.; Choudhury, B.K.; Sarkar, T.; Gogoi, S.K.; Kakati, N.; Baishya, D.; Abdul, K.Z.; Edinur, H.A. *Nanomater*. **2021**. 11, 1999.

28. Sathishkumar, M.; Sneha, K.; Won, S.W.; Cho, C.W.; Kim, S.; Yun, Y.S. *Coll. Surf. B: Bioint.* **2009**. 73, 332-338.

29. Shetty, P.; Supraja, N.; Garud, M.; Prasad, T.N.V.K.V. *Journ. Nanostruc. Chem*. **2014**. 4, 161-170.

30. Arya, K.; Kumari, R.M.; Gupta, N.; Kumar, A.; Chandra, R.; Nimesh, S. *Artific. Cell. Nanomedic. Biotechnol.* **2018**. 46, 985-993.

31. Bankar, A.; Joshi, B.; Kumar, A.R.; Zinjarde, S. *Coll. Surf. A: Physic. Engin. Asp.* **2010.** 368, 58-63.

32. Behravan, M.; Panahi, A.H.; Naghizadeh, A.; Ziaee, M.; Mahdavi, R.; Mirzapour, A. *Inter. Journ. Biol. Macromol*. **2019**. 124, 148-154.

33. Venkatadri, B.; Shanparvish, E.; Rameshkumar, M.R.; Arasu, M.V.; Al-Dhabi, N.A.; Ponnusamy, V.K.; Agastian, P. *Saudi Journ. Biol. Sci*. **2020**. 27, 2980-2986.

34. Satpathy, S.; Patra, A.; Ahirwar, B.; Delwar, H.M. *Artific. Cell. Nanomedic. Biotechnol.* **2018**. 46, 71-85.

35. Bar, H.; Bhui, D.Kr.; Sahoo, G.P.; Sarkar, P.; Pyne, S.; Misra, A. *Coll. Surf. A: Physic. Engin. Asp*. **2009**. 348, 212-216.

36. Vidhu V.K.; Aromal, S.A.; Philip, D. *Spectr. Acta Part A: Molec. Biomol. Spectr*. **2011**. 83, 392-397.

37. Ya, T.; Ren, Z. *J. Syst. Evol*. **1996**. 34(3), 254-264.

38. Günal, N. *Act Turc*. **2013**. 5(1), 1-22.

39. Tuttu, G.; Ursavaş, S.; Söyler, R. *Anatol. J. For. Res*. **2017**. 3(1), 60-66.

40. Evans, W.C. *Trease and evans pharmacognosy, 16th edition.*; WB Saunders, Edinburg, 2010.

41. Guerin, J.C.; Reveillere, H.P. Antifungal activity of plant extracts used in therapy. *I Study of 41 plant extracts against 9 fungi species*; Annales Pharmaceutiques Francaises, 1984; pp 553-559.

42. Fitsiou, I.; Tzakou, O.; Hancianu, M.; Poiata, A. *J. Ess. Oil Res*. **2007**. 19, 183-185.

43. Bisset, N.G.; Wichtl, M. *Herbal drugs and phytopharmaceuticals*, CRC Press, Boca Raton, London, New York, Washington, 2001.

44. Konvičková, Z.; Holišová, V.; Kolenčík, M.; Niide, T.; Kratošová, G.; Umetsu, M.; Seidlerová, J. *Coll. Poly. Sci*. **2018**. 296(4), 677-687.

45. Cochran, W.G.; Cox, G.M. *Experimental designs*, 2nd ed. New York: USA, 1992.

46. Türkkan, M. *J. Agr. Sci*. **2013**. 19, 178-187.

47. Thompson, D.P. *Mycol*. 1989. 81, 151-153.

48. Tripathi, P.; Dubey, N.K.; Banerji, R.; Chansouria, J.P.N. *W. J. Micr. Biotech*. **2004**. 20, 317-321.

49. Veerasamy, R.; Xin, T.Z.; Gunasagaran, S.; Xiang, T.F.W.; Yang, E.F.C.; Jeyakumar, N.; Dhanaraj, S.A. *J. Saudi Chem. Soc*. **2011**. 15, 113-120.

50. Vanaja, M.; Gnanajobitha, G.; Paulkumar, K.; Rajeshkumar, S.; Malarkodi, C.; Annadurai, G. *J. Nano. Chem.* **2013**. 3, 1-8.

51. Khalil, M.M.; Ismail, E.H.; El-Baghdady, K.Z.; Mohamed, D. *Arab. J. Chem.* **2014**. 7(6), 1131-1139.

DOI: http://dx.doi.org/10.32571/ijct.1194356 **E-ISSN: 2602-277X**

52. Reddy, L.V.A.; Wee, Y.J.; Yun, J.S.; Ryu, H.W. *Bio. Techn*. **2008**. 99, 2242-2249.

53. Mondal, P.; Purkait, M.K. *Separ. Sci.Techn*. **2017**. 52, 2338-2355.

54. Cai, Y.; Piao, X.; Gao, W.; Zhang, Z.; Nie, E.; Sun, Z. *RSC Advan*. **2017**. 7(54), 34041-34048.

55. Nikaeen, G.; Yousefinejad, S.; Rahmdel, S.; Samari, F.; Mahdavinia, S. *Sci. Rep*. **2020**. 10, 1-16.

56. Mulvaney, P.,. *Langmuir*. **1996**. 12, 788-800.

57. Njagi, E.C.; Huang, H.; Stafford, L.; Genuino, H.; Galindo, H.M.; Collins, J.B.; Hoag, G.E.; Suib, S.L. Langmuir. **2011**. 27, 264-271.

58. Alahmad, A.; Al-Zereini, W.A.; Hijazin, T.J.; Al-Madanat, O.Y.; Alghoraibi, I.; Al-Qaralleh, O.; Al-Qaraleh, S.; Feldhoff, A.; Walter, J.G.; Scheper, T. *Pharm*. **2022**. 14(5), 1104.

59. Vijayaraghavan, K.; Nalini, S.P.K.; Prakash. N.U.; Madhankumar, D. *Mat. Lett*. **2012**. 75, 33–35.

60. Magudapathy, P.; Gangopadhyay, P.; Panigrahi, B.K.; Nair, K.G.M.; Dhara, S. *Physc. B: Conden. Matt*. **2001**. 299, 142-146.

61. Al-Zahrani, S.S.; Al-Garni, S.M. *J. Bio. Nanobiotech*. **2019**. 10, 11-25.

62. Ali, M.; Kim, B.; Belfield, K.D.; Norman, D.; Brennan, M.; Ali, G.S. *Phytopathol*. **2015**. 105, 1183-1190.

63. Buzea, C.; Pacheco, I.I.; Robbie, K. *Biointerph*.. **2007**. 2, 17-64.

DOI: http://dx.doi.org/10.32571/ijct.1135173 **E-ISSN: 2602-277X**

International Journal of Chemistry and Technology

http://dergipark.org.tr/ijct

Research Article

HOMO–LUMO, NBO, NLO, MEP analysis and molecular docking using DFT calculations in DFPA molecule

Mehmet BAGLAN[1]*, Kenan GÖREN[1], Ümit YILDIKO[2]

[1]*Faculty of Arts and Sciences Department of Chemistry, Kafkas University, Kars, Türkiye*

[2]*Faculty of Engineering and ArchitectureDepartment of Bioengineering, Kafkas University, Kars, Türkiye.*

Received: 14 June 2022; Revised: 31 December 2022; Accepted: 17 May 2023

*****Corresponding author e-mail: mehmetbaglan36@gmail.com

Citation: Baglan, M.; Gören, K.; Yıldıko,Ü. *Int. J. Chem. Technol.* **2023**, 7(1), 38-47

ABSTRACT

Using the Gaussian09 software package, N-(6-(2-(dimethylamino) ethoxy)-5-fluoropyridin-3-yl)-2-(4-fluorophenyl)-5-(trifluoromethyl) pyrazolo[1,5 α]pyrimidine-7-amine(DFPA) the theoretically optimal molecular structure, vibration frequencies and related vibrational movements of the molecule were researched. The DFT(B3PW91 and B3LYP) techniques' 6-311G(d,p) basis set was used to perform quantum chemical computations. HOMO and LUMO analysis were performed for charge transfer in the molecule. NBO analysis was used to examine the stability of the molecule as a result of both charge delocalization and hyperconjugative interaction. DFT approach was used to perform MEP and expected infrared sensitivities and Raman activity are also presented. Geometric parameters of both calculated DFT methods are compatible. Binding affinity values and molecular coupling studies show that the title substance forms a stable complex with MtPanK and PanK. It is possible that the molecule has inhibitory activity against MtPanK and PanK, paving the way for new anti-tuberculosis drugs' the development.

Keywords: DFPA, DFT, MEP, NBO, molecular doking.

DFPA molekülünde DFT hesaplamaları kullanılarak HOMO–LUMO, NBO, NLO, MEP analizi ve moleküler yerleştirme

ÖZ

Gaussian09 yazılım paketi kullanılarak, N-(6-(2-(dimetilamino) etoksi)-5-floropiridin-3-il)-2-(4-florofenil)-5-(triflorometil) pirazolo[1,5-α] pirimidin-7-amin (DFPA) molekülünün teorik olarak optimal moleküler yapısı, titreşim frekansları ve ilgili titreşim hareketleri araştırıldı. Kuantum kimyasal hesaplamaları, DFT (B3PW91 ve B3LYP) yöntemlerinin 6-311G(d,p) temel seti kullanılarak yapılmıştır. Molekül içindeki yük transferini için HOMO ve LUMO analizi yapıldı. Hem hiperkonjugatif etkileşim hem de yük delokalizasyonunun bir sonucu olarak molekülün stabilitesini incelemek için NBO analizi kullanıldı. MEP'i gerçekleştirmek için DFT yaklaşımı kullanıldı ve beklenen kızılötesi duyarlılıkları ve Raman aktivitesi de sunuldu. Hesaplanan her iki DFT yönteminin geometrik parametreleri uyumludur. Bağlanma afinite değerleri ve moleküler eşleşme çalışmaları, başlıktaki bileşiğin MtPanK ve PanK ile stabil bir kompleks oluşturduğunu göstermektedir. Molekülün MtPanK ve PanK'ya karşı inhibitör aktiviteye sahip olması, yeni anti-tüberküloz ilaçlarının geliştirilmesine yol açması mümkündür.

Anahtar Kelimeler: DFPA, DFT, MEP, NBO, moleküler yerleştirme.

DOI: http://dx.doi.org/10.32571/ijct.1135173 **E-ISSN: 2602-277X**

1.INTRODUCTION

For thousands of years, humanity has been affected by tuberculosis (TB), an extremely contagious disease brought on by Mycobacterium tuberculosis.[1] Tuberculosis has become an epidemic disease that covers the whole world, with 1.4 million fatalities and over 9 million new cases each year.[2] In the next decade, it is estimated that the cost of TB to the least developed countries could be between one and three trillion dollars.[3] Although the global prevalence of TB that is extensively drug-resistant (XDR) and multi-drug-resistant (MDR) has increased dramatically since 1990, the overall number of new cases has decreased by 40%.[4] TB can lay dormant for years after infection, only to resurface when the host's immune system is impaired, such as in HIV co-infected people.[5] Not only has there been significant progress in TB drug discovery recently, but a number of drug candidates have entered various phases of clinical trials.[6] Drug resistor to the existing standard treatment of Mycobacterium tuberculosis (M.tb), known as TB's the causative agent of, is increasing with the discovery of multi-drug resistor TB (MDR-TB) and rifampicin-resistor TB (RR-TB).[7] In 2019, rates of treatment success for drug-sensitive TB were 85%, while for MDR-TB, the rate dropped to 56%.[8] These resistor M.tb stretches require long-term treatment regimens (inclusive injectability) that are more expensive and challenging to obtain. Discovery of new tuberculosis drugs is critical to treat M.tb strains with these resistances.[9] Recently, significant development has been made in new drugs' the development for the treatment of tuberculosis, and many of these agents have been in clinical tests combination therapy's as part.

Density Functional Theory (DFT) is used in theoretical materials research not only to explain material properties, but also to predict entirely new materials with unique properties for a variety of uses.[10] It is done through the use of computational techniques such as Gaussian through DFT calculations.[11] Gaussian is a computer-based application that uses the fundamental principles of quantum mechanics to study the electronic structure of molecules, spectroscopic data, and energies.[12] Quantum calculations including geometry optimization were performed using Gaussian-09 software; Because the software uses a quantum technique, the results are more precise and accurate.[13] Various physicochemical properties can also be calculated using DFT analysis, and also DFT is a low-cost, high-precision computational method for analyzing the electronic structures of molecules used in various scientific fields.[14]

In this study, the B3PW91 and B3LYP methods and the 6-311G(d,p) basis set were used for the theoretical calculation of the DFPA molecule. The charge distribution and quality of the optimized structures of the compounds were determined using NBO analysis. It was possible to visualize and simulate the MEP surface. The polarizability, dipole moment, first-order hyperpolarizability, and thermodynamic characteristics are derived to the title compound. DFT calculations with a base set were also performed to calculate the energy of the Highest Occupied Molecular Orbit (HOMO) and the Least Occupied Molecular Orbit (LUMO). The results of molecular docking studies were conducted to see how the molecules interact with the target binding site of the ligand molecule. Discovered what the minimum binding energy is. Millions of people currently suffer from Mycobacterium tuberculosis, the bacterial cause of tuberculosis. The rise of drug-resistant bacteria has made the search for new antibiotics to fight bacteria a worldwide health priority. The goal of this research was targeted to find new TB drugs by targeting pantothenate kinase, a key enzyme in the universal production of coenzyme CoA.

2. MATERIALS AND METHODS

For DFT calculation, DFT(B3PW91 and B3LYP)/6-311G(d,p) methods were performed bu using Gaussian09 software.[15,16] A quasi-experimental technique is adopted for conformational analysis. The geometry of the resulting molecule was optimized as the computational analysis's the first step. In particular, it requires low energy sensitivity to changes in molecular structure caused by displacement of the core position of DFPA. The DFT method in the Gaussian 09 program was used to calculate the optimum geometries, vibrational frequencies and energies of the molecular structure of DFPA.

The Lee's-Yang-Parr correlation function was created based on the DFT/(B3PW91 and B3LYP) methods and the 6-311G(d,p) base set based program package. Visualization and input file were taken using ChemBio Ultra Drive 3D and GaussView 6.0.16. The binding affinity of the molecule (Maestro Molecular Modeling platform of the Schrödinger, LLC model (version 11.8)) was used to calculate the binding affinity of the molecule. The crystal structure of M. tuberculosis pantothenate kinase (MtPanK) protein (PDB ID: 3AF3) with a resolution factor of 2.35 and the crystal structure of Pantothenate kinase (PanK) protein (PDB ID: 4BFT) with a resolution factor of 2.29 Å were resolved using X-ray diffraction method. Retrieved from the PDB extension file and the RCSB Protein Data Bank (see https://www.rcsb.org/pdb). SDF files from PubChem website for ligand were used separately. It was synthesized with the previous implementation of the Ligprep module. Suspended to prepare protein and retrieve data in the wizard module. Meanwhile, water molecules were separated in a crystal structure. This module of protein ion balance was reconsidered and this time adjusted by selecting active sites due to the flexible binding of the protein. In order to enable flexible insertion by building networks at the protein-binding sites, the receptor meshing module was constructed around mesh boxes. A ligand-protein was inserted using the slip insertion module. Optimal coupling energies were calculated with reference to protein and ligand interactions, alkyl and π interactions, π-π interactions and hydrogen bonds. They provide the highest level of access with the lowest energy configurations. Discovery Studio 4.5 was used to show 2D and 3D interactions as well as the resulting receiver models.

3. RESULTS AND DISCUSSION

3.1. Structure Details and Analysis

Geometric optimization calculations used the B3PW91 vs B3LYP approach with 6-311G(d,p) basis sets for investigate the DFPA molecule effect of the DFT technique on geometric parameters.[17, 18] The most stable optimum geometry parameters determined by DFT of DFPA are shown in Table 1. The largest deviations are between C26–F34 and C1–F7 structures, with bond lengths of 0.00709Å and 0.00655 Å, respectively. Similarly, it was determined that the bond angle between H51–C33–H52 in trihedral structures had the greatest deviation with 0.102987°. It was determined that the bond angle between C25-O28-C29-C30 in tetrahedral structures had the greatest deviation with 1.22219◦. The smallest difference in C5–H37 bond length is -0.00101 Å. The lowest variation in the C15–C14–C17 bond angle is -0.00392◦. The lowest variation in the N12–N11–C16-C15 bond angle is -0.04192.

Table 1. Theoretically obtained some bond lengths (Å) and bond angles (°) of the molecule.

Bond Lengths	**B3PW91/ 6-311G(d,p)**	**B3LYP/ 6-311G(d,p)**	**Bond Lengths**	**B3PW91/ 6311G(d,p)**	**B3LYP/ 6-311G(d,p)**
C1-C6	1.38503	1.38648	**C27-H42**	1.08333	1.08217
C3-C4	1.39994	1.40259	**C29-H43**	1.09176	1.09045
C9-C10	1.38847	1.38982	**C33-H51**	1.09025	1.09146
C4-C8	1.46644	1.47034	**C1-F7**	1.34369	1.35024
C14-C17	1.51736	1.52013	**C26-F34**	1.34565	1.35274
C15-C16	1.38615	1.38845	**C17-F19**	1.34130	1.34643
C25-C26	1.40536	1.40695	**C33-N31**	1.45238	1.45893
C29-C30	1.52002	1.52451	**N11-N12**	1.33926	1.34750
C5-H37	1.08415	1.08314	**C23-N24**	1.32602	1.32923
C9-H39	1.07668	1.07577	**C25-O28**	1.34115	1.34595
Bond Angles	**B3PW91/ 6-311G(d,p)**	**B3LYP/ 6-311G(d,p)**	**Bond Angles**	**B3PW91/ 6-311G(d,p)**	**B3LYP/ 6-311G(d,p)**
C1-C6-C5	118.72921	118.70525	**C5-C6-H38**	121.62112	121.64106
C3-C4-C8	120.50005	120.55906	**H51-C33-H52**	107.98561	108.01548
C15-C14-C17	119.38130	119.37738	**C25-O28-C29**	121.01355	121.35501
C16-N21-C22	127.54936	127.72487	**C30-N31-C33**	112.53976	112.62533
C23-N24-C25	120.28953	120.24030	**C14-C17-F18**	111.46092	111.53785
Bond Angles	**B3PW91/ 6-311G**	**B3LYP/ 6-311G(d,p)**	**Bond Angles**	**B3PW91/ 6-311G(d,p)**	**B3LYP/ 6-311G(d,p)**
C3-C4-C8-C9	164.77960	165.07147	**C23-N24-C25-O28**	-179.97602	-179.85731
C16-C15-C14-C17	-178.62637	-178.61233	**C3-C2-C1-F7**	179.96671	179.97025
C25-O28-C29-C30	160.25046	161.47265	**N12-N11-C16-C15**	-178.78116	-178.82308
N13-C14-C17-F18	173.72071	173.73681	**C30-N31-C32-H47**	-175.79271	-175.67547

3.2. Non-Linear Optical Properties (NLO)

Nonlinear optical (NLO) molecules with asymmetric polarization in molecules conjugated to pi-electrons by electron acceptor and electron donor groups can be helpful in computations, telecommunications, and optical signal processing.[19,20] The polarization (α), hyperpolarization (β) and electric dipole moment (μ) of the NLO behavior of DFPA were determined and investigated using the B3PW91/6-311G(d,p) and B3LYP/6-311G(d, p) basis sets.[21,22] In Table 2, values calculated have presented. The criterions for a molecule to function as an efficient NLO is that the first hyperpolarizability (β) is of a large value. A 3x3x3 matrix can be used to describe the first hyperpolarizability, which is a third order tensor. Due to Kleinman symmetry[23] the 3D matrix's 27 components can be broken down into just 10 elements. Equation (1)-(3) gives the mean values of the total first static hyperpolarizability (β), static dipole moment (μ), and polarizability (Δα) of the x, y, and z components. The calculated βtot values of DFPA computed using the DFT/B3PW91/6-311G(d,p) and DFT/B3LYP/6-311G(d,p) method are 3.51x10^{-30} esu and 3.57x10^{-30} esu, in turn. The calculated dipole moment of the DFPA molecule was computed as 3.6962 and 3.6689 Debye, respectively.

$$\mu = \left(\mu_x^2 + \mu_y^2 + \mu_z^2\right)^{1/2} \tag{1}$$

$$\beta_{Total} = (\beta^2 x + \beta^2 y + \beta^2 z)^{1/2} \tag{2}$$

$$= [(\beta xxx + \beta xyy + \beta xzz)^2 + (\beta yyy + \beta yxx + yzz)^2 + (\beta zzz + \beta zxx + \beta zyy)^2]^{\frac{1}{2}} \tag{3}$$

Table 2. The value of the DFPA molecule belongs to the dipole moments (Debye), polarizability (au), β components and β total value calculated with the 6-311G(d,p) basis set by the DFT/B3PW91-B3LYP method.

Parameters	**B3PW91/ 6-311G(d,p)**	**B3LYP/ 6-311G(d,p)**	**Parameters**	**B3PW91/ 6-311G(d,p)**	**B3LYP/ 6-311G(d,p)**
μ_x	-2.8386	-2.8082	β_{XXX}	-276.5719	-281.3087
μ_y	-2.3210	-2.3143	β_{YYY}	-18.6724	-17.6063
μ_z	0.4657	0.4684	β_{ZZZ}	6.7777	6.6844
$\mu_{(D)}$	3.6962	3.6689	β_{XYY}	-33.5448	-36.2407
α_{XX}	-172.8153	-175.8009	β_{XXY}	81.9227	87.5145
α_{YY}	-216.3029	-218.7078	β_{XXZ}	-17.4260	-16.4248
α_{ZZ}	-194.3745	-195.5322	β_{XZZ}	-31.4392	-28.4143
α_{XY}	2.0899	2.4043	β_{YZZ}	19.9700	20.5157
α_{XZ}	-3.5615	-3.5036	β_{YYZ}	15.3104	15.3594
α_{YZ}	-2.4141	-2.4376	β_{XYZ}	2.6743	3.4133
α (au)	-194.4975	-196.6803	**β (esu)**	3.51x10^{-30}	3.57x10^{-30}

3.3. Mulliken Atomic Charges

Atomic charge has been used to characterize charge transfer and electronegativity equalization in processes as well as to predict the electrostatic potential outside of molecule surfaces.[24, 25] The Mulliken atomic charges computed at B3PW91/6-311G(d,p) and B3LYP/6-311G(d,p) levels for various atoms of DFPA are shown in Table 3. The aromatic ring's negative values of at atoms C2, C4, C5, C14, N11 and N24 cause electron density redistribution. C5 and C27 become more acidic as a result of their strong negative charges, allowing them to harbor higher positive charges. Mulliken, bond angles, atomic masses and structure optimization views of DFPA molecule at B3PW91/6-311G(d,p) and B3LYP/6-311G(d,p) levels are as in Figure 1a.

Table 3. DFT/ B3PW91 and B3LYP techniques with 6-311G(d,p) base sets computed Mulliken atomic charges.

	B3PW91/ 6-311G(d,p)	**B3LYP/ 6-311G(d,p)**		**B3PW91/ 6-311G(d,p)**	**B3LYP/ 6-311G(d,p)**
C1	0.262	0.251	**O28**	-0.327	-0.326
C2	-0.144	-0.126	**N11**	-0.420	-0.374
C4	-0.154	-0.132	**N12**	-0.349	-0.18
C5	-0.046	-0.042	**N24**	-0.331	-0.289
C8	0.303	0.259	**N31**	-0.371	-0.357
C9	-0.317	-0.273	**F7**	-0.227	-0.230
C10	0.504	0.437	**F18**	-0.220	-0.221
C14	-0.125	-0.119	**F34**	-0.218	-0.222
C16	0.635	0.583	**H35**	0.124	0.112
C22	0.006	0.022	**H39**	0.120	0.110
C25	0.357	0.326	**H40**	0.155	0.136
C27	-0.005	-0.003	**H42**	0.157	0.141
C29	-0.021	0.010	**H46**	0.125	0.111
C30	-0.155	-0.115	**H47**	0.098	0.083
C32	-0.216	-0.179	**H49**	0.119	0.105
C33	-0.212	-0.176	**H51**	0.274	0.261

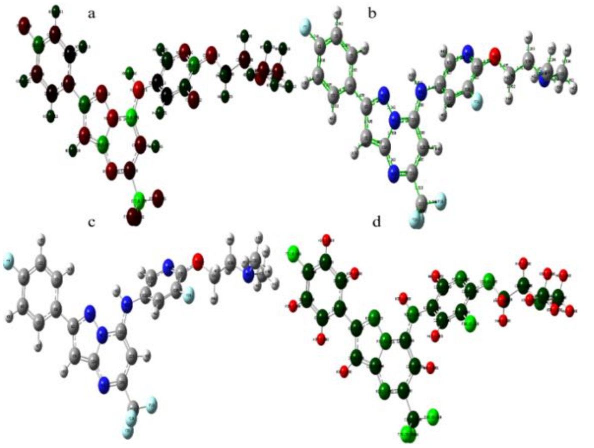

Figure 1. DFPA molecule with DFT/B3LYP/6-311G(d,p) basis set a) mulliken b) bond lengths c) atomic mass d) structure optimization

3.4. HOMO and LUMO Analysis

The terms "Highest Filled Molecular Orbital (HOMO)" and "Lowest Unoccupied Molecular Orbital" are used to express the most fundamental characteristics of quantum chemistry (LUMO).[26] The eigenvalues and energy gaps of the HOMO and LUMO molecules express the molecule's biological activity.[27] A molecule with narrow boundary orbital spacing can be more polarized and has higher chemical reactivity and lower kinetic stability.[28] It is possible to think of the HOMO as the outer orbital holding the electrons, and the ionization potential as being proportional to HOMO energy.[25] Like electron donors, HOMO frequently donates these electrons, so the ionization potential is proportional to the HOMO's the energy.[29] Besides, LUMO can take electrons in and has energy proportional to its affinity for electrons. For the HOMO and LUMO energies, two important molecular orbitals were investigated as shown in Figure 2 and Figure 3.

In Table 4 have calculated quantum chemical parameters (in eV) for low energy compatibilities by DFT/B3PW91/6-311G(d,p)-DFT/B3LYP/6-311G(d,p) methods of the DFPA molecule. Utilizing DFT-based descriptors, chemical potential, spherical stiffness and electrophilicity will guide to understanding the molecule's the structure and reactivity. The electron affinity and ionization energy could be computed by using the orbital energies of LUMO and HOMO as follows: $A=-E_{LUMO}$, $I=-E_{HOMO}$, ($\mu = -(I+A)/2$) and $\eta = (I-A)/2$.[30] This index evaluates the system's energy stability when it receives an additional electronic charge from the environment by calculating the global electrophilic power of a ligand as being equal to = 2/2. A system is said to be electrophilic if it resists exchanging electrons with its surroundings and has the ability to store more electrons than a system that is not.[31] Because it includes information on both stability (hardness) and electron transit (chemical potential), it is a better indicator of overall chemical reactivity. The chemical potential μ and hardness η are determined by the following equations: $\eta = (I-A)/2$ and $\mu = -(I+A)/2$, where, chemical species are the ionization potential (I) and electron affinity(A). Since the chemical potential the title compound's is stable and negative due to this negativity, the elements from which they are formed do not spontaneously decompose.[32] The resistance of an electron cloud in a chemical system to deformation due to slight disturbances during chemical processing is referred to as its stiffness. The concept of hardness is used in physics and chemistry, but it cannot be observed experimentally. Hard systems are less polarized and generally small, although soft systems can be highly and highly polarized.[33]

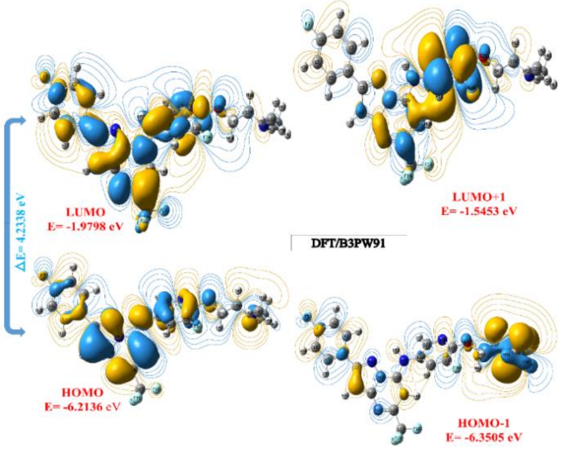

Figure 2. Boundary molecular orbitals of the DFPA compound according to the DFT/B3PW91/6-311G(d,p) level.

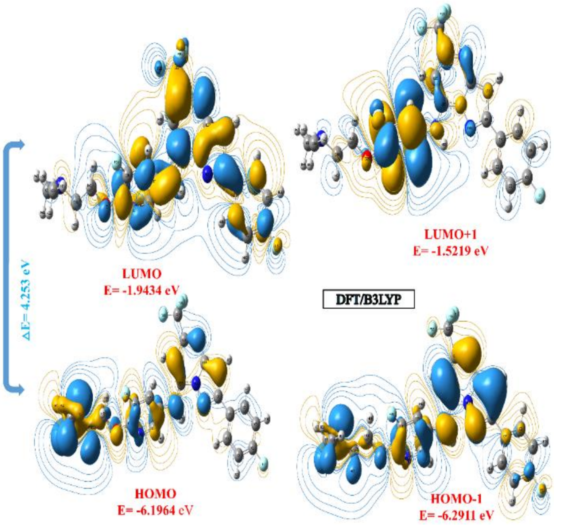

Figure 3. Boundary molecular orbitals of the DFPA compound according to the DFT/B3LYP/6-311G(d,p) level.

DOI: http://dx.doi.org/10.32571/ijct.1135173 **E-ISSN: 2602-277X**

Table 4. Calculated quantum chemical parameters⁎(in eV) for low energy compatibilities by DFT/B3PW91/6-311G(d,p)-DFT/B3LYP/6-311G(d,p) methods of the DFPA molecule.

Molecules Energy		**DFT/ B3PW91 /6-311G(d,p)**	**DFT/B3LYP/ 6-311G(d,p)**
ELUMO		-1.9798	-1.9434
EHOMO		-6.2136	-6.1964
ELUMO+1		-1.5453	-1.5219
EHOMO-1		-6.3505	-6.2921
Energy Gap	(Δ)|EHOMO- ELUMO|	4.2338	4.2530
Ionization Potential	(I = −EHOMO)	6.2136	6.1964
Electron Affinity	$(A = -E_{LUMO})$	1.9798	1.9434
Chemical hardness	$(\eta = (I - A)/2)$	2.1169	2.1260
Chemical softness	$(s = 1/2\ \eta)$	1.0584	1.063
Chemical Potential	$(\mu = -(I + A)/2)$	-4.0967	-4.0699
Electronegativity	$(\chi = (1 + A)/2)$	1.4899	1.4717
Electrophilicity index	$(\omega = \mu^2/2\ \eta)$	3.9640	3.8956

3.5. Molecular Electrostatic Potential (MEP)

MEP is a valuable descriptor describing nucleophilic and electrophilic processes, as well as hydrogen bond interactions, and it is connected to electron density (ED).[34] In research procedures requiring the recognition of one molecule by another, such as interactions between drugs and receptors and enzymes and substrates, the electrostatic potential V(r) is ideally suited.[35] Because these two species first see each other through their potential. The nucleophilic and electrophilic regions of the studied molecule were predicted using MEP in optimized geometry by the B3PW91/6-311G,p) and B3LYP/6-311G(d,p) basis sets. Electrophilic reactivity is represented by MEP's negative (red or yellow) portions while nucleophilic reactivity is represented by positive (blue) regions as shown in Figure 4.

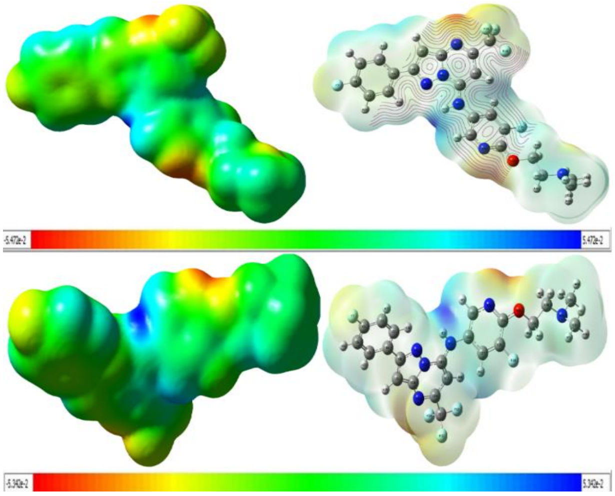

Figure 4. Molecular electrostatic potential surface by DFT/ B3PW91 and DFT/B3LYP methods with 6-311G(d,p) and 6-311G(d,p) basis set.

3.6. NBO Analizi

Conjugative interaction in a molecular system becomes clear with NBO analysis.[36] The stabilization of molecular systems is based on orbital interactions between occupied (donor) and vacant (acceptor) bonding orbitals. For DFPA, a quadratic. The receiver(j) and donor(i) relationship was predicted using Fock marix. This orbital intelligence is capable of both forming and weakening bonds.[37] The stabilizing value associated with delocalization for every donor (i) and recipient (j) is expected to be as follows.

$$E(2) = \Delta Eij = qi\frac{(Fi,j)^{2}}{(\varepsilon i - \varepsilon j)} \qquad (4)$$

Fock matrix NBO element is F(i,j), diagonal elements are Ɛi and Ɛj, and donor orbital occupancy is qi. The higher the stabilization energy, the more likely it is that electrons will be donated to the acceptor orbitals. NBO study of DFPA revealed molecular hybridization, charge density delocalization and conjugative interaction. Table 5 shows the electron density, E(2), E(j)–E(i) and f(i,j) values, as well as NBO calculations for a few selected donors and acceptors. The interaction between the stabilization energy E(2), filled and vacant NBO type Lewis orbitals, and electron delocalization from the bonding (BD) to the

DOI: http://dx.doi.org/10.32571/ijct.1135173 **E-ISSN: 2602-277X**

antibonding (BD*) orbitals is described using NBO analysis. The more intense the connection between recipients and donors, the higher the E(2) value. Bond (σ/π) and anti-bond (σ*/π*) interactions also contributed significantly to the stability of the structure, with π(C9-C10) /π*(C8-N12) interaction having the highest E(2), followed by π(C15-C16) /π*(N13-C14) with 30.17 kcal/mol. Afterwards, it was determined that the σ (C8-C9)/σ* (C10-N13) interaction had the highest E(2) value with 7.54 kcal/mol.

Table 5. Selected NBO results for DFPA utilizing the B3PW91/6-311G(d, p) theory level to show the generation of Lewis and non-Lewis orbitals

NBO(i)	Type	ED/e	NBO(j)	Type	ED//e	E(2)^a (Kcal/mol)	E (j)-E(i)^b (a.u.)	F (i, j)^c (a.u)
C2-C1	σ	1.98135	**C6-C1**	σ*	0.02824	4.28	1.28	0.066
C6-C1	σ	1.98127	**C2-C1**	σ*	0.02844	4.27	1.28	0.066
C6-C1	π	1.64891	**C3-C2**	π*	0.31928	18.13	0.30	0.066
C1-C6	π	1.64891	**C5-C4**	π*	0.37881	21.44	0.30	0.072
C3-C2	π	1.68221	**C6-C1**	π*	0.37287	23.50	0.28	0.073
C3-C32	π	1.68221	**C5-C4**	π*	0.37881	18.28	0.29	0.066
C2-H35	σ	1.97610	**C4-C3**	σ*	0.02406	4.02	1.08	0.059
C3-C4	σ	1.97137	**C5-C4**	σ*	0.02343	4.30	1.25	0.066
C3-H36	σ	1.97796	**C5-C4**	σ*	0.02343	4.54	1.08	0.062
C5-C4	α	1.97205	**C4-C3**	σ*	0.02406	4.31	1.25	0.066
C5-C4	π	1.64037	**C6-C1**	π*	0.37287	19.76	0.27	0.066
C5-C4	π	1.64037	**C3-C2**	π*	0.31928	21.45	0.28	0.070
C5-C4	π	1.64037	**C8-N12**	π*	0.48673	21.19	0.25	0.067
C6-C5	σ	1.97294	**C1-F7**	σ*	0.03252	4.00	0.97	0.056
C5-H37	σ	1.97864	**C4-C3**	σ*	0.02406	4.41	1.08	0.062
C6-H38	σ	1.97606	**C5-C4**	σ*	0.02343	4.02	1.09	0.059
C9-C8	α	1.97187	**C10-N13**	σ*	0.02329	7.54	1.19	0.085
C8-N12	α	1.98034	**N11-C16**	σ*	0.03782	5.67	1.25	0.075
C8-N12	π	1.83693	**C5-C4**	π*	0.37881	7.70	0.34	0.049
C8-N12	π	1.83693	**C10-C9**	π*	0.41273	10.14	0.33	0.055
C10-C9	π	1.70562	**C8-N12**	π*	0.48673	36.85	0.26	0.091
C10-C9	π	1.70562	**N13-C14**	π*	0.39238	15.41	0.26	0.058
C16-C15	π	1.68460	**N13-C14**	π*	0.39238	30.17	0.29	0.085
C23-C22	π	1.65654	**N24-C25**	π*	0.43824	16.77	0.27	0.062
C23-C22	π	1.65654	**C27-C26**	π*	0.35645	23.02	0.28	0.072
N24-C25	π	1.70897	**C23-C22**	π*	0.36961	26.36	0.32	0.084
C27-C26	π	1.70782	**C23-C22**	π*	0.36961	16.50	0.30	0.064
C27-C26	π	1.70782	**N24-C25**	π*	0.43824	23.57	0.29	0.076

The energy of a hyper conjugative interaction is denoted by a E (2). (stabilization energy).

b The energy disparity between the acceptor and donor NBO orbitals.

The Fock matrix element between the I and j NBO orbitals is called c F(i, j).

3.7. Molecular Docking Studies

Molecular docking is for seeing and interpreting interactions between a ligand and a protein sensor.[38,39] This method of drug design is highly reliable, fast and cost-effective. Docking score of DFPA-MtPanK and DFPA-PanK are shown Table 6. The Schrödinger program was used to carry out molecular insertion studies of molecules synthesized by Pantothenate kinase (MtPanK) from Mycobacterium tuberculosis in complex with 5'-Guanylyl methylene diphosphonate (GMPPCP) and Pantothenate protein. It was discovered in the Protein Data Bank as the crystal structure (PDB ID:3AF3) of pantothenate kinase (MtPanK). Both proteins and ligands were subjected to editing and optimization. Automatic nesting tecnical were used to create the grid and place the parameter files. A grid was created to arrange the xyz coordinates around binding site's of the enzyme. Discovery Studio Visualizer was used to see and understand the embedding outcomes. The insertion score and H-bond interactions were calculated for the compound included in this study. Here, the binding mechanism is fluoro-bonded TYR-235 (6.43 Å), GOL-321 (3.78). ALA-100 (4.27 Å) and LYS-103 (4.93 Å) are hydrogen bonded to conventional hydrogen bonds. LYS-103 (5.49 Å) bonded to hydroxyl, hydrogen bonded to conventional hydrogen bond. VAL-99 (4.90 Å) Pi-Alkyl is attached to the phenyl center, MET-242 (6.50 Å) Pi-Alkyl is attached to the pyrazolone center and PHE-254 (5.63 Å) is Pi-Alkyl is attached to the carbon. ASP-129 (3.88 Å) Pi-Cation, bound to nitrogen. HIS-179 (4.30 Å) is attached to the pyrazolone center. HIS-179 (4.91 Å)

DOI: http://dx.doi.org/10.32571/ijct.1135173 E-ISSN: 2602-277X

and ARG-238 (6.34 Å) Salt Bridge are connected to the center of the phenyl center. VAL-99 (4.09 Å) bound to flora, ASP-129 (5.10 Å), TYR-153 (5.69 Å), ASP-129 (3.83 Å) and TYR-153 (5.80 Å) bound to nitrile group Van der Waals is an example as shown in Figure 5.

Table 6. Docking score of DFPA-MtPanK and DFPA-PanK.

Compound	**Docking Score**	
	MtPanK (PDB: 3AF3)	**PanK** (PDB: 4BFT)
DFPA	-6.977	-7.096

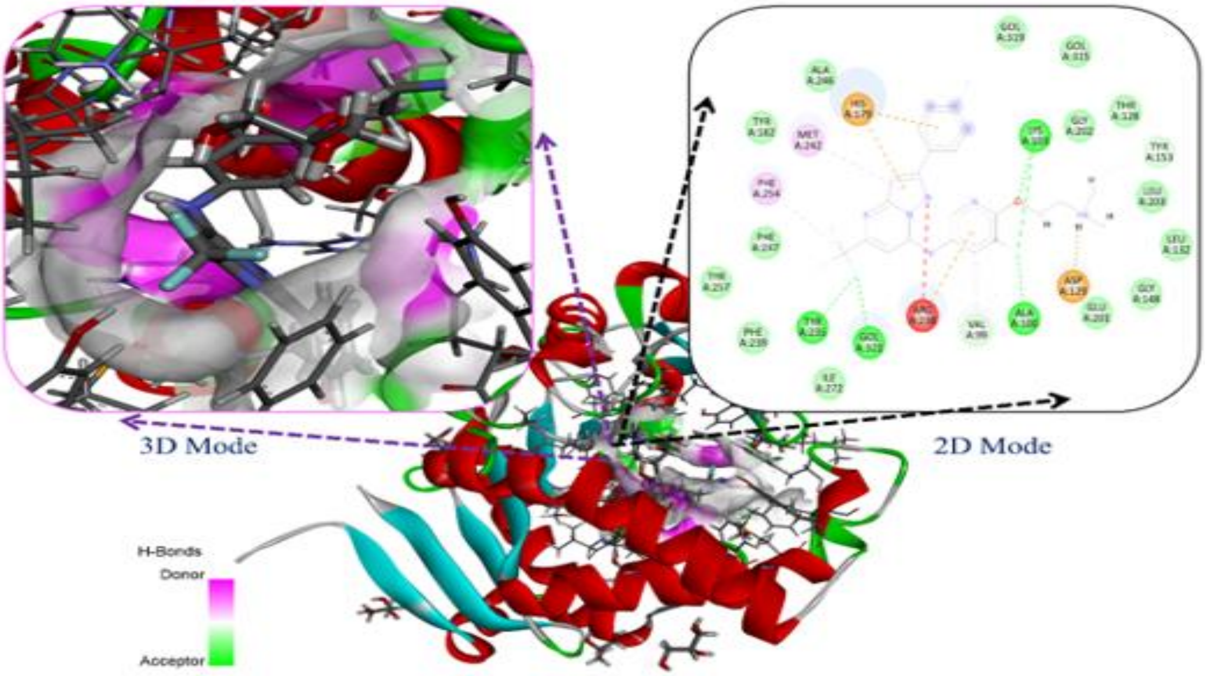

Figure 5. 3D representation of the receptor's aromatic surface and a 2D image of the DFPA-MtPanK enzyme contacts.

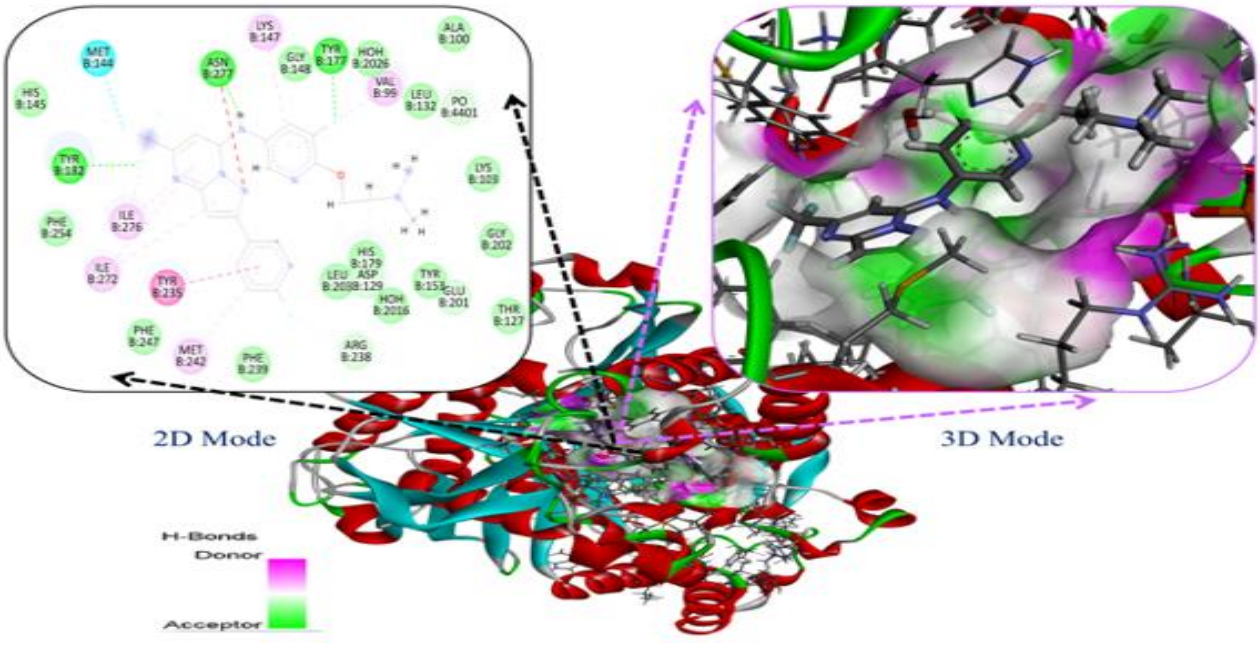

Figure 6. 3D representation of the receptor's aromatic surface and a 2D image of the DFPA-PanK enzyme contacts.

DOI: http://dx.doi.org/10.32571/ijct.1135173 E-ISSN: 2602-277X

It was used to conduct molecular docking studies of molecules synthesized by Pantothenate kinase(PanK) from the Crystal structure of Mycobacterium tuberculosis in complex by a triazole inhibitor compound and phosphate protein. Here, the bonding mechanism is TYR-235 (5.82 Å), ASN-277 (5.20 Å) hydrogen bond attached to the conventional hydrogen bond attached to the pyrazolone and LYS-147 (5.05 Å) hydrogen bond attached to the conventional hydrogen bond attached to the nitrile. The TYR-235 (5.57 Å) benzene ring is attached to the center stacked Pi-Pi. META-242 (5.54 Å) Pi-Sulfur bond attached to the center of the benzene ring and PHE-239 (5.56 Å) Pi-Sulfur bond attached to Sulfur. Pi-alkyl bond ARG-238 (6.16 Å) attached to the benzene ring's the center o and ILE-272 (6.04 Å) attached to the pyrazolone ring. ILE-276 (4.44 Å), TYR-182 (5.37 Å), PHE-254 (5.75 Å), and PHE-254 (6.09 Å) are examples of added Alkyl bond as shown in Figure 6.

4. CONCLUSION

The geometry of the optimized molecule was revealed and its molecular parameters, bond length and bond angle were determined. Due to its high hyperpolarizability, the DFPA molecule has strong NLO activity. HOMO-LUMO analysis of the DFPA molecule revealed the compound's the stability and chemical reactivity. In the MEP study, the calculated energy gap and the reactive regions of the investigated molecule demonstrated the compound's the chemical stability. The stabilization energy by the NBO technique has been used to explain both intramolecular and intermolecular processes. Molecular docking was performed with MtPanK (shift score; -6.977) and PanK (shift score; -7.096) protein receptors, and the best and lowest binding energy obtained was -7.096 Kcal/mol with PanK protein. According to the molecular insertion data, the chemical may have inhibitory activity against MtPanK and PanK, which may lead to the development new anti-tuberculosis drugs's.

Conflict of interests

I declares that there is no a conflict of interest with any person, institute, company, etc.

REFERENCES

1. H.-J. Eun et al., *Biochemical and Biophysical Research Communications,* **2022,** *616*, 19-25.

2. H. Fei et al., *The Lancet Regional Health - Western Pacific,* **2020,** *3*, 100032.

3. M. J. Brennan et al., *Tuberculosis,* **2012,** *92*, S6-S13.

4. A. K. Alame Emane et al *Tuberculosis,* **2021,** *129*, 102092.

5. S. Ashenafi et al., *The American Journal of Pathology,* **2022,** *192* (4), 653-670.

6. S. S . Swain et al., *European Journal of Medicinal Chemistry,* **2022,** *232*, 114173.

7. S. Koirala et al., *Pulmonology,* **2021,** *27* (5), 403-412.

8. Global tuberculosis report 2020. *World Health Organization,* **2020**.

9. P. J . Choi et al., *Tetrahedron Letters,* **2022,** *90*, 153611.

10. M.J. Frisch et al., *Revision, E E.01.*

11. J. I.. Ahamed et al., *Journal of Molecular Structure,* **2022**, 133548.

12. M. Mirnezhad et al., *Journal of Molecular Graphics and Modelling,* **2021,** *104*, 107843.

13. J. Geethapriya et al., *Journal of the Indian Chemical Society,* **2022,** *99* (4), 100418.

14. A. Abdou et al., *Inorganica Chimica Acta,* **2022,** *539*, 121043.

15. M . Sucheta et al., *Materials Today: Proceedings,* **2022**.

16. R. K. Mohapatra et al., *Journal of King Saud University - Science,* **2021,** *33* (2), 101315.

17. N. Kanagathara et al., *Computational and Theoretical Chemistry,* **2021,** *1202*, 113301.

18. S. Budania et al., *Journal of the Indian Chemical Society,* **2022,** *99* (5), 100419.

19. C. Raveendiran et al., *Materials Today: Proceedings,* **2022**.

20. S. Muhammad et al., *Journal of Molecular Graphics and Modelling,* **2022,** *114*, 108209.

21. V. Krishna Kumar et al., *Spectrochimica Acta Part A: Molecular and Biomolecular Spectroscopy,* **2014,** *118*, 663-671.

22. A. S. Karne et al., *Chemical Physics Letters,* **2015,** *635*, 168-173.

23. D. A. Kleinman et al., *Phys. Rev.* **1977-1979.**, 126 (1962).

DOI: http://dx.doi.org/10.32571/ijct.1135173 **E-ISSN: 2602-277X**

24. R. Satheeshkumar et al., *Journal of Molecular Structure*, **2022**, 133552.

25. M. K. Priya et al., *Materials Today: Proceedings*, **2019,** *8*, 37-46.

26. S. Demir aet al., *Journal of Molecular Structure*, **2016,** *1108*, 637-648.

27. K. Sarojini et al., *Molecular and Biomolecular Spectroscopy*, **2012,** *96*, 657-667.

28. E. O. Akintemi et al., *Computational and Theoretical Chemistry*, **2022,** *1210*, 113658.

29. A. T. Tekeş, et al., *Journal of the Institute of Science Tehnology*, **2021,** *11* (4), 2955-2966.

30. N. Jeeva Jasmine et al., *Spectrochimica Acta Part A: Molecular and Biomolecular Spectroscopy*, **2015,** *144*, 215-225.

31. V. Balachandran et al., *Spectrochimica Acta Part A: Molecular and Biomolecular Spectroscopy*, **2013,** *106*, 284-298.

32. R. T. Ulahannan et al., *Spectrochimica Acta Part A: Molecular and Biomolecular Spectroscopy*, **2015,** *151*, 184-197.

33. A. D. Isravel et al., *Computational and Theoretical Chemistry*, **2021,** *1202*, 113296.

34. M. Buvaneswari et al., *Journal of Molecular Structure*, **2021,** *1243*, 130856.

35. R. R. Saravanan et al., *Spectrochimica Acta Part A: Molecular and Biomolecular Spectroscopy*, **2015,** *139*, 321-328.

36. M. A. S . Sakr et al., *Journal of Molecular Structure*, **2022,** *1258*, 132699.

37. A. A. Aboalhassan et al., *Journal of Photochemistry and Photobiology A: Chemistry*, **2022,** *431*, 114039.

38. E. D. Kaya et al., *Journal of Biomolecular Structure and Dynamics*, **2021**, 1-14.

39. R. T. Ulahannan et al., *Spectrochimica Acta Part A: Molecular and Biomolecular Spectroscopy*, **2015,** *150*, 190-199.

DOI: http://dx.doi.org/10.32571/ijct.1201634 **E-ISSN: 2602-277X**

International Journal of Chemistry and Technology

http://dergipark.org.tr/ijct

Research Article

Detection of chlorophyll a on the Black Sea Coast with Sentinel-2 Satellite

Nehir UYAR[1*], Aycan Murat MARANGOZ[2], Sefa KOCABAŞ[3], Sabri MUTLU[4], Hakan ATABAY[4]

[1] *Zonguldak Vocational School, Zonguldak Bulent Ecevit University, Zonguldak, Turkey*
[2] *Geomatics Engineering Department, Zonguldak Bulent Ecevit University, Zonguldak, Turkey*
[3] *Environmental Engineering Department, Zonguldak Bulent Ecevit University, Zonguldak, Turkey*
[4] *Vice Precidency of Climate Change and Sustainability, TUBITAK MRC, Kocaeli, Turkey,*

Received: 9 November 2022; Revised: 25 December 2022; Accepted: 30 December 2022

*Corresponding author e-mail: nehiruyar@beun.edu.tr

Citation: Uyar, N.; Marangoz, A.M.; Kocabaş, S.; Mutlu, S.; Atabay, H., I. *Int. J. Chem. Technol.* **2023**, 7 (1), 48-56.

ABSTRACT

It is costly and time-consuming to determine coastal pollution with ground measurements. One of the most basic parameters to determine pollution in these areas is Chlorophyll A. This study aims to investigate the determination of this parameter using Remote Sensing (RS) techniques. In the study, the Sentinel-2 satellite was used to determine the parameter Chlorophyll A in the coastal areas of the Black Sea. 19 algorithms were used in the application. The algorithms are related to luminance reflections and the 8 bands of the satellite were used for the study. An Artificial Neural Network model was published as the best result. Pollution was observed in the coastal areas of the Black Sea between 2021 and 2017. As a result of the analysis, it is possible to observe coastal pollution quickly, without cost and/or at very low cost, with RS techniques. In this sense, RS techniques are of great importance in detecting environmental pollution, and relevant algorithms should be developed and supported by local measurements.

Keywords: Chlorophyll A, Remote Sensing, Sentinel 2, Artificial Neural Network Model, pollution

Sentinel-2 Uydusu ile Karadeniz Kıyısında Klorofil A Tespiti

ÖZ

Kıyı kirliliğinin yer ölçümleri ile tespit edilmesi maliyetli ve zaman alıcıdır. Bu alanlardaki kirliliğin belirlenmesinde en temel parametrelerden biri Klorofil A'dır. Bu çalışma, bu parametrenin Uzaktan Algılama (UA) teknikleri ile belirlenmesini araştırmayı amaçlamaktadır. Çalışmada Karadeniz kıyı bölgelerinde Klorofil A parametresini belirlemek için Sentinel-2 uydusu kullanıldı. Uygulamada 19 algoritma kullanılmıştır. Algoritmalar parlaklık yansımaları ile ilgilidir ve çalışmada uydunun 8 band kullanılmıştır. En iyi model Yapay Sinir Ağ Modeli çıkmıştır. 2021-2017 yılları arasında Karadeniz kıyı bölgelerinde kirlilik gözlemlenmiştir. Yapılan analizler sonucunda UA teknikleri ile kıyı kirliliğinin kısa sürede, masrafsız ve/veya çok düşük maliyetle gözlemlenebileceği görülmüştür. Bu anlamda çevre kirliliğinin tespitinde UA teknikleri büyük önem taşımakta olup, ilgili algoritmalar geliştirilmeli ve yerel ölçümlerle desteklenmelidir.

Anahtar Kelimeler: Klorofil A, Uzaktan Algılama, Sentinel 2, Yapay Sinir Ağ Modeli, kirlilik

DOI: http://dx.doi.org/10.32571/ijct.1201634 **E-ISSN: 2602-277X**

1. INTRODUCTION

Water is essential for life. Given global population growth and environmental trends, the Environment Program UN estimates that 1.8 billion people will face water scarcity by 2025. Water means survival for the people and other species we depend on, making proper management of our water resources essential. Good decisions require good data[1]. Remote sensing (RS) makes it possible to collect temporal and spatial information over large areas, in a short period of time, and at specific intervals. Nowadays, more and more environmental pollution is detected with the help of remote sensing.
Some studies on water quality assessment using satellite imagery images are presented below;

In the study conducted by[2], a temporal analysis (Landsat 1975-1987) of Tuz Gölü was conducted in relation to the change of surface water quality. In this application, which is carried out using ISODATA algorithm, one of the remote sensing techniques, the current situation of the lake is studied using Terra Aster (2004) satellite data. The results obtained from the processed and interpreted satellite images show that the water quality of the lake has drastically decreased between 1975 and 2004.

Gholizadeh et al. [3], widely used approaches and sensors to assess and measure water quality parameters studied. The parameters include: Chlorophyll A (Chl-a), colored dissolved organic matter (CDOM), Secchi disc depth (SDD), turbidity, total suspended sediments (TSS), water temperature (WT), sea surface salinity (SSS).

A water quality measurement model based on multivariate probabilistic logic was developed. This model is based on[4] water quality parameters such as water turbidity, chlorophyll-a, vegetation index, and surface temperature described in the scientific literature, and probabilistic functions derived from the distribution of pixel values of these parameters are used. The procedure was applied to the Centla wetlands in southeastern Mexico. A qualitative scale for water quality assessment was proposed.

In the study conducted by [5], emote sensing and GIS applications were used to monitor water quality parameters such as suspended solids, phytoplankton, turbidity, and dissolved organic matter.

Following the early empirical approach developed by [6], he statistical relationship between spectral reflectance value and water quality parameter was evaluated. It can provide information on bands or wavelengths from spectral reflectance and has been shown to be suitable for this water quality parameter.

In the study conducted by[7] a direct method was developed to predict summer total phosphorus and chlorophyll A levels in a wide range of lakes. These two parameters were measured in 16 Iowa lakes, and phosphorus loading was estimated.

The measurement data used in the study were obtained from “Integrated Marine Pollution Monitoring Program” funded by the Turkish Ministry of Environment and Urbanization/General Directorate of EIA, Permit and Inspection/ Department of Laboratory, Measurement and coordinated by TUBITAK- MRC CC&S for the provisioning of the data used in this study[8]. he field measurements were conducted between 2017 and 2021 and the algorithms were applied to the satellite image with the measurement date. 19 algorithms were used for the application.

2. STUDY AREA and MATERIAL

The fact that the northern Anatolian mountains extend parallel to the coast of the Black Sea has prevented the formation of significant inlets and promontories on the southern shores of the Black Sea. This extension of the mountains has resulted in the Black Sea coast of Anatolia having a poor appearance in terms of roads providing access to the bays, gulfs and inner regions. It is an inland sea with an average depth of 1300 m, a width of 600 km, a length of 1200 km and a total area of about 423000 km^2. It extends east-west across the Balkan and Anatolian peninsulas, the Caucasus and the Eastern European platform. The Black Sea, which flows into the Mediterranean Sea through the straits of Istanbul and Çanakkale, represents one of the most important strategic points of Asia Minor. Moreover, the rich underground and surface resources of the areas around the Black Sea have increased interest in this sea since ancient times. All these characteristics have made the Black Sea a sea that determines the location of ports and plays an important role in trade activities[9]. The Google Earth image of the Black Sea Coast of the Study Area is shown in Figure 1.

It is mainly the process of pollution and eutrophication, accompanied by natural fluctuations and climate changes, which are shown by changes in the ecological system and resources of the Black Sea. However, the environmental crisis of the Black Sea is closely related to the unique features of the marine environment [10].

The Sentinel-2 satellite used for the study area is a multi-band satellite developed by the European Space Agency (ESA) under the Copernicus Land Monitoring

Services. The satellite has 13 spectral bands and spatial resolutions of 10 m, 20 m, and 60 m. 11.

Figure 1. Google Earth image of the Study Area (Black Sea Coast).

3. CHLOROPHYLL A

The main problem affecting the health and integrity of coastal marine ecosystems is eutrophication. This is a process that not only leads to pollution or an increase in the supply of organic matter, but also increases the primary production of the ecosystem [12], which is a fundamental change in the energy base of the same by nutrients [13]. The eutrophication process leads to the gradual displacement of seagrasses and slow-growing macroalgae by fast-growing macroalgae and phytoplankton, and eventually to their dominance at high nutrient loads [14]. When eutrophication is high, it includes hypoxia events, foam events, nutrient imbalances, chlorophyll and toxic algae blooms, massive deaths of benthic animals and changes in species patterns and even community structure [15].

Chlorophyll A is found in algae and phytoplankton in surface waters. Chlorophyll A is one of the ecological indicators used to assess the ecological status of the marine environment. This pigment cell is used to extract energy from sunlight to produce oxygen to sustain life. Monitoring chlorophyll content is one way to monitor algae growth. High chlorophyll content means high nutrient content in surface water. Food causes algae to grow. When algae populations flourish, they collapse and die in response to changing ecological conditions. As a result, dissolved oxygen levels drop. High nutrient levels are an indicator of pollution from anthropogenic sources. Therefore, chlorophyll measurement can be considered an indicator of nutrient levels [16].

Chlorophyll A fluorescence from microalgae is a compelling indicator of dissolved water contaminant toxicity because it is easy to measure and responds quickly. While several Chl a fluorescence parameters have been studied, most studies have focused on single species and/or a narrow range of toxins [17].

Remote sensing data and technologies are efficient tools for monitoring extreme hydroclimatic events, water quality, and water quantity [18]. Chlorophyll A, colored dissolved organic matter, suspended solids (TSS), Secchi disc depth, and turbidity, which are water quality parameters, have been determined using remote sensing data [3, 18, 19]. Chlorophyll A concentration monitoring is possible by using reflected and absorbed sunlight information, which provides valuable information about the marine environment [20].

4.METHOD AND APPLICATION

Images from 2017 to 2021 were used for the application. 19 Algorithms were used, and correlation and regression analyzes were applied to Sentinel satellite images of 13 different dates. 19 satellite images were used in the models.

All Sentinel 2A and 2B images used in the study were acquired on the day of fieldwork. The ESA Snap program was used for the atmospheric correction. After atmospheric correction, all images were converted to RGB pixel size by applying the interpolation method.

After atmospheric correction and resampling, all images were geometrically corrected, i.e., the measurement points were positioned correctly. All images were converted to WGS-84 datum and coordinates in the UTM projection system.

The relationships between the measured values of 40 points in the models were examined according to the applied models. The analysis was performed with chlorophyll A readings from 38 points and fluorescence readings from 2 points.

A second measurement, which serves as an independent indicator of biological activity, uses a byproduct of photosynthesis: fluorescence emanating from the light-collecting complex of the photosystem II. Fluorescence is one of several quenching mechanisms for the excited state of chlorophyll A. The quantum yield of fluorescence varies primarily due to non-photochemical quenching effects by sunlight [21, 22] but can also be affected by nutrient stress [23, 24.]

We used models; Multiple regression model, Polynomial regression model, Response surface regression model, Nas et al. (2007) [25], Tenjo et al. (2015) and Ruiz-Verdú et al. (2016) [26], Cândido et al. (2016) (1-7)[27], El-Magd and Ali (2008) (1-2) [28], Toming et al. (2016) [29], Watanabe et al. (2015) [30], Jaelani et al. (2016) [31], Lim and Choi (2015) [32], ANN (Artificial Neural Network Model) methods. Accuracy analysis was made by comparing the estimation methods, and the method giving the most accurate result was determined. The method and analysis results are

DOI: http://dx.doi.org/10.32571/ijct.1201634 **E-ISSN: 2602-277X**

given in Table 1. According to the analysis result, the Chl a significance value gave more accurate results for the ANN model than the other models according to according to the measurement values are given in Figure 3.

$p=0.00001<0.05$ p and R² value. As a result of the algorithm; Chlorophyll A inferences of the models are shown in Figure 2. The graphic analyzes of the models

Table 1. Chl A estimation methods and accuracy analyzes

Number	Sensor	Number of Variables	Number of Samples	Model	R	R^2	P
1	Sentinel 2	19	40	Artificial Neural Network Model	0.56601	0.32037	0.0001
2	Sentinel 2	19	40	Watanabe et al. (2015)[30]	0.4097	0.16785	0.0001
3	Sentinel 2	19	40	Cândido et al. (2016)(1)[27]	0.37727	0.14233	0.0001
4	Sentinel 2	19	40	Cândido et al. (2016)(2)[27]	0.34081	0.11615	0.0001
5	Sentinel 2	19	40	Cândido et al. (2016)(5)[27]	0.34081	0.11615	0.01831
6	Sentinel 2	19	40	Cândido et al. (2016)(3)[27]	0.31746	0.10078	0.0001
7	Sentinel 2	19	40	Cândido et al. (2016)(6)[27]	0.31746	0.10078	0.04805
8	Sentinel 2	19	40	Multiple Regression Model	0.29166	0.08506	0.0001
9	Sentinel 2	19	40	Toming et al. (2016)[29]	0.28602	0.08181	0.0001
10	Sentinel 2	19	40	Tenjo et al. (2015) and Ruiz-Verdu et al. (2016)[26]	0.26453	0.06997	0.0018
11	Sentinel 2	19	40	Nas et al. (2007)[25]	0.26446	0.06994	0.0001
12	Sentinel 2	19	40	Cândido et al. (2016)(4)[27]	0.25242	0.06371	0.14646
13	Sentinel 2	19	40	Cândido et al. (2016)(7)[27]	0.19373	0.03753	0.51982
14	Sentinel 2	19	40	Response Surface Regression Model	0.16606	0.02757	0.03024
15	Sentinel 2	19	40	Polynomial Regression Model	0.13977	0.01953	0.0001
16	Sentinel 2	19	40	El-Magd and Ali (2008) (1)[28]	0.08594	0.00738	0.00325
17	Sentinel 2	19	40	Jaelani et al. (2016)[31]	0.03495	0.00122	0.96082
18	Sentinel 2	19	40	Lim and Choi (2015)[32]	0.03495	0.00122	0.90085
19	Sentinel 2	19	40	El-Magd and Ali (2008) (2)[28]	0.00801	6.42E-05	0.01981

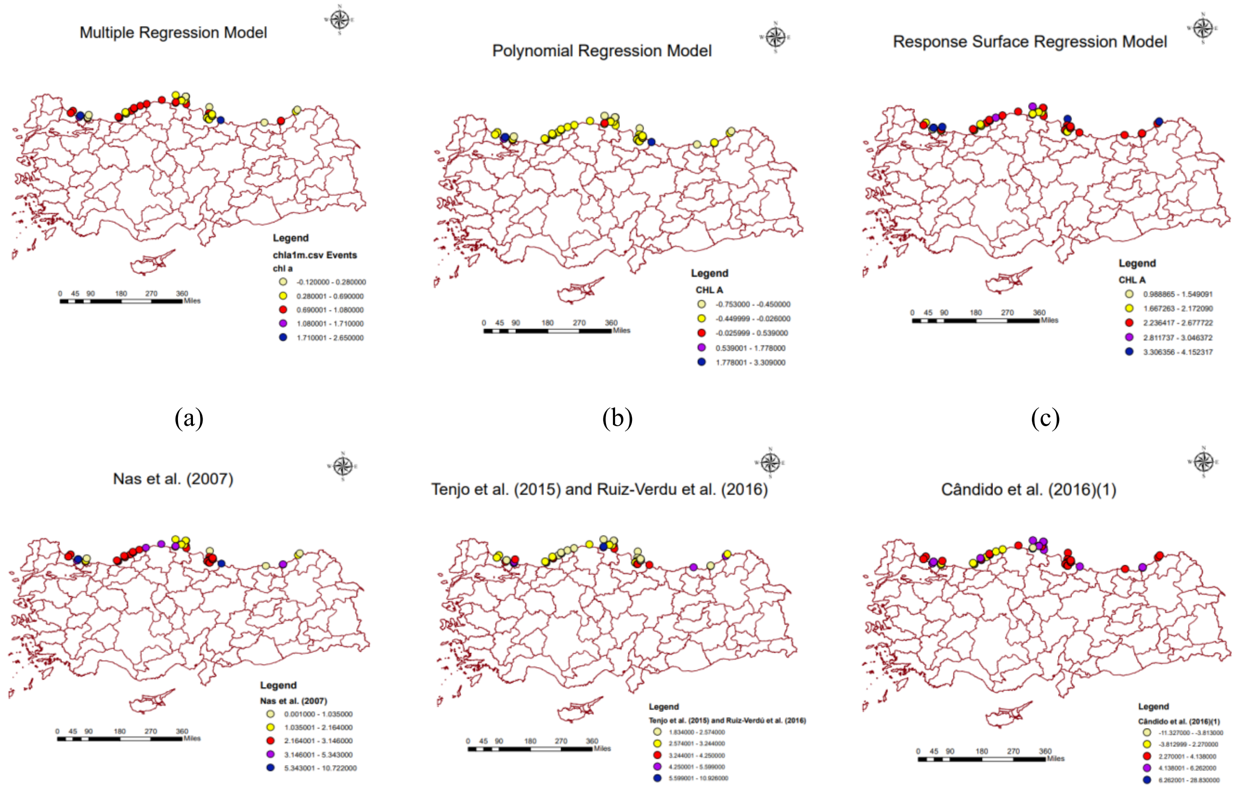

(a) (b) (c)

(d) (e) (f)

DOI: http://dx.doi.org/10.32571/ijct.1201634 **E-ISSN: 2602-277X**

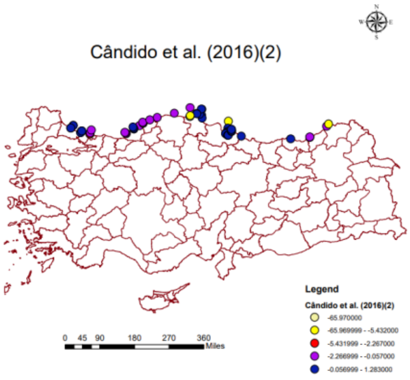

(g)

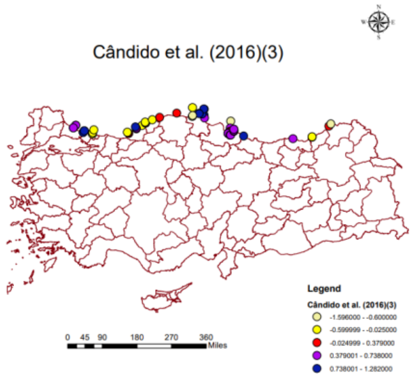

(h)

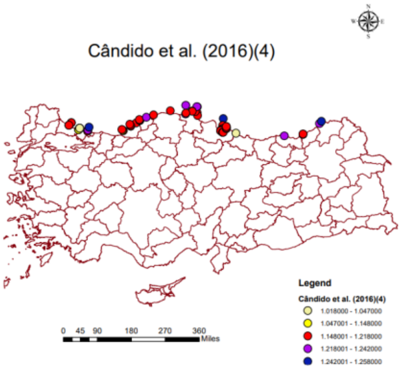

(i)

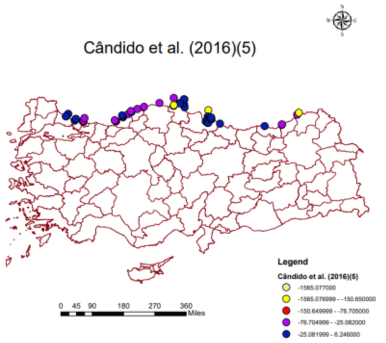

(j)

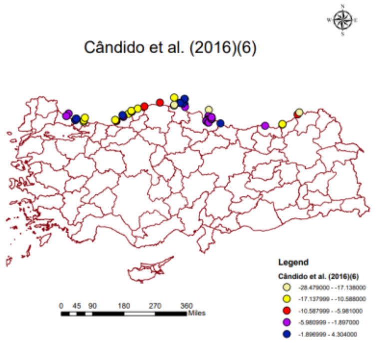

(k)

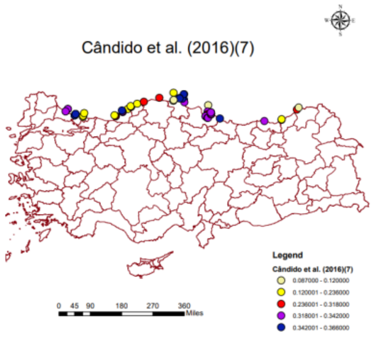

(l)

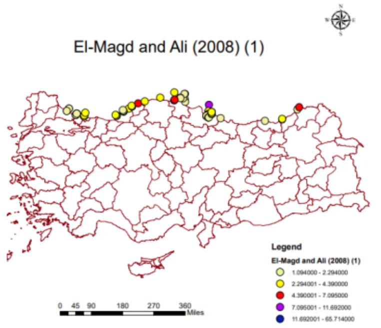

(m)

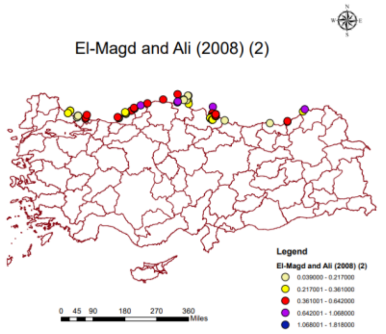

(n)

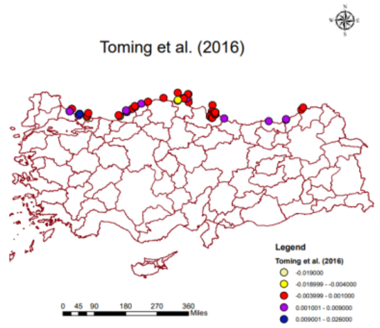

(o)

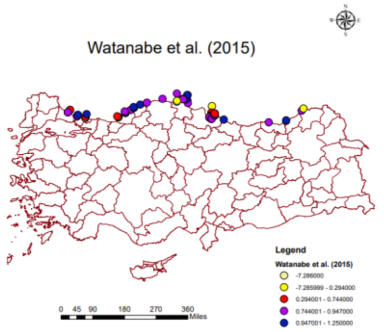

(p)

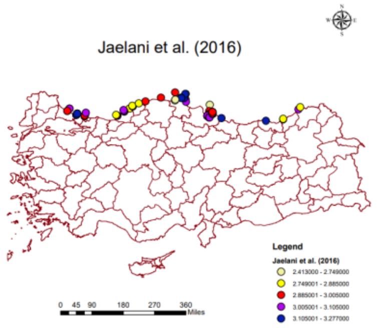

(q)

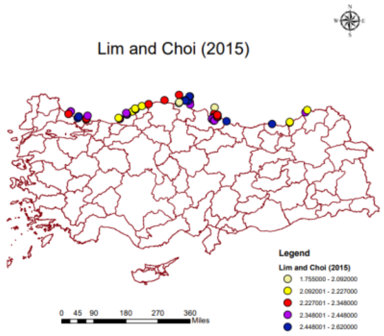

(r)

DOI: http://dx.doi.org/10.32571/ijct.1201634 **E-ISSN: 2602-277X**

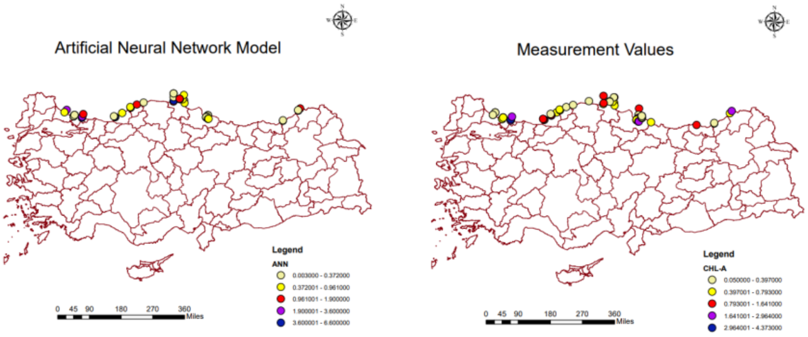

Figure 2. Chlorophyll A models; Multiple regression model (a), Polynomial regression model (b) , Response surface regression model (c) , Nas et al. (2007) [25] (d), Tenjo et al. (2015) and Ruiz-Verdú et al. (2016) [26] (e), Cândido et al. (2016)(1) [27] (f), Cândido et al. (2016)(2) [27] (g), Cândido et al. (2016)(3) [27] (h) Cândido et al. (2016)(4) [27] (i) Cândido et al. (2016)(5) [27] (j), Cândido et al. (2016)(6) [27] (k), Cândido et al. (2016)(7) [27] (l), El-Magd and Ali (2008) (m) [28] (l), El-Magd and Ali (2008) (2) [28] (n), Toming et al. (2016) [29] (o), Watanabe et al. (2015) [30] (p), Jaelani et al. (2016) [31] (q), Lim and Choi (2015) [32] (r), ANN (Artificial Neural Network Model (s) and Chlorophyll A measurement values (t)

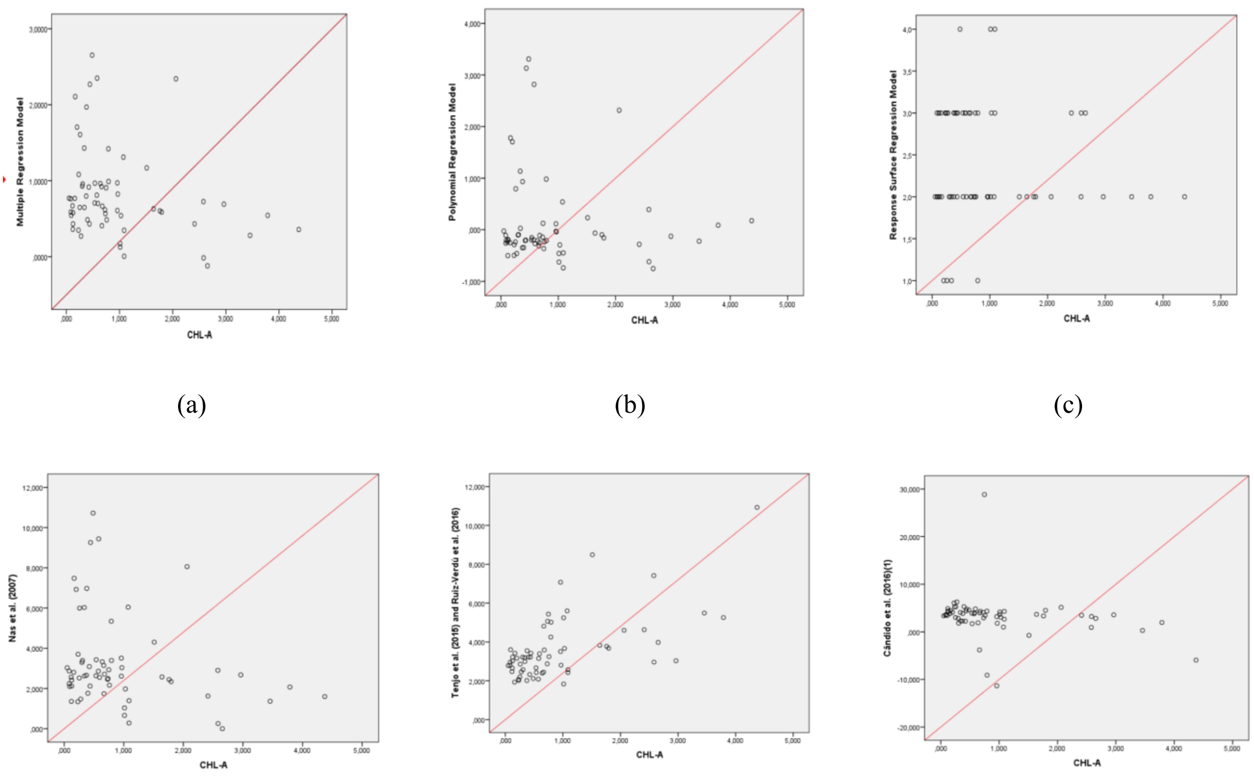

(a) (b) (c)

(d) (e) (f)

DOI: http://dx.doi.org/10.32571/ijct.1201634 **E-ISSN: 2602-277X**

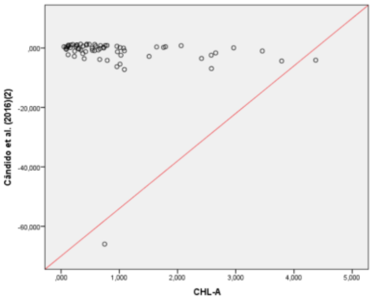

(g)

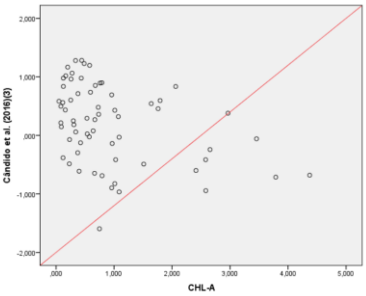

(h)

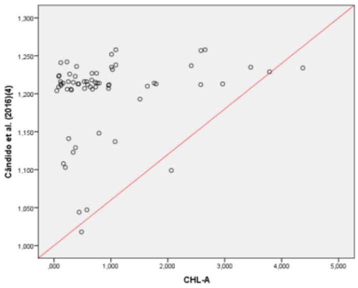

(i)

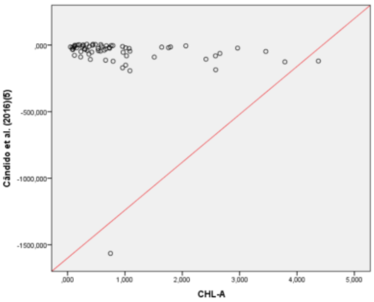

(j)

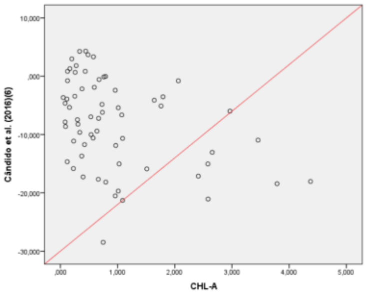

(k)

5

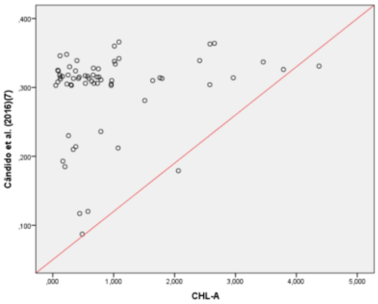

(l)

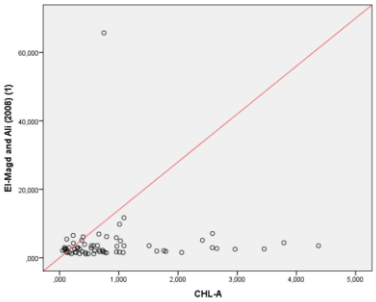

(m)

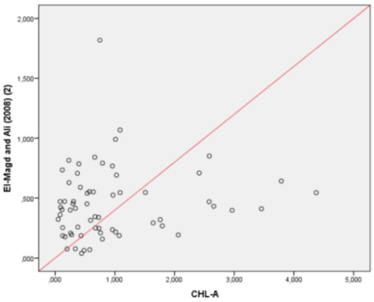

(n)

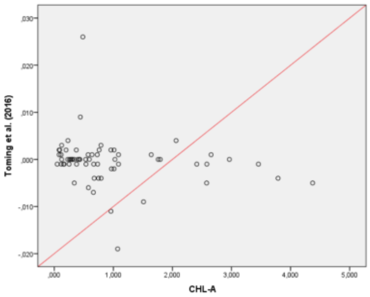

(o)

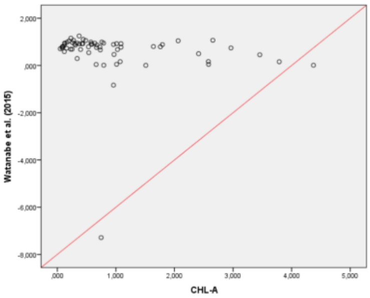

(p)

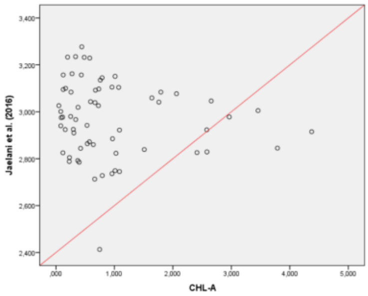

(q)

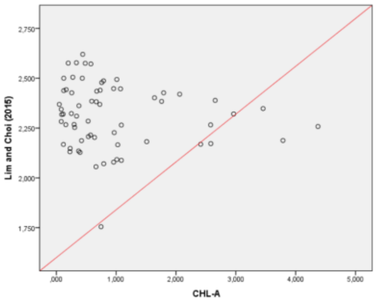

(r)

DOI: http://dx.doi.org/10.32571/ijct.1201634 **E-ISSN: 2602-277X**

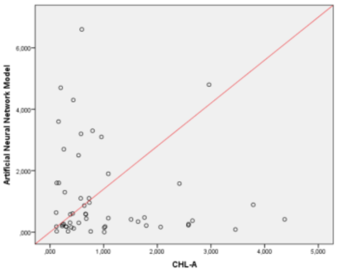

Figure 3. Chlorophyll A models; Multiple regression model (a), Polynomial regression model (b) , Response surface regression model (c) , Nas et al. (2007) [25] (d), Tenjo et al. (2015) and Ruiz-Verdú et al. (2016) [26] (e), Cândido et al. (2016)(1) [27] (f), Cândido et al. (2016)(2) [27] (g), Cândido et al. (2016)(3) [27] (h) Cândido et al. (2016)(4) [27] (i) Cândido et al. (2016)(5) [27] (j), Cândido et al. (2016)(6) [27] (k), Cândido et al. (2016)(7) [27] (l), El-Magd and Ali (2008) (m) [28] (l), El-Magd and Ali (2008) (2) [28] (n), Toming et al. (2016) [29] (o), Watanabe et al. (2015) [30] (p), Jaelani et al. (2016) [31] (q), Lim and Choi (2015) [32] (r), ANN (Artificial Neural Network Model (s) graphics

5.RESULTS

Between 2017 and 2021, measurements were made at 40 points in the coastal regions of the Black Sea, including summer and winter periods. At these terrestrial measurement points, the water quality of the Black Sea coast was monitored using remote sensing methods. 13 Sentinel-2 satellites were used for the study.

The most important parameter for determining water quality is Chlorophyll a. This is because chlorophyll has a relationship that is directly proportional to the reflectance of the surface. In this study, the parameter Chlorophyll A was investigated. 19 algorithms were used. An artificial neural network model was published as the best result. It was found that the proportions of Chlorophyll A, which are the main parameters of pollution, are higher in the Bosphorus and its coasts, on the shores of Sinop and around the Black Ereğli Sea than in other regions.

The Black Sea coast working area is rainy, windy and choppy in all seasons. For this reason, the steps of field measurement and satellite image processing are difficult. From many studies, it is easier to determine water quality in a closed area such as a lake than in open coastal areas. This is because the lake has a stagnant water surface and its parameters do not fluctuate much. In open areas, it is difficult to measure the parameters due to problems such as wind and waves. The parameters also have fluctuations.

It has been shown that it is possible to observe coastal pollution in a short time, without cost and/or at very low cost using remote sensing techniques. On-site measurement is costly and very time consuming. Moreover, measurement on the ground is not possible in all weather conditions. In this sense, remote sensing techniques are of great importance for pollution detection and are used in many studies.

6. CONCLUSION

Water quality parameters can vary depending on weather conditions, time, space, and many other factors. Repeated sampling to analyze periodic changes in water quality is expensive and time consuming. Remote sensing makes it possible to collect information over a wide range of areas and in a short period of time. As a result of the study, it was found that the capabilities offered by RS can be a solution to many problems faced by classical spatial methods that are widely used in water quality determination (such as mustilage), creating a more economical, faster, and labor-saving system for water quality determination projects by ensuring that the two methods work in harmony. These developments show that RS may be an alternative for water quality surveys in the future. Remote sensing technology has proven to be an effective method for monitoring pollution.

ACKNOWLEDGEMENTS

The authors thank the “Integrated Marine Pollution Monitoring 2017–2021 Program” funded by the Turkish Ministry of Environment and Urbanization/General Directorate of EIA, Permit and Inspection/ Department of Laboratory, Measurement and coordinated by TUBITAK- MRC CC&S for the provisioning of the data used in this study. We thank all the crew of R/V TÜBİTAK MARMARA and the Marine Research & Technologies Group [8].

Conflict of interest

DOI: http://dx.doi.org/10.32571/ijct.1201634 **E-ISSN: 2602-277X**

Authors declare that there is no a conflict of interest with any person, institute, company, etc.

REFERENCES

1. Landsat's Critical Role in Water Management. **2020**. https://landsat.gsfc.nasa.gov/benefits/water/ (accessed June 14, 2020).

2. Örmeci, C.; Ekercin, S. *Water Quality Change Analysis in Tuz Gölü with Remote Sensing Technique,* TMMOB Cham. of Surv. and Cad. Eng. 10th Turkey Sci. and Tech. Map. Congress, Ankara, 2005

3. Gholizadeh, M.H.; Melesse, A.M.; Reddi, L. A. *Sensors.* **2016,** 16, 1298; doi:10.3390/s16081298

4. Lira, J.A. *Geof. Inter.* **2020,** 59-1: 13-25

5. Usali, N.; Ismai, M.H. *EJSD.* **2010,** 3 (3)

6. Ritchie, J.C.; Schiebe, F.R.; Mchenry J. *J. Am. Soc. Photogramm.* **1976,** 1976;42:1539–1545.

7. Jones J. R,; Bachmann R.W. *Prediction of Phosphorus and Chlorophyll Levels in Lakes Journal*, Annual Conference Issue (Sep., 1976), 48 (9), 2176-2182 (7 pages)

8. Integrated Marine Pollution Monitoring 2017–2021 Program, Turkish Ministry of Environment and Urbanization/General Directorate of EIA, Permit and Inspection/ Department of Laboratory, Measurement and coordinated by TUBITAK- MRC CC&S, 2021.

9.Doğanay, S. *A Study in Terms of Transportation Geography Trabzon Port and Hinterland.* 2014, ISBN 978-605-364-677-8, 1-2.

10.Bat, L.; Öztekin, A.; Şahin, F.; Arıcı, E.; Özsandıkçı, U. *MedFAR.* **2018,** 1(2) 67-86.

11.Sentinel-2, 2020. http://nik.com.tr/content_sistem_uydu.asp?id=102 (accessed 13.03.20).

12. European Environment Agency. *Eutrophication in Europe's Coastal Waters,* Topic Report 7. Copenhagen 2001.

13. Nixon, S.W. *Hydrobiologia,* **2009,** 629, 5–19. doi: 10.1007/s10750-009-9759-z.

14. Gamito, S.; Gilabert, J.; Marcos, C.; Pérez-Ruzafa, A. *Boca Ratón., FL: CRC Press,* **2005,** 193–229.

15. Desmit, X.; Thieu, V.; Billen, G.; Campuzano, F.; Dulière, V.; Garnier, J. *Sci. Total Environ.* **2018,** 635, 1444–1466. doi: 10.1016/j.scitotenv.2018.04.181.

16. Gitelson, A., *Int. J. Remote Sens.* **1992**, 13: 3367-3373.

17. Choi, C.J.; Berges, J.A.; Young, E.B. *Water Res.* **2012,** 15;46(8):2615-26. doi: 10.1016/j.watres.2012.02.027. Epub 2012 Feb 24

18. Chawla, I; Karthikeyan, L; Mishra, A.K. *Jour. of Hydr.* **2020,** 585(6), 124826.

19. Tuzcu, A.; Dervişoğlu, A.; Musaoğlu, N.; Tanık, A.G. *ISAG.* **2019,** 1(1), 154- 158.

20.Chlorophyll, 2021. https://earthobservatory.nasa.gov/global-maps/MY1DMM_CHLORA, 2021 (accessed 21.04.2021)

21. Cullen, J.J.; Lewis, M.R., *JGR.* **1995,** 100(C7), 13,255–13,266.

22. Morrison, J.R. *Lim. and Ocean.* **2003,** 48(2), 618– 631.

23.Behrenfeld, M.J.; Halsey, K.H.; Milligan, A.J. *Bio. Sci.* **2008,** 363(1504), 2687– 2703.

24.Behrenfeld, M.J.; Westberry, T.K.; Boss, E.; O'Malley, R.T.; Siegel, D.A.; Wiggert, J.D.; Franz, B.; McClain, C. R.; Feldman, G.; Doney, S.C.; Moore, J.K.; Dall'Olmo, G.; Milligan, A.J.; Lima, I.; Mahowald, N. *Biogeosciences.* **2009,** 6, 779– 794.

25.Nas, B.; Karabork, H.; Ekercin, S.; and Berktay, A. *Assessing water quality in the Beysehir Lake (Turkey) by the application of GIS, Geost. and Remote Sens.* 2007, 12th World Lake Conference, 28 October-2 November 2007, Jaipur, India, 2007.

26.Tenjo, C.; Ruiz-Verdú, A.; Delegido, J.; Peña, R.; and Moreno, J. *GEOMÁTICA.* **2015,** 9, 37-46.

27.Cândido, A.K.A.A.; Filho, P.A.C.; Haupenthal, M.R.; Silva, N.M.; Correa, S.J.; Ribeiro, M.L. *Water, Air, & Soil Pollution.* **2016,** 227(7), 224.

28.El-Magd, I.A.; and Elham, M. *AJBAS.* **2008,** 2(4): 1307-1314.

29.Toming, K.; Kutser, T.; Laas, A.; Sepp, M.; Paavel, B.; Nõges, T., *Remote Sens.* **2016,** 8(8), 640.

30.Watanabe, F.S.Y; Alcântara, E.; Rodrigues, T.W.P.; Imai, N.N.; Barbosa, C.C.F.; Rotta, L.H.D.S. *Int J Environ. Res. Pub. Health.* **2015,** 12(9), 10391-10417.

31.Jaelani, L.M.; Limehuwey, R.; Kurniadin, N.; Pamungkas, A.; Koenhardono, E.S.; Sulisetyono, A. *IPTEK JTS.* **2016,** 27(1), 16-23.

32.Lim, J.; Choi, M. *EMAS.* **2015,** 187(6), 384

DOI: http://dx.doi.org/10.32571/ijct.1060520 **E-ISSN: 2602-277X**

International Journal of Chemistry and Technology

http://dergipark.org.tr/ijct

Research Article

Heat energy transport characteristics of microchannel reactors for hydrogen production by steam-methanol reforming on copper-based catalysts

Junjie CHEN[1,*]

[1] *Department of Energy and Power Engineering, School of Mechanical and Power Engineering, Henan Polytechnic University, 2000 Century Avenue, Jiaozuo, Henan, 454000, P.R. China*

Received: 20 April January 2022; Revised: 3 November 2022; Accepted: 8 November 2022

*Corresponding author e-mail: cjjtpj@163.com

Citation: Chen, J. *Int. J. Chem. Technol.* **2023**, 7 (1), 57-66.

ABSTRACT

Numerical simulations are carried out to understand the heat energy transport characteristics of microchannel reactors for hydrogen production by steam-methanol reforming on copper-based catalysts. Enthalpy analysis is performed and the evolution of energy in the oxidation and reforming processes is discussed in terms of reaction heat flux. The effects of solid thermal conductivity, gas velocity, and flow arrangement on the thermal behavior of the reactor is evaluated in order to fully describe the thermal energy change in the reactor. The results indicate that the thermal behavior of the reactor depends upon the thermal properties of the walls. The change in enthalpy is of particular importance in exothermic and endothermic reactions. The net enthalpy change for oxidation and reforming is negative and positive, but the net sensible enthalpy change is always positive in the reactor. The wall heat conduction effect accompanying temperature changes is important to the autothermal design and self-sustaining operation of the reactor. The solid thermal conductivity is of great importance in determining the operation and efficiency of the reactor. The reaction proceeds rapidly and efficiently only at high solid thermal conductivity. The reaction heat flux for oxidation and reforming is positive and negative. The change in flow arrangement significantly affects the reaction heat flux in the reactor. The parallel flow design is advantageous for purposes of enhancing heat transfer and avoiding localized hot spots.

Keywords: Hydrogen production, thermal properties, reforming reactions, oxidation reactions, flow arrangements, heat fluxes.

1. INTRODUCTION

Steam reforming reactions have vast importance in chemical reaction engineering.[1,2] Steam reforming reactions are endothermic, accompanied by the consumption of a large amount of heat.[3,4] Accordingly, heat energy transport is considered essential for steam reforming. This endothermic process involves a variety of individual reactions leading to the desired product hydrogen and undesired product carbon monoxide. The amount of heat energy must be large to make steam reforming reactions proceed rapidly in reformers containing an array of tubes.[5,6] For example, steam-methane reforming reactions proceed usually at temperatures from around 800 °C to around 900 °C.[7,8] The rate of steam-methane reforming reactions depends upon both pressure and temperature. The heat-supplying furnaces usually operate at much higher temperatures. Heating devices for hydrogen production utilize industrial flames in furnaces, and reformer design is often decided empirically, including operation conditions and reaction routes. Diffusion flames can be designed for these purposes.

Optimization of endothermic steam reforming processes in its practical hydrogen fuel cell applications can be made possible with the results of investigations about heat energy transport characteristics. Hydrocarbons and alcohols can be converted to hydrogen-rich gas, and steam reforming processes are the most primary method for hydrogen production. The need for power generation creates new opportunities for the development of hydrogen fuel cells.[9,10] Hydrogen fuel cells are important in supporting power not only for remote areas but also for inaccessible areas.[11,12] Hydrogen fuel cells are also of importance in the transportation field.[13,14] Practical hydrogen fuel cells are necessarily complex systems. Hydrogen fuel cells can convert a fuel to useful energy at a very high level of efficiency, including heptane[15,16], methane [17,18], methanol [19,20], kerosene[21], and gasoline[22], and therefore much less fuel is required for specify requirements of energy.

Microchannel reactors are being developed for hydrogen fuel cell purposes. Autothermal methods can be used to maintain the required temperatures with internal heating by catalytic combustion.[23] Alternating reforming and combustion spaces are designed for this purpose, but precise rates of fuel and steam or air are required for the two preceding processes with substantially lower reaction temperatures than conventional methods. Such microchannel reactors offer design and efficiency advantages,[24] depending upon factors responsible for the rate of the reforming reaction, for example, the conductive heating area.[25,26] Higher conversion can be achieved due to the improved heat energy transport characteristics, but this type of reactor has its specified temperature design range. Additionally, the loss in pressure drop is a primary concern in reactor design.

Heat integrated reactors are being developed to properly address the above concern. [27] Heat recirculation methods are employed and a concentric cylinder geometry is used, which will lead to improvements in heat energy transport. Additionally, structured catalysts are used to reduce the pressure drop across the cylindrical tubes.[27,28] Compact design methods can be used to take advantages of the large heat energy transport area of the reactor. In this case, reforming and combustion reactions can proceed simultaneously at the specified temperatures. However, scale-up issues must be addressed for this type of reactor, and the inherent advantages of this design remain to be further exploited, for example, by improving its heat energy transport characteristics.

Heat integrated reactors offer distinct advantages of carrying out simultaneous multiple chemical reactions, for example, reforming and combustion.[29,30] The heat energy released from combustion processes is used to meet the heat demand of reforming processes.[31,32] The two important influencing factor in determining the feasibility for heat recirculation are the quantity of heat produced and the temperature of the dividing walls.[33,34] These influencing factor must be controllable in the reforming process, and heat energy transport occurs through conduction across the dividing walls.[35,36] With the use of heat integrated reactors, scale-up issues and heat recirculation needs can be addressed.[37,38] Additionally, heat integrated reactors offer improvements in both heat and mass transport.[39,40] While heat exchanger methods are used extensively, the mechanism differs from that of heat integrated reactors in that multiple chemical reactions occur, for example, reforming and combustion.[41,42] Steam reforming and heat integrated reactors are of importance in hydrogen production and useful for practical applications in hydrogen fuel cells.[43,44] However, the heat energy transport characteristics of heat integrated reactors with flow microchannels are still not fully understood.

The present study relates to hydrogen production in a microchannel reactor by steam-methanol reforming on copper-based catalysts. Mathematical expressions are derived for the reactor system based upon the principles of chemical kinetics and fluid mechanics. Numerical simulations are carried out to understand the heat energy transport characteristics of the autothermal reactor. Enthalpy analysis is performed and the evolution of energy in the oxidation and reforming processes is discussed in terms of reaction heat flux. The effects of solid thermal conductivity, gas velocity, and flow arrangement on the thermal behavior of the autothermal reactor is evaluated in order to fully describe the thermal energy change in the reactor. The objective of the present study is to understand the heat energy transport characteristics of microchannel reactors for hydrogen production by steam-methanol reforming on copper-based catalysts. Emphasis is placed on the effects of solid thermal conductivity, gas velocity, and flow arrangement on the thermal behavior of autothermal reactors.

2. METHODS

2.1. Reactor representation

The complex reactor must be adaptable to continuous self-sustaining operation of the steady-stream type, and the wall material must be selected for strength. The complex reactor for producing hydrogen is illustrated schematically in Figure 1 by steam-methanol reforming on a copper-based catalyst. The reactor operates upon the principles of chemical kinetics and fluid mechanics. The channels can be designed using different flow arrangement methods.[45,46] The channels are coated with a catalyst, and the reactor walls are constructed of stainless steel.

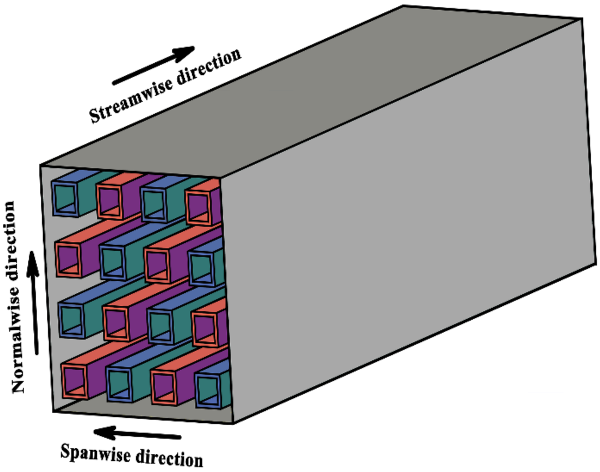

Figure 1. Schematic representation of the complex reactor for producing hydrogen by steam-methanol reforming on a copper-based catalyst.

DOI: http://dx.doi.org/10.32571/ijct.1060520 **E-ISSN: 2602-277X**

At the channel inlets, the pressure of the mixtures is 20 atmospheres and the temperature is 100 °C. The molar ratio of steam to carbon is 140.0:100.0 and the mole ratio of methanol to air is 11.2:100.0. At the channel inlets, the gas velocity is 0.6 and 2.0 m/s, respectively, for the oxidation and reforming reactant streams. The channels are 700 microns in height and in width, 50.0 mm in length, and square in cross section. The solid thermal conductivity is 200 W/(m·K) at a temperature of 20 °C. The structured catalyst is 100 microns in thickness. The un-coated walls are 700 microns in thickness.

The computational domain of the complex reactor for producing hydrogen is illustrated schematically in Figure 2 by steam-methanol reforming. The energy released in the oxidation process is the basis of the complex reactor. The oxidation and reforming reactions must be sustained at constant rates and maintained at a controlled level.[47,48] In this case, the operation of the reactor will remain steady. The oxidation and reforming reactions must proceed at temperatures above 200 °C but below 300 °C. During reactor start-up, the gas mixtures are ignited in the oxidation channels. Properly ignited, the energy released in the oxidation process must raise the temperature of the reactor sufficiently.

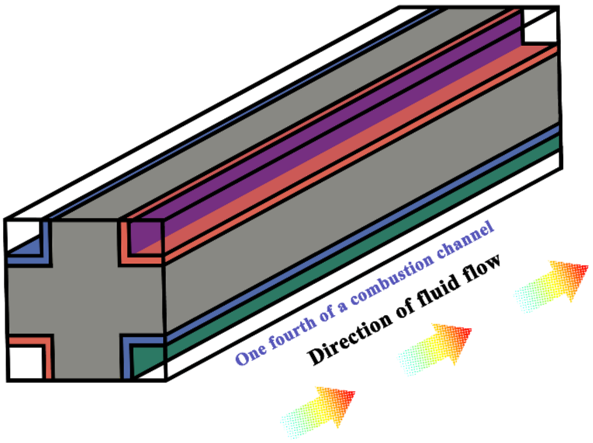

Figure 2. Schematic representation of the computational domain of the complex reactor for producing hydrogen by steam-methanol reforming.

2.2. Mathematical representation

The structured mesh of the complex reactor for producing hydrogen is illustrated in Figure 3 by steam-methanol reforming on a copper-based catalyst. Oxidation and reforming in the reactor are complex physical and chemical process processes. Under the reaction conditions specified above, mathematical expressions are derived for the reactor system.

The mechanism of the oxidation or reforming reaction can be represented as

$$\sum_{s=1}^{K_s} v'_{si}\chi_s \Leftrightarrow \sum_{s=1}^{K_s} v''_{si}\chi_s\,, (i = 1, \dots, \delta) \quad (1)$$

where K_s is the number of species, v is the stoichiometric coefficient, χ_s is the surface species s, and δ is the number of surface reactions.

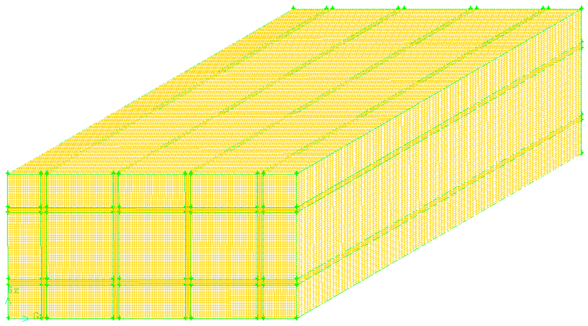

Figure 3. Structured mesh of the complex reactor for producing hydrogen by steam-methanol reforming on a copper-based catalyst.

The production rate $\dot{s}_s$ is given by

$$\dot{s}_s = \sum_{i=1}^{I} v_{si} q_i\,, (s = 1, \dots, K_s), \quad (2)$$

$$v_{si} = v''_{si} - v'_{si}. \quad (3)$$

The rate-of-progress variable q_i is defined as

$$q_i = k_{fi} \prod_{s=1}^{K_s} [\chi_s]^{v'_{si}} - k_{ri} \prod_{s=1}^{K_s} [\chi_s]^{v''_{si}}, \quad (4)$$

where k is the rate constant.

The forward reaction rate constant is defined as

$$k_{fi} = A_i T^{\beta_i} e^{\frac{-E_i}{RT}}, \quad (5)$$

where β is the temperature exponent, E is the activation energy, and A is the pre-exponential factor.

The reverse reaction rate constant is defined as

$$k_{ri} = \frac{k_{fi}}{K_{ci}}, \quad (6)$$

where K is the equilibrium constant.

The gas-phase species must be balanced in each channel:

$$\frac{\partial}{\partial x}\left(\rho w_k V_{k,x}\right) + \frac{\partial}{\partial y}\left(\rho w_k V_{k,y}\right) + \frac{\partial}{\partial z}\left(\rho w_k V_{k,z}\right) + \frac{\partial(\rho u_x w_k)}{\partial x} + \frac{\partial(\rho u_y w_k)}{\partial y} + \frac{\partial(\rho u_z w_k)}{\partial z} - \dot{\xi}_k W_k = 0,$$
(7)

where x, y, and z are coordinate variables, k denotes gas-phase species, V is the diffusion velocity, W is the molecular mass, ρ is the density, w is the mass fraction, and $\dot{\xi}$ is the gas-phase reaction rate.

The Knudsen diffusivity is calculated in terms of mean pore diameter d as

$$D_i^K = \frac{d}{3}(8RT)^{\frac{1}{2}}(\pi W_i)^{-\frac{1}{2}}. \qquad (8)$$

The momentum balance in each channel can be stated as

$$\frac{\partial}{\partial x}\left[\mu\left(\frac{\partial u_x}{\partial x}+\frac{\partial u_x}{\partial x}\right)\right]+\frac{\partial}{\partial y}\left[\mu\left(\frac{\partial u_x}{\partial y}+\frac{\partial u_y}{\partial x}\right)\right]+\frac{\partial}{\partial z}\left[\mu\left(\frac{\partial u_x}{\partial z}+\frac{\partial u_z}{\partial x}\right)\right] -\frac{\partial}{\partial x}\left[\frac{2}{3}\mu\left(\frac{\partial u_{xx}}{\partial x}+\frac{\partial u_{yx}}{\partial y}+\frac{\partial u_{zx}}{\partial z}\right)\right]-\frac{\partial p}{\partial x}=0, \qquad (9)$$

$$\frac{\partial}{\partial x}\left[\mu\left(\frac{\partial u_y}{\partial x}+\frac{\partial u_x}{\partial y}\right)\right]+\frac{\partial}{\partial y}\left[\mu\left(\frac{\partial u_y}{\partial y}+\frac{\partial u_y}{\partial y}\right)\right]+\frac{\partial}{\partial z}\left[\mu\left(\frac{\partial u_y}{\partial z}+\frac{\partial u_z}{\partial y}\right)\right] -\frac{\partial}{\partial y}\left[\frac{2}{3}\mu\left(\frac{\partial u_{xy}}{\partial x}+\frac{\partial u_{yy}}{\partial y}+\frac{\partial u_{zy}}{\partial z}\right)\right]-\frac{\partial p}{\partial y}=0, \qquad (10)$$

$$\frac{\partial}{\partial x}\left[\mu\left(\frac{\partial u_z}{\partial x}+\frac{\partial u_x}{\partial z}\right)\right]+\frac{\partial}{\partial y}\left[\mu\left(\frac{\partial u_z}{\partial y}+\frac{\partial u_y}{\partial z}\right)\right]+\frac{\partial}{\partial z}\left[\mu\left(\frac{\partial u_z}{\partial z}+\frac{\partial u_z}{\partial z}\right)\right] -\frac{\partial}{\partial z}\left[\frac{2}{3}\mu\left(\frac{\partial u_{xz}}{\partial x}+\frac{\partial u_{yz}}{\partial y}+\frac{\partial u_{zz}}{\partial z}\right)\right]-\frac{\partial p}{\partial z}=0, \qquad (11)$$

where μ is the dynamic viscosity, u is the velocity, and p is the pressure.

The mass must also be balanced in each channel:

$$\frac{\partial(\rho u_x)}{\partial x}+\frac{\partial(\rho u_y)}{\partial y}+\frac{\partial(\rho u_z)}{\partial z}=0. \qquad (12)$$

The conservation of energy in each channel can be stated as

$$\frac{\partial}{\partial x}\left(-k_g\frac{\partial T}{\partial x}+\rho\sum_{k=1}^{\gamma}w_k h_k V_{k,x}\right)+\frac{\partial}{\partial y}\left(-k_g\frac{\partial T}{\partial y}+\rho\sum_{k=1}^{\gamma}w_k h_k V_{k,y}\right)+\frac{\partial}{\partial z}\left(-k_g\frac{\partial T}{\partial z}+\rho\sum_{k=1}^{\gamma}w_k h_k V_{k,z}\right) +\frac{\partial(\rho u_x h)}{\partial x}+\frac{\partial(\rho u_y h)}{\partial y}+\frac{\partial(\rho u_z h)}{\partial z}=0, \qquad (13)$$

where γ is the number of gas-phase species, k is the thermal conductivity, g denotes the gas mixture, T is the temperature, and h is the enthalpy.

The chemical species must be balanced on each catalyst surface:

$$\frac{\theta_m\dot{\zeta}_m}{\gamma'}=0, \qquad (14)$$

where θ is the coverage, m denotes surface species, γ' is the site density, and $\dot{\zeta}$ is the reaction rate.

The conservation of energy in each wall can be stated as

$$\frac{\partial}{\partial x}\left(k_{wall}\frac{\partial T}{\partial x}\right)+\frac{\partial}{\partial y}\left(k_{wall}\frac{\partial T}{\partial y}\right)+\frac{\partial}{\partial z}\left(k_{wall}\frac{\partial T}{\partial z}\right)=0. \qquad (15)$$

2.3. Chemistry representation

The oxidation reaction is described by

$$\mathrm{CH_3OH} + 1.5\mathrm{O_2} \Leftrightarrow 2\mathrm{H_2O} + \mathrm{CO_2}. \qquad (16)$$

The reforming reactions are described by

$$\mathrm{CH_3OH} + \mathrm{H_2O} \Leftrightarrow 3\mathrm{H_2} + \mathrm{CO_2}. \qquad (17)$$

$$\mathrm{CH_3OH} \Leftrightarrow 2\mathrm{H_2} + \mathrm{CO}. \qquad (18)$$

The water-gas shift reaction is described by

$$\mathrm{CO} + \mathrm{H_2O} \Leftrightarrow \mathrm{H_2} + \mathrm{CO_2}. \qquad (19)$$

The oxidation and reforming processes are accounted for by chemical kinetic models.[49,50] The reforming reaction rate is given by

$$r_{reforming} = \left[k_R K^{\vartheta}_{\mathrm{CH_3}O(\alpha)}\left(p_{\mathrm{CH_3OH}}p_{H_2}^{-0.5}\right)\left(1 - k_R^{-1}p_{H_2}^{3}p_{\mathrm{CO_2}}p_{\mathrm{CH_3OH}}^{-1}p_{H_2O}^{-1}\right)c^{\pi}_{S_\alpha}c^{\pi}_{S_{\alpha a}}\right] \cdot\left[\left(1+K^{\vartheta}_{\mathrm{CH_3}O(\alpha)}\left(p_{\mathrm{CH_3OH}}p_{H_2}^{-0.5}\right)+K^{\vartheta}_{\mathrm{HCOO}(\alpha)}p_{\mathrm{CO_2}}p_{H_2}^{0.5}+K^{\vartheta}_{\mathrm{OH}(\alpha)}\left(p_{H_2O}p_{H_2}^{-0.5}\right)\right)\left(1+K^{0.5}_{H(\alpha a)}p_{H_2}^{0.5}\right)\right]^{-1}, \qquad (20)$$

where c^{π} is the total surface concentration and ϑ denotes the composite parameter.

The water-gas shift reaction rate is given by

$$r_{water-gas\,shift} = \left[k^{\vartheta}_W K^{\vartheta}_{\mathrm{OH}(\alpha)}\left(p_{\mathrm{CO}}p_{H_2O}p_{H_2}^{-0.5}\right)\left(1 - k_W^{-1}p_{H_2}p_{\mathrm{CO_2}}p_{\mathrm{CO}}^{-1}p_{H_2O}^{-1}\right)\left(c^{\pi}_{S_\alpha}\right)^2\right] \cdot\left[\left(1+K^{\vartheta}_{\mathrm{CH_3}O(\alpha)}\left(p_{\mathrm{CH_3OH}}p_{H_2}^{-0.5}\right)+K^{\vartheta}_{\mathrm{HCOO}(\alpha)}p_{\mathrm{CO_2}}p_{H_2}^{0.5}+K^{\vartheta}_{\mathrm{OH}(\alpha)}\left(p_{H_2O}p_{H_2}^{-0.5}\right)\right)\right]^{-2}. \qquad (21)$$

The decomposition reaction rate is given by

$$r_{decomposition} = \left[k_D K^{\vartheta}_{\mathrm{CH_3}O(\beta)}\left(p_{\mathrm{CH_3OH}}p_{H_2}^{-0.5}\right)\left(1 - k_D^{-1}p_{H_2}^{2}p_{\mathrm{CO}}p_{\mathrm{CH_3OH}}^{-1}\right)c^{\pi}_{S_\beta}c^{\pi}_{S_{\beta a}}\right] \cdot\left[\left(1+K^{\vartheta}_{\mathrm{CH_3}O(\beta)}\left(p_{\mathrm{CH_3OH}}p_{H_2}^{-0.5}\right)+K^{\vartheta}_{\mathrm{OH}(\beta)}\left(p_{H_2O}p_{H_2}^{-0.5}\right)\right)\left(1+K^{0.5}_{H(\beta a)}p_{H_2}^{0.5}\right)\right]^{-1}. \qquad (22)$$

2.4. Model validation

Comparisons are performed between the predicted results and the data obtained by measurements.[51,52] The reaction temperature remains constant. The channels are 600 microns in height, 500 microns in width, 33.0 mm in length, and rectangular in cross section. The reaction temperature is 200 °C, 220 °C, 240 °C, and 260 °C,

DOI: http://dx.doi.org/10.32571/ijct.1060520 **E-ISSN: 2602-277X**

respectively. The effect of reaction temperature is illustrated in Figure 4 and Figure 5 in terms of the rate of hydrogen production and the conversion of methanol. The predicted results agree with the data obtained by measurements.

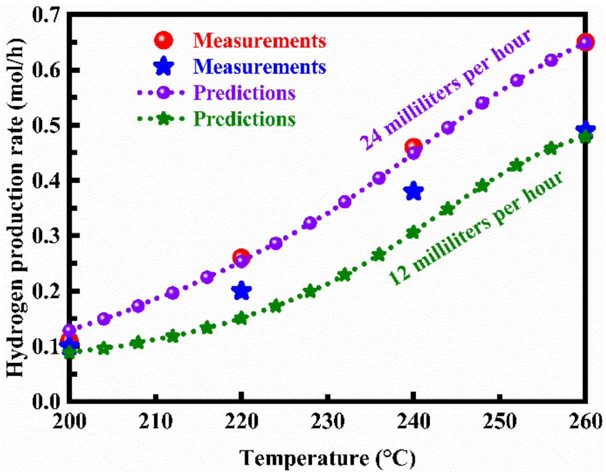

Figure 4. Effect of reaction temperature on the rate of hydrogen production. The data obtained by measurements[51,52] are also presented to validate the model.

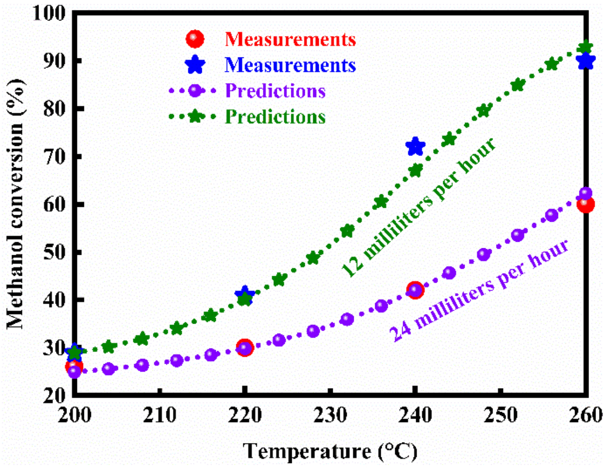

Figure 5. Effect of reaction temperature on the conversion of methanol. The data obtained by measurements[51,52] are also presented to validate the model.

3. RESULTS AND DISCUSSION

3.1. Enthalpy analysis

Enthalpy is a particularly important concept in the design of an autothermal reactor. The enthalpy contour maps in the reactor are illustrated in Figure 6 with different solid thermal conductivity. The reactor walls are constructed of stainless steel, and the behavior of fluids in the reactor can be fully described by laminar flow. Enthalpy can be entirely calculated by the local composition, pressure, and temperature in the reactor, depending upon the volume, pressure, and internal energy. The amount of heat evolved in the chemical reactions is calculated for the reactor, including the amount of heat released and absorbed. The exchange of heat arises from the difference in temperature between adjacent channels of the reactor. Various efficient heat exchange methods offer the opportunity to design microchannel reactors.[53,54] Both dimensions and geometry are very important from the standpoint of design.[55,56] The heat released by the oxidation reaction accounts for the temperature rise in the reactor. The heat energy released by the oxidation reaction is much greater than the heat energy consumed by the reforming reaction. However, the total energy contained in the reactor is conserved. The oxidation and reforming reactions occur rapidly in the reactor. However, oxidation differs from reforming in enthalpy change, depending upon the solid thermal conductivity. The change in enthalpy is of particular importance in exothermic and endothermic reactions, as heat must be balanced in the reactor. The net enthalpy change for oxidation is negative at constant pressure, as an amount of energy flows out of its channels. The net enthalpy change is positive for reforming at constant pressure, as an amount of energy flows into its channels. While the oxidation and reforming reactions proceed in the reactor, the total amount of energy does not change. The thermal behavior of the reactor depends upon the thermal properties of the walls. The net enthalpy change is thermal conductivity-dependent. The concept of thermal conductivity is fundamental to the design of the autothermal reactor. The importance of thermal conductivity will be discussed in more detail below. The net enthalpy change at low thermal conductivity is small for either oxidation or reforming. In contrast, the net enthalpy change is significant at high thermal conductivity.

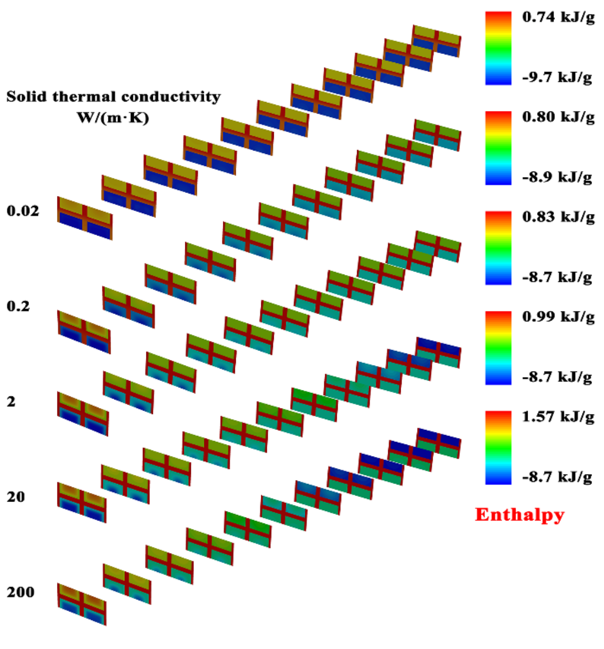

Figure 6. Enthalpy contour maps in the reactor with different solid thermal conductivity. The reactor walls are constructed of stainless steel.

The sensible enthalpy change is accompanied by the change in temperature. The sensible enthalpy contour maps in the reactor are illustrated in Figure 7 with different solid thermal conductivity. The net change between the sensible enthalpy at the end of the oxidation or reforming reaction and the sensible enthalpy at the start of the reaction is always positive in the reactor. The net sensible enthalpy change accompanying the reforming process is small at low thermal conductivity. The net sensible enthalpy change accompanying the oxidation process is large at high thermal conductivity. In contrast, the net sensible enthalpy change is significant for reforming at high thermal conductivity or for oxidation at low thermal conductivity. Furthermore, the net sensible enthalpy change depends upon not only the solid thermal conductivity but also the chemical reaction. Consequently, the net sensible enthalpy change is always positive in the reactor, but depending upon the solid thermal conductivity and the chemical reaction. Due to the overall increase in sensible enthalpy, the reforming reaction is product-favored.

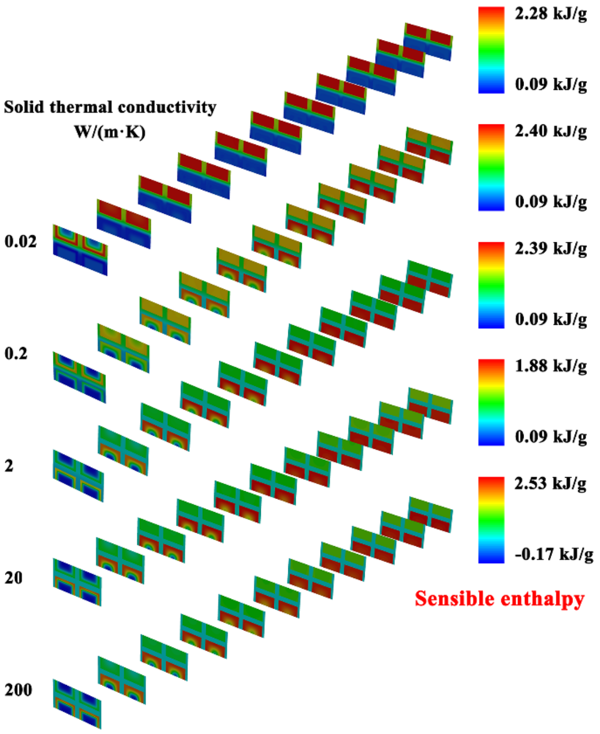

Figure 7. Sensible enthalpy contour maps in the reactor with different solid thermal conductivity. The reactor walls are constructed of stainless steel.

The species mole fraction contour maps in the reactor are illustrated in Figure 8 when the reactor walls are constructed of stainless steel. The reforming reaction proceeds rapidly in the reactor and the conversion is nearly complete due to the high solid thermal conductivity. Energy is evolved in the reactor in the form of heat as the oxidation and reforming reactions proceed simultaneously. The production of hydrogen from methanol is always endothermic. The amount of carbon monoxide is very small doe to almost complete conversion of methanol to carbon dioxide, which is of great importance in practical hydrogen fuel cell applications. The endothermic reaction occurs rapidly since stainless steel is better at conducting heat between adjacent channels of the reactor.

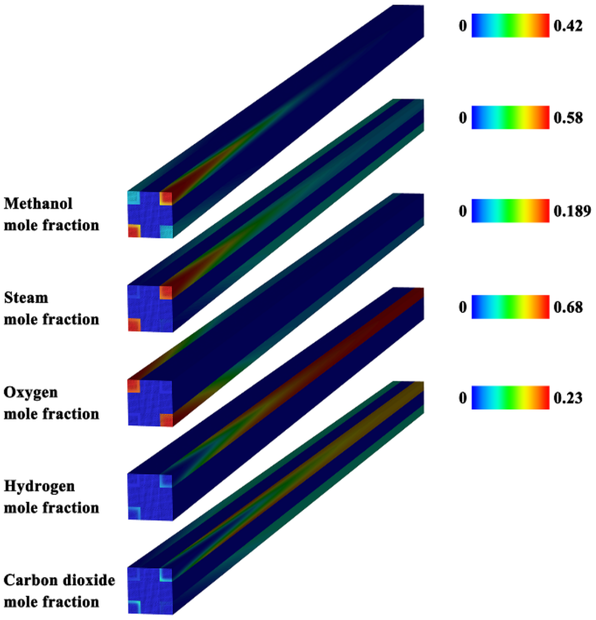

Figure 8. Species mole fraction contour maps in the microchannel reactor when the reactor walls are constructed of stainless steel.

3.2. Effect of solid thermal conductivity

The effect of solid thermal conductivity is studied in order to fully describe the thermal energy change in the reactor. The temperature contour maps in the microchannel reactor are illustrated in Figure 9 with different solid thermal conductivity. The solid thermal conductivity is 0.02, 0.2, 2, 20, and 200 W/(m·K), respectively. The reactor walls are constructed of stainless steel. The temperature in the reactor is thermal conductivity-dependent. The heat effect accompanying the change in solid thermal conductivity is manifested by decreases or increases in reactor temperature. Appropriate values of solid thermal conductivity are necessary for the design of the autothermal microchannel reactor for use in the steam-methanol reforming process. Since heat does flow from the oxidation region to the reforming region, the reactor temperature depends up not only the solid thermal conductivity but also the amount of heat evolved in the oxidation and reforming processes. The reforming region absorbs heat with an increase in temperature, and the oxidation region generates heat with also an increase in temperature. An exact relationship exists between the amounts of heat absorbed and generated and the amount of heat required to raise the temperatures of both the oxidation and reforming regions. The wall heat conduction effect accompanying temperature changes is important to the autothermal design and self-sustaining operation of the reactor. The total energy of the reactor system is constant. The amount of heat involved in the processes can be calculated at constant pressure based on the principles of thermodynamics, since the amount of heat involved in the oxidation and reforming processes depends partly upon pressure. All the heat flowing into the reforming channels raises the temperature of the gas mixture so that the reactants can be converted to the desired product hydrogen. At low solid thermal conductivity, the difference in temperature between the oxidation and reforming regions is very large, which leads to steep temperature gradients. At high solid thermal conductivity, the difference in temperature between the oxidation and reforming regions is very small, accompanied by very small temperature gradients. The solid thermal conductivity is of great importance in determining the operation and efficiency of the reactor. The reaction proceeds rapidly and efficiently only at high solid thermal conductivity. In this case, the solid thermal conductivity greatly contributes to transport of energy between the oxidation and reforming regions. Conditions must be such that the walls are highly conductive solids.

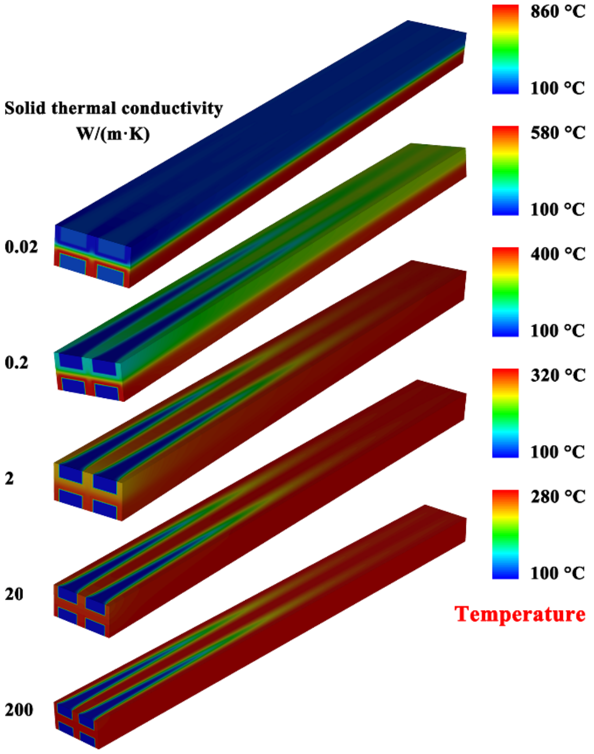

Figure 9. Temperature contour maps in the microchannel reactor with different solid thermal conductivity. The reactor walls are constructed of stainless steel.

The effect of solid thermal conductivity on the hydrogen yield of the microchannel reactor is illustrated in Figure 10 at different inlet gas velocities. The solid thermal conductivity is 0. 2, 0.6, 2, 6, 20, and 60 W/(m·K), respectively. At the channel inlets, the gas velocity is 0.6 and 2.0 m/s or 0.6 and 3.0 m/s for the oxidation and reforming reactant streams. The hydrogen yield generally increases with solid thermal conductivity, and the reactions must therefore be carried out in the reactor with high solid thermal conductivity, at which methanol reacts so rapidly steam that the conversion is nearly complete. At high flow rates for the reforming reactant stream, the conversion is incomplete due to the excess absorption of thermal energy in the reforming region, since heat must be balanced in the reactor. Accordingly, the hydrogen yield is relatively low, especially at low solid thermal conductivity. Stainless steel is cost effective and has relatively high thermal conductivity. When the reactor walls are constructed of stainless steel, nearly complete conversion can be achieved in the reactor.

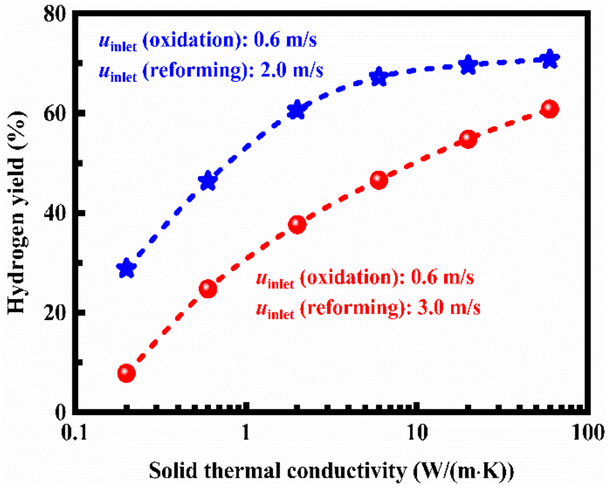

Figure 10. Effect of solid thermal conductivity on the hydrogen yield of the microchannel reactor at different inlet gas velocities.

3.3. Reaction heat fluxes

The effect of gas velocity on the thermal behavior of the reactor is evaluated based upon reaction heat flux in order to understand the evolution of heat in the system. The effect of the gas velocity at the channel inlets on the heat fluxes of the oxidation and reforming reactions is illustrated in Figure 11 for the reactor. The reaction heat flux for oxidation and reforming is positive and negative, respectively. The reaction heat flux for oxidation is positive, since the heat released by the oxidation reaction flows out of its region.

The reaction heat flux for reforming is negative, since the heat consumed by the reforming reaction flows into its region. The reaction heat flux in magnitude increases with the gas velocity when heat is balanced in the reactor. The positive heat flux is larger in magnitude than the negative heat flux, and therefore the net reaction heat flux is positive. There is a mathematical relation between heat flux and temperature gradient, depending upon the solid thermal conductivity. The total heat flux across the walls is proportional to the gradient of temperature within the walls.

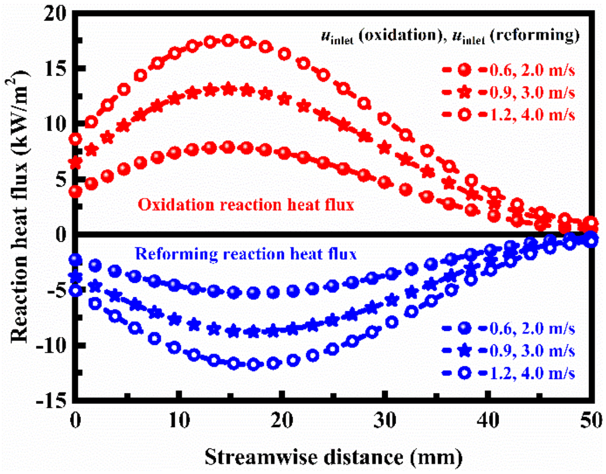

Figure 11. Effect of the gas velocity at the channel inlets on the heat fluxes of the oxidation and reforming reactions in the reactor.

The effect of flow arrangement on the heat fluxes of the oxidation and reforming reactions is illustrated in Figure 12 for the reactor. The heat flux results are presented for the parallel flow design and for the counter-current design. Several factors influence the operation of an autothermal reactor.[57,58] The factor considered here is the flow arrangement.

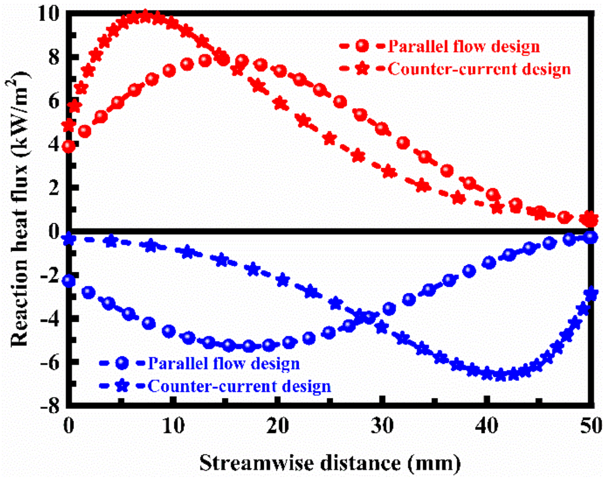

Figure 12. Effect of flow arrangement on the heat fluxes of the oxidation and reforming reactions in the reactor. The heat flux results are presented for the parallel flow design and for the counter-current design.

4. CONCLUSIONS

Numerical simulations are carried out to understand the thermal transport characteristics of autothermal reactors for hydrogen production. Enthalpy analysis is performed and the evolution of energy in the chemical processes is discussed based upon heat flux. The effects of solid thermal conductivity, gas velocity, and flow arrangement on the thermal behavior of the reactor is evaluated in order to fully describe the thermal energy change in the reactor. The major conclusions are summarized as follows:

- Oxidation differs from reforming in enthalpy change, depending upon the solid thermal conductivity. The change in enthalpy is of particular importance in exothermic and endothermic reactions.
- The net enthalpy change for oxidation and reforming is negative and positive, respectively. The thermal behavior of the reactor depends upon the thermal properties of the walls. The net enthalpy change is thermal conductivity-dependent.
- The net sensible enthalpy change is always positive in the reactor, but depending upon the solid thermal conductivity and the chemical reaction.
- The reactor temperature is also thermal conductivity-dependent. The wall heat conduction effect accompanying temperature changes is important to the autothermal design and self-sustaining operation of the reactor.
- The solid thermal conductivity is of great importance in determining the operation and efficiency of the reactor. The reaction proceeds rapidly and efficiently only at high solid thermal conductivity.
- The reaction heat flux for oxidation and reforming is positive and negative, respectively. The positive heat flux is larger in magnitude than the negative heat flux, and the net reaction heat flux is positive.
- The change in flow arrangement significantly affects the reaction heat flux in the reactor. The parallel flow design is advantageous for purposes of enhancing heat transfer and avoiding localized hot spots.

Conflict of interests

I declares that there is no a conflict of interest with any person, institute, company, etc.

REFERENCES

1. Ming, Q.; Healey, T.; Allen, L.; Irving, P. *Catal. Today* 77(1-2), 2002, 51-64.

2. Rostrup-Nielsen, J.R. *Catal. Today* 145(1-2), 2009, 72-75.

3. Dincer, I. *Int. J. Hydrogen Energy* 37(2), 2012, 1954-1971.

DOI: http://dx.doi.org/10.32571/ijct.1060520 **E-ISSN: 2602-277X**

4. Muradov N.Z.; Veziroğlu, T.N. *Int. J. Hydrogen Energy* 30(3), 2005, 225-237.

5. Tacchino, V.; Costamagna, P.; Rosellini, S.; Mantelli, V.; Servida, A. *Chem. Eng. J.* 428, 2022, 131492.

6. Tutar, M.; Üstün, C.E.; Campillo-Robles, J.M.; Fuente, R.; Cibrián, S.; Arzua, I.; Fernández, A.; López, G.A. *Comput. Chem. Eng.* 155, 2021, 107504.

7. Wang, J.; Wei, S.; Wang, Q.; Sundén, B. *Int. J. Hydrogen Energy* 46(29), 2021, 15241-15256.

8. Taji, M.; Farsi, M.; Keshavarz, P. *Int. J. Hydrogen Energy* 43(29), 2018, 13110-13121.

9. Fadzillah, D.M.; Kamarudin, S.K.; Zainoodin, M.A.; Masdar, M.S. *Int. J. Hydrogen Energy* 44(5), 2019, 3031-3054.

10. Wang, Y.; Diaz, D.F.R.; Chen, K.S.; Wang, Z.; Adroher, X.C. *Mater. Today* 32, 2020, 178-203.
11. Zhang, X.; Jin, Y.; Li, D.; Xiong, Y. *J. Power Sources* 506, 2021, 230135.

12. Alias, M.S.; Kamarudin, S.K.; Zainoodin, A.M.; Masdar, M.S. *Int. J. Hydrogen Energy* 45(38), 2020, 19620-19641.

13. Luo, M; Zhang, J.; Zhang, C.; Chin, C.S.; Ran, H.; Fan, M.; Du, K.; Shuai, Q. *Appl. Therm. Eng.* 201, 2022, 117816.

14. Wei, X.; Leng, J.; Sun, C.; Huo, W.; Ren, Q.; Sun, F. *J. Power Sources* 518, 2022, 230598.

15. Rakib, M.A.; Grace, J.R.; Lim, C.J.; Elnashaie, S.S.E.H. *J. Power Sources* 195(17), 2010, 5749-5760.

16. Abashar, M.E.E. *Int. J. Hydrogen Energy* 38(2), 2013, 861-869.

17. Park, S.; Yoo, J.; Han, S.J.; Song, J.H.; Lee, E.J.; Song, I.K. *Int. J. Hydrogen Energy* 42(22), 2017, 15096-15106.

18. Bang, Y.; Han, S.J.; Seo, J.G.; Youn, M.H.; Song, J.H.; Song, I.K. *Int. J. Hydrogen Energy* 37(23), 2012, 17967-17977.

19. Wang, Y.; Sun, K.; Zhang, S.; Xu, L.; Hu, G.; Hu, X. *J. Energy Inst.* 98, 2021, 85-97.

20. Li, Y.; Zhang, L.; Zhang, Z.; Liu, Q.; Zhang, S.; Liu, Q.; Hu, G.; Wang, Y.; Hu, X. *Appl. Catal., A* 584, 2019, 117162.
21. Guo, Y.; Li, H.; Kameyama, H. *Chem. Eng. Sci.* 66(23), 2011, 6287-6296.

22. Chick, L.A.; Marina, O.A.; Coyle, C.A.; Thomsen, E.C. *J. Power Sources* 236, 2013, 341-349.

23. Belzunce, P.S.; Cadús, L.E.; Rodríguez, M.L. *Chem. Eng. Process.* 164, 2021, 108383.

24. Zanfir, M.; Gavriilidis, A. *Chem. Eng. Sci.* 56(8), 2001, 2671-2683.

25. Fukuhara, C.; Igarashi, A. *Chem. Eng. Sci.* 60(24), 2005, 6824-6834.

26. Kawamura, Y.; Ogura, N.; Yamamoto, T.; Igarashi, A. *Chem. Eng. Sci.* 61(4), 2006, 1092-1101.

27. Ioannides, T.; Verykios, X.E. *Catal. Today* 46(2-3), 1998, 71-81.

28. Piga, A.; Verykios, X.E. *Catal. Today* 60(1-2), 2000, 63-71.
29. Zanfir, M.; Gavriilidis, A. *Chem. Eng. Sci.* 57(9), 2002, 1653-1659.

30. Zanfir, M.; Gavriilidis, A. *Chem. Eng. J.* 86(3), 2002, 277-286.

31. Lakhete, P.; Janardhanan, V.M. *Chem. Eng. Sci.* 110, 2014, 13-19.

32. Janardhanan, V.M.; Appari, S.; Jayanti, S.; Deutschmann, O. *Chem. Eng. Sci.* 66(3), 2011, 490-498.

33. Brown, R.C. *Joule*, 4(11), 2020, 2268-2289.

34. Tonkovich, A.Y.; Perry, S.; Wang, Y.; Qiu, D.; LaPlante, T.; Rogers, W.A. *Chem. Eng. Sci.* 59(22-23), 2004, 4819-4824.

35. Roychowdhury, S.; Sundararajan, T.; Das, S.K. *Int. J. Heat Mass Transfer* 139, 2019, 660-674.

36. Tonkovich, A.L.Y.; Yang, B.; Perry, S.T.; Fitzgerald, S.P.; Wang, Y. *Catal. Today* 120(1), 2007, 21-29.

37. Tonkovich, A.; Kuhlmann, D.; Rogers, A.; McDaniel, J.; Fitzgerald, S.; Arora, R.; Yuschak, T. *Chem. Eng. Res. Des.* 83(6), 2005, 634-639.

38. Gavriilidis, A.; Angeli, P.; Cao, E.; Yeong, K.K.; Wan, Y.S.S. *Chem. Eng. Res. Des.* 80(1), 2002, 3-30.
39. Mettler, M.S.; Stefanidis, G.D.; Vlachos, D.G. *Chem. Eng. Sci.* 66(6), 2011, 1051-1059.

40. Cao, C.; Zhang, N.; Dang, D.; Cheng, Y. *Fuel Process. Technol.* 167, 2017, 78-91.

41. Lerou, J.J.; Tonkovich, A.L.; Silva, L.; Perry, S.; McDaniel, J. *Chem. Eng. Sci.* 65(1), 2010, 380-385.

42. Murphy, D.M.; Manerbino, A.; Parker, M.; Blasi, J.; Kee, R.J.; Sullivan, N.P. *Int. J. Hydrogen Energy* 38(21), 2013, 8741-8750.

43. Baldea, M.; Daoutidis, P. *Chem. Eng. Sci.* 62(12), 2007, 3218-3230.

44. Zanfir, M.; Gavriilidis, A. *Chem. Eng. Res. Des.* 82(2), 2004, 252-258.

45. Kolios, G.; Frauhammer, J.; Eigenberger, G. *Chem. Eng. Sci.* 55(24), 2000, 5945-5967.

46. Tiemersma, T.P.; Kolkman, T.; Kuipers, J.A.M.; Annaland, M.V.S. *Chem. Eng. J.* 203, 2012, 223-230.

47. Herdem, M.S.; Mundhwa, M.; Farhad, S.; Hamdullahpur, F. *Energy Convers. Manage.* 180, 2019, 149-161.

48. Engelbrecht, N.; Everson, R.C.; Bessarabov, D.; Kolb, G. *Chem. Eng. Process.* 157, 2020, 108164.

49. Reitz, T.L.; Ahmed, S.; Krumpelt, M.; Kumar, R.; Kung, H.H. *J. Mol. Catal. A: Chem.* 162(1-2), 2000, 275-285.

50. Peppley, B.A.; Amphlett, J.C.; Kearns, L.M.; Mann, R.F. *Appl. Catal., A* 179(1-2), 1999, 31-49.

51. Park, G.G.; Seo, D.J.; Park, S.H.; Yoon, Y.G.; Kim, C.S.; Yoon, W.L. *Chem. Eng. J.* 101(1-3), 2004, 87-92.

52. Park, G.G.; Yim, S.D.; Yoon, Y.G.; Kim, C.S.; Seo, D.J.; Eguchi, K. *Catal. Today* 110(1-2), 2005, 108-113.

53. Chu, X.; Zeng, X.; Zheng, T.; Zhuang, W.; Yang, Y.; Zhou, W.; Hong, Y. *Int. J. Hydrogen Energy* 45(41), 2020, 20859-20874.

54. Lu, W.; Zhang, R.; Toan, S.; Xu, R.; Zhou, F.; Sun, Z.; Sun, Z. *Chem. Eng. J.* 429, 2022, 132286.

55. Stefanidis, G.D.; Vlachos, D.G.; Kaisare, N.S.; Maestri, M. *AIChE J.* 55(1), 2009, 180-191.

56. Stefanidis, G.D.; Vlachos, D.G. *Chem. Eng. Technol.* 31(8), 2008, 1201-1209.

57. Zanfir, M.; Gavriilidis, A. *Chem. Eng. Sci.* 58(17), 2003, 3947-3960.

58. Cao, C.; Dang, D.; Li, Y.; Xu, J.; Cheng, Y. *Chem. Eng. Process.* 132, 2018, 218-228.

DOI: http://dx.doi.org/10.32571/ijct.1279701 **E-ISSN: 2602-277X**

International Journal of Chemistry and Technology

http://dergipark.org.tr/ijct

Research Article

Isotherm and kinetic modeling of the adsorption of methylene blue, a cationic dye, on pumice

Kübra GÜNEŞ[1*]

[1]*Department of Chemistry, K. K. Education Faculty, Ataturk University, 25240 Erzurum, Türkiye*

Received: 10 April 2023; Revised: 22 June 2023; Accepted: 26 June 2023

*Corresponding author e-mail: kgunes@atauni.edu.tr

Citation: Güneş, K. *Int. J. Chem. Technol.* **2023**, 7(1), 67-74.

ABSTRACT

The removal of dyes from aqueous solution with cheap and abundant adsorbents is becoming increasingly important for the solution of a serious environmental problem such as wastewater treatment. In this study, isotherm and kinetic modeling of the adsorption of methylene blue on pumice, a porous and glassy volcanic rock resistant to physical and chemical factors, was aimed. For this, the compatibility of the experimental data with the isotherm and kinetic models was examined, and information about the efficiency, effectiveness and rate of adsorption was tried to be obtained. Experimental data have been applied to isotherm models such as Langmuir, Freundlich, Temkin, Brenuer-Emmet-Teller (BET), Dubinin- Radushkevich, and Harkins-Jura, and kinetic models such as pseudo-first order, pseudo-second order, and intraparticle diffusion. While the order of fit for the isotherm models was determined as Freundlich > Harkins-Jura > Dubinin- Radushkevich based on the results of the regression analysis, the highest fit was obtained with the Freundlich equation (R^2:0.993). Thus, the adsorption intensity (n) of methylene blue on pumice was calculated as 1.14 and the adsorption capacity (k) of pumice was calculated as 6.43. On the other hand, the order of fit of the experimental data to the kinetic models was determined as pseudo-second order > pseudo-first order > intra particle diffusion according to the regression coefficients. However, the highest consistency among the kinetic models was obtained with the pseudo-second order kinetic model(R^2:1.000).

Keywords: Adsorption, pumice, methylene blue, ısotherm models, adsorption kinetics.

Katyonik bir boya olarak, metilen mavisinin pomza üzerine adsorpsiyonunun izoterm ve kinetik modellemesi

ÖZ

Boyaların sulu çözeltiden ucuz ve bol bulunan adsorbentlerle giderimi, atık su arıtımı gibi ciddi bir çevre sorununun çözümü için giderek önem kazanmaktadır. Bu çalışmada metilen mavisinin fiziksel ve kimyasal etkenlere dayanıklı, gözenekli ve camsı bir volkanik kayaç olan pomza üzerine adsorpsiyonunun izoterm ve kinetik modellemesi amaçlanmıştır. Bunun için deneysel verilerin izoterm ve kinetik modellere uyumu incelenerek, adsorpsiyon verimi, etkinliği ve hızı hakkında bilgiler edinilmeye çalışmıştır. Deneysel veriler, Langmuir, Freundlich, Temkin, Brenuer- Emmet-Teller (BET), Dubinin- Radushkevich ve Harkins-Jura gibi izoterm modellerine ait denklemlere ve yalancı birinci derece, yalancı ikinci derece ve parçacık içi difüzyon gibi hız denklemlerine uygulanmış hem izoterm hem de kinetik modellere ait parametreler hesaplanmıştır. İzoterm modellerine uyum sırası, regresyon analiz sonuçları esas alınarak, Freundlich>Harkins-Jura > Dubinin- Radushkevich şeklinde belirlenmiş olmakla birlikte, en yüksek uyum, Freundlich denklemiyle elde edilmiştir(R^2:0,993). Böylece Metilen mavisinin pomza üzerindeki adsorpsiyon şiddeti (n), 1,14 ve pomzanın adsorpsiyon kapasitesi (k) ise 6,43 olarak hesaplanmıştır. Diğer yandan deneysel verilerin kinetik modellere uyum sıralaması da yine regresyon katsayılarına göre yalancı ikinci derece>yalancı birinci derece> parçacık içi difüzyon olarak belirlenmiştir. Ancak kinetik modeller arasında en yüksek uyum yalancı ikinci mertebe kinetik modelle elde edilmiştir(R^2:1,000).

Anahtar Kelimeler: Adsorpsiyon, pomza, metilen mavisi, izoterm modelleri, adsorpsiyon kinetiği.

DOI: http://dx.doi.org/10.32571/ijct.1279701 **E-ISSN: 2602-277X**

1.INTRODUCTION

Industrial wastewater is one of the most significant environmental pollutants, and textile production, which is a major industry in every nation, is a major source of colored wastewater due to the usage of dyes.[1-3] However, colored wastewater is produced not only by the textile industry, but also by various industries such as paint, cosmetics, medicine, leather, food, health, and paper.[4] Moreover, colored wastewaters not only change the color of water bodies in terms of aesthetics, but also affect photosynthesis and the aquatic ecosystem by preventing light transmission, and may cause the extinction of many aquatic organisms.[5] Methylene blue (MB) is extensively used in many areas such as paper dyeing, temporary hair dye, cotton, and wool dyeing, and the environmental impact of its discharge can cause health problems such as eye burns and permanent eye injuries in humans and animals.[6,7] It has also been reported to cause vomiting, drowsiness, cyanosis, jaundice, tissue necrosis, increased heart rate, shock, and tetraplegia in humans.[7,8] For this reason, it is extremely critical to remove methylene blue and similar dyestuffs from domestic and industrial wastewater, primarily due to health and other environmental reasons.[9] Complete removal of methylene blue is difficult because it has a stable aromatic structure that consists of chromophores and polar groups, and so many methods have been proposed for effective removal up to date.[10] Adsorption[11-16], flocculation[17], membrane filtration[18], electrolysis, biological processes, oxidation[19,20], precipitation, reverse osmosis[21], and photocatalytic degradation[22] have been used to remove dyes from industrial wastewater. Adsorption, however, has been found to be superior to other strategies in terms of initial cost, ease of design, and efficiency.[23-25] Various adsorbents such as perlite[26,27], bentonite[28], silica gel[29], fly ash[30], lignite[30], peat[31], silica[32], metal ions, and organic substances from aqueous solutions for the removal of dyes have been widely used. Pumice, which is a volcanic rock with low density and porous structure, which is found in many parts of the world and does not require calcination, which is a high-energy pre-stage, has a high specific surface area due to its microporous structure and has a great potential for usage as an adsorbent.[5] Today, natural pumice is gaining popularity with its porous structure and large surface area for the removal of pollutants from wastewater. Since most of the internal pores of pumice, especially the micro and meso pores are not connected to each other, it may exhibit low permeability, and the fact that it is a relatively hard material due to its silica content makes it a potential adsorbent. [33-35]

Although there are many studies on the adsorption of a cationic dye such as methylene blue from an aqueous solution onto many other natural materials, those related to the use of pumice are extremely limited. Therefore, this study aims to analyze the isotherm and kinetic modeling of the adsorption of methylene blue onto pumice as a representative cationic dye sample as well as to elucidate its adsorption mechanism.

2. MATERIALS AND METHODS

In this study, granulated pumice from BlokBims Co., Çankırı, Turkey was used as an adsorbent and its chemical composition is given in Table 1.

Table 1. Chemical composition of pumice (wt%).

Component	%	Component	%
SiO_2	73.35	TiO_2	0.08
Al_2O_3	12.88	MnO	0.05
CaO	0.77	Cr_2O_3	0.01
MgO	0.08	SrO	0.01
Fe_2O_3	1.10	SO_3	0.44
K_2O	4.40	P_2O_5	0.01
Na_2O	3.82	LOI*	3.88

For use in adsorption experiments, granulated pumice was dried, ground and then sieved using sieves in keeping with ASTM standard, and finally 180-250 µm size fraction was taken and stored. The chemical structure and properties of methylene blue, a cationic dye selected as an adsorbate, are given in Table 2. Cationic dye, methylene blue, analytical purity, and purchased from Merck Co.

Table 2. Chemical structure and properties of methylene blue.

Chemical structure	Chemical formula	CI	λ_{max} (nm	MW (g/mol)
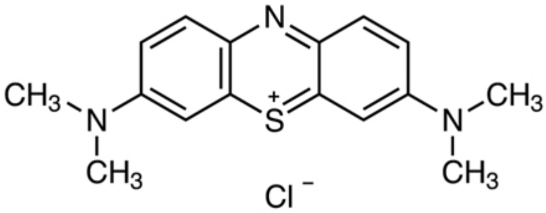	$C_{16}H_{18}N_3SCl$	52015	666	319.85

DOI: http://dx.doi.org/10.32571/ijct.1279701 **E-ISSN: 2602-277X**

2.1. Adsorption experiments

For the adsorption experiments, methylene blue stock solution at 500 mg/L was prepared and diluted to the desired concentrations. Dye solutions prepared at various concentrations (10-80 mg/L) were taken into 100 mL round bottom flasks and 0.2 g pumice was added to them at a solid/liquid ratio of 0.2 g/100 mL. Afterwards, the balloons placed in the thermostatic shaker were mixed at room temperature (25°C), 150 rpm stirring speed and natural pH (pH:8.0) for different times. The samples taken from the suspensions were centrifuged at 500 rpm for five minutes at the end of the adsorption period in order to separate the phases from one another. The equilibrium concentration (C_e) of methylene blue in the aqueous phase was identified by UV spectrophotometer (Shimadzu 1201 UV-Vis) at 666 nm, the wavelength at which the dye solution gives maximum absorbance.

Equation (1) was used for the calculation of the amount of dye adsorbed (mg/g) by pumice after adsorption.

$$q = \frac{(C_0 - C_e)V}{m} \quad (1)$$

where C_o and C_e are the initial and equilibrium dye concentrations (mg/L), V is the total volume (L), and m is the mass of pumice (g).

3. RESULTS AND DISCUSSION

3.1. Adsorption isotherms

Equilibrium adsorption isotherms can provide very critical information about adsorption efficiency, effectiveness, adsorbent capacity and orientation of adsorbate at the interface, and therefore isotherm analysis results are widely used in the design of adsorption systems. The experimental isotherm drawn using the data obtained in this study is shown in Figure 1.

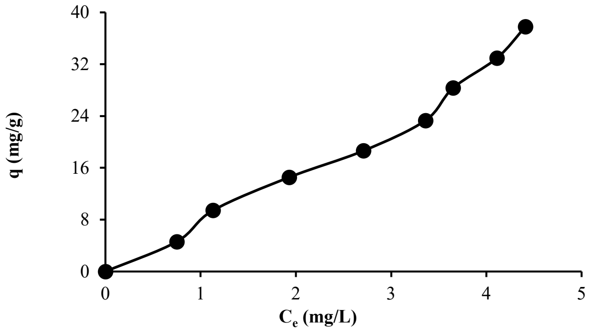

Figure 1. Experimental adsorption isotherm for the adsorption of methylene blue at the pumice aqueous solution interface at 25°C.

It can be detected from Figure 1 that the variation of adsorption with equilibrium dye concentration exhibits high adsorption efficiency at low equilibrium dye concentrations, partially low at medium equilibrium dye concentrations, and quite high at high equilibrium dye concentrations. This behaviour can be explained by the predominance of different adsorption mechanisms. Accordingly, it can be said that adsorption occurs with ion exchange at low equilibrium dye concentrations, ion pairing at medium equilibrium dye concentrations, and pi-pi stacking interactions at high equilibrium dye concentrations.

For modelling experimental equilibrium adsorption data, the data were applied to isotherm models such as Freundlich, Langmuir, Dubinin-Raduskhevic (D-R), BET, Harkins-Jura and Temkin. Mathematical equations of these models and Freundlich's empirical equation are given in Table 3 along with the calculated isotherm parameters and regression coefficients.

Although the adsorption isotherm model of Langmuir is generally suitable in order to describe chemical adsorption, it can be easily extended to explain the behaviour of adsorption systems where physical adsorption occurs through relatively strong interactions. The Langmuir model is based on the assumption that monolayer coating, no lateral interaction between adsorbed species, and that the surface is homogeneous in both energy and morphology.[36]

The Freundlich isotherm is an experimental equation that takes into account that adsorption can be multi layered and that the adsorbent surface can also be heterogeneous both morphologically and energetically.

According to the Temkin isotherm model, heats of adsorption linearly decrease with increasing adsorbent surface coverage up to their maximal binding energies for adsorption, and is characterized by a regular distribution of binding energies.

The Dubinin-Radushkevich isotherm (D-R isotherm) model is often used to estimate adsorption energies, especially in porous adsorbents, taking into account the characteristic porosity of the adsorbent and a heterogeneous surface.

As can be seen from Table 3, the highest fit of the experimental information received from methylene blue's adsorption on pumice at 25°C was obtained with the Freundlich equation. The coefficients related to the calculated adsorbent capacity (k) and adsorbent intensity (n) show that pumice is an effective adsorbent.

In the study of Koochakzadeh et al., the adsorption of crystal violet, a cationic dye, on pumice stone investigated and it was found to be compatible with the Freundlich isotherm. Furthermore, the coefficients related to the adsorbent capacity (k) and adsorbent density (n) were found to be 6.86 and 3.24, respectively.

It was reported in the study of Akbal (2005), the adsorption experiments indicated that pumice powder was effective in removing basic dyes such as methylene blue and crystal violet from aqueous solution and compatible with the Freundlich isotherm.

Table 3. Linear equations, related parameters and regression coefficients of the investigated adsorption isotherm models for the adsorption of methylene blue on pumice at 25°C.

Isotherm model	Equation	Parameters and R^2	
Langmuir	$\frac{C_e}{q_e} = \frac{1}{q_m.K} + \frac{C_e}{q_m}$	q_m	-188.68
		K	-0.0356
		R^2	0.235
Freundlich	$lnq_e = lnk + nlnC_e$	n	1.139
		k	6.425
		R^2	0.993
Temkin	$q_e = \frac{RT}{b_T} lna_T + \frac{RT}{b_T} lnC_e$	b_T	0.448
		a_T	1.523
		R^2	0.887
BET	$\frac{C_e}{q(1-C_e)} = \frac{1}{q_m k} + \frac{(k-1)C_e}{q_m k}$	q_m	5.178
		k	0.855
		R^2	0.006
Dubinin- Radushkevich	$lnq_e = lnQ_{DR} - K\varepsilon^2$ $\varepsilon = RTln\left[1 + \frac{1}{C_e}\right]$	K	$4.23x10^{-7}$
		Q_{DR}	28.47
		R^2	0.931
Harkins-Jura	$\frac{1}{q_e^2} = \frac{B}{A} - \left(\frac{1}{A}\right) logC_e$	B	0.642
		A	57.80
		R^2	0.960

3.2. Adsorption kinetics

Information about the rate and mechanism of adsorption can be obtained by examining the adsorption kinetics. For this reason, in this study, for different initial dye concentrations, the variation of the amount of adsorbed dye with the adsorption period was examined, and the findings are given in Figure 2.

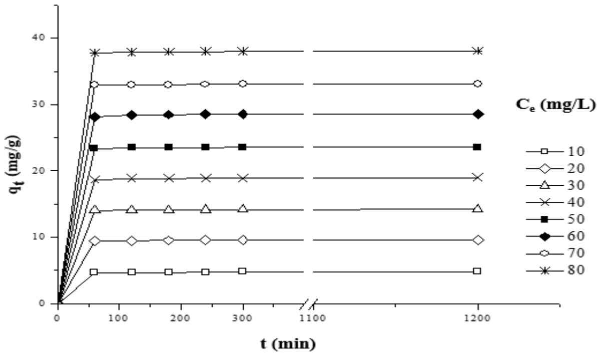

Figure 2. Variation of adsorbed dye amount with adsorption time for different initial concentrations (25°C).

Generally, two different mechanisms are proposed for adsorption on the solid surface, namely fast binding of the adsorbate on the adsorbent surface and relatively slow intraparticle diffusion.

The mathematical equation of the pseudo-first-order kinetic model by Lagergren is as follows:

$$\ln(q_e - q_t) = \ln q_e - k_1 t$$

In this formula, q_t is the quantity of substance adsorbed per gram of adsorbent at any given time t, q_e is the amount of substance adsorbed per gram of adsorbent at equilibrium (mg/g), k_1 is the rate constant (min^{-1}), and t is the adsorption time. The rate constant k_1 is calculated from the slope of the graph of ln (q_e-q_t) against t, and the theoretical q $_e$ value is calculated from the shift of the curve.[39]

The pseudo-second-order kinetic model equation is as follows:

$$\frac{t}{q_t} = \frac{1}{k_2 q_e^2} + \frac{1}{q_e} t \qquad (3)$$

where, q_t is the amount of substance adsorbed per gram of adsorbent at any time t (mg/g), q_e is the amount of substance adsorbed per gram of adsorbent at equilibrium (mg/g), k_2 is the rate constant (g/mg. min). The rate constant k_2 and theoretical q_e values are calculated from the slope and slip point of the graph of t/q_t against t.[40]
The intra-particle diffusion can be explained in three steps.[41]

DOI: http://dx.doi.org/10.32571/ijct.1279701 **E-ISSN: 2602-277X**

(i) Transport of adsorbate by particle diffusion from the bulk solution to the outer surface or film layer of the adsorbent.

(ii) Transport of the adsorbate from the adsorbent surface to the pores is known as internal diffusion.

(iii) Adsorption on pore surfaces.

The slowest rate-limiting step determines the average adsorption rate. In adsorption systems where intra particle diffusion is the rate limiting phase, the Weber and Morris intra particle diffusion approach is used and the rate constants for intra particle diffusion (k_i) are obtained using the following equation.[42-44]

$$q_t = k_i t^{1/2} + c \tag{4}$$

where k_i and c are the intraparticle diffusion rate constant (mg/gmin$^{1/2}$) and a constant, respectively, and k_i is the slope of the linear portions of the plot of q_t versus $t^{1/2}$.

The kinetic curves plotted at different concentrations at 25°C, considering three different kinetic models, are given in Figure 3, Figure 4, Figure 5 and the calculated model coefficients, together with the regression coefficients, are shown in Table 4.

Table 4 shows that the pseudo-second-order model has highest fit for the experimental adsorption data of methylene blue by pumice. Accordingly, it can be asserted that the dye and the active groups on the pumice surface interacted quite effectively.

For methylene blue adsorption on pumice, Sharafi et al. and Soltanian et al. reported that the kinetic data showed a high fit to the pseudo-second-order kinetic model. In addition, Table 5 provides a concise comparison of results from this study with results from other studies.

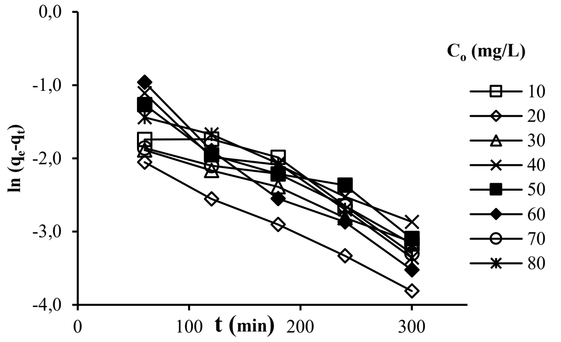

Figure 3. Pseudo-first order kinetic plots for the adsorption of pumice on dye at 25^{0}C.

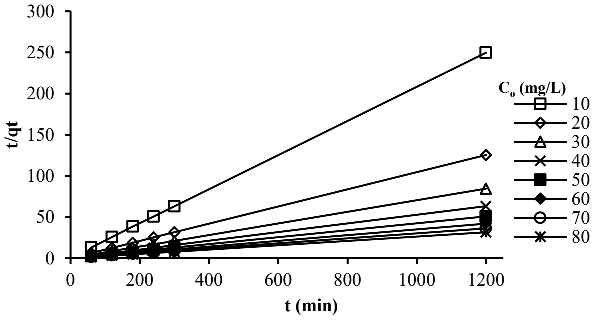

Figure 4. Pseudo-second-order kinetic plots for the adsorption of pumice on dye at 25^{0}C.

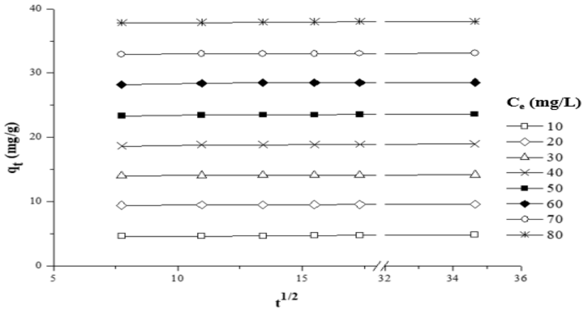

Figure 5. The intraparticle diffusion model plots for the dsorption of pumice on the dye at 25^{0}C.

Table 4. Kinetic parameters and regression coefficients obtained from the application of data on the adsorption of cationic dye on pumice to kinetic models (25^{0}C).

C_i	Pseudo-first order		Pseudo-second-order				Intraparticle diffusion		
mg L^{-1}	k_1 min^{-1} (10^{-3})	R^2	k_2 gmg^{-1}min^{-1}	$q_{e,exp}$ mg g^{-1}	$q_{e,cal}$ mg g^{-1}	R^2	k_i mg min$^{-1/2}$ g^{-1}	C	R^2
10	6.27	0.890	0.0431	5.18	4.81	1.000	0.0013	4.594	0.779
20	7.16	0.997	0.0109	10.43	9.57	1.000	0.0009	9.437	0.993
30	5.27	0.989	0.0050	15.80	14.20	1.000	0.0011	14.023	0.917
40	6.76	0.934	0.0028	21.02	18.98	1.000	0.0023	18.652	0.967
50	6.79	0.943	0.0018	26.36	23.64	1.000	0.0020	23.330	0.980
60	10.16	0.973	0.0012	31.43	28.57	1.000	0.0028	28.209	0.958
70	5.72	0.915	0.0005	26.56	43.44	1.000	0.0011	32.922	0.868
80	8.10	0.964	0.0007	41.98	38.02	1.000	0.0018	37.777	0.938

DOI: http://dx.doi.org/10.32571/ijct.1279701 E-ISSN: 2602-277X

Table 5. Comparison of the results obtained from this study with those obtained from other studies.

Adsorbent	Adsorbate	q_{max}(mg/g)	Reference
Chitosan/Fe_3O_4	Methylene Blue	149.20	[46]
Chitosan/ Fe_3O_4/GO	Methylene Blue	180.83	[47]
Modified pumice stone	Methylene Blue	15.87	[5]
Agar/κ-carrageenan	Methylene Blue	242.30	[48]
Modified pumice	Congo Red	23.32	[49]
$CaCO_3$/chitin aerogel	Methylene Blue	266.40	[50]
Activated carbon		53.00	
Fe3O4/bentonite	Methylene Blue	181.82	[51]
Pumice powder	Remazol Red RB	38.90	[52]
Raw pumice	Remazol Black B	5.26	[35]
Pumice	Methylene Blue	2.80	[53]
Pumice-nZVI		4.27	
Mesoporous silica	Methylene Blue	5.58	[54]
Zeolite	Methylene Blue	3.79	[55]
Pumice	Methylene Blue	37.79	**This study**

4. CONCLUSION

The results obtained in this research, in which the adsorption of methylene blue, a cationic dyestuff, on pumice was investigated, are as follows:

- An hour is sufficient to reach the adsorption equilibrium and this is a very short time.

- It was observed that the isotherms reflecting the relationship between the equilibrium dye concentration and the amount of dye adsorbed at constant temperature were partially similar to the Type IV isotherm, that is, methylene blue was adsorbed on pumice in a multilayered manner.

- Although the shape similarity to the Type IV isotherm was observed, the experimental data were found to be strongly in accord with the Freundlich isotherm model.

- It was determined that the experimental data showed a high fit to the pseudo-second-order kinetic model and it was concluded that the interactions between the dye and the active groups were quite effective.

Conflict of interest

I hereby certify that I have no financial or other relationships with any institution, business, or individual.

REFERENCES

1. Sapci, Z.; Ustun, B. *Elec. J. Env. Agricult. Food Chem.* **2003**, *2*(2), 286-290.

2. Samarghandi, M. R.; Zarrabi, M.; Amrane, A.; Safari, G. H.; Bashiri, S. *Iran. J. Environ. Health Sci. Eng.* **2012**, *9*(1), 1-10.

3. Ahmad, A.; Banat, F.; Alsafar, H.; Hasan, S. W. *Sci. Total Environ.* **2022**, *806*, 150585.

4. Okoro, H. K.; Pandey, S.; Ogunkunle, C. O.; Ngila, C. J.; Zvinowanda, C.; Jimoh, I., Lawal, I. A.;

5. Orosun, M. M.; Adeniyi, A. G. *Emerg. Contam.* **2022**, *8*, 46-58.

6. Derakhshan, Z.; Baghapour, M. A.; Ranjbar, M.; Faramarzian, M. *Health. Scope.* **2013**, *2*(3), 136-144.

7. Kasbaji, M.; Mennani, M.; Boussetta, A.; Grimi, N.; Barba, F. J.; Mbarki, M.; Moubarik, A. *Sep. Sci. Technol.* **2023**, *58*(2), 221-240.

8. Wang, J.; Xu, J.; Wu, N. *J. Exp. Nanosci.* **2017a** *12*(1), 297-307.

9. Thakur, S.; Pandey, S.; Arotiba, O. A. *Carbohydr. Polym.* **2016**, *153*, 34-46.

10. Guarin, J. R.; Moreno-Pirajan, J. C.; Giraldo, L. *J. Chem.* **2018**, vol. 2018, Article ID 2124845, 12 pages.

11. Liu, X.; Ma, S.; He, P.; Wang, M.; Duan, X.; Jia, D.; Colombo, P.; Zhou, Y. *J. Phys. Chem. Solids.* **2023**, *174*, 111158.

12. Wang, H.; Yang, L.; Qin, Y.; Chen, Z.; Wang, T.; Sun, W.; Wang, C. *Colloids Surf. A: Physicochem. Eng. Asp.* **2023***, 656*, 130290.

13. Luo, M.; Wang, L.; Li, H.; Bu, Y.; Zhao, Y.; Cai, J. *Bioresour. Technol.* **2023**, *372*, 128676.

14. Gürses, A.; Doğar, Ç.; Yalçın, M.; Açıkyıldız, M.; Bayrak, R.; Karaca, S. *J. Hazard. Mater.* **2006**, *131*(1-3), 217-228.

15. Belaid, K. D.; Kacha, S.; Kameche, M.; Derriche, Z. *J. Environ. Chem. Eng.*, **2013**, *1*(3), 496-503.

16. Gong, R.; Li, M.; Yang, C.; Sun, Y.; Chen, J. *J. Hazard. Mater.* **2005**, *121*(1-3), 247-250.

17. Gürses, A.; Karaca, S.; Aksakal, F.; Acikyildiz, M. *Desalination*, **2010**, *264*(1-2), 165-172.

18. Nkosi, N.; Basson, A.; Ntombela, Z.; Dlamini, N.; Maliehe, T.; Pullabhotla, R. *Pure Appl. Chem.* **2023**

19. Zhafiri, S.; Ali, B. T. I.; Gunawan, T.; Widiastuti, N. *Mater. Today Proc.* **2023**, *74*, 471-475.

20. Luo, X. P.; Fu, S. Y.; Du, Y. M.; Guo, J. Z.; Li, B. *Microporous Mesoporous Mater.* **2017**, *237*, 268-274.

21. Alverez-Gallegos, A.; Pletcher, D. *Electrochim. Acta.* **1999**, *44*(14), 2483-2492.

22. Aysan, H.; Edebali, S.; Ozdemir, C.; Karakaya, M. C.; Karakaya, N. *Microporous Mesoporous Mater.* **2016**, *235*, 78-86.

23. Wang, F.; Zhang, L.; Wang, Y.; Liu, X.; Rohani, S.; Lu, J. *Appl. Surf. Sci.* **2017**b, *420*, 970-981.

24. Bhattacharjee, A.; Ahmaruzzaman, M.; Sinha, T. *Spectrochim. Acta A Mol. Biomol. Spectrosc.* **2015**, *136*, 751-760.

25. Fei, P.; Zhong, M.; Lei, Z.; Su, B. *Mater. Lett.* **2013**, *108*, 72-74.

26. Zhang, J.; Li, B.; Yang, W.; Liu, J. *Ind. Eng. Chem. Res.* **2014**, *53*(26), 10629-10636.

27. Yang, J.; Qiu, K. *Chem. Eng. J.* **2010**, *165*(1), 209-217.

28. Santhy, K.; Selvapathy, P. *Bioresour. Technol.* **2006**, *97*(11), 1329-1336.

29. Bereket, G.; Arog, A. Z.; Özel, M. Z. *J. Colloid Interface Sci.* **1997**, *187*(2), 338-343.

30. Mohamed, M. M. *Colloids Surf. A: Physicochem. Eng. Asp.* **1996**, *108*(1), 39-48.

31. Mohan, D.; Singh, K. P.; Singh, G.; Kumar, K. *Ind. Eng. Chem. Res.* **2002**, *41*(15), 3688-3695.

32. Ho, Y. S.; McKay, G. *Chem. Eng. J.* **1998**, *70*(2), 115-124.

33. Mckay, G.; Otterburn, M. S.; Sweeney, A. G. *Water Res.* **1981**, *15*(3), 327-331.

34. Kalantaryan, M. A.; Abrahamyan, G. E.; Hoveyan, H. A. *J. Archit. Eng. Res.* **2022**, *2*, 36-40.

35. Sharafi, K.; Mansouri, A. M.; Zinatizadeh, A. A.; Pirsaheb, M. *Environ. Eng. Manag. J.* **2015**, *14*(5), 1067-1078.

36. Soleimani, H.; Sharafi, K.; Parian, J. A.; Jaafari, J.; Ebrahimzadeh, G. *Heliyon*, **2023**, *9*(4), e14743.

37. Liu, L.; Luo, X. B.; Ding, L.; Luo, S. L. In *Nanomaterials for the removal of pollutants and resource reutilization*; Luo, X.; Deng, F., Eds.; Elsevier; London, **2019**; pp 83-147.

38. Koochakzadeh, F.; Norouzbeigi, R.; Shayesteh, H. *Environ. Sci. Pollut. Res.* **2023**, *30*(7), 19167-19181.

39. Akbal, F. *J. Colloid Interface Sci.* **2005**, *286*(2), 455-458.

40. Yalçın, M.; Gürses, A.; Doğar, Ç.; Sözbilir, M. *Adsorption*, **2004**, *10*(4), 339-348.

41. Kul, A. R.; Elik, H.; Benek, V. *Erciyes University Journal of Institue of Science and Technology,* **2019**, *35*(2), 26-31.

42. Ugurlu, M.; Gurses, A.; Yalcin, M.; Dogar, C. *Adsorption*, **2005**, *11*(1), 87-97.

43. Jain, C. K.; Sharma, M. K. *Water Air Soil Pollut.* **2002**, *137*(1), 1-19.

44. Basibuyuk, M.; Forster, C. F. *Process Biochem.* **2003**, *38*(9), 1311-1316.

45. Sivaraj, R.; Namasivayam, C.; Kadirvelu, K. *Waste manag.* **2001**, *21*(1), 105-110.

DOI: http://dx.doi.org/10.32571/ijct.1279701 **E-ISSN: 2602-277X**

46. Soltanian, M.; Almasi, A.; Moradi, M.; Sharafi, K.; Soltanian, S. *J. Toloo Behdasht.* **2016**, *14*(5), 50-63.

47. Cho, D.-W.; Jeon, B.-H.; Chon, C.-M.; Schwartz, F. W.; Jeong, Y.; Song, H. *J. Ind. Eng. Chem.* **2015**, *28*, 60-66.

48. Fan, L.; Luo, C.; Sun, M.; Li, X.; Lu, F.; Qiu, H. *Bioresour.Technol.* **2012**,*114*, 703-706.

49. Duman, O.; Polat, T. G.; Diker, C. Ö.; Tunç, S. *Int. J. Biol. Macromol.* **2020**, *160*, 823-835.

50. Shayesteh, H.; Rahbar-Kelishami, A.; Norouzbeigi, R. *J. Mol. Liq.* **2016**, *221*, 1-11.

51. Ling, C.; Wang, Z.; Ni, Y.; Zhu, Z.; Cheng, Z.; Liu, R. *Environ. Prog. Sustain. Energy.* **2022**, *41*(6), e13923.

52. Linh, H. X.; Trung, N. T.; Van Thanh, D.; Huy, N. N.; Dung, N. Q.; Toan, T. Q.; Mai, N. T.; Thuy, N. T.; Khai, N. M. *Vietnam J. Chem.* **2022**, *60*, 41-45.

53. Gürses, A.; Güneş, K.; Şahin, E.; Açıkyıldız, M. *Front. Chem.* **2023**, *11*, 1156577.

54. Genişoğlu, M.; Gören, A. Y.; Balcı, E.; Recepoğlu, Y. K.; Ökten, H. E. *SDU J Nat. Appl. Sci.***2019**, *23*(2), 574-581.

55. Sheng, L.; Zhang, Y.; Tang, F.; Liu, S. *Microporous Mesoporous Mater.* **2018**, *257*, 9-18.

56. Han, R.; Wang, Y.; Zou, W.; Wang, Y.; Shi, J. *J. Hazard. Mater.* **2007**, *145 (1-2)*, 331–335.

DOI: http://dx.doi.org/10.32571/ijct.1292871 **E-ISSN: 2602-277X**

International Journal of Chemistry and Technology

http://dergipark.org.tr/ijct

Research Article

Tribological performance of polyamide 6/wax blend for rolling bearing, bushing and gear applications

Hüseyin ÜNAL[1*], Salih Hakan YETGİN[2], Sinan KÖSE[3]

[1]Sakarya University of Applied Sciences, Faculty of Technology, Metallurgy and Materials Eng. Department Sakarya, Türkiye

[2] Tarsus University, Faculty of Engineering, Department of Mechanical Engineering, Mersin, Türkiye

[3] Tarsus University, Vocatıonal School Of Technıcal Sciences at Mersin Tarsus Organized Industrial Zone, Department of Machinery and Metal Technologies, Mersin, Türkiye

Received: 5 May 2023; Revised: 10 May 2023; Accepted: 9 June 2023

*Corresponding author e-mail: unal@sakarya.edu.tr

Citation: Ünal, H.; Yetgin, S. H.; Köse, S. *Int. J. Chem. Technol.* **2023**, 7 (1), 75-81.

ABSTRACT

In this experimental study, polyamide6 polymer, which is among the engineering plastics used in rolling bearings, gears, rollers and bushings, was used. In addition, PA6 polymer blends with 6% wax solid lubricant were produced to increase wear resistance and their tribological performances were investigated. The polyamide 6/wax blend was first produced in granule form in twin screw extruder by compound production method. Then, test specimens were injection molded using the granules. AISI 316L stainless steel was used as a counter-disc in tribology tests. The tests were carried out under dry sliding conditions and at room temperature. Wear tests were carried out on a pin-disc wear tester at two different loads and four different sliding speeds. The coefficient of friction (CoF) and specific wear rate (SWR) of the materials were determined. According to the test results, an increase in the CoF and SWR of both PA6 polymer and PA6/6% wax blend was observed with increasing sliding speed. At the load and speed ranges studied, the CoF of pure PA6 polymer varied between 0.25 and 0.36, while the CoF of PA6/6% wax blend varied between 0.10 and 0.13. The SWR of PA6 polymer was obtained in the range of 1.2-12x10^{-4} $mm^3/N^{-1}m^{-1}$, while the SWR of PA6/6% wax blend was obtained in the range of 1.2-3.0x10^{-5} $mm^3/N^{-1}m^{-1}$. The addition of 6% wax to PA6 polymer caused a significant decrease in both CoF and SWR and contact surface temperature.

Keywords: Polyamide 6, tribology, wax, wear, polymer.

Tribological performance of polyamide 6/wax blend for rolling bearing, bushing and gear applications

ÖZ

Bu deneysel çalışmada, rulmanlı yataklar, dişli, makara ve burç yapımında kullanılan mühendislik plastikleri arasında yer alan poliamit6 polimeri (PA6) kullanılmıştır. Buna ilaveten aşınma direncini artırmak için %6 oranında vaks katkılı PA6 polimer karışımları (PA6/%6vaks) üretilmiş ve tribolojik performansları araştırılmıştır. Poliamit6/vaks karışımı önce kompound üretim yöntemi ile çift vidalı ekstruderde granül formda üretilmiştir. Sonrasında ise granüller kullanılarak test numuneleri enjeksiyonla kalıplanmıştır. Triboloji testlerinde karşı disk olarak AISI 316L paslanmaz çelik kullanılmıştır. Deneyler kuru kayma şartlarında ve oda sıcaklığında yapılmıştır. Deneyler iki farklı yükte ve dört farklı kayma hızında pim-disk aşınma test cihazında gerçekleştirilmiştir. Aşınma testlerinde malzemelerin sürtünme katsayısı ve spesifik aşınma hızı belirlenmiştir. Test sonuçlarına göre, kayma hızının artmasına bağlı olarak hem PA6 polimeri hem de PA6/vaks karışımının sürtünme katsayısı (SK) ve spesifik aşınma hızında artış gözlenmiştir. Çalışılan yük ve hız aralıklarında SK, saf PA6 polimeri için 0.25-0.36 arasında iken PA6/vaks karışımı için 0.10-0.13 arasında değişim göstermiştir. PA6 polimerinin aşınma hızı 1.2-12x10^{-4} $mm^3/N^{-1}m^{-1}$ aralığında elde edilirken PA6/vaks karışımının aşınma hızı ise 1.2-3x10^{-5} $mm^3/N^{-1}m^{-1}$ aralığında elde edilmiştir. %6 oranındaki vaks PA6/6Vaks kompozitin hem sürtünme katsayısında ve aşınma hızında hem de temas yüzey sıcaklığında önemli azalmaya sebep olmuştur.

Anahtar Kelimeler: Poliamit 6, triboloji, vaks, aşınma, polimer.

DOI: http://dx.doi.org/10.32571/ijct.1292871 **E-ISSN: 2602-277X**

1. INTRODUCTION

Polyamide 6 (PA6) polymer is a semi-crystalline engineering polymer with high mechanical properties and high crystallinity. With these properties, it is an engineering polymer that is widely used in the production of engineering products in many sectors such as the automotive sector, the electrical/electronics sector and the packaging sector. However, the use of PA6 polymer in wider applications limited due to its properties such as low impact strength at low temperatures, low thermal degradation temperature, poor dimensional stability and high wear under dry sliding conditions.[1-4] Although there are different ways to improve the mechanical and thermal properties of PA6 polymer, one of the simplest and most preferred methods is the incorporation of filler materials such as glass fibers (GF), carbon fibers (CF) and aramid fibers (AF) into the polymer. There are some studies on fiber reinforced polyamide based polymer composites in the literature. Among these, Nuruzzaman et al.[5] investigated the tensile and impact properties of GF (5-20% by weight) reinforced PA6 polymer composites. Their results showed that the modulus of elasticity, the yield strengths, tensile strength and fractural strength increased by 329%, 230%, 113% and 159%, respectively. They stated that the elongation at break decreased by 1300% by increasing the GF ratio in the polymer matrix from 5% to 20%. Hyo Jin et al.[6] investigated the mechanical and thermal properties of long CF reinforced with PA6 polymer composites. They demonstrated that the tensile strength of the unfilled PA6 polymer was 38.7 MPa, while 110.3 MPa was obtained for the PA6/18% long carbon fibre (LCF) polymer composite. The tensile modulus increased from 0.52 GPa to 6.49 GPa. At the same time, elongation at break decreased from 38.7% to 21.0%. They also reported that while the melting temperature (T_m) and thermal decomposition temperature of the PA6 composite were not affected by the CF addition, the addition of the CF had an effect of the crystallization temperature (Tc). Li et al.[7] investigated the heat deflection temperature (HDT) properties of PA6-based composites, the properties of fibre type (carbon or glass) and ratio (0-5% by weight) on mechanical and thermal conductivity. Their results showed that the thermal conductivity of the composites increased with the increasing CF ratio, while it decreased slightly with the increment of GF ratio. However, they demonstrated that the tensile modulus and heat deflection temperature of PA6-based composites can be achieved with increasing fibre content. Yi-Lan et al.[8] studied the effect of 0%-25% GF to PA6 polymer on tribological properties. It has been stated that the addition of 15% GF to the polymer matrix reduces the CoF and SWR by 92% and 95%, respectively. Kumar and Panneerselvam[9] investigated the mechanical and abrasive wear properties of pure PA6 and GF filled PA6 composites. The study was carried out under atmospheric conditions at a sliding distance of 500 m. The effects of applied load (5, 10, 15 and 20 N) and GF ratio (0, 10, 20 and 30 wt%) on wear were analysed. The results demonstrated that while the SWR decreased with the increase in GF ratio, the lowest wear rate was obtained in 30wt.% GF reinforced PA6 composite. As a result of the analysis, the abrasive wear loss increased with the increase in applied load. The tribological properties of polymer materials are significantly affected by environmental and process conditions. The effects of test conditions such as applied load, sliding speed, sliding distance, contact geometry and environmental conditions (dry or wet) on the friction and wear properties of PA6 polymer have been extensively studied. Various studies demonstrated that the CoF of polymers decreases with increasing sliding speed and load.[10-13] Kumar and Kanagaraj[13], Umesh[14], Lakshmi[15], Kumar and Kanagaraj[12] found that SWR increased with increasing load while Kumar and Kanagaraj[13], and Umesh[14] stated that SWR increased with increasing sliding speed.

Solid lubricants such as poly-tetra-fluoro-ethylene (PTFE), graphite, paraffin wax, ultra high molecular weight polyethylene (UHMWPE) and molybdenum-di-sulphide (MoS_2) are widely used to improve the friction and wear properties of PA6 polymer.[16-21] Li et al.[19] investigated the effects of PTFE, graphite, UHMWPE and their combinations on the mechanical and tribological properties of PA6/15%GF composite. While the tensile strength of PA6/15%GF composite increased with the addition of graphite filler, the graphite/UHMWPE combination significantly increased the impact strength of PA6/15%GF composite. In addition, it was stated that the CoF decreased at the maximum ratio with the addition of 5wt.% PTFE filler, and PTFE/UHMWPE combination solid lubricant would be the best choice to increase both the friction and wear performance of the PA6/15%GF composite. Demirci et al.[22] studied the effects of sliding speed, contact pressure and temperature on the wear loss of PA66, PA66+30%GF and PA66+25%GF+3%MoS_2 composites. They showed that the transfer film layer formed between the contact surfaces due to the presence of MoS_2 solid lubricant improves the wear resistance of PA66 polymer. Among solid lubricants, paraffin wax is chemically inert, non-corrosive, long-lasting, inexpensive, ecologically harmless and non-toxic.[23] Paraffin waxes show stable behaviour up to 250°C and therefore do not boil even at high temperatures.[24] Paraffin wax is one of the potential candidate materials as solid lubricant filler for polymer composites with these properties. Unal et al.[25] examined the effect of wax solid lubricant on the electrical, thermal and tribological properties of graphite filled PA6 composites. The results of the study showed that the CoF and SWR of PA6 composite is reduced with the addition of wax to the 15wt.% graphite/PA6 polymer. However, it has been stated that glass transition (T_g) and melting temperature (T_e) are not affected by the wax lubricant ratio. It was also reported that optimum friction and wear performance were obtained in 6wt.% of wax contents. Jozwik et al.[26] also examined the tribological characteristics of the wax filled PA6, M_oS_2 filled PA6, aluminium filled poly-oxy-methylene (POM), PTFE filled polyethylene terephthalate (PET), bronze filled PTFE and graphite filled PTFE composites. Their results showed that one of the most important factors affecting the tribological characteristics is the filler type and the best tribological performance was obtained in the case wax added PA6 mixture. It has been stated that the CoF of all materials tested with increasing load is reduced.

There are limited studies on this material in the literature. Therefore, the aim of this study was to examine the tribological performances of polyamide 6 and PA6/6wt.% wax polymer composites, which is among the high -performance engineering plastics, under dry sliding conditions against the AISI 316L stainless steel disc. Wear tests were performed on Pin-on-Disc test device. This study was carried out to understand the tribological problems that may occur in materials such as bearings, gears, bushings and rollers. The study was carried out at different sliding speeds (0.5-1.0-1.5-2.0 m/s^{-1}) and under loads (50 N -100 N). Experimental studies were planned to a using sliding distance in 2000 m, under atmospheric conditions and in a dry sliding environment. The variation of CoF and SWR of unfilled PA6 and PA6/6%wax blend produced under the above-mentioned conditions were investigated.

2. MATERIALS AND METHODS

Polyamide 6 polymer used in wear experiments was obtained from Domopolymer as known as Domamid commercial name. The wear test samples were produced with injection moulding technique in accordance with the ASTM G99 standard. In wear experiments were performed under dry conditions using the Pin-on-Disc wear system under atmospheric conditions. The PA6 polymer and PA6/6wt.%wax polymer blend pin samples for wear tests produced by injection moulding method. Pin sample dimensions were 6 mm diameter and 50 mm length. AISI 316L stainless steel which has surface roughness of 0.32 Ra, is used as a counter-disc material. The specific wear rate (K_O) was determined with Equation 1. L; sliding distance (m), ρ; the density of the material (g/cm^{-3}) and F; applied load (N).

$$K_o = \frac{\Delta m}{L * \rho * F} \qquad (1)$$

The coefficient of friction measurements of the test specimens were measured with the help of a load-cell in a wear test setup designed to have a pin on the disc. The lateral force measured by the load cell is transferred to a computer and recorded in the excell program. Approximately 65.000 data measuring the lateral load were obtained during the experimental period. This lateral load data was recorded in a column in the Excel program and then divided by the applied load to calculate the coefficient of friction. The coefficient of friction (μ) between the pin specimens used in the experiments and the opposing SS disc is the ratio of the lateral force to the normal force and is calculated by the formula given in Equation (2). In the formula, μ is the coefficient of friction, Fs is the frictional force (N) and Fn is the normal force (N).

$$\mu : Fs/Fn \qquad (2)$$

Before the wear tests, the specimen and disc surfaces were smoothed with 1200 grit sandpaper and the surfaces were then cleaned with acetone.

3. RESULTS AND DISCUSSION

Table 1 shows the results of the CoF depending on the sliding speed for unfilled PA6 polymer and PA6/6%wax blend. The sliding speed-CoF graph of pure PA6 and PA6/6% wax blend are given in Figure 1. The figure shows that the CoF of unfilled PA6 polymer and PA6/6% wax blend increased with increase in sliding speed.

Table 1. Results for sliding speed-friction coefficient of unfilled PA6 and PA6/6wt.% wax blend.

Materials	Load, N	Sliding speed m s^{-1}			
		0.5	1.0	1.5	2.0
		CoF, μ			
PA 6	50	0.25	0.28	0.30	0.35
	100	0.27	0.30	0.32	0.36
PA6/6wt.%wax	50	0.10	0.11	0.12	0.13
	100	0.10	0.11	0.11	0.12

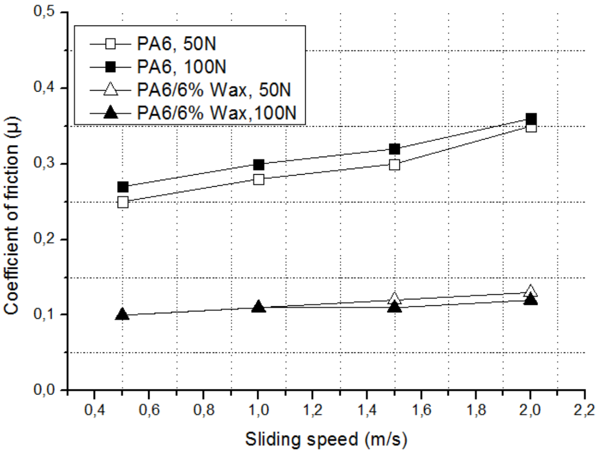

Figure 1. CoF-sliding speed graphs of PA6/6wt.% wax blend and unfilled PA6 polymers.

This increase was obtained under 50N load as 40% and 30% for unfilled PA6 and PA6/6wt.% wax blend, respectively. For 150 N load, the increase in CoF for unfilled PA6 polymer and PA6/6wt.% wax blend was

DOI: http://dx.doi.org/10.32571/ijct.1292871 **E-ISSN: 2602-277X**

obtained as 33.3% and 20%, with increasing sliding speed ratio with 300%. Therefore, this study demonstrates that increasing the load from 50N to 100N did not affect the CoF. For unfilled PA6 polymer, the CoF at different sliding speed decreased by an average of 6.6 %, while the CoF for PA6/6wt.% wax blend did not change. The 6wt.% wax filled into PA6 polymer played an important role in reducing the CoF in the range of sliding speed and applied load. The CoF of PA6/6wt.% wax blend under 50N and 150N loads decreased by 156 % and 183 %, respectively, compared to the pure PA6 polymer. In the experiments carried out at 50-100N load and 0.5-2.0 m/s sliding speed ranges, the highest CoF was obtained in unfilled PA6 polymer under 2.0 m/s^{-1} sliding speed and 100N load, while the lowest CoF was found at 0.5 m/s^{-1} sliding speed and under 50 and 100N loads for PA6/6wt.%wax blend.

Figure 2 shows the variation of pin and disc surface temperatures at the contact point of unfilled PA6 and PA6/6wt.% wax blend working against AISI 316L stainless steel disc depending on the sliding distance. As expected, it was determined that both pin and disc surface temperatures increased depending on the sliding distance. The initial temperature of the unfilled PA6 polymer, which was about 23°C, increased to the range of 42-44 °C depending on the sliding distance. The addition of 6wt.% wax reduced both the pin and disc surface temperature by half, and the temperature value was obtained in the range of 27-31 °C when the sliding distance was 2000 m. The most important reason for the decrease in pin material and steel disc temperatures can be explained by the high thermal conductivity of the steel disc material. The wax solid lubricant added to the polyamide 6 polymer main matrix showed high lubricant properties, causing a decrease in the CoF and a decrease in the surface temperature of the polymer pin and steel disc.

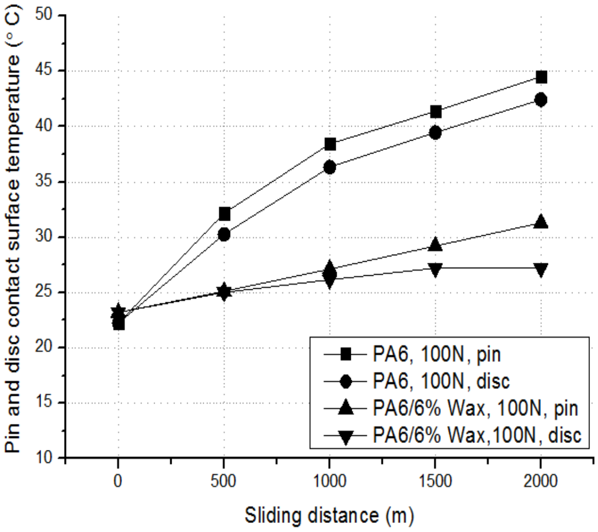

Figure 2. Variation of sliding path-pin and disc contact surface temperatures of PA6/6wt.% wax blend and unfilled PA6 polymers.

The results of the sliding speed and the SWR depending on the load for unfilled PA6 and PA6/6wt.%wax blend were presented in Table 2. The sliding speed-SWR graph is given in Figure 3. The SWR for pure PA6 polymer was obtained as 10^{-4} mm^3 N^{-1}m^{-1}. The SWR was obtained as 10^{-5} mm^3 N^{-1}m^{-1} for PA6/6wt.% wax blend. The lowest SWR was provided in the PA6/6wt.% wax blend sample with a sliding speed of 0.5 m s^{-1} and a load of 100N, with a value of 1.20x10^{-5} mm^3 N^{-1}m^{-1}.

Table 2. Results of sliding speed-SWR of unfilled PA6 and PA6/6wt.% wax blend.

Materials	Load, N	Sliding speed, m s^{-1}			
		0.5	1.0	1.5	2.0
		Specific wear rate, mm^3 N^{-1}m^{-1}			
PA 6	50	1.20 E^{-04}	1.26 E^{-04}	1.32 E^{-04}	1.37 E^{-04}
	100	8.00 E^{-04}	9.00 E^{-04}	9.1 E^{-04}	1.20 E^{-03}
PA6/6wt.%wax	50	1.50 E^{-05}	2.20 E^{-05}	2.60 E^{-05}	3.00 E^{-05}
	100	1.20 E^{-05}	1.40 E^{-05}	1.50 E^{-05}	1.80 E^{-05}

The highest SWR was obtained in unfilled PA6 polymer with a sliding speed of 2.0 m s^{-1} and a load of 50 N, with a value of 1.37x10^{-4} mm^3 N^{-1}m^{-1}. It was observed that the SWR increased with the increase in sliding speed. By increasing the sliding speed by 300%, the SWR of unfilled PA6 polymer increased by 14.1% under 50 N load and 50% under 100 N load. For PA6/6wt.%wax composite, the specific wear rate increased by 100% and 50%, respectively, under 50 N and 100 N loads, depending on the sliding speed. The addition of 6wt.%wax played a much more effective role in reducing the SWR. For example, under 2.0 m s^{-1} sliding speed and 50 N load, the SWR of PA6/6wt.% wax blend decreased by 356.6% compared to unfilled PA6 polymer.

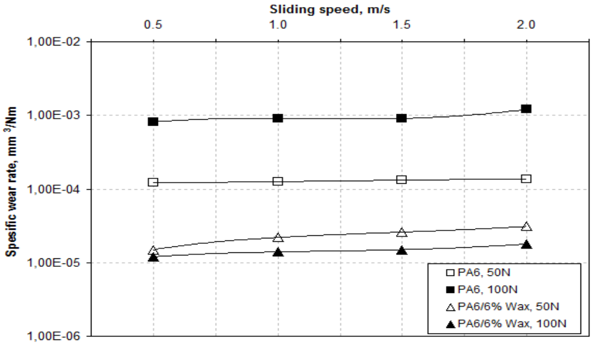

Figure 3. SWR-sliding speed graph of unfilled PA6 polymer and PA6/6wt.%wax blend.

Pin Disc

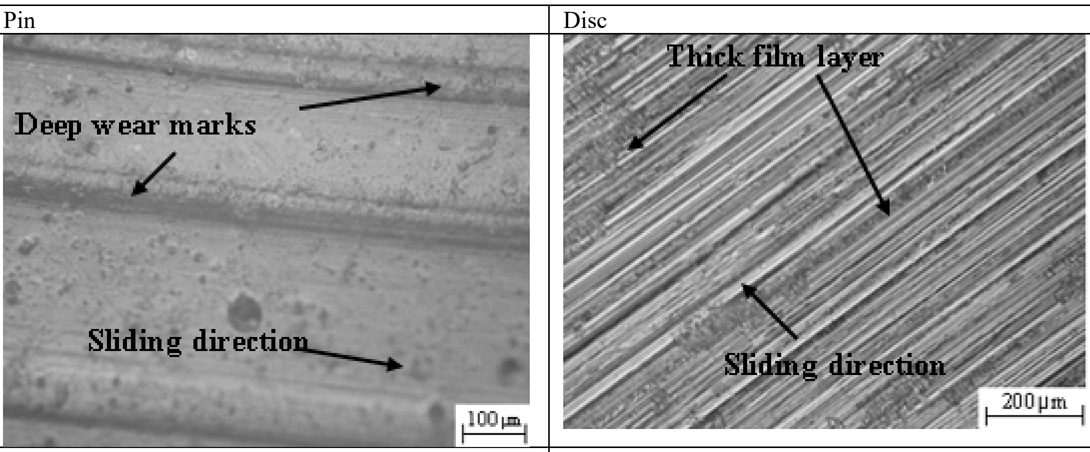

a) PA6 pin b) PA6 pin/AISI 316L stainless steel disc

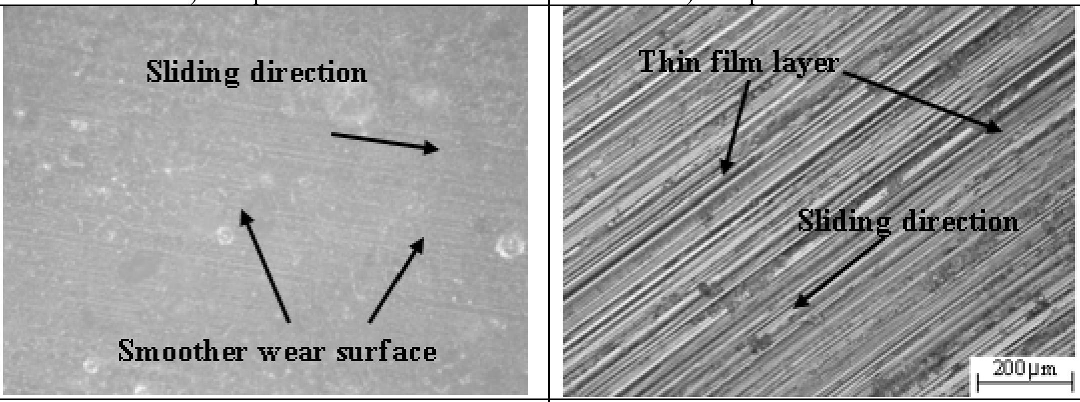

c) PA6/6wt.%wax pin d) PA6/6wt.%wax pin/AISI316L stainless steel disc

Figure 4. Optical microscope images of stainless steel disc and pin wear surface (Load:100 N, Speed: 2.0m s^{-1}).

Optical microscope images of worn unfilled PA6 polymer pin surface and PA6/6wt.wax blend pin surface against AISI 316 stainless steel disc under high sliding speed (2.0 m s^{-1}) and high load (100 N) are given in Figure 4a- Figure 4d. When Figure 4b and Figure 4d SS disc surfaces are investigated, it is observed that a transfer film layer (TFL) is formed that prevent the pin and disc contact. While the TFL formed unfilled PA 6 polymer was observed as a thicker TFL on the disc surface (see Figure 4b), it was determined that the transfer film layer was formed locally. Figure 4d shows that the TFL on the disc surface was thinner in PA6/6wt.% wax blend. When the pin surfaces of the unfilled PA6 polymer were examined, it was observed that deep and wider wear marks were formed in the sliding direction of pin material and therefore the wear mechanism can be announced abrasive wear (see Figure 4a). Moreover, it was observed that the wear marks decreased in the sliding direction on the PA6/6wt.%wax blend pin sample, while a smoother wear surface was observed (see Figure 4c). Addition of 6wt.% wax to the PA6 polymer changed the wear mechanism to an adhesive wear mechanism. This result is consistent with the reduced CoF and increased wear resistance (see Figure 1 and Figure 3).

4. CONCLUSIONS

1. The CoF of unfilled PA6 polymer increased by 12%, 20% and 40%, respectively, with the sliding speed.
2. The CoF of PA6/6wt.%wax blend slightly increased with the increase in sliding speed. As a result of increasing the sliding speed from 0.5 m s-1 to 2.0 m s^{-1}, CoF increased by 10%, 10% and 20%, respectively.
3. Compared to the CoF of unfilled PA6 polymer, the CoF of PA6/6wt.% wax blend is approximately 156% and 183% lower under 50 N and 100 N loads.
4. Pin and disc surface temperatures increased with increasing sliding speed from 0.5 m s^{-1} to 2.0 m s^{-1}. While the highest pin and disc surface

DOI: http://dx.doi.org/10.32571/ijct.1292871 **E-ISSN: 2602-277X**

temperature was obtained in the range of 42-44 °C for unfilled PA6 polymer, it was found to be approximately 27-31 °C for PA6/6wt.% wax blend.

5. The wear rate of unfilled PA6 polymer increased with the increase in sliding speed. The wear rate increased by 14.1% at 50 N load and 50% at 100 N load, respectively.
6. The SWR of the PA6/wax polymer blend increased slightly due to the increase in sliding speed. The SWR increased by approximately 100% at 50 N load and 50% at 100 N load.
7. Compared to unfilled PA6 polymer, the wear rate of the PA6/6wt.%wax blend was 80% lower at 50 N load and 96% reduction at 100 N load.
8. As a result, it can be stated that the use of PA6/6wt.%wax blend instead of unfilled PA6 polymer in rolling bearing, gear and bushing applications will increase the material service life by about two times.

Conflict of interests

I declare that there is no a conflict of interest with any person, institute, company, etc.

REFERENCES

1. Liang, J.; Yuqiang, X.; Zhiyong, W.; Ping, S.; Guangyi, C.; Wanxi, Z. *J. Therm. Anal.* **2014**, *115*, 209-218.

2. Dryzek, E.; Wrobel, M.; Juszynska-Gałazka, E. *Acta Phys. Pol.* **2017**, *132(5)*, 1501-1505.

3. Titire, L.C.; Andrea, E.M.; Alina, C.C.; George, C.C.; George, G.O.; Lorena, D. *Mater. Plast.* **2021**, *58(3)*, 51-63.

4. Tarun, S.G.; Sridhar, A.; Namrata, V.; Doddipatla, P. *Polym Eng Sci.* **2020**, *60*, 1717-1759.

5. Nuruzzaman, D.M.; Asif Iqbal, A.K.M.; Oumer, A.N.; Ismail, N.M.; Basri, S. *IOP Conf. Ser.: Mater.* **2016**, 114.

6. Hyo Jin, A.; Jung, S.K.; Ki-Young, K.; Dae, Y.L.; Dong, H.K. *Fiber Polym.* **2014**, *15(11)*, 2355-2359.

7. Li, M.; Yizao, W.; Zhifang, G.; Guangyao, X.; Xiaoming, W.; Changbiao, W.; Honglin, L. *Mater. Des.* **2013**, *51*, 257–261.

8. Yi-Lan, Y.; Du-Xin, L.; Gao-Jie, S.; Ruo-Yun, L.; Xin, D. *J. Thermoplast. Compos. Mater.* 2016, *29(4)*, 494-507.

9. Kumar, S.; Panneerselvam, K. *Procedia Technology.* **2016**, *25*, 1129-1136.

10. Mihai, T. L.; Radu, V.; Cornel, C.G. *Mater.* **2019**, *12*, 3452.

11. Horovistiz, A.; Laranjeira, S.; Paulo Davim J. *Polym. Bull.* **2018**, *75*, 5113–5131.

12. Kumar, S.S.; Kanagaraj, G. *Arab J Sci Eng.* **2016**, *41*, 4347–4357.

13. Kumar, S.S.; Kanagaraj, G. *Bull. Mater. Sci.* **2016**, *39(6)*, 1467–1481.

14. Umesh, G.L.; Krishna Prasad, N.J.; Rudresh, B.M.; Lingesh, B.V. *AIP Conf Proc.* **2020**, *2274*, 030005.

15. Lakshmi S.; Sarcar, M.M.M.; Suman, K.N.S. *Int. J. Mech. Eng. Robot. Res.* **2012**, *1(3)*, 157-162.

16. Bermudez, M.D.; Carrıon-Vilches, F.J.; Martinez-Mateo, I.; Martinez-Nicolas, G. *J. Appl. Polym. Sci.* **2001**, *81*, 2426–2432.

17. Dajana, J.; Simon, K.; Mitjan, K.; Janez, S.; Blaz, N.; Miroslav, H. *Adv. Polym. Technol.* **2022**, 9974889.

18. Jian, L. *Adv. Mater. Res.* **2011**, *284-286*, 2370-2373.

19. Li, D,; Xie, Y.; Wenjuan, L.; Yilan, Y.; Xin, D. *Sci. World J.* **2013**, 320837.

20. Du-Xin, L.; Yi-Lan, Y.; Xin, D.; Wen-Juan, L.; Ying, X. *Mater. Des.* **2013**, *46*, 809–815.

21. Du Xin, L.; Wen-Juan, L.; Xie, Y.; Xiang, L. *J. Appl. Polym. Sci.* **2012**, *124*, 4239–4248.

22. Demirci, M.T.; Hayrettin, D.; Rifat, Y. *J. Mater. Sci.* **2013**, *3(11)*, 738-742.

23. Sanchez-Silva, L.; John, T.; Donald, S.; Sanchez, P.; Juan, F.R. *Ind. Eng. Chem. Res.* **2010**, *49*, 12204–12211.

24. Wakaki, M.; Shibuya, T.; Kudodeceased, K. *Physical properties and data of optical materials*. 1st Ed.; CRC Press, 2007.

DOI: http://dx.doi.org/10.32571/ijct.1292871 **E-ISSN: 2602-277X**

25. Unal, H.; Ficici, F.; Mimaroglu, A.; Demirkol, A.; Kırdar, A. *J. Braz. Soc. Mech. Sci. Eng.* **2016**, *38*, 2097-2104.

26. Jozwik, J.; Krzysztof, D.; Marcin, B.; and Mykhaylo, P. *Mater.* **2020**, *13(1)*, 75.

DOI: http://dx.doi.org/10.32571/ijct.1288819 **E-ISSN: 2602-277X**

International Journal of Chemistry and Technology

http://dergipark.org.tr/ijct

Research Article

Antioxidant and oxidant status, DPPH activity, total phenolic and flavonoid contents of mountain tea (*Sideritis libanotica* subsp. *kurdica* (Bornm.) Hub.-Mor)

İmran UYSAL[1*], Falah Saleh MOHAMMED[2], Oğuzhan KOÇER[3],
Muhittin DOĞAN[4], Mustafa SEVİNDİK[5]

[1]*Osmaniye Korkut Ata University, Bahçe Vocational School, Department of Food Processing, Osmaniye, Türkiye*
[2] *University of Zakho, Department of Biology, Faculty of Science, Duhok, Iraq*
[3]*Osmaniye Korkut Ata University, Department of Pharmacy Services, Vocational School of Health Services, Osmaniye, Türkiye*
[4]*Gaziantep University, Department of Biology, Faculty of Science and Literature, Gaziantep, Türkiye*
[5]*Osmaniye Korkut Ata University, Department of Biology, Faculty of Science and Literature, Osmaniye, Türkiye*

Received: 27 April 2023; Revised:9 June 2023; Accepted: 26 June 2023

*Corresponding author e-mail: uysal-imran@hotmail.com

Citation: Uysal, İ.; Mohammed, F.S.; Koçer, O.; Doğan, M.; Sevindik, M. *Int. J. Chem. Technol.* **2023**, 7 (1), 82-85.

ABSTRACT

Samples of *Sideritis libanotica* subsp. *kurdica* (Bornm.) Hub.-Mor, often known as mountain tea, were gathered in Iraq and analyzed for their antioxidant and oxidant status, DPPH activity, total phenolic and total flavonoid contents. The plant's aerial parts were utilized for this purpose. The levels of antioxidants and free radicals were measured by Rel assay kits. The ability to scavenge free radicals was evaluated using the DPPH technique. Folin-Ciocalteu and aluminum chloride reagent are used. As a result TAS values of 7.934±0.179 mmol/L, TOS values of 10.626±0.275 µmol/L, and OSI values of 0.134±0.001. The total phenolic and flavonoid contents were found to be 129.75±2.37 and 111.47±3.15 mg/g, respectively. Furthermore, DPPH activity at 2 mg/mL was calculated to be 75.15±1.45 *S. libanotica* subsp. *kurdica* has been found to have antioxidant activity and is thus a viable natural antioxidant source in this context.

Keywords: Antioxidant, phenolic, flavonoid, ironwort, mountain tea.

Dağ çayının (Sideritis libanotica subsp. kurdica (Bornm.) Hub.-Mor) antioksidan ve oksidan durumu, DPPH aktivitesi, toplam fenolik ve flavonoid içerikleri

ÖZ

Genellikle dağ çayı olarak bilinen *Sideritis libanotica* subsp. *kurdica* (Bornm.) Hub.-Mor Irak'tan toplanmıştır. Toplam antioksidan ve oksidan durumu, DPPH aktivitesi, toplam fenolik ve toplam flavonoid içerikleri açısından analiz edilmiştir. Bu amaçla bitkinin toprak üstü kısımlarından yararlanılmıştır. Toplam antioksidan ve oksidan durumları, Rel assay kitleri ile ölçülmüştür. Serbest radikalleri temizleme yeteneği, DPPH tekniği kullanılarak değerlendirilmiştir. Toplam fenolik ve flavonoid içeriği için sırasıyla Folin-Ciocalteu ve aliminyum klorür reaktifi kullanılmıştır. TAS değeri 7.934±0.179 mmol/L, TOS değeri 10.626±0.275 µmol/L ve OSI değeri 0.134±0.001 olduğu belirlenmiştir. Toplam fenolik ve flavonoid içerikleri sırasıyla 129.75±2.37 ve 111.47±3.15 mg/g olarak belirlenmiştir. Ayrıca 2 mg/mL'de DPPH aktivitesi 75.15±1.45 olarak hesaplanmıştır. *S. libanotica* subsp. *kurdica*'nın antioksidan aktiviteye sahip olduğu ve bu bağlamda doğal antioksidan kaynağı olduğu bulunmuştur.

Anahtar Kelimeler: Antioksidan, fenolik, flavonoid, demirotu, dağ çayı.

1. INTRODUCTION

Plants are one of the constant elements of human life. The human race has found several uses for various plants. [1] Plants have been utilized by people all across the world for anything from building materials to food to medicine.[2] Plants are one of the few permanent aspects in human medicine, especially in the treatment of illnesses. The antioxidant, anticancer, anti-inflammatory, anti-allergic, anti-aging, DNA-protective, antibacterial, and hepatoprotective properties of plants have been the subject of many research. [3–7] Determining the biological activity of plants is, therefore, crucial for their application as supplementary medicines in this setting. They have further pharmacological use as natural materials.[8]

The bioactive chemicals found in many plants provide them unique biological characteristics.[9] These bioactive compounds are not nutritional but are also very important medicinally. Compounds having antioxidant activity are produced by many different plant species.[10,11] They can serve as a natural antioxidant source if sufficient quantities of antioxidant molecules are produced.[12] The purpose of this research was to evaluate the antioxidant properties of *Sideritis libanotica* subsp. *kurdica* (Bornm.) Hub.-Mor. In addition, Total flavonoid and phenolic content was also determined.

Ironwort, often called mountain tea or shepherd's tea, is a species of *Sideritis* (Lamiaceae). It is a herb that is commonly used to make tea. It thrives in high altitude regions with scant soil and often directly on the rocks itself. They are 8-50 cm in height and are xerophytic plants. Because of its pleasant scent, it is a popular herbal tea ingredient in many cultures. The plant's stem, leaves, and flowers are employed in a boiling lemon or honey concoction.[13,14]

In this work, we analyzed samples of *S. libanotica* subsp. *kurdica* from Iraq (Duhok) to assess its antioxidant, oxidant potential, DPPH activity, total phenolic, and total flavonoid content.

2.MATERIALS AND METHODS

2.1. Materials

Specimens of *S. libanotica* subsp. *kurdica* were obtained from the city of Duhok (Iraq). Shaded and well-ventilated space was used for the drying operations of the plant samples. After that, we cartridged 30 g of the plant sample and extracted it with 250 mL of ethanol at 50 ^{0}C for around 6 hours. The solvents of the obtained extracts were removed in the concentrator. (Heidolph Laborota 4000 Rotary Evaporator).

2.2. Methods

2.2.1. Antioxidant tests

The plant's antioxidant (TAS) and oxidant (TOS) levels were measured using Rel Assay kits. Calibrators included trolox for the antioxidant test and hydrogen peroxide for the oxidant test.[15,16] The oxidative stress index was determined by dividing the TOS value with the TAS value. [17]

The ability to scavenge free radicals was measured using the DPPH assay. Plant extracts were dissolved in DMSO to make 1 mg/mL stock solutions. To 50 L of this solution, 160 L of a 0.039% DPPH solution was added. After a 30-minute room-temperature incubation, the sample's absorbance was measured at 517 nm. All plant preparation concentrations were tested again. The antioxidant ascorbic acid served as a standard.[18] DPPH free radical scavenging percentages were calculated using the following formula: % inhibition = [(Abs control-Abs sample)\Abs control]x100.

2.2.2. Total phenolic and flavonoid tests

Plant extract (originally 0.1 mL) was diluted with 1 mL of distilled water. After that, we added 1 mL of Folin-Ciocalteu reagent (1:9, v/v) and gave it a good whirl. The finished product added 0.75 mL of 1% Na2CO3. The mixture was then allowed to incubate at room temperature for 2 hours. The incubation period was followed by a 760 nm measurement. From the gallic acid standard solution calibration curve, the total phenolic content was calculated and represented as mg.GAE/g.[19]

Measurement of flavonoids was performed using aluminum chloride.[20] Quercetin (0.5 mL), plant extract (0.5 mL), methanol (4.3 mL), 10% Al(NO3)3, and 1 M NH4CH3COO (0.1 mL) were mixed together. After a 40-minute incubation period, the absorbance was measured at 415 nm. Flavonoids were reported as mg.QE/g.

3. RESULTS AND DISCUSSION

3.1. Antioxidant activity

Oxidant molecules are byproducts of metabolic processes in all living things.[21] When these oxidant molecules accumulate, the body's antioxidant defense mechanism steps in to neutralize them. When the body's antioxidant defenses against oxidizing substances are deficient, a condition known as oxidative stress can develop.[22,23] Many illnesses, including cancer, Alzheimer's, Parkinson's, and cardiovascular disease, may develop in humans as a result of oxidative stress.[24] The consequences of oxidative stress can be mitigated or even prevented with the use of antioxidant supplements.[25] We investigated the antioxidant capacity of mountain tea in this work. The results are shown in Table 1 and Table 2.

Table 1. TAS, TOS, OSI, TPC and TFC values of *S. libanotica* subsp. *Kurdica*.

	TAS mmol/L	*TOS* µmol/L	*OSI*	*TPC mg/g*	*TFC mg/g*
Mountain tea	7.934±0.179	10.626±0.275	0.134±0.001	129.75±2.37	111.47±3.15

DOI: http://dx.doi.org/10.32571/ijct.1288819 E-ISSN: 2602-277X

Table 2. DPPH activity of *S. libanotica* subsp. *Kurdica*.

	0.25 mg/mL	**0.5** mg/mL	**1** mg/mL	**2** mg/mL
Mountain tea	47.45±1.39	58.15±0.89	62.93±1.46	75.15±1.45
Ascorbic acid	76.91±0.86	88.07±0.90	92.90±0.85	96.77±0.42

Antioxidant chemicals are produced by the bodies of many plants. Because of these qualities, they are used into alternative medicine as antioxidant agents.[26] . We investigated the antioxidant capacity of mountain tea in this work. The maximum DPPH activity was seen at a concentration of 2 mg/mL (75.15±1.45). The value of 2 mg/mL ascorbic acid, which was employed as a standard, was found to be 96.77±0.42. We observed that mountain tea has less DPPH activity than ascorbic acid. Antioxidant activity in many species of *Sideritis* has been described in the scientific literature.[27–29] In our experiment, the DPPH activity of the mountain tea was found to be high.

The total antioxidant capacity (TAS) of a product is a measure of all of its antioxidant components.[30] TAS, TOS and OSI values of *Sideritis libanotica* subsp. *kurdica* have not been reported in the literature. It was determined for the first time in our study. Numerous plant species have had their TAS, TOS, and OSI published in the scientific literature. Among these studies, TAS values of *Mentha longifolia* ssp. *longifolia*, *Rhus coriaria* var. *zebaria*, *Alcea kurdica*, *Rumex scutatus*, *Helianthemum salicifolium* and *Scorzonera papposa* were reported as 3.628, 7.342, 3.298, 8.656, 9.490 and 6.328, respectively. TOS values were reported as 4.046, 5.170, 8.312, 4.951, 14,839 and 11,525, respectively. OSI values are reported as 0.112, 0.071, 0.252, 0.057, 0.157 and 0.182, respectively.[1,29,31–33] Compared to this study, the TAS value of mountain tea used in our study was determined to be higher than *M. longifolia* ssp. *longifolia*, *R. coriaria* var. *zebaria*, *A. kurdica* and *S. papposa*, and lower than *R. scutatus* and *H. salicifolium*. In this context, it has been determined that mountain tea has an important antioxidant potential.

The total oxidant status (TOS) measures the total amount of oxidant components in an organic product.[30] Our research showed that the mountain tea had a lower TOS value than both *H. salicifolia* and *S. papposa*, and a higher TOS value than *M. longifolia* ssp. *longifolia*, *R. coriaria* var. *zebaria*, *A. kurdica*, and *R. scutatus*. The oxidant components in the mountain tea we tested in this investigation were found to be within normal ranges.

When the TOS value is divided by the TAS value, the OSI value emerges. The higher the OSI number, the more likely it is that the product contains harmful levels of oxidant chemicals and should not be consumed.[30] In this study, we found that mountain tea had a lower OSI than *A. kurdica*, *H. salicifolium*, and *S. papposa*, but a higher OSI than *M. longifolia* ssp. *longifolia*, *R. coriaria* var. *zebaria*, and *R. scutatus*. Our findings suggest that the mountain tea utilised in this study has significant promise as a means of reducing oxidant chemicals.

3.2. Total phenolic and flavonoid contents

Secondary metabolites include the phenolic and flavonoid chemicals found in plants.[34] The health advantages of these non-nutritional substances are comparable to those of natural goods.[35] Our research looked on the overall phenolic and flavonoid content of mountain tea. Total phenolic contents as 35.5-366.9 mg/g and total flavonoid contents as 14.2-155.7 mg/g of different *Sideritis* species (*S. rubriflora*, *S. libanotica* subsp. *violascens*, *S. erythrantha* var. *cedretorum*, *S. congesta*, *S. brevidens* and *S. viralli*) have been reported in the literatüre.[36]

Total phenolic contents of *S. lycia* and *S. libanotica* subsp. *linearis* have been reported as 16.52 and 10.33 g/kg, and total flavonoid contents as 14.30 and 9.68 g/kg.[28] Instead of using these species, we assessed the total phenolic and flavonoid contents of *S. libanotica* subsp. *kurdica*. Our research indicates that the mountain tea we utilised can be a natural supply of phenolics and flavonoids in this setting.

4. CONCLUSION

The antioxidant capacity of mountain tea was investigated in this study. Total phenolic and flavonoid concentrations in the plant were also calculated. The research indicated that the plant has potential as a useful natural antioxidant source. In addition, it is thought to be a source of phenolics and flavonoids. Therefore, mountain tea has been identified as a potential supplementary antioxidant source for reducing oxidant chemicals.

Conflict of interest

Authors declare that there is no a conflict of interest with any person, institute, company,

REFERENCES

1. Kına, E.; Uysal, İ.; Saleh Mohammed, F.; Doğan, M.; Sevindik, M. *agrifoodscience.org* **2021**, *9*, 1905–1907.

2. Mohammed, F. S.; Karakas, M.; Akgul, H.; Sevindik, M. *Fresen Environ Bull.* **2019**, *28*, 7419-7426

3. Akgul, H.; Korkmaz, N.; Dayangaç, A.; Sevindik, M. *Turjaf.* **2020**, *8*, 2222–2224.

4. Szekalska, M.; Sosnowska, K.; Tomczykowa, M.; Winnicka, K.; Kasacka, I.; Tomczyk, M. *Biomed pharmacother.* **2020**, *121*. 109681

5. Deepak, M.; Sulaiman, C. T.; Balachandran, I.; Chandran, K. P. S. *Vegeto.s.* **2022**. 1–10.

6. Meshack, S.; Gupta, S. *Journal of Drug Delivery and Therapeutics.* **2022**, 12 (1), 194–202.

7. Uysal, I.; Koçer, O.; Saleh Mohammed, F.; Lekesiz, Ö.; Doğan, M.; Şabik, A. E.; Sevindik, E.; Özbas Gerç Eker, F.; Sevindik, M. *Advances in Pharmacology and Pharmacy*. **2023**. *11*, 140–155.

8. Pehlivan, M.; Saleh Mohammed, F.; Şabik, A. E.; Kına, E.; Dogan, M.; Yumrutaş, Ö.; Sevindik, M. *Turjaf.* **2021**. *9*, 1129–1132.

9. Lefebvre, T.; Destandau, E.; Lesellier, E. *J Chromatogr A*. **2021**, *1635* 461770

10. Tran, N.; Pham, B.; Le. L. *biology*. **2020**. *9*, 252

11. Neshat, M.; Abbasi, A.; Hosseinzadeh, A.; Sarikhani, M. R.; Dadashi Chavan, D.; Rasoulnia, A. *Physiol Mol Biol Plants*. **2022**, *28*, 347–361.

12. Jafarzadeh, S.; Jafari, S. M.; Salehabadi, A.; Nafchi, A. M.; Uthaya Kumar, U. S.; Khalil, H. P. S. A. *Trends Food Sci Technol*. **2020**, *100*, 262–277.

13. González-Burgos, E.; Carretero, M. E.; Gómez-Serranillos, M. P. *J Ethnopharmacol.* **2011**, *135*, 209–225.

14. Tadićnja, V. M.; Jeremic, I.; Dobric, S.; Isakovic, A.; Markovic, I.; Trajkovic, V.; Bojovic, D.; Arsic, I. *Planta Med*. **2012**, *78*, 415–427.

15. Erel, O. *Clin Biochem*. **2004**, *37*, 277–285.

16. Erel, O. *Clin Biochem*. **2005**, *38*, 1103–1111.

17. Sevindik, M. *Fresen Environ Bull.* **2019**, *28*, 3713-3717

18. Shimada, K.; Fujikawa, K.; Yahara, K.; Nakamura, T. *J Agric Food Chem*. **1992**. *40*, 945–948.

19. Uysal, S.; Zengin, G.; Locatelli, M.; Bahadori, M. B.; Mocan, A.; Bellagamba, G.; Luca, E. De; Mollica, A.; Aktumsek, A. *Front Pharmacol*. **2017**. *8*:290

20. Chang, C.-C.; Yang, M.-H.; Wen, H.-M.; Chern, J.-C. *J Food Drug Anal*. **2002**, *10*, 178-182.

21. Selamoglu, Z.; Sevindik, M.; Bal, C.; Ozaltun, B.; Sen, İ.; Pasdaran. A. *Biointerface Research in Applied Chemistry*. **2020**. *10*, 5500-5506.

22. Saridogan, B.; Islek, C.; Baba, H.; Akata, I.; Sevindik, M. *Fresen Environ Bull*. **2021**, *30*, 5400-5404

23. Krupodorova, T.; Barshteyn, V.; Sevindik, M. *Bio Technologia*. **2022**. *103*, 19-28

24. Korkman, N.; Dayangaç, A.; Sevindik, M. *J. Fac. Pharm. Ankara*. **2021**. *45*, 554-564.

25. Eraslan, E. C.; Altuntas, D.; Hayri, B.; Celal, B.; Akgül, H.; Akata, I.; Sevindik, M. *Sigma Journal of Engineering and Natural Sciences*. **2021**, *39*, 24–28.

26. Laxa, M.; Liebthal, M.; Telman, W.; Chibani, K.; Dietz, K-D. *antioksidants*. **2019**. *8*, 94

27. Formisano, C.; Oliviero, F.; Rigano, D.; Arnold, N. A.; Senatore, F. *Nat Prod Commun*. **2015**, *10*, 1075-8.

28. Dincer, C.; Torun, M.; Tontul, I.; Topuz, A.; Sahin-Nadeem, H.; Gokturk, R. S.; Tugrul-Ay, S.; Ozdemir, F. *J Appl Res Med Aromat Plants*. **2017**, *5*, 26–32.

29. Sevindik, M.; Akgul, H.; Pehlivan, M.; Selamoğlu Z. *Fresen Environ Bull*. **2014**, *26*, 4757-4763

30. Islek, C.; Özbey, B. G.; Sevindik, M.; Akata, I. *Fresenius Environ Bull*. **2021**, *30*, 6109–6114.

31. Mohammed, F. S.; Akgul, H.; Sevindik, M.; Khaled, B. M. T. *Fresenius Environ Bull*. **2018**, *27*, 5694–5702.

32. Mohammed, F. S.; Sevindik, M.; Uysal, I.; Sevindik, E.; Akgül, H. A *Biology Bulletin* **2022**, *49*, S59–S66.

33. Unal, O.; Eraslan, C. E.; Uysal, İ.; Mohammed, F. S.; Sevindik, M.; Akgül, H. *Fresenius Environ Bull*. **2022**, *31*, 7341–7346.

34. Tungmunnithum, D.; Thongboonyou, A.; Pholboon, A.; Yangsabai, A. *medicines*. **2018**. *5*, 93.

35. Anokwuru, C. P.; Anyasor, G. N.; Ajibaye, O.; Fakoya, O.; Okebugwu, P.. *Nat Sci (East Lansing)* **2011**, *9*, 53–61.

36. Sevindik, E.; Gübeş, İ.; Murathan, Z. T.; Tümen, G. *Eur J Biol Res*. **2021**. *11*, 260–266.

DOI: http://dx.doi.org/10.32571/ijct.1199179 **E-ISSN: 2602-277X**

International Journal of Chemistry and Technology

http://dergipark.org.tr/ijct

Research Article

Function of cascade compressors and power consumption optimization in ammonia liquefaction process: A system evaluation with a 6 sigma approach

Ahmet Ozan GEZERMAN[1*] Ali YETGİN[1]

[1] *Toros Agri Industry, Research & Development Center, Mersin, Turkey*

Received: 3 November 2022; Revised: 3 June 2023; Accepted: 5 June 2023

*Corresponding author e-mail: ozan.gezerman@toros.com.tr

Citation: Gezerman, A. O.; Yetgin, A. *Int. J. Chem. Technol.* **2023**, 7(1), 86-90

ABSTRACT

Ammonia is stored as a liquefied raw material as it is used in the fertilizer and cooling industries. The use of multistage compressors during storage is essential, as the boiling point is very low (-33°C) due to a typical petroleum derivative. Because pressure-temperature optimization with a typical single-stage compressor does not allow ammonia to be stored under atmospheric conditions. The use of condenser and throttling valves used in cooling systems together with multi-stage compressors for storage in atmospheric conditions allows ammonia to be stored in liquid form during storage. In this study, a method has been developed to optimize the energy consumption by calculating the power consumption for the pressure and temperature conditions determined for the liquefaction of anhydrous ammonia, to improve the liquefaction conditions and to minimize the energy consumption.

Keywords: Ammonia, multi-stage compressor, power consumption, consumption optimization, compressor liquefaction capacity.

Amonyak sıvılaştırma işleminde kademeli kompresörlerin fonksiyonu ve güç tüketim optimizasyonu

ÖZ

Amonyak, gübre ve soğutma endüstrilerinde kullanıldığı şekli ile hammadde olarak sıvılaştırılarak depolanmaktadır. Kaynama noktasının tipik bir petrol türevi olması sebebiyle çok düşük (-33 °C) olmasından ötürü, depolama sırasında çok kademeli kompresörlerin kullanılması elzemdir. Zira, tipik bir tek kademeli kompresör ile basınç- sıcaklık optimizasyonu amonyağın atmosferik şartlarda depolanmasına izin vermez. Atmosferik şartlarda depolanması amacıyla, soğutma sistemlerinde kullanılan kondenser ve kısılma vanalarının çok kademeli kompresörler ile birlikte kullanımı amonyağın depolama esnasında sıvı halde depolanabilmesine olanak verir. Bu çalışmada, susuz amonyağın sıvılaştırılması için belirlenen basınç ve sıcaklık şartları için güç tüketim hesabı yapılarak enerji tüketiminin optimize edilerek, sıvılaştırma şartlarını iyileştirilmesi ve enerji tüketiminin minimize edilmesi için bir yöntem geliştirilmiştir.

Anahtar Kelimeler: Amonyak, çok kademeli kompresör, güç tüketimi, tüketim optimizasyonu, kompresör sıvılaştırma kapasitesi.

1. INTRODUCTION

Multistage compressors are used in many production sectors due to the number of cylinders they contain. Two-stage and two-cylinder compressors are the most widely used among multi-stage compressors.[1] However, the design of multistage compressors may differ according to the industry in which the pressurization will be performed.[2] Although multistage compressors are used for liquefaction processes, they are used with condensers, throttling and expansion valves, apart from compressors, for the storage of liquefied gases.[3] Therefore, many models have been developed for the design of compressors and other pressurization equipment.[4] These are formulated on the enthalpy changes and flow rate during the movement of the refrigerant in the liquefaction process.[5]

Another model developed for compressor design is the enthalpy differences caused by temperature differences and the mathematical model put forward due to these differences.[6] The dimensionless mass flow parameter

DOI: http://dx.doi.org/10.32571/ijct.1199179 **E-ISSN: 2602-277X**

defined in this model allows real results to be obtained under liquefaction conditions in measurements made in multistage compressors.[7] It forms the basis of another mathematical model in which enthalpy changes are calculated to determine the power consumption of multistage compressors.[8] "Mach number" is determined as an important parameter in the design of multistage compressors for ammonia liquefaction.[9] The Mach number is used to plot performance curves during the pressurization process [10]

Multi-stage compressors can provide a higher flow rate than single-stage compressors in ammonia pressurization – liquefaction process, thus providing a more efficient operating performance.[11] Multistage compressors consist of three parts. These sections are; The induction mechanism where the gas to be pressurized/liquefied enters can be expressed as the impeller system where the kinetic energy of the gas is increased during liquefaction and the discharge point after liquefaction.[12] A cooling system that allows storage at the discharge point can be used. Energy consumption in multistage compressors depends on the number of cylinders that compress. As the number of cylinders increases, the compression ratio will increase, so an increase in energy consumption is expected. The Mach dimensionless number approaches 1 depending on the increase in the number of cylinders, which means an increase in the performance value. In two-stage compressors, the temperatures reached during the compression process to the desired pressure, the enthalpy change in the compressor design, are among the parameters that determine the energy consumption of the compressors during the operating period.[13]

In this study, the compressor conditions that provide the ambient conditions for the storage of anhydrous ammonia under atmospheric conditions and the resulting energy consumption increase, and the results obtained are optimized. Because, with the optimization study here, it is aimed to prevent the energy consumption of the facility that performs the compression (pressurization) / liquefaction process and the system loss, leakage and unpredictable consumption of the raw material (ammonia).

2. MATERIALS AND METHODS

2.1. Materials

The power consumption in the ammonia liquefaction process by means of a two-stage two-cylinder Compressor can be expressed mathematically as follows.

$$\mathrm{P} = \sqrt{3}.\mathrm{V}.\mathrm{I}.\cos\varphi$$ [14]

Here, V is the voltage in volts, I is the current in amperes, and cos ϕ is the phase difference between the current and voltage, and the cosine of this angle is the power factor. The most ideal situation is that the angle is close to 0, that is, the power factor is close to 1.

Here, when it is desired to calculate the amount of energy consumed for its operation at pressures for a two-stage two-cylinder compressor; Ampere value, 41 A, 6.3 kVolt, for a compressor operating at 100% capacity, the cos φ value measured at this amperage and voltage value is 0.88. The power consumed in this case

$$\mathrm{P} = \sqrt{3} \times 6.3\ \mathrm{kV} \times 41\ \mathrm{A}.0.88 = 393\ \mathrm{kW}$$

can be calculated as

In case the compressor capacity drops to 75%, the amperage value is 35 A, 6.3 kV. and the cos φ value measured at this amperage and voltage value was measured as 0.77. In this case, the power consumed for this process can be calculated as

$$\mathrm{P} = \sqrt{3} \times 6.3\ \mathrm{kV} \times 35\ \mathrm{A}.0.77 = 291\ \mathrm{kW}$$

In case the compressor capacity is reduced to 50%, the amperage value is 29 A, 6.3 kVolt, the cos φ value measured at this amperage and voltage value was measured as 0.75. Accordingly, when the expressed numerical values are substituted in the formulation, a calculation as follows can be made;

$$\mathrm{P} = \sqrt{3} \times 6.3\ \mathrm{kV} \times 29\ \mathrm{A}.0.75 = 237.3\ \mathrm{kW}$$

However, when the obtained consumption amounts are associated with the pressure value of the ammonia gassed in the ammonia tanks, it is necessary to express each ammonia pressure value mathematically by relating it to the electricity consumption. The energy consumption corresponding to each pressure value can be expressed mathematically by making typical interpolation between the measured pressure values in the ammonia tanks and the energy consumed by the compressors for pressurization. In this case, any instantaneous pressure change can be represented as follows.

P_1: Pressure value in ammonia tanks at 50% compressor operating capacity
P_2: Pressure value in ammonia tanks at 75% compressor operating capacity
P_3 : Pressure value in ammonia tanks at the compressor working capacity to be calculated
W_1: Amount of energy consumed to pressurize in ammonia compressor at 50% compressor operating capacity
W_2: The amount of energy consumed to pressurize the ammonia compressor at 75% compressor operating capacity
W_3: Pressure value in ammonia tanks at the compressor operating capacity to be calculated;

DOI: http://dx.doi.org/10.32571/ijct.1199179 E-ISSN: 2602-277X

$$\frac{(P_1 - P_2)}{(P_1 - P_3)} = \frac{(W_1 - W_2)}{(W_1 - W_3)}$$

Accordingly, in the optimization study carried out with reference to the amount of energy consumed for 50%, 75% and 100% capacities, it is the case that a single compressor consumes the least energy when it operates at 75% capacity. Because for such a case, when high tank pressures are taken as reference, at least 75% of energy was used for liquefaction.

3. RESULTS AND DISCUSSION

Ammonia is the most widely used industrial raw material. Storing ammonia in the industry where it is used requires the use of various equipment such as compressors. Maintaining the pressure-temperature balance with expansion and throttling valves in the refrigeration cycle of ammonia used with its refrigerant feature is an absorber system requirement. For a refrigeration system, ammonia is not stored under atmospheric conditions. Because ammonia consumption is not realized for such a system. However, due to production conditions, in systems where ammonia is used as raw material, ammonia consumption causes the steam pressure to vary in storage conditions.

Various mechanisms have been developed for the storage of ammonia for consumption. All the developed mechanisms require cryogenic conditions and include condenser, compressor and expansion valves (Figure 1). Depending on the climatic conditions in which the ammonia storage facility is built, the number of all equipment forming the storage mechanisms may differ. This number of equipment is a system requirement to be able to maintain ammonia at its solidification point under atmospheric conditions.

In ammonia storage systems, the amount of liquefied ammonia is directly related to the system pressure. System pressure is the most important parameter that determines the power consumption in the ammonia storage system. In the literature, the number of studies related to the liquefaction of ammonia and, accordingly, power consumption is very limited. Because parameters such as the type and number of compressors used during ammonia liquefaction directly affect the liquefaction capacity. The power consumption of the cascade compressors used to store ammonia at its boiling point also determines the energy costs of the ammonia storage facility. Studies of ammonia liquefaction and its energy cost so far are limited to single-stage compressors. In this respect, calculating the power consumption of multistage compressors and optimizing the day consumption for different pressure values will significantly affect the energy costs in ammonia storage facilities.

In this study, the amount of energy required during the liquefaction of ammonia needed in a facility using 75 mtons of anhydrous ammonia per hour was calculated. The use of multistage compressors during the Liquefaction of Ammonia process requires an optimization study in terms of energy consumed.

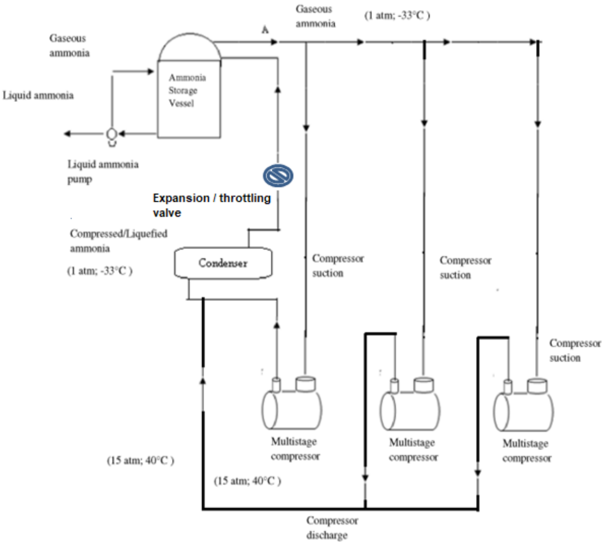

Figure 1. Ammonium liquefaction / storage system with 2-stage compressor system.

3.1. Energy consumed in the ammonia liquefaction process and optimization from a 6 sigma perspective

In order to optimize energy consumption for the ammonia liquefaction process according to the number of compressors and their capacities, the data shown in Table 1 were taken as reference and a "Box Plot" analysis, which is a 6 Sigma statistical analysis form, was performed over these values.

In the "Box Plot" analysis as an evaluation method that can be applied within the 6 Sigma quality management system, the Median and mode values show the most frequently observed energy consumption levels for the number and capacity of compressors used in the liquefaction system (Figure 2).

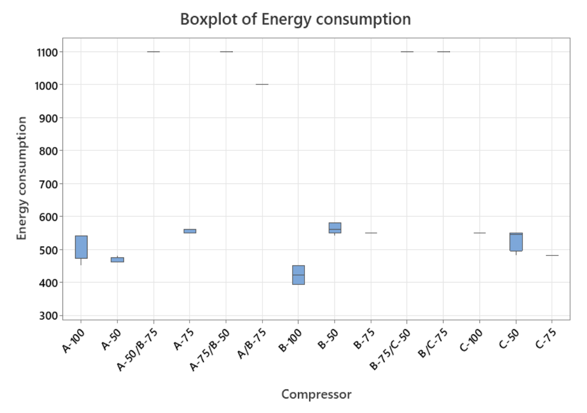

Figure 2. Box plot of compressor (number) and energy consumption (kWh).

DOI: http://dx.doi.org/10.32571/ijct.1199179 **E-ISSN: 2602-277X**

These findings can provide insights into the energy efficiency and performance characteristics of compressors, allowing for further analysis and optimization in terms of energy consumption.

Table 1. Number/capacity of compressors used and amount of energy consumed for the ammonia liquefaction process.

Compressor Number(A,B,C) and Capacity(%)	Energy consumption (kWh)
A(75)+B(75)	1000.0
A(75)+B(75)	1000.0
A(50)	470.0
C(50)	480.0
C(50)	480.0
A(50)	480.0
A(50)	460.0
A(50)	460.0
A(50)	460.0
C(50)	550.0
C(50)	550.0
C(50)	540.0
C(50)	540.0
B(50)	540.0
B(50)	580.0
B(50)	580.0
B(50)	550.0
C(50)	550.0
C(50)	550.0
C(75)	480.0
A(100)	450.0
B(100)	450.0
B(100)	393.7
A(75)	560.0
B(50)	560.0
B(50)	560.0
B(50)	560.0
B(75)	550.0
B(75)	550.0
A(100)	540.0
A(75)	550.0
C(100)	550.0
B(75)+C(75)	1100.0
B(75)+C (75)	1100.0
A(50)+B(75)	1100.0
A(50)+B(75)	1100.0
A(75)+B(50)	1100.0
A(75)+B(50)	1100.0
A(75)+B(50)	1100.0
A (75)+B(50)	1100.0
A(75)+B(50)	1100.0
A(75)+B(50)	1100.0
B(75)+C(50)	1100.0
A(100)	540.0
A(100)	540.0
A(75)	560.0

Statistical evaluation of the number of Compressors used during liquefaction and their energy consumption patterns provides valuable information for evaluating energy efficiency and identifying potential areas for optimization. Analysis of the mean, median, mode, standard deviation, range and count provides a comprehensive understanding of the energy consumption characteristics of each compressor. This information can be used to make informed decisions and develop strategies for energy optimization, leading to more efficient, sustainable compressor operations.

4. CONCLUSIONS

Due to its low boiling point (33°C), ammonia cannot be stored under atmospheric conditions. Compressors used to store ammonia in liquid form alone will not be sufficient to keep ammonia at its boiling point. Condenser and throttling valve are used to achieve this. In this study, liquefaction process was carried out with three two-stage two-cylinder ammonia compressors in three different pressurization capacities as 50%, 75% and 100% in ammonia pressurization process and energy consumption and compressor outlet temperatures were monitored during this pressurization process. When the compression pressure data obtained were examined, although the amount of liquefied ammonia increased as the pressurization capacity of a single compressor increased, the change in the pressure value did not change linearly in parallel with the increase in the capacity value. Therefore, in the interpolation study between pressure and energy consumption values, a predictable energy consumption model is presented for all pressure values according to the modeling process carried out throughout this study. It is seen that the pressure values caused by the amount of liquefied ammonia versus the amount of energy consumed by more than one compressor during compression during operation do not change significantly compared to 75% capacity, but energy consumption increases when more than one compressor is used. In this research study, a similar optimization study was carried out using the 6 sigma statistical analysis method and the compressor capacity needed in energy consumption was determined. In such a calculation model, considering the working capacity of the compressor and the amount of energy consumed, the amount of energy consumed versus the amount of liquefied ammonia is approximately 531.4 kWh, if a single compressor operates at 75% capacity, a plant that produces 2000 tons/day of fertilizer produces its own energy. It can be said that ammonia meets its own needs for the liquefaction process.

Conflict of interests

I declares that there is no a conflict of interest with any person, institute, company, etc.

REFERENCES

1. Horlock, J. H., ASME, *J. Basic Eng.*, **1971**, 93, 587-593.

2. Galvas, M. R., Analytical Correlation of Multi-stage Compressor Design Geometry for Maximum Efficiency with Specific Speed, NASA TN D, 1972;pp. 39-59.

DOI: http://dx.doi.org/10.32571/ijct.1199179 **E-ISSN: 2602-277X**

3. Whitfield, A.; Baines, N. C. A. *Int. J. Mech. Sci.,* **1976**, 18, 179-184.

4. Toyoma, K.; Runstadler, P. W.; Dean, R. C. *J. Fluids Eng.*,**1977**,1, 115-131.

5. Baines, N. C. ; Wallace F. J., *J. Eng. Gas Turbines Power*, **1979**, 101, 440-448

6. Koçak, S., Preliminary Design of Centrifugal Compressors. *ASME*, Energy Week, Engineering Technology, Houston, 1996, p308-313.

7. Rodgers, C., A Diffusion Factor Correlation for Multi-stage Impeller Stalling. *ASME paper* 78- GT-61, 1978.

8. Whitfield, A. ;Baines, N. C., Design of Radial Turbomachines, New York, Longman Scientific Technical, 1990.

9. Koçak, S., *J. Eng. Sci.*, **2001**, 10, 259-265.

10. Aksel, M. H. ; Eralp, O. C., Gas Dynamics, New York, Prentice Hall, 1994.

11. Öztürk, E., Aerothermodynamics of Turbine Engines and Mechanics, Istanbul, Birsen Yayınevi, 1997.

12. Brauembussche, R. A. *NATO ASI Series E,* 1990, 97, 829-885.

13. Koçak, S., *J. Technol*., **2001**, 4 , 119-125

14. Debyendu C., *j. Instrum. Innov. Sci.,* **2014**, 4, pp 1-6

DOI: http://dx.doi.org/10.32571/ijct.1207544 **E-ISSN: 2602-277X**

International Journal of Chemistry and Technology

http://dergipark.org.tr/ijct

Research Article

Production and characterization of polyamide-6 (PA6) and cellulose acetate (CA) based nanofiber membranes by electrospinning method

Abdullah GUL[1*] Ismail TIYEK[2]

[1]*Department of Materials and Energy, Hemp Research Institute, Yozgat Bozok University, 66200, Yozgat, Türkiye*

[2]*Department of Textile Engineering, Faculty of Engineering and Architecture, Kahramanmaras Sutçu İmam University, 46050, Kahramanmaras, Türkiye*

Received: 20 November 2022; Revised: 2 June 2023; Accepted: 9 June 2023

*Corresponding author e-mail: abdullahgul46@gmail.com

Citation: Gul, A.; Tiyek, I. *Int. J. Chem. Technol.* **2023**, 7(1), 91-101.

ABSTRACT

In this study, electrospinning of Polyamide-6 (PA6)/Cellulose Acetate (CA) polymers prepared in different mixing ratios (100/0, 90/10, 80/20, 70/30, 60/40, 50/50) for nanostructured membrane production. It aims to produce nanofiber membranes with the method.
With the study, the average nanofiber diameters of the membranes were calculated. It has been determined that the average diameter of the nanofibers in the structure of the membranes produced by the electrospinning method is between 150 and 300 nm. From the characteristic peak bands obtained as a result of the FTIR analysis, it was determined that the PA6/CA structure was not deteriorated in the nanofiber material. In addition, it was determined that smooth and very fine nanofibers were formed in the materials produced from SEM images. It was observed that the conductivity of the solution decreased with the increase of the CA mixing ratio in the PA6/CA polymer solution and accordingly the fiber diameter became thinner.

Keywords: Nanofiber, membrane, electrospinning, oolyamide-6, cellulose acetate.

Elektrospinning yöntemiyle poliamid-6 (PA6) ve selüloz asetat (CA) esaslı nanofiber membranların üretimi ve karakterizasyonu

ÖZ

Bu çalışmada farklı karışım oranlarında (100/0, 90/10, 80/20, 70/30, 60/40, 50/50) hazırlanan Poliamid-6 (PA6)/Selüloz Asetat (CA) polimerlerinin elektrospinning yöntemi ile nanoyapılı membranların üretilmesi amaçlanmıştır. Çalışma ile membranların ortalama nanolif çapları hesaplanmıştır. Elektrospinning yöntemiyle üretilen membranların yapısındaki nanoliflerin ortalama çapının 150 ile 300 nm arasında olduğu tespit edilmiştir. FTIR analizi sonucunda elde edilen karakteristik pik bantlarından nanolif malzemede PA6/CA yapısının bozulmadığı belirlenmiştir. Ayrıca SEM görüntülerinden üretilen malzemelerde pürüzsüz ve çok ince nanoliflerin oluştuğu belirlenmiştir. PA6/CA polimer çözeltisinde CA karışım oranının artmasıyla çözeltinin iletkenliğinin azaldığı ve buna bağlı olarak fiber çapının inceldiği gözlenmiştir.

Anahtar Kelimeler: Nanolif, membran, elektrospinning, polyamid 6, selüloz asetat.

1.INTRODUCTION

Recently, interest in nano-sized fiber-based materials produced by electrospinning method has increased considerably due to their superior properties (large surface area relative to volume, very small pore size, flexible surface functionality, superior mechanical properties) and common application areas (filtration, composite, medical). Therefore, nano-structured fibers and nanofiber-based materials are becoming increasingly popular and important both in research and development studies and in industry.[1-5]

Electrospinning has become a popular technique for the production of nanofibers with diameters in the range of a few microns and submicrons.[6] Electrospinning method, in which polymeric filaments are produced using electrostatic force, was patented for the first time by Formhals in 1934.[9] Unlike the conventional fiber spinning systems like melt spinning, wet spinning, dry spinning etc., the electrospinning process uses electric field force instead of mechanical force to draw and stretch a polymer jet.[7,8] When an electric field is applied to a polymer solution, the polymer solution will be charged and the charged solution drawn out of the capillary tip. The jet with small diameter will undergo stretching and bending instability. At this stage, the solvent rapidly evaporates and the polymer solution solidifies on a collector in the form of nanofibers.[10]

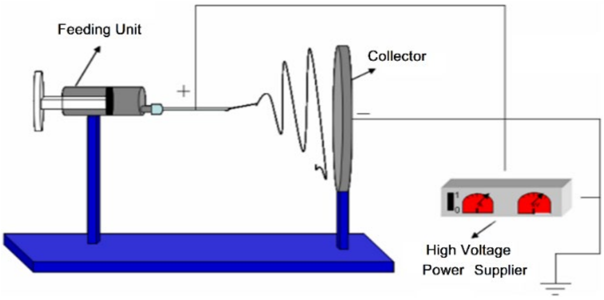

Figure 1. Basic electrospinning system.[10]

A basic electrospinning system mainly consists of a feeding unit, a highvoltage power supplier and a collector (Figure 1).[6,9] The parameters in the electrospinning process can be classified as system, solution and environmental parameters. System parameters are applied electric field, the distance between collector and needle tip, feeding rate of polymer solution, etc., solution parameters are concentration, viscosity, conductivity, surface tension, etc., and environmental parameters are climate humidity, temperature, etc. The structure and morphology of nanofibers are determined by a synergetic effect of system, solution and environmental parameters morphology. For example, finer fiber diameters are spun from smaller diameter needle tips; increasing the fluid ratio results in a larger fiber diameter; higher voltage application reduces the fiber diameter, but a beaded fiber structure emerges.[10,11]

The material properties affecting the electrospinning fiber production technique are as follows; polymer concentration, solution viscosity value, electrical conductivity of the solution and solvent of the polymer. Among the membrane material properties, the solution concentration plays an important role in keeping the nanofiber structure stable. Because it also affects the solution viscosity value, the surface tension of the solution and other characteristic properties of the solution, such as the conductivity value. The type of solvent used is another important factor. Because the solvent property affects the surface tension of the solution and the evaporation process in the electric field. Solvents with volatile properties affect the surface morphology of the fiber and the formation of a wide reticulated structure.[12,13]

PA6 (Figure 2) is a biocompatible and biodegradable synthetic polymer with good mechanical and physical properties. It is generally obtained by ring-opening polymerization of 'ε-caprolactam'. It has a very wide usage area, especially in the textile industry. Electrospinning method is preferred for the production of more robust and biocompatible nanofiber-based scaffolds in tissue engineering applications.[14]

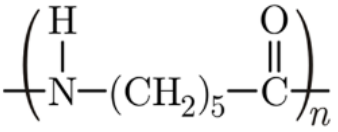

$$\left(\overset{\overset{\displaystyle H}{|}}{N}-(CH_2)_5-\overset{\overset{\displaystyle O}{||}}{C}\right)_n$$

Figure 2. Chemical structure of Polyamide 6.[17]

Cellulose acetate (Figure 3) is the most important organic acid-based cellulose derivative. It is used to obtain plastic products, films and fibers. Film strips obtained from cellulose acetate can preserve their structure for a long time without deteriorating.[15] The most important features of cellulose acetate are; mechanical durability, high wear resistance, dyeability, machinability and mouldability.[16].

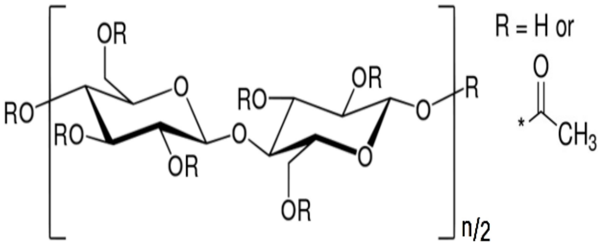

Figure 3. Chemical structure of cellulose acetate.

There has been a huge requirement for efficient water filtration technologies because of population growth, global warming, contamination of freshwater and reduction of clean water resource, and this has prompted increased attention to the development of advanced nanomaterials. Nanofibers are the latest generation of membranes, which contribute extraordinary features. The size-dependent filtration is conceivable by means of nanofiber membranes as they have superior porosity, and this pore size is adjustable through the manufacturing procedure. Consequently, it is time to thoroughly review the different nanofiber production techniques along with their benefits and drawbacks, and use of nanofiber membranes in desalination and water treatment; which will format future trends in the research of nanofiber membranes.[17]

DOI: http://dx.doi.org/10.32571/ijct.1207544 **E-ISSN: 2602-277X**

Membranes, which are the most important parameter of membrane-structured filtration treatment methods, act as an intermediate phase in the form of a semi-permeable barrier between two phases. Membrane processes are classified on the basis of membrane pore sizes and driving force.[18] The functions of the filtration systems and the pore sizes of the membranes are clearly shown in Figure 4.[10]

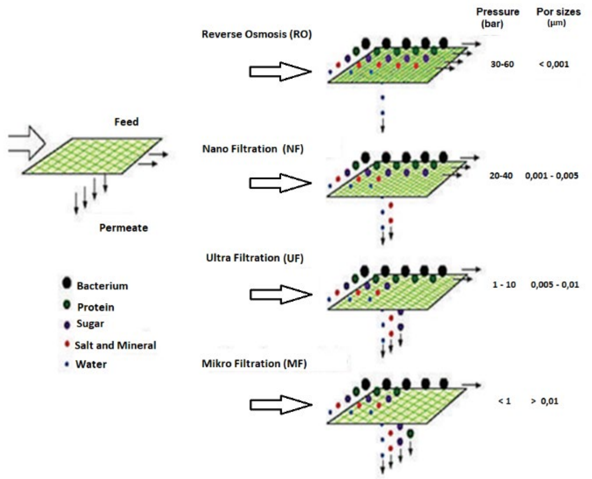

Figure 4. Identification of membranes according to their pore size and the components they capture.[13]

Polyamide 6 (PA6) was selected as a raw material because of the low-cost performance ratio. It also has good mechanical properties such as high tensile strength, flexural strength, and impact resistance. In addition, it is recyclable and has resistant to mildew and bacteria.[19-21] Being hydrophilic, cellulose acetate (CA) offers a good fouling resistance. The fouling of membranes by proteins and other biomolecules is generally attributed to the hydrophobic nature of membranes, which leads to high interfacial energy with water-rich media that is reduced upon biomolecule adsorption.[8] Many researchers have demonstrated that an increase in the hydrophilicity of membranes significantly reduces membrane fouling as a result of the reduced hydrophobic interaction between proteins and membrane surfaces.[11,22-24] In addition, CA is a potentially outstanding ultrafiltration membrane material because of the advantages such as better permeability, moderate flux, high salt rejection properties, relatively easy manufacture, cost-effectiveness, and renewable source of raw material Through this study, the interactions of PA6 and CA polymers have been extensively studied. Analyzes of both solutions and nanofiber membrane structures were performed with different mixing ratios of PA6/CA combinations. This study focused on that the most suitable PA6/CA mixing ratio could be used in the production of nanofiber membranes.

2. MATERIALS AND METHODS

2.1. Materials

PA6 pellet (Formula Weight: 113.6 g/mol, density: 1.084 g/mL), cellulose acetate (CA) ($C_{12}H_{16}O_8$, Mn ~30,000 by GPC), formic acid (HCOOH, >98%) and acetic acid (CH_3COOH, 100%) were obtained from Sigma Aldrich.

2.2. Methods

Solutions were prepared at different mixing ratios, with a total solids content of 20% by weight. A total of 6 different solutions were prepared with these mixed ratios, the ratio of PA6/CA for each solution being 100/0, 90/10, 80/20, 70/30, 60/40 and 50/50 by weight. Formic acid and acetic acid were used as the solvent at a ratio of 1:1. Each solution was first stirred at 50 °C for 30 minutes in a magnetic stirrer with a heater, then stirred at room temperature for 12 hours. The mixed solutions were finally washed for 30 minutes, processed in an ultrasonic bath at room temperature.

Electrospinning processes were carried out on Inovenso brand NanoSpinner PilotLine model semi-industrial multi-needle electrospinning device (Figure 5), located in Kahramanmaraş Sütçü İmam University Materials Research Laboratory in USKIM. During the extraction of the mixtures from the device, parameters such as power, feeding, and needle tip-collector distance were determined with precision. The prepared polymer solutions were placed in the device after being drawn into a 10 mL plastic syringe, respectively. A 48 cm wide white spunbond nonwoven fabric with a weight of 12 g/m^2 and a polypropylene-based, calender-treated base material was used as the base material in the electrospinning device. The electrospinning parameters used in this study to obtain a smooth and continuous nanofiber membrane surface are given in Table 1.

Table 1. Electrospinning production parameters.

Feed Rate (mL/h)	Distance (mm)	Voltage (kV)	Total solid ratio (%)	Membrane ply
0,5±0,1	190	27	20	50

Viscosity values of the solutions used in the production of membrane samples were carried out in Brookfield DV-I + Viscometer device, using spindle no. 4, at room temperature, at 50 and 100 rpm, according to ISO 2555 standard, at two different rotational speeds. For the electrical conductivity analysis of the mixture solutions, it was measured separately as mV in the InoLab PH 7110 brand conductivity measuring device and as µS in the Hanna HI brand conductivity device.

In order to examine the morphological structure of the produced membrane samples, firstly, the samples were gold-plated in a Cressington 108auto gold-plating device,

DOI: http://dx.doi.org/10.32571/ijct.1207544 **E-ISSN: 2602-277X**

and then SEM photographs were taken with the ZEISS brand EVO / LS10 model scanning electron microscope (SEM). The average nanofiber diameters of the membrane samples were determined by making 20 measurements on the SEM images of each sample. Membrane thickness measurements were carried out for each sample in 5 different regions using a digital micrometer. Strength tests were carried out according to EN ISO 2062 standard, with 0.05 MPa prestress at 50 mm/min jaw speed and 12 cm between jaws. Three different strength tests were performed for each sample.

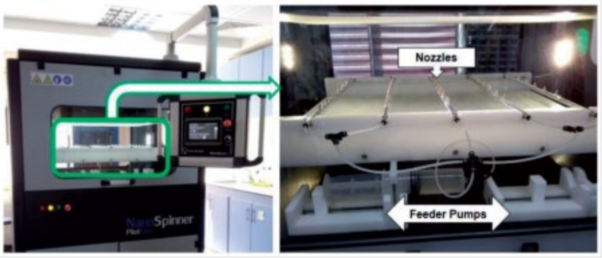

Figure 5. INOVENSO NanoSpinner PilotLine semi-industrial multi-needle electrospinning device.[18]

3. RESULTS AND DISCUSSION

For the characterization of the prepared polymer solutions, their density, electrical conductivity and viscosity were measured. The chemical and morphological structures of the nanofiber filter membrane materials produced by the electrospinning method were investigated by FTIR and SEM analyses, respectively. In addition, thickness and strength tests of nanofiber membranes were carried out.

3.1. Solution characterization studies

In this study, the effects of solution density, electrical conductivity, pH and viscosity values of prepared PA6/CA solutions on the nanofiber structures were investigated.

3.1.1. Solution density analyzes

Density studies of PA6/CA solutions prepared in different mixing ratios (100/0, 90/10, 80/20, 70/30, 60/40 and 50/50) were carried out according to TS ISO 3507 standard. The density graph of PA6/CA solutions prepared at different mixing ratios is given in Figure 6.

As seen in Figure 6, as the weight ratio of CA in the solution at different mixing ratios increases, the density values of the mixed solution also increase. This increase in density can be attributed to the increase in the ratio of CA, whose density value is higher than PA6, in the solution mixing ratio. In addition, the results obtained were found to be compatible with studies in the literature.[25]

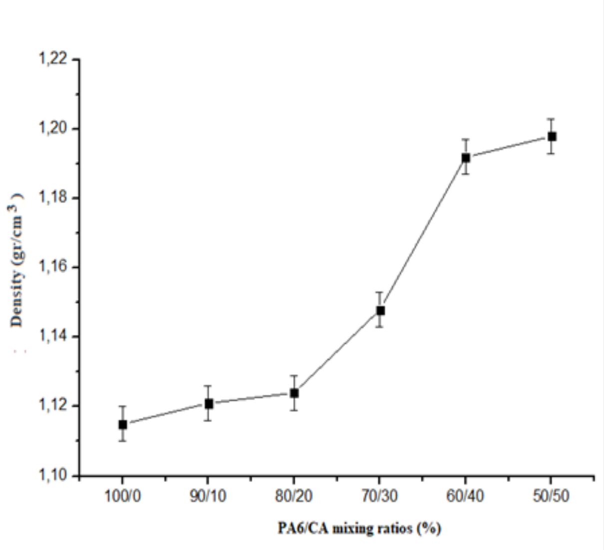

Figure 6. Density values of PA6/CA solutions at different mixing ratios.

3.1.2. Solution conductivity analyzes

Depending on the CA mixing ratios in the solution, the electrical conductivity measurement results of the mixtures are graphically given in Figure 7.

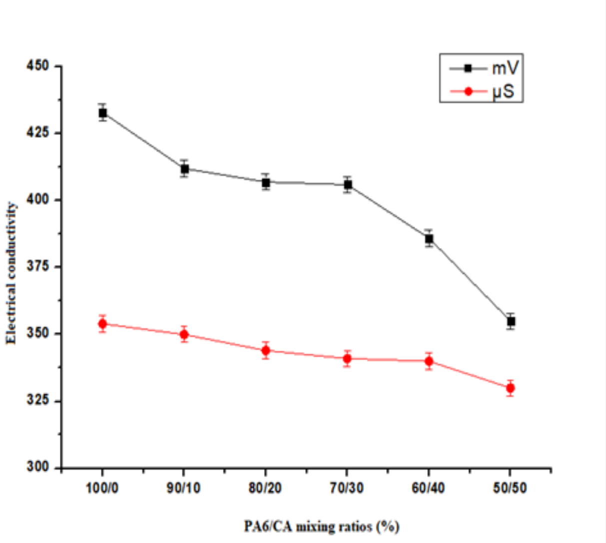

Figure 7. Effect of PA6/CA mixing ratios on the electrical conductivity µS and mV.

The electrical conductivity of the solution decreased with increasing CA in the solution mixing ratios. This decreasing electrical conductivity value directly affected the working process of the polymer solutions with the electrospinning device, and it was observed that the solution solidifications on the jet increased due to the increase in the CA ratio in the polymer mixture.[26]

3.1.3. Solution viscosity analyzes

The viscosity value graph obtained from the kinematic viscosity measurement of the polymer solutions prepared depending on the CA mixing ratios is given in Figure 8. For the viscosity study, the values were compared at two different speeds, 50 and 100 rpm. Viscosity results at both speeds have been found to support each other.

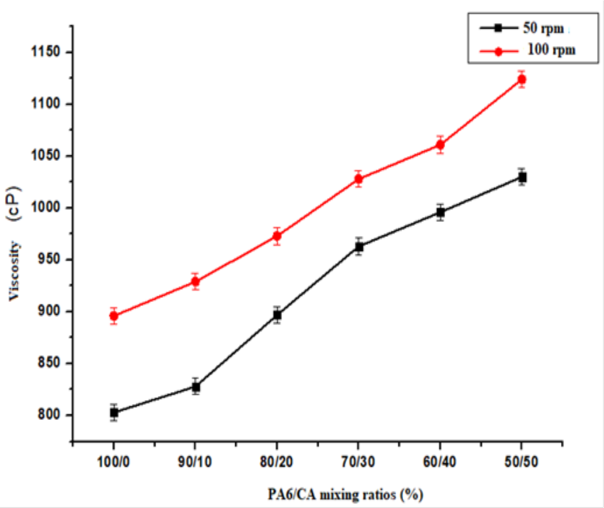

Figure 8. Viscosity value graph of PA6/CA solutions.

According to the results obtained, the viscosity value increased visibly as the CA ratio in the solution mixing ratios increased. In the studies conducted in the literature, studies supporting this result were presented.[27,28]

3.2. Membrane characterization studies

In this section, the effects on FTIR, SEM, membrane thickness and strength values on nanofiber membranes produced depending on the PA6/CA ratios in different mixing ratios obtained by the electrospinning method were investigated.

3.2.1. Fourier transform infrared (FTIR) analysis

FTIR spectra of the pure CA polymer and PA6/CA nanofiber membranes in the wavenumber range of 4000 to 450 cm^{-1} are given in Figure 9. Probable assignments for bands in the FTIR spectrum corresponding to chemical structures are described below.

The FTIR spectrum of 100 % PA6 membrane showed a peak at wavenumber of 3295 cm^{-1}which correspond to the NH bending vibration in primary amine and hydrogen-bonded NH stretching.[29,30] The band at 3095 cm^{-1}was assigned to NH fermi resonance. The peaks at 2933 cm^{-1} and 2856 cm^{-1} were assigned to CH_2 asymmetric and symmetric stretching vibrations, respectively.[30] The bands at 1640 cm^{-1} and 1548 cm^{-1} were assigned to C=O amide I and N–H and C–N combination amide II stretch, respectively.[30,31] The bands of CH_2 scissoring were obeserved at 1460 cm^{-1} and 1435 cm^{-1} .[35] The bands corresponding to vibration of amide III and CH_2 wag were observed at 1367 cm^{-1}, 1262 cm^{-1} and 1208 cm^{-1}.[30,33] The bands at 1170 cm^{-1} and 1118 cm^{-1} were assigned to CONH skeletal motion and CC stretching (amorphous) .[30] The bands at 975 cm^{-1} and 705 cm^{-1} were assigned to CONH in plane vibration(γ) and CH_2 rocking (amide V).[29,30,34]

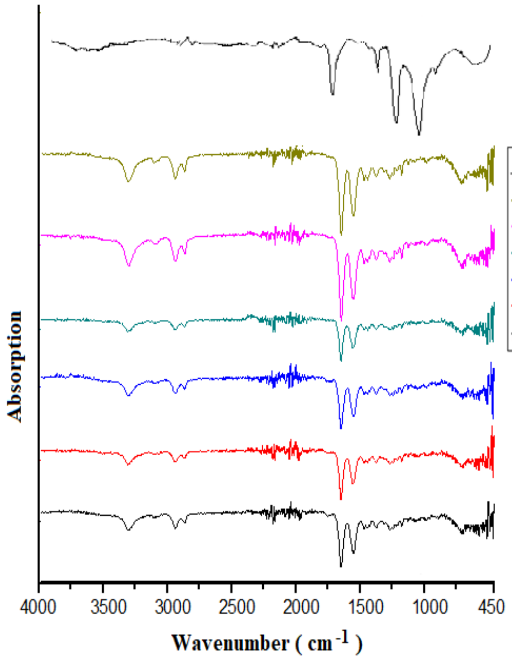

Figure 9. FTIR spectra of PA6/CA nanofiber membranes produced by electrospinning method.

The FTIR spectrum of pure CA polymer showed peaks at wavenumber of 2978 cm^{-1} and 2877 cm^{-1} corresponded to the stretching of C–H of CH_3 and CH_2, respectively.[35-37] The characteristic peaks at 1745 cm^{-1}, 1369 cm^{-1} and 1221 cm^{-1} were attributed to the C=O stretching band of the ester carbonyl group, C–H bending vibration of CH_3 in the acetyl group (CH_3−C=O) and C–O stretching of acetyl group (–O(C=O) –CH_3), respectively.[35,36,38-40] The peak at 1036 cm^{-1}were assigned to C–O–C of the cellulose backbone.[40] The peak at 897 cm^{-1} was attributed to the combined contributions from C-O stretching and CH_2 rocking vibrations.[41]

Peaks of PA6 and CA were detected in PA6/CA nanofiber membranes. However, as a result of the interaction of the chemical structures in PA6 and CA, some shifts in the wavelengths of the peaks and changes in the transmittance values of some of them were observed. It has been observed that the peak values in the FTIR spectrum of PA6/CA nanofiber membranes are fully consistent with the literature.

3.2.2. Scanning electron microscopy (SEM) analysis

SEM images of produced PA6/CA-based nanofiber membrane samples and fiber diameter distribution obtained from SEM images are given in Figure 10.

DOI: http://dx.doi.org/10.32571/ijct.1207544 **E-ISSN: 2602-277X**

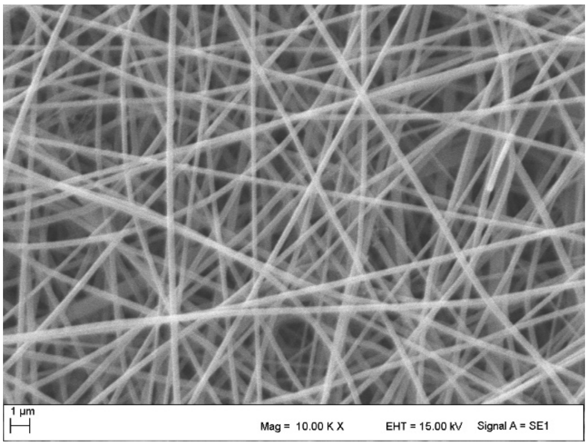

a

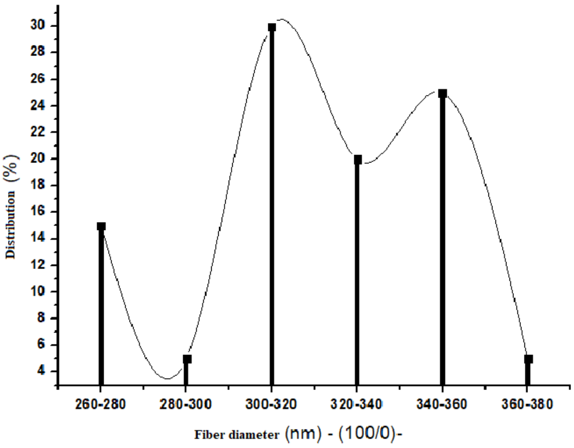

a-1

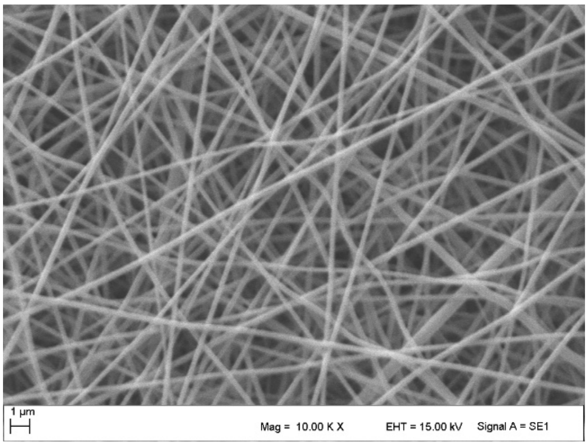

b

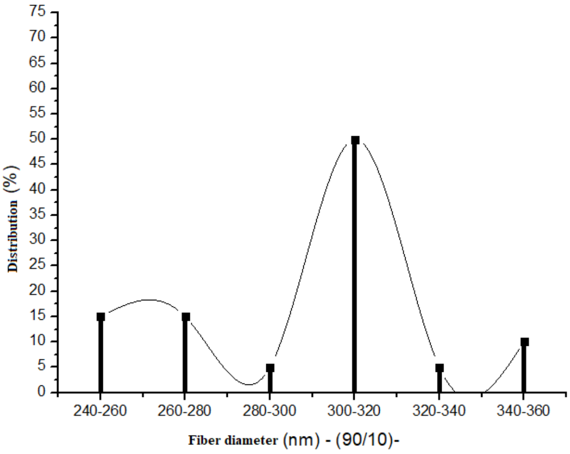

b-1

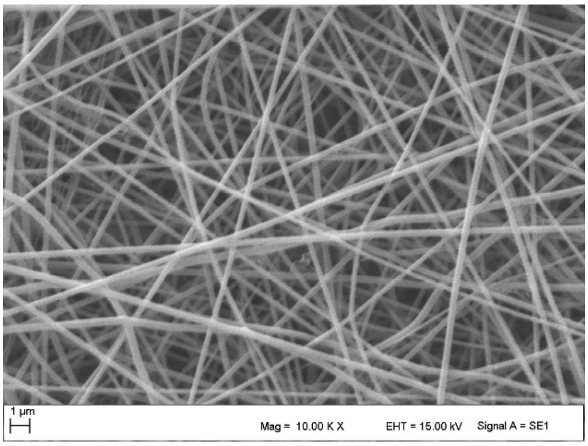

c

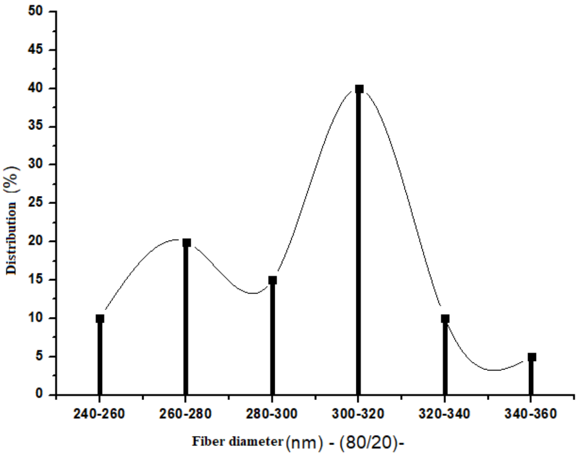

c-1

DOI: http://dx.doi.org/10.32571/ijct.1207544 **E-ISSN: 2602-277X**

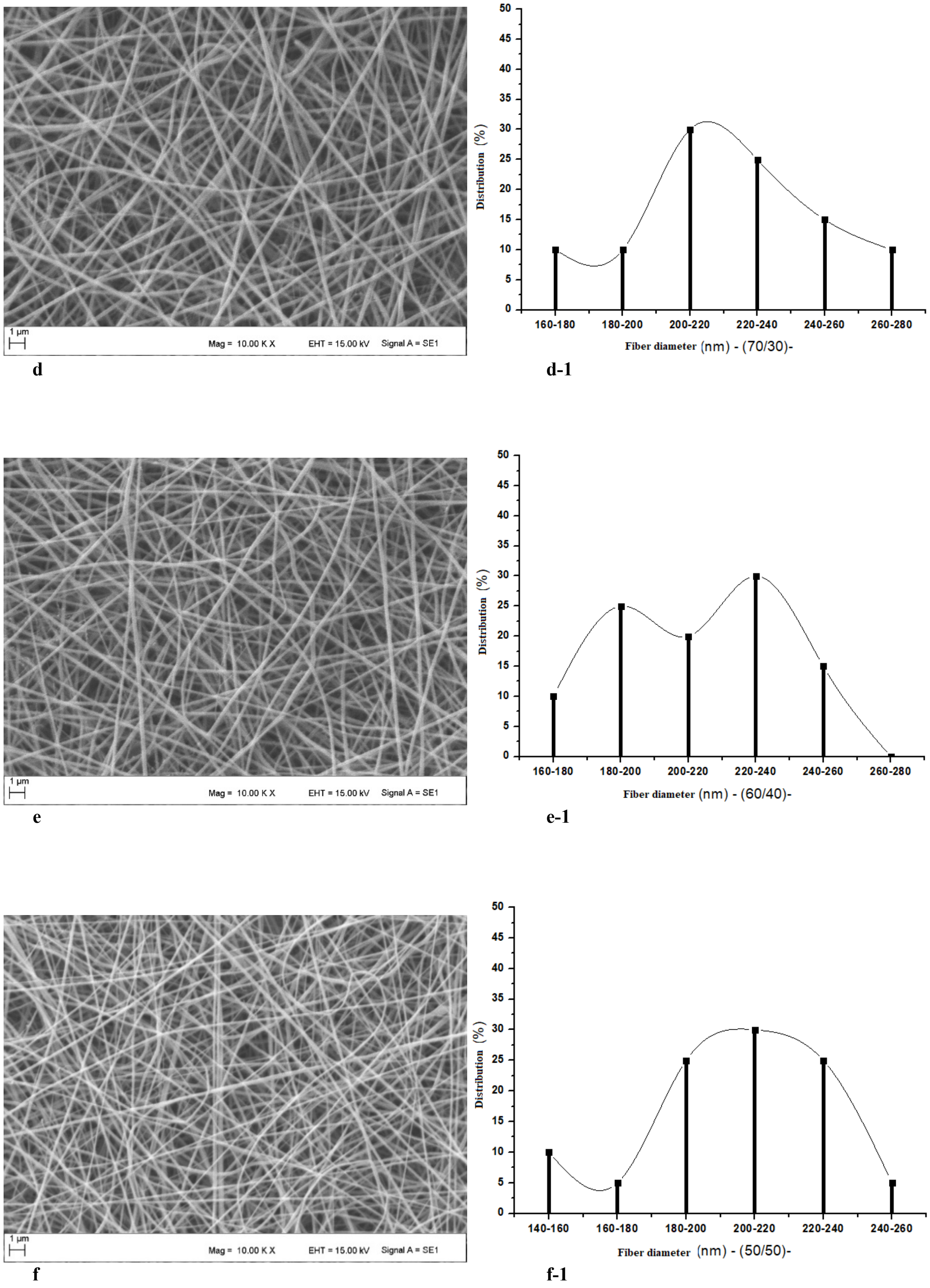

d **d-1**

e **e-1**

f **f-1**

Figure 10. SEM images of nanofiber materials (10 kX) produced by electrospinning method, respectively; a:100/0, b:90/10, c:80/20, d:70/30, e:60/40, f:50/50 and fiber diameter distributions, respectively; a-1:100/0, b-1:90/10, c-1:80/20, d-1:70/30, e-1:60/40, f-1:50/50.

DOI: http://dx.doi.org/10.32571/ijct.1207544 **E-ISSN: 2602-277X**

When the morphological structure of nanofibers obtained from SEM images is examined, nanofiber structures are clearly seen in general. The absence of the bead structure in these images indicates that a suitable viscosity value for the electrospinning process has been achieved. Thus, it shows that a uniform nanofiber structure is formed for all samples.In addition, the graph of average fiber diameter values of 20 different measurements obtained from SEM images of PA6/CA nanofiber membranes prepared at different mixing ratios is given in Figure 11.

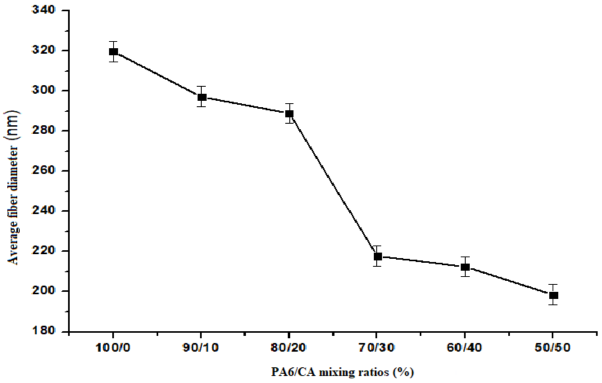

Figure 11. Measured fiber diameter graph of PA6/CA nanofiber membranes at different mixing ratios.

As can be seen in Figure 11, the diameters of the nano-structured membrane fiber can differ with the change in the mass ratios of the PA6 and CA components. In the average fiber diameter evaluation made over the CA mixture ratio, it is seen that the sample with the thinnest average fiber diameters is the sample with 50/50 ratio.

3.2.3. Membrane thickness analysis

The change graph of the membrane thickness values increasing depending on the PA6/CA ratios in different mixing ratios of the membrane structures obtained in nanostructure is shared in Figure 12.

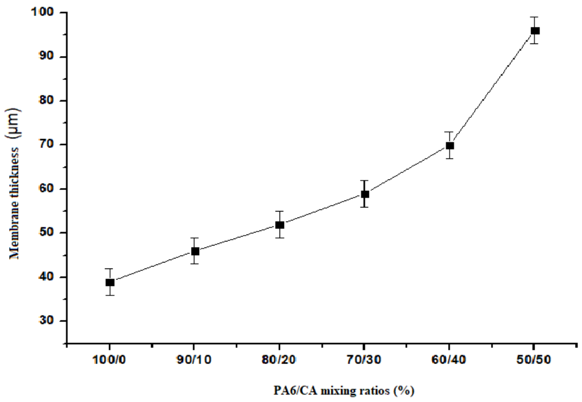

Figure 12. Membrane thickness graph of PA6/CA nanofiber membranes with different mixing ratios.

As seen in Figure 12, it is observed that the thickness measurement values of the obtained membranes increase as the amount of cellulose acetate increases.

It was observed that the obtained membrane thickness values increased with the increase of the CA ratio in the solution with different mixing ratios. It has been determined that these results have produced parallel results with the results in the literature.[42]

3.2.4. Membrane strength properties

The graphs of the membrane mechanical tests for each sample performed depending on the increasing CA ratio in the PA6/CA mixing ratios are in Figure 13, the Young's modulus graph in Figure 14, the elongation graph in Figure 15 and the tensile strength graph in Figure 16. has also been presented.

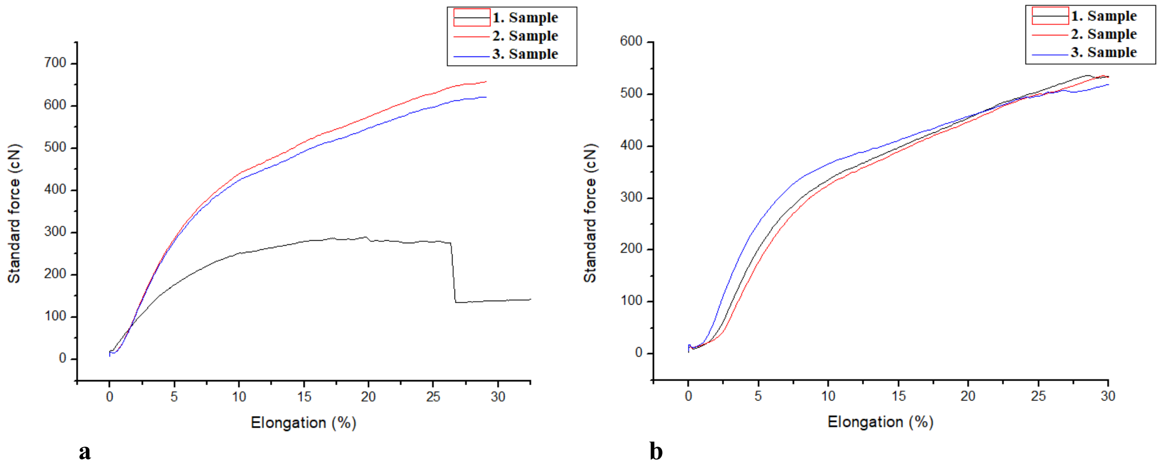

DOI: http://dx.doi.org/10.32571/ijct.1207544 **E-ISSN: 2602-277X**

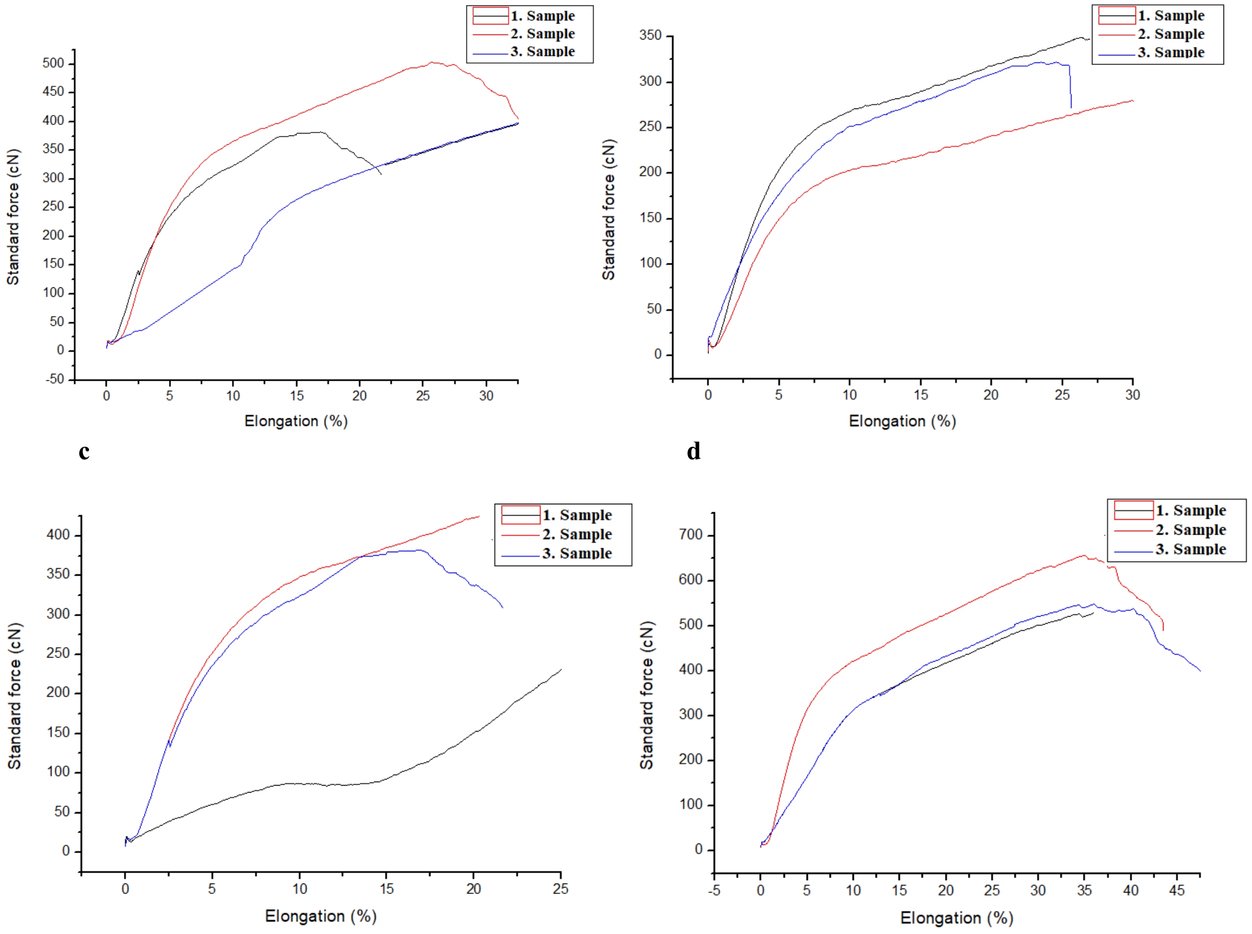

c **d**

e **f**

Figure 13. Tensile strength graphs of PA6/CA membranes at different mixing ratios:(a:50-50, b:60-40, c:70-30, d:80-20, e:90-10, f:100-0).

When the changes in the mechanical properties of the nano-structured membranes were examined with the increase in the ratio of the CA amount in the PA6/CA mixtures, it was observed that the Young's modulus in general increased with the increase in the CA ratio.

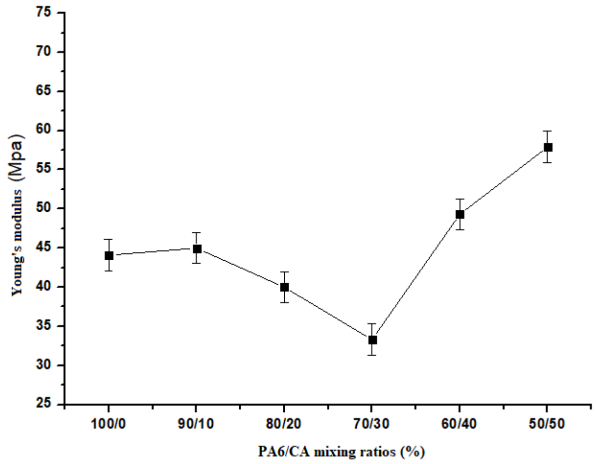

Figure 14. Young's modulus plot of PA6/CA membranes at different mixing ratios.

The result obtained as a result of this observation is compatible with the literature, and Huang et al. attributed this to the formation of high cohesion forces due to the decrease in average fiber diameter.[43] In addition, in another literature study, it was stated that the strength of the nanofibers in the membrane structure increased with the decrease in diameter.[44]

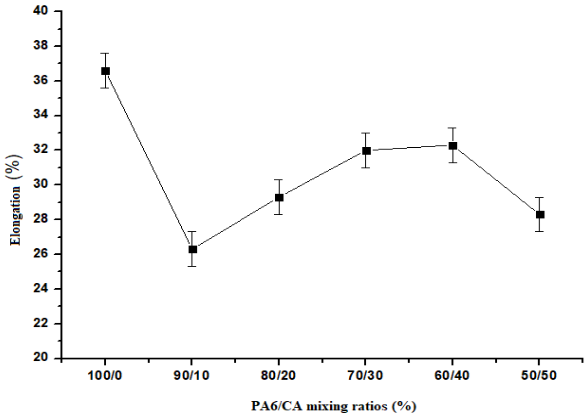

Figure 15. Elongation plot of PA6/CA membranes at different mixing ratios.

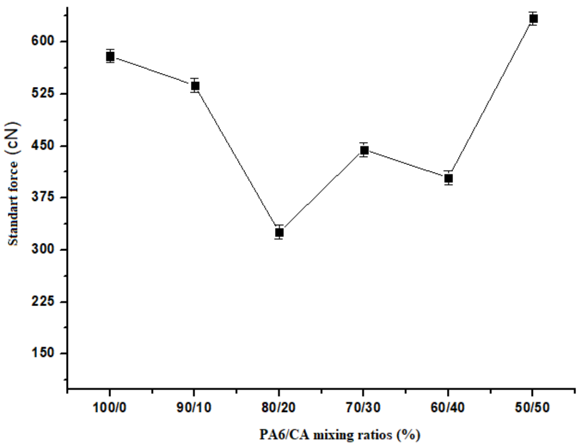

Figure 16. Standard force graph of PA6/CA membranes at different mixing ratios.

4. CONCLUSION

In the study, polymer solutions were prepared from PA6/CA mixtures (100/0, 90/10, 80/20, 70/30, 60/40, 50/50) to produce nanofiber surfaces to be used as filter membranes. The most suitable electrospinning parameters for the production of nanofibers were determined to produce from prepared PA6/CA polymer solutions. Using these parameters, the production of nanofiber surfaces by electrospinning method has been carried out successfully. From the characteristic peak bands obtained as a result of the FTIR analysis, it was determined that the PA6/CA structure was intact in the nanofiber material. In addition, it was determined that smooth and very fine nanofibers were formed in the materials produced from SEM images. It was observed that the conductivity of the solution decreased with the increase of the CA mixing ratio in the PA6/CA polymer solution and accordingly the fiber diameter became thinner. Accordingly, it was concluded that the mechanical properties of the membrane generally increased with the increase in the weight ratio of CA. The results show that these nanofiber surfaces can be used as new membrane materials for industrial applications.

ACKNOWLEDGEMENTS

This study was supported by Kahramanmaras Sütçü İmam University BAP (Scientific Research Projects) unit with project number 2019/1-21D and the 100/2000 PhD scholarship awarded by YÖK (Council of Higher Education) in the field of smart materials.

Conflict of interest

Authors declare that there is no a conflict of interest with any person, institute, company, etc.

REFERENCES

1. Teo, W.E.; Ramakrishna, S. *Nanotechnology*. **2006,** 17(2), 89-106.

2. Gipson, P.; Schreuder-Gibson, H.; Rivin, D. *Nanofibers, Colloids and Surfaces A: Physicochemical and Engineering Aspects*. **2001**, 187/188, 469–481.

3. Lee, K.; Lee, B.; Kim, C.; Kim, H.; Kim, K.; Nah, C. *Macromolecular Research*. **2005**, 13, 441-445.

4. Pedicini, A.; Farris, R.J. *Polymer***.** **2003**, 44, 6857-6862.

5. Çetin, E.; Tiyek, İ. *Journal of the Faculty of Engineering and Architecture of Gazi University*, **2021**, 36(4), 1893-1908.

6. Kılıç, A.; Oruç, F.; Demir, A. *Textile Res. J.* **2008**, 78(6), 532–539.

7. Formhals, A. Process and Apparatus for Preparing Artificial Threads. U.S. Patent 1,975,**504**. 1934.

8. Danwanichakul, P.; Danwanichakul. D.; Sueviriyapan, N.; Sumruan, B. Nylon 6/Chitosan Nanofibrous Structures for Filtration, In Proceedings of the 1st Mae Fah Luang University International Conference, **2012**, 1-18.

9. Kozanoğlu, G.S. Elektrospinning Yöntemiyle Nanolif Üretim Teknolojisi. Masters Thesis İstanbul Technical University, İstanbul, **2006.**

10. Tiyek, İ.; Gündüz, A.; Yalçınkaya, F.; Chaloupek, J. *Journal of Nanoscience and Nanotechnology***.** **2019**, 19, 7251-7260.

11. Deitzel, J.; Kleinmeyer, J.; Harris, D.; Tan, N. *Polymer*. **2001**, 42, 261-272.

12. Yener, F.; Jırsak, O.; Yalçınkaya, B. *Tekstil Tekn. Elekt. Derg.* **2011**.5(2), 26-34.

13. Nirmala, R.; Nam, K.; Soo-Jin, P.; Yu-Shik, S.; Hak, Y.; Kim, H.; Navamathavan, R. *App. Surface Sci.* **2010**, 256: 6318–6323.

14. Nylon 6. wikipedia.org. https://en.wikipedia.org/wiki/Nylon_6. (accessed October 20, **2022**).

15. Kırcı, H.; Ateş, S.; Akgül, M.. *Fen ve Mühendislik Derg.* **2001**, 4(2), 119-130.

16. Ott, E.; Grafflin, M. *Adgewandte Chem.*, **1956**, 68(14), 471.

17. Saleema, H.; Kılıç, A.; Zaidi, S.J. Desalination, **2020**, 478(2020) 1-40.

DOI: http://dx.doi.org/10.32571/ijct.1207544 E-ISSN: 2602-277X

18. Aslan, M. *Membran Teknolojileri*, T.C. Çevre ve Şehircilik Bakanlığı, TUÇEV Türkiye Çevre Koruma Vakfı Yayınları. Ankara, **2016**.

19. Li, L.; Bellan, L.M.; Craighead, H.G.; Frey, M.W. *Polymer*. **2006**, 47, 6208-6217.

20. Li, Q.; Wei, Q.; Wu, N.; Cai, Y.; Gao. W. *J. App. Poly. Sci.* **2008**, 107, 3535–3540.

21. Polat, Y.; Çalışır, M.; Gungor, M.; Sagirli, M.N.; Atakan, R.; Akgul,, Y.; Demir, A.; Kılıç, A. *J. Ind. Text.* **2021**, 51(5), 821-834.

22. Lee, K.H.; Kim, K.W.; Pesapane, A., Kim, H.Y.; Rabolt, J.F. *Macromolecules*. **2008**, 41(4), 1494-1498.

23. Sivakumar, M.; Mohan, D.R.; Rangarajan, R.; J. Memb. Sci. **2006**, 268(2), 208-219.

24. Jayalakshmi, A.; Rajesh, S.; Mohan, D. App. Surf. Sci. **2012**, 258(24), 9770-9781.

25. Shashidhara, G.M.; Guruprasad, K.H.; Varadarajulu, A. *European Poly. J.* **2002**, 38, 611–614.

26. Joshi, M.K.; Tiwari, A.P.; Maharjan, B.; Won, K.S.; Kim, H.J.; Park, C.H.; Kim, C.S. *Carbohydrate Poly.* **2016**, 147, 104-113.

27. Liaoa, N.; Unnithana, A.R.; Joshi, M.K.; Tiwari, A.P.; Hong, S.T.; Parka, C.H.; Kim, C.S. *Kolloidler ve Yüzeyler A: Fizikokimyasal ve Mühendislik Yönleri*. **2015**, 469(1), 194-201.

28. Khaparde, D. *Carbohydrate Poly.* **2017**, 173(1), 338-343.

29. Mindivan, F. *Machines Tech. Mat.* **2016**, 10(11), 56-59.

30. Lee, K.H.; Kim, K.W.; Pesapane, A.; Kim, H.Y.; Rabolt, J.F. *Macromolecules*, **2008**, 41(4), 1494-1498.

31. Kherroub, D.E.; Belbachir, M.; Lamouri, S.; Bouhadjar, L.; Chikh, K. *Oriental J. Chem.* **2013**, 29(4), 1429.

32. Schneider, B.; Schmidt, P.; Wichterle, O. *Collection of Czechoslovak Chem. Com.* **1962**, 27(8), 1749-1759.

33. Meşeli, H. Alifatik Naylon 6 Liflerinin Karbon Lif Üretiminde Hammadde Olarak Değerlendirilmesi ve Karakterize Edilmesi. Masters Thesis Kayseri Erciyes University, Kayseri, **2014**.

34. Karacan, I.; Meşeli, H. *J. Indust. Text.* **2018**, 47(6), 1185-1211.

35. Sudiarti, T.; Wahyuningrum, D.; Bundjali, B.; Arcana, I.M. *Materials Sci. Eng.* **2016**, 223, 120.

36. Song, J.; Liu, M.; Yang, Z.; Xu, S.; Cheng, B.; Fei, P. *e-Polymers*. **2017**, 17(4), 333-340.

37. Hassan, H.S.; Elkady, M.F.; Farghali, A.A.; Salem, A.M.; Abd El-Hamid, A.I. *J. Taiwan Inst. Chem. Eng.* **2016**, 78, 307–316.

38. Cao, Y.; Wu, J.; Meng, T.; Zhang, J.; He, J.; Li, H.; Zhang, Y. *Carbohydrate Poly.* **2007**, 69, 665-672.

39. He, X. *Membranes*. **2017**, 7(27), 1-9.

40. Fei, P.; Liao, L.; Chen, B.; Song, J. *Analytical Methods*. **2017**, 9, 6194-6201.

41. Selvakumar, M.; Bhat, D.K. *J. App. Poly. Sci.* **2008**, 110, 594–602.

42. Chattopadhyay, S.; Hatton, T.A.; Rutledge, G.C.; *J. Mat. Sci.* **2016**, 51(1), 204-217.

43. Huang, L.; McCutcheon, J.R. *J. Memb. Sci.* **2014**, 457, 162-169.

44. Baji, A.; Mai, Y.W.; Wong, S.C.; Abtahi, M.; Chen, P. *Comp. Sci. and Tech.* **2010**,70(5), 703-718.

DOI: http://dx.doi.org/10.32571/ijct.1184571 **E-ISSN: 2602-277X**

International Journal of Chemistry and Technology

http://dergipark.org.tr/ijct

Research Article

Fruit fly (Diptera: Tephritidae) fauna in Tokat province (Türkiye)

Tugce ISINI[1], Murat KUTUK[1], Mehmet YARAN[1*]

[1]*Biology Department of Biology, Faculty of Science and Arts Gaziantep University, 27310 Gaziantep, Türkiye*

Received: 5 October 2022; Revised: 18 May 2023; Accepted: 22 May 2023

*****Corresponding author e-mail: yaran@gantep.edu.tr

Citation: Isini, T.; Kutuk, M.; Yaran, M. I. *Int. J. Chem. Technol.* **2023**, 7(1), 102-107.

ABSTRACT

This study reports the findings of fieldwork based on adult fruit fly samples collected from the province of Tokat in the spring and summer months of 2016–2018. Adult fruit fly samples were caught by using insect nets from possible host plants, taken into killing bottles, and then transferred to storage jars. As a result of the diagnostic procedures, a total of 28 fruit fly species belonging to 11 genera of the Tephritidae family were identified. The findings of this study offered significant contributions to the body of knowledge regarding the determination of the fruit fly fauna of Türkiye and the dispersion of fruit flies in our country.

Keywords: Fauna, fruit-fly, Tephritidae, Tokat, Türkiye.

This research was produced from the first author's MSc thesis.

Tokat ili (Türkiye) meyve sinekleri (Diptera: Tephritidae) faunası

ÖZ

Bu çalışma, 2016–2018 ilkbahar ve yaz aylarında Tokat ilinden toplanan ergin meyve sineği örneklerine dayalı saha çalışmasının bulgularını rapor etmektedir. Yetişkin meyve sineği örnekleri muhtemel konukçu bitkilerden atraplar aracılığıyla yakalanmış, öldürme şişelerine alınmış ve daha sonra saklama kavanozlarına aktarılmıştır. Yapılan teşhis işlemleri sonucunda Tephritidae familyasına ait 11 cinse ait toplam 28 meyve sineği türü tespit edilmiştir. Bu çalışmanın bulguları, Türkiye meyve sineği faunasının belirlenmesi ve ülkemizdeki meyve sineği dağılımına ilişkin bilgi birikimine önemli katkılar sunmaktadır.

Anahtar Kelimeler: Fauna, meyve sineği, Tephritidae, Tokat, Türkiye.

1. INTRODUCTION

The fruit flies (Diptera: Tephritidae) is an economically important Diptera family in terms of cultivated fruits, which has a wide distribution area all over the world. The existence of 4716 species and 492 genera has been reported in the world.[1] However, it is thought that the number of species is increasing by means of described new species in worldwide. In Türkiye, many important faunistic research carried out in the last 20 years and up to date more than 177 species has been reported so far.[2-10] Main purpose of this study, is to identify the fruit fly species found in the Tokat province of Türkiye. As a result of the study, a total of 28 species of fruit flies were identified, and all of the species were reported for the first time from the Tokat province in this study.

2. MATERIALS AND METHODS

Field studies were carried out in 30 different localities in Tokat province (Figure 1) and 728 adult fruit fly samples were collected. The samples were caught by using insect nets over possible host plants, put into killing bottles and brought to Gaziantep University, Department of Biology, Entomology Museum and taken under protection. Dry fruit fly samples were relaxed and prepared for needling, similar to the study.[11] Identification of the samples was made by using the identification keys and species descriptions in previous literature sources.[12-24]

3. RESULTS AND DISCUSSION

3.1. Results

A total of 28 species belonging to 11 genera of Tephritidae were identified. The following list includes examined materials from the identified species. The species are listed alphabetical order.

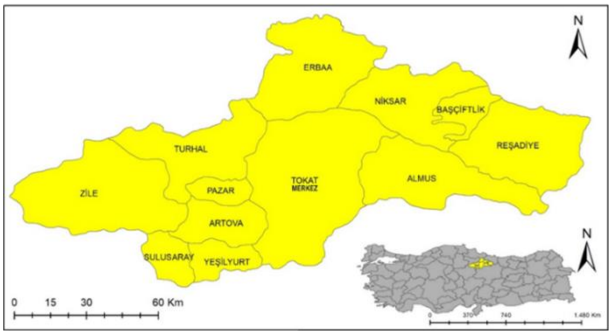

Figure 1. The map of the research region.

Acanthiophilus helianthi (Rossi, 1794)

Examined material: **Tokat**, Center, Kat Town, 40°18' N, 36°04' E, 555 m, 01.05.2016, 1♀, 2♂♂; Center, Çerçi, 40°19' N, 36°25' E, 560 m, 29.05.2016, 2♂♂; Turhal, Güzeldere, 40°17' N, 36°22' E, 598 m, 02.06.2016, 1♀; Center, Çamlıbel Pass, 39°57' N, 36°31' E, 1650 m, 02.06.2016, 2♀♀, 1♂; Almus, Bakımlı, 40°37' N, 36°80' E, 826 m, 17.05.2017, 1♂; Niksar, Gökçeoluk, 40°44' N, 37°03' E, 1239 m, 17.05.2017, 2♀♀; Niksar, Mutluca, 40°25' N, 37°07' E, 436 m, 18.05.2017, 3♀♀, 2♂♂; Niksar, Özdemir, 40°39' N, 36°59' E, 1300 m, 18.06.2017, 4♀♀, 2♂♂; Turhal, Arzupınar, 40°19' N, 36°10' E, 900 m, 29.06.2017, 1♀; Turhal, Küçükbağlar, 40°17' N, 36°19' E, 830 m, 29.06.2017, 1♂; Niksar, Derindere, 40°30' N, 36°55' E, 355 m, 29.06.2017, 1♂; Niksar, 40°34' N, 36°57' E, 856 m, 30.06.2017, 1♀, 2♂♂; Erbaa, Değirmenli, 40°41' N, 36°31' E, 271 m, 01.07.2017, 1♀, 1♂; Turhal, Güzeldere, 40°17' N, 36°22' E, 598 m, 13.06.2018, 2♂♂; Zile, Emirören, 40°18' N, 35°58' E, 810 m, 14.06.2018, 1♀; Reşadiye, Çayırpınar, 40°24' N, 37°16' E, 478 m, 14.06.2018, 2♀♀; Almus, Oğulbey, 40°39' N, 37°00' E, 927 m, 02.08.2018, 2♀♀, 3♂♂; Center, Çamlıbel Pass, 39°57' N, 36°31' E, 1650 m, 02.08.2018, 1♀, 2♂♂.

Chaetorellia jaceae (Robineau-Desvoidy, 1830)

Examined material: **Tokat**, Zile, Akkılıç, 40°14' N, 35°63' E, 749 m, 01.07.2016, 1♀, 2♂♂; Niksar, Gökçeoluk, 40°44' N, 37°03' E, 1239 m, 17.05.2017, 3♀♀, 2♂♂; Zile, Emirören, 40°18' N, 35°58' E, 810 m, 29.06.2017, 1♀, 3♂♂; Reşadiye, Center, 40°22' N, 37°21' E, 690 m, 29.06.2017, 1♀; Erbaa, Değirmenli, 40°41' N, 36°31' E, 271 m, 01.07.2017, 1♂; Zile, Emirören, 40°18' N, 35°58' E, 810 m, 14.06.2018, 1♂; Center, Çamlıbel Pass, 39°57' N, 36°31' E, 1650 m, 02.08.2018, 1♀.

Chaetorellia loricata (Rondani, 1830)

Examined material: **Tokat**, Erbaa, Değirmenli, 40°41' N, 36°31' E, 271 m, 01.07.2017, 1♀, 1♂.

Euaresta bullans Wiedemann, 1830

Examined material: **Tokat**, Center, Kat Town, 40°18' N, 36°04' E, 555 m, 01.05.2016, 15♀♀, 21♂♂; Center, Çerçi, 40°19' N, 36°25' E, 560 m, 29.05.2016, 3♀♀, 5♂♂; Zile, Akkılıç, 40°14' N, 35°63' E, 749 m, 01.07.2016, 7♀♀, 6♂♂; Reşadiye, Çayırpınar, 40°24' N, 37°16' E, 478 m, 18.05.2017, 2♀♀, 4♂♂; Zile, Emirören, 40°18' N, 35°58' E, 810 m, 29.06.2017, 3♀♀, 1♂; Center, Kılıçlı, 40°21' N, 36°38' E, 775 m, 29.06.2017, 3♀♀, 7♂♂; Niksar, Güdüklü, 40°33' N, 36°52' E, 300 m, 01.07.2017, 5♀♀, 2♂♂; Erbaa, Değirmenli, 40°41' N, 36°31' E, 271 m, 01.07.2017, 1♀, 1♂; Turhal, Güzeldere, 40°17' N, 36°22' E, 598 m, 13.06.2018, 6♀♀, 8♂♂; Turhal, Arzupınar, 40°19' N, 36°10' E, 900 m, 05.07.2018, 1♀, 2♂♂; Center, Çamlıbel Pass, 39°57' N, 36°31' E, 1650 m, 02.08.2018, 3♀♀, 5♂♂.

Myopites cypriacus (Hering, 1938)

Examined material: **Tokat**, Niksar, Güdüklü, 40°33' N, 36°52' E, 300 m, 01.07.2017, 1♀, 1♂.

Orellia stictica (Gmelin, 1790)

Examined material: **Tokat**, Erbaa, Değirmenli, 40°41' N, 36°31' E, 271 m, 01.07.2017, 1♀, 2♂♂.

Sphenella marginata (Fallen, 1814)

Examined material: **Tokat**, Niksar, Gülçeşme, 40°35' N, 36°49' E, 260 m, 01.05.2016, 2♀♀; Center, Çamlıbel Pass, 39°57' N, 36°31' E, 1650 m, 02.06.2016, 2♂♂; Almus, Bakımlı, 40°37' N, 36°80' E, 826 m, 17.05.2017, 1♀; Reşadiye, Çayırpınar, 40°24' N, 37°16' E, 478 m, 18.05.2017, 1♂; Niksar, Mutluca, 40°25' N, 37°07' E, 436 m, 18.05.2017, 1♂; Turhal, Küçükbağlar, 40°17' N, 36°19' E, 830 m, 29.06.2017, 1♀, 2♂♂; Reşadiye, Center, 40°22' N, 37°21' E, 690 m, 29.06.2017, 1♀, 2♂♂; Niksar, Gülçeşme, 40°35' N, 36°49' E, 260 m, 13.06.2018, 1♀, 1♂; Reşadiye, Çayırpınar, 40°24' N, 37°16' E, 478 m, 14.06.2018, 1♀, 1♂; Almus, Oğulbey, 40°39' N, 37°00' E, 927 m, 02.08.2018, 2♀♀; Center, Çamlıbel Pass, 39°57' N, 36°31' E, 1650 m, 02.08.2018, 1♂.

Tephritis bardanae (Schrank, 1803)

Examined material: **Tokat**, Niksar, Gökçeoluk, 40°44' N, 37°03' E, 1239 m, 17.05.2017, 1♀, 3♂♂; Zile, Emirören, 40°18' N, 35°58' E, 810 m, 29.06.2017, 1♀; Erbaa, Değirmenli, 40°41' N, 36°31' E, 271 m, 01.07.2017, 1♂; Zile, Emirören, 40°18' N, 35°58' E, 810 m, 14.06.2018, 1♀; Almus, Oğulbey, 40°39' K, 37°00' E, 927 m, 02.08.2018, 1♂.

Tephritis divisa Rondani, 1871

Examined material: **Tokat**, Center, Kat Town, 40°18' N, 36°04' E, 555 m, 01.05.2016, 2♂♂; Niksar, Gülçeşme, 40°35' N, 36°49' E, 260 m, 01.05.2016, 1♀; Artova, Madas, 40°10' N, 36°26' E, 1138 m, 02.06.2016, 3♀♀, 2♂♂; Almus, Bakımlı, 40°37' N, 36°80' E, 826 m, 17.05.2017, 2♀♀, 1♂; Niksar, Mutluca, 40°25' N, 37°07'

DOI: http://dx.doi.org/10.32571/ijct.1184571 **E-ISSN: 2602-277X**

E, 436 m, 18.05.2017, 2♀♀; Niksar, Özdemir, 40°39' N, 36°59' E, 1300 m, 18.06.2017, 1♂; Turhal, Küçükbağlar, 40°17' N, 36°19' E, 830 m, 29.06.2017, 1♂; Niksar, 40°34' N, 36°57' E, 856 m, 30.06.2017, 1♀; Erbaa, Değirmenli, 40°41' N, 36°31' E, 271 m, 01.07.2017, 1♂; Zile, Emirören, 40°18' N, 35°58' E, 810 m, 14.06.2018, 2♂♂; Turhal, Arzupınar, 40°19' N, 36°10' E, 900 m, 05.07.2018, 1♀; Center, Çamlıbel Pass, 39°57' N, 36°31' E, 1650 m, 02.08.2018, 1♀.

Tephritis formosa (Loew, 1844)

Examined material: **Tokat**, Center, Kat Town, 40°18' N, 36°04' E, 555 m, 01.05.2016, 2♀♀; Center, Çerçi, 40°19' N, 36°25' E, 560 m, 29.05.2016, 1♀, 2♂♂; Center, Çamlıbel Pass, 39°57' N, 36°31' E, 1650 m, 02.06.2016, 1♂; Almus, Bakımlı, 40°37' N, 36°80' E, 826 m, 17.05.2017, 2♂♂; Reşadiye, Çayırpınar, 40°24' N, 37°16' E, 478 m, 18.05.2017, 1♂; Niksar, Özdemir, 40°39' N, 36°59' E, 1300 m, 18.06.2017, 1♀; Turhal, Küçükbağlar, 40°17' N, 36°19' E, 830 m, 29.06.2017, 1♂; Reşadiye, Center, 40°22' N, 37°21' E, 690 m, 29.06.2017, 1♀, 1♂.

Tephritis nigricauda (Loew, 1856)

Examined material: **Tokat**, Erbaa, Değirmenli, 40°41' N, 36°31' E, 271 m, 01.07.2017, 1♀, 1♂.

Tephritis postica (Loew, 1844)

Examined material: **Tokat**, Center, Kat Town, 40°18' N, 36°04' E, 555 m, 01.05.2016, 3♀♀; Niksar, Gülçeşme, 40°35' N, 36°49' E, 260 m, 01.05.2016, 2♂♂; Turhal, Güzeldere, 40°17' N, 36°22' E, 598 m, 02.06.2016, 1♀, 3♂♂; Artova, Madas, 40°10' N, 36°26' E, 1138 m, 02.06.2016, 2♂♂; Zile, Akkılıç, 40°14' N, 35°63' E, 749 m, 01.07.2016, 2♀♀, 4♂♂; Almus, Oğulbey, 40°39' N, 37°00' E, 927 m, 17.05.2017, 2♀♀; Niksar, Gökçeoluk, 40°44' N, 37°03' E, 1239 m, 17.05.2017, 3♀♀, 2♂♂; Niksar, Özdemir, 40°39' N, 36°59' E, 1300 m, 18.06.2017, 2♀♀, 2♂♂; Turhal, Küçükbağlar, 40°17' N, 36°19' E, 830 m, 29.06.2017, 4♀♀, 2♂♂; Niksar, Derindere, 40°30' N, 36°55' E, 355 m, 29.06.2017, 1♀, 2♂♂; Niksar, Güdüklü, 40°33' N, 36°52' E, 300 m, 01.07.2017, 2♂♂; Niksar, Gülçeşme, 40°35' N, 36°49' E, 260 m, 13.06.2018, 2♀♀; Zile, Emirören, 40°18' N, 35°58' E, 810 m, 14.06.2018, 1♂; Turhal, Arzupınar, 40°19' N, 36°10' E, 900 m, 05.07.2018, 1♀, 3♂♂; Center, Çamlıbel Pass, 39°57' N, 36°31' E, 1650 m, 02.08.2018, 3♀♀, 2♂♂.

Tephritis simplex (Loew, 1844)

Examined material: **Tokat**, Erbaa, Değirmenli, 40°41' N, 36°31' E, 271 m, 01.07.2017, 1♀, 1♂.

Tephritomyia lauta (Loew, 1869)

Examined material: **Tokat**, Center, Kat Town, 40°18' N, 36°04' E, 555 m, 01.05.2016, 2♀♀, 3♂♂; Turhal, Güzeldere, 40°17' N, 36°22' E, 598 m, 02.06.2016, 2♀♀, 5♂♂; Zile, Akkılıç, 40°14' N, 35°63' E, 749 m, 01.07.2016, 3♀♀, 1♂; Niksar, Gökçeoluk, 40°44' N, 37°03' E, 1239 m, 17.05.2017, 1♂; Reşadiye, Çayırpınar, 40°24' N, 37°16' E, 478 m, 18.05.2017, 2♀♀; Pazar, Center, 40°17' N, 36°19' E, 552 m, 18.05.2017, 3♀♀, 4♂♂; Turhal, Arzupınar, 40°19' N, 36°10' E, 900 m, 29.06.2017, 1♀, 4♂♂; Niksar, Derindere, 40°30' N, 36°55' E, 355 m, 29.06.2017, 2♀♀, 2♂♂; Niksar, Güdüklü, 40°33' N, 36°52' E, 300 m, 01.07.2017, 2♂♂; Erbaa, Değirmenli, 40°41' N, 36°31' E, 271 m, 01.07.2017, 1♂; Niksar, Gülçeşme, 40°35' N, 36°49' E, 260 m, 13.06.2018, 2♀♀, 3♂♂; Reşadiye, Çayırpınar, 40°24' N, 37°16' E, 478 m, 14.06.2018, 1♂; Turhal, Arzupınar, 40°19' N, 36°10' E, 900 m, 05.07.2018, 2♀♀; Almus, Oğulbey, 40°39' N, 37°00' E, 927 m, 02.08.2018, 3♂♂; Center, Çamlıbel Pass, 39°57' N, 36°31' E, 1650 m, 02.08.2018, 1♀, 1♂.

Trupanea amoena (Frauenfeld, 1857)

Examined material: **Tokat**, Niksar, Gülçeşme, 40°35' N, 36°49' E, 260 m, 01.05.2016, 1♂; Artova, Madas, 40°10' N, 36°26' E, 1138 m, 02.06.2016, 1♀; Almus, Oğulbey, 40°39' N, 37°00' E, 927 m, 17.05.2017, 1♀; Niksar, Mutluca, 40°25' N, 37°07' E, 436 m, 18.05.2017, 1♂; Zile, Emirören, 40°18' N, 35°58' E, 810 m, 29.06.2017, 1♂; Center, Kılıçlı, 40°21' N, 36°38' E, 775 m, 29.06.2017, 1♀; Niksar, 40°34' N, 36°57' E, 856 m, 30.06.2017, 1♀; Erbaa, Değirmenli, 40°41' N, 36°31' E, 271 m, 01.07.2017, 1♂; Reşadiye, Çayırpınar, 40°24' N, 37°16' E, 478 m, 14.06.2018, 1♀, 1♂; Center, Çamlıbel Pass, 39°57' N, 36°31' E, 1650 m, 02.08.2018, 1♂.

Trupanea stellata (Fuesslin, 1775)

Examined material: **Tokat**, Artova, Madas, 40°10' N, 36°26' E, 1138 m, 02.06.2016, 1♂; Pazar, Center, 40°17' N, 36°19' E, 552 m, 18.05.2017, 1♂; Turhal, Arzupınar, 40°19' N, 36°10' E, 900 m, 29.06.2017, 1♀; Erbaa, Değirmenli, 40°41' N, 36°31' E, 271 m, 01.07.2017, 1♂.

Terellia gynaecochroma (Hering, 1937)

Examined material: **Tokat**, Niksar, Gülçeşme, 40°35' N, 36°49' E, 260 m, 01.05.2016, 1♀; Center, Çamlıbel Pass, 39°57' N, 36°31' E, 1650 m, 02.06.2016, 1♂; Reşadiye, Çayırpınar, 40°24' N, 37°16' E, 478 m, 18.05.2017, 1♀; Zile, Emirören, 40°18' N, 35°58' E, 810 m, 29.06.2017, 1♂; Center, Kılıçlı, 40°21' N, 36°38' E, 775 m, 29.06.2017, 1♀, 1♂; Reşadiye, Center, 40°22' N, 37°21' E, 690 m, 29.06.2017, 1♂; Niksar, 40°34' N, 36°57' E, 856 m, 30.06.2017, 2♀♀; Turhal, Güzeldere, 40°17' N, 36°22' E, 598 m, 13.06.2018, 1♀, 2♂♂; Reşadiye, Çayırpınar, 40°24' N, 37°16' E, 478 m, 14.06.2018, 2♀♀; Turhal, Arzupınar, 40°19' N, 36°10' E, 900 m, 05.07.2018, 1♂.

Terellia luteola (Wiedemann, 1830)

Examined material: **Tokat**, Niksar, Gökçeoluk, 40°44' N, 37°03' E, 1239 m, 17.05.2017, 1♀, 1♂; Niksar, Derindere, 40°30' N, 36°55' E, 355 m, 29.06.2017, 1♀; Niksar, Güdüklü, 40°33' N, 36°52' E, 300 m, 01.07.2017, 1♀; Erbaa, Değirmenli, 40°41' N, 36°31' E, 271 m, 01.07.2017, 1♀, 1♂.

Terellia quadratula (Loew, 1869)

Examined material: **Tokat**, Reşadiye, Center, 40°22' N, 37°21' E, 690 m, 29.06.2017, 2♀♀, 5♂♂.

Terellia serratulae (Linnaeus, 1758)

Examined material: **Tokat**, Niksar, Gülçeşme, 40°35' N, 36°49' E, 260 m, 01.05.2016, 1♂; Turhal, Güzeldere, 40°17' N, 36°22' E, 598 m, 02.06.2016, 1♀; Center, Çamlıbel Pass, 39°57' N, 36°31' E, 1650 m, 02.06.2016, 6♀♀, 4♂♂; Almus, Oğulbey, 40°39' N, 37°00' E, 927 m, 17.05.2017, 1♂; Reşadiye, Çayırpınar, 40°24' N, 37°16' E, 478 m, 18.05.2017, 8♀♀, 4♂♂; Zile, Emirören, 40°18' N, 35°58' E, 810 m, 29.06.2017, 9♀♀, 11♂♂; Center, Kılıçlı, 40°21' N, 36°38' E, 775 m, 29.06.2017, 1♀, 2♂♂; Niksar, Gülçeşme, 40°35' N, 36°49' E, 260 m, 13.06.2018, 12♀♀, 15♂♂; Turhal, Arzupınar, 40°19' N, 36°10' E, 900 m, 05.07.2018, 2♀♀, 6♂♂; Center, Çamlıbel Pass, 39°57' N, 36°31' E, 1650 m, 02.08.2018, 3♀♀, 2♂♂.

Terellia virens (Loew, 1846)

Examined material: **Tokat**, Center, Kat Town, 40°18' N, 36°04' E, 555 m, 01.05.2016, 2♀♀, 2♂♂; Center, Çerçi, 40°19' N, 36°25' E, 560 m, 29.05.2016, 1♀; Artova, Madas, 40°10' N, 36°26' E, 1138 m, 02.06.2016, 2♀♀, 3♂♂; Zile, Akkılıç, 40°14' N, 35°63' E, 749 m, 01.07.2016, 1♀, 4♂♂; Reşadiye, Çayırpınar, 40°24' N, 37°16' E, 478 m, 18.05.2017, 1♀, 1♂; Pazar, Center, 40°17' N, 36°19' E, 552 m, 18.05.2017, 2♀♀; Niksar, Özdemir, 40°39' N, 36°59' E, 1300 m, 18.06.2017, 1♂; Turhal, Arzupınar, 40°19' N, 36°10' E, 900 m, 29.06.2017, 6♀♀; Turhal, Küçükbağlar, 40°17' N, 36°19' E, 830 m, 29.06.2017, 2♀♀, 2♂♂; Center, Kılıçlı, 40°21' N, 36°38' E, 775 m, 29.06.2017, 1♀, 2♂♂; Niksar, Güdüklü, 40°33' N, 36°52' E, 300 m, 01.07.2017, 2♀♀, 1♂; Almus, Oğulbey, 40°39' N, 37°00' E, 927 m, 02.08.2018, 2♀♀, 3♂♂.

Urophora affinis (Frauenfeld, 1857)

Examined material: **Tokat**, Niksar, Gülçeşme, 40°35' N, 36°49' E, 260 m, 01.05.2016, 8♀♀, 5♂♂; Center, Çerçi, 40°19' N, 36°25' E, 560 m, 29.05.2016, 7♀♀, 6♂♂; Turhal, Güzeldere, 40°17' N, 36°22' E, 598 m, 02.06.2016, 3♀♀, 1♂; Zile, Akkılıç, 40°14' N, 35°63' E, 749 m, 01.07.2016, 1♀, 5♂♂; Niksar, Gökçeoluk, 40°44' N, 37°03' E, 1239 m, 17.05.2017, 2♀♀, 6♂♂; Pazar, Center, 40°17' N, 36°19' E, 552 m, 18.05.2017, 4♀♀, 4♂♂; Turhal, Arzupınar, 40°19' N, 36°10' E, 900 m, 29.06.2017, 2♀♀, 1♂; Turhal, Küçükbağlar, 40°17' N, 36°19' E, 830 m, 29.06.2017, 3♀♀, 5♂♂; Center, Kılıçlı, 40°21' N, 36°38' E, 775 m, 29.06.2017, 2♀♀, 5♂♂; Reşadiye, Center, 40°22' N, 37°21' E, 690 m, 29.06.2017, 1♀; Niksar, Güdüklü, 40°33' N, 36°52' E, 300 m, 01.07.2017, 5♀♀, 7♂♂; Turhal, Güzeldere, 40°17' N, 36°22' E, 598 m, 13.06.2018, 4♀♀, 3♂♂; Reşadiye, Çayırpınar, 40°24' N, 37°16' E, 478 m, 14.06.2018, 1♀, 3♂♂; Almus, Oğulbey, 40°39' N, 37°00' E, 927 m, 02.08.2018, 5♀♀, 4♂♂.

Urophora congrua Loew, 1862

Examined material: **Tokat**, Erbaa, Değirmenli, 40°41' N, 36°31' E, 271 m, 01.07.2017, 1♀, 1♂.

Urophora cuspidata (Meigen, 1826)

Examined material: **Tokat**, Erbaa, Değirmenli, 40°41' N, 36°31' E, 271 m, 01.07.2017, 3♀♀, 2♂♂.

Urophora jaceana (Hering, 1935)

Examined material: **Tokat**, Niksar, Gülçeşme, 40°35' N, 36°49' E, 260 m, 01.05.2016, 4♀♀, 5♂♂; Artova, Madas, 40°10' N, 36°26' E, 1138 m, 02.06.2016, 2♀♀; Center, Çamlıbel Pass, 39°57' N, 36°31' E, 1650 m, 02.06.2016, 1♂; Almus, Oğulbey, 40°39' N, 37°00' E, 927 m, 17.05.2017, 2♂♂; Reşadiye, Çayırpınar, 40°24' N, 37°16' E, 478 m, 18.05.2017, 1♀; Niksar, Özdemir, 40°39' N, 36°59' E, 1300 m, 18.06.2017, 2♀♀; Turhal, Arzupınar, 40°19' N, 36°10' E, 900 m, 29.06.2017, 2♂♂; Center, Kılıçlı, 40°21' N, 36°38' E, 775 m, 29.06.2017, 1♀; Reşadiye, Center, 40°22' N, 37°21' E, 690 m, 29.06.2017, 1♂; Erbaa, Değirmenli, 40°41' N, 36°31' E, 271 m, 01.07.2017, 2♀♀, 3♂♂; Turhal, Güzeldere, 40°17' N, 36°22' E, 598 m, 13.06.2018, 1♀; Reşadiye, Çayırpınar, 40°24' N, 37°16' E, 478 m, 14.06.2018, 1♀, 1♂; Almus, Oğulbey, 40°39' N, 37°00' E, 927 m, 02.08.2018, 1♂; Center, Çamlıbel Pass, 39°57' N, 36°31' E, 1650 m, 02.08.2018, 2♀♀, 1♂.

Urophora mauritanica (Macquart, 1851)

Examined material: **Tokat**, Center, Kılıçlı, 40°21' N, 36°38' E, 775 m, 29.06.2017, 1♀; Niksar, Derindere, 40°30' N, 36°55' E, 355 m, 29.06.2017, 7♀♀, 5♂♂; Erbaa, Değirmenli, 40°41' N, 36°31' E, 271 m, 01.07.2017, 4♂♂.

Urophora quadrifasciata (Meigen, 1826)

Examined material: **Tokat**, Center, Çerçi, 40°19' N, 36°25' E, 560 m, 29.05.2016, 1♀; Center, Çamlıbel Pass, 39°57' N, 36°31' E, 1650 m, 02.06.2016, 1♀, 2♂♂; Reşadiye, Çayırpınar, 40°24' N, 37°16' E, 478 m, 18.05.2017, 2♀♀, 2♂♂; Zile, Emirören, 40°18' N, 35°58' E, 810 m, 29.06.2017, 1♂.

Urophora stylata (Fabricius, 1775)

Examined material: **Tokat**, Center, Kat Town, 40°18' N, 36°04' E, 555 m, 01.05.2016, 2♀♀, 3♂♂; Center, Çerçi, 40°19' N, 36°25' E, 560 m, 29.05.2016, 1♀; Turhal, Güzeldere, 40°17' N, 36°22' E, 598 m, 02.06.2016, 2♂♂; Artova, Madas, 40°10' N, 36°26' E, 1138 m, 02.06.2016, 1♀; Zile, Akkılıç, 40°14' N, 35°63' E, 749 m, 01.07.2016, 2♀♀; Almus, Oğulbey, 40°39' N, 37°00' E, 927 m, 17.05.2017, 2♀♀, 2♂♂; Pazar, Center, 40°17' N, 36°19' E, 552 m, 18.05.2017, 1♀, 3♂♂; Turhal, Arzupınar, 40°19' N, 36°10' E, 900 m, 29.06.2017, 1♀, 2♂♂; Center, Kılıçlı, 40°21' N, 36°38' E, 775 m, 29.06.2017, 1♂; Reşadiye, Center, 40°22' N, 37°21' E, 690 m, 29.06.2017, 1♀, 1♂; Niksar, Güdüklü, 40°33' N, 36°52' E, 300 m, 01.07.2017, 1♀, 1♂; Erbaa, Değirmenli, 40°41' N, 36°31'

DOI: http://dx.doi.org/10.32571/ijct.1184571 **E-ISSN: 2602-277X**

E, 271 m, 01.07.2017, 1♂; Niksar, Gülçeşme, 40°35' N, 36°49' E, 260 m, 13.06.2018, 2♀♀, 1♂; Zile, Emirören, 40°18' N, 35°58' E, 810 m, 14.06.2018, 3♀♀, 2♂♂; Turhal, Arzupınar, 40°19' N, 36°10' E, 900 m, 05.07.2018, 2♀♀, 1♂; Center, Çamlıbel Pass, 39°57' N, 36°31' E, 1650 m, 02.08.2018, 1♀, 1♂.

4. DISCUSSION

Fruit flies are an important family of flies that have been the subject of many studies. With the faunistic studies carried out in Türkiye, the fauna of many regions has been determined and important contributions have been made to the literature with the data obtained. These contributions also laid the groundwork for molecular and morphological studies. It is likely that future studies will make significant contributions both to the of fruit fly fauna of Türkiye and in other fields.[25-29]

ACKNOWLEDGEMENTS

The authors are grateful to YYÜ Scientific Research Projects Presidency for their financial support for project numbered 2013-FBE-D058.

Conflict of interests

I declares that there is no a conflict of interest with any person, institute, company, etc.

REFERENCES

1. Pape, T.; Vladimir, B.; Mikhail, B.M. **2011**, *Zootaxa*, 3148: 222-229.

2. Yaran, M.; Kütük, M.; Görmez, V.; Koyuncu, M.Ö. **2018a**, *Turk. J. Zool.*, 42: 661-665.

3. Yaran, M.; Kütük, M.; Görmez, V.; Koyuncu, M.Ö. **2018b**, *Biodivers. Conserv.*, 11(3): 141-144.

4. Çalışkan, Keçe, A.F.; Çatal, B.Ö.; Ulusoy, M.R. **2019**, *Turk. Entomol. Derg.-Tu.*, 43(1): 25-30.

5. Görmez, V.; Kütük, M. **2020**, *Turk. Entomol. Derg.-Tu.* 44(1): 23-38.

6. Kütük, M.; Yaran, M. **2020**, *Turk. Entomol. Derg-Tu.*, 22(2): 215-222.

7. Yaran, M.; Görmez, V. **2020**, *Zootaxa*, 4838(2):283-288.

8. Yaran, M.; Görmez, V.; Koyuncu, M.Ö. **2021**, *Turk. J. Food Agric. Sci.*, 9(12): 2233-2237.

9. Görmez, V.; Kütük, M. **2022**, *KSU J. Agric Nat.*, 25 (4): 723-734.

10. Yaran, M.; Görmez, V.; Koyuncu, M.Ö.; Tarla, G. **2023**, *J. Entomol. Res. Soc.*, 25(1):137-141.

11. Koyuncu, M.Ö.; Kütük, M. **2022**, *KSU J. Agric Nat.*, 25 (1): 127-132.

12. Hendel, F. **1927**, 49. Trypetidae die Fliegen der Palaerktischen Region, E. Schweizerbart: Stuttgard. 221 p.

13. White, I.M. **1988**, Tephritid flies (Diptera: Tephritidae). Handbook for the identification of British insects. Dorset Press, London.

14. White, I. M.; Marquardt, K.A. **1989**, *Bull. Entomol. Res*. P. 453–487.

15. Freidberg, A.; Kugler, J. **1989,** Fauna Palaestina Insecta IV. Diptera: Tephritidae. Israel at Keterpress Enterprises: Jerusalem, 212 p.

16. Korneyev, V.A.; White, I.M. **1993**, *Ent. Obozr.*, 72(1): 232–247.

17. Korneyev, V.; White, I.M. **1999**, *Ent. Obozr.*, 78(2): 464 – 482.

18. Kütük M. Güneybatı Anadolu bölgesi Tephritidae faunası ve sistematiği üzerine araştırmalar. Doktora Tezi. Çukurova Üniversitesi, Fen Bilimleri Enstitüsü: Adana, 2003a.

19. Korneyev, V.A. **2003**, *Vestn. Zool.*, 37(3): 3–12.

20. Korneyev, V.A. **2006**, *Isr. J. Entomol.*, 36: 341-366.

21. Kütük, M. **2006**, *Turk. J. Zool.*, 30: 345-356.

22. Korneyev, V.A.; Evstigneev, D.A.; Karimpour, Y.; Kütük, M.; Mohamadzade, Namin, S.; Koyuncu M.Ö.; Yaran M. **2013**. *Vestn. Zool.*, 47 (1): 3-25.

23. Merz, B. **1994**, Diptera, Tephritidae. Insecta Helvetica fauna, HGE pres: Geneva. 74.

24. Yaran, M. Aksaray, Mersin, Nevşehir ve Niğde illerinde meyve sinekleri (Diptera: Tephritidae) faunası ve sistematiği üzerine araştırmalar. Doktora Tezi. Gaziantep Üniversitesi, Fen Bilimleri Enstitüsü, Gaziantep, **2014**.

25. Akpınar, A.; Junaid, F.; Görmez, V.; Kütük, M.; Can, C. **2019**. *KSÜ Tarım ve Doğa Derg,* 22(2): 361-364.

26. Kütük, M.; Junaid, F. M.; Akpinar, A.; Görmez, V.; Can, C. **2022.** *Entomological News*, 130(2), 137-150.

27. Yaran, M.; Özkan Koca, A.; Kütük, M. **2021**, *Türk. Entomol. Derg.*, 45(3):295-304.

28. Kütük, M.; Doğan, E.; Yaran, M. **2018**, *Türk. Entomol. Derg.,* 41(3):319-324.

29. Kütük, M.; Doğan, E. **2020**. *KSU J. Agric Nat*, 23 (1): 172-180.

DOI: http://dx.doi.org/10.32571/ijct.1186924 **E-ISSN: 2602-277X**

International Journal of Chemistry and Technology

http://dergipark.org.tr/ijct

Research Article

Evaluation of the genotoxic effect of nonylphenol applied in different doses on the bone marrow

Nazmiye BITGEN[1,2*], Ozge GOKTEPE[3,2], Munevver BARAN[4], Eren Kaan IPEK[1], Arzu YAY[3,2]

[1]*Department of Medical Biology, Faculty of Medicine, Erciyes University, Kayseri, Türkiye*

[2]*Genome and Stem Cell Center (GENKOK), Erciyes University, Kayseri, Türkiye*

[3]*Department of Histology and Embryology, Faculty of Medicine, Erciyes University, 38039 Kayseri, Türkiye*

[4]*Department of Pharmaceutical Basic Science, Faculty of Pharmacy, Erciyes University, Kayseri, Türkiye*

Received: 10 September 2022; Revised: 24 April 2023; Accepted: 9 May 2023

*Corresponding author e-mail: nazmiyebitgen@gmail.com.tr

Citation: Bitgen, N.; Goktepe, Ö.; Baran, M.; Ipek, E. K.; Yay, A. *Int. J. Chem. Technol.* **2023**, 7 (1), 108-112.

ABSTRACT

Nonylphenols are endocrine disrupting toxic compounds and are widely used. For this reason, our study aimed to investigate the genotoxic effect of nonylphenols applied at different doses on mouse bone marrow cells. Groups were classified as control group, the sham administered only group, low dose, medium dose and high dose nonylphenol administered group. After euthanasia, polychromatic erythrocyte/Normochromatic erythrocyte ratio and micronuclear polychromatic erythrocyte count were determined in femur bone marrow cells and analyzed to detect DNA damage. While polychromatic erythrocyte/Normochromatic erythrocyte ratio was found to be lower in the groups treated with different doses of nonylphenol, especially in the group treated with high-dose nonylphenol, this decrease was not statistically significant. When the micronucleated polychromatic erythrocyte values were examined, it was observed that there was a statistically significant increase, especially in the medium and high dose groups compared to the control. High-dose nonylphenol has a toxic effect and may have a long-term genotoxic effect such as cancer development by interacting with genotoxic agents.

Keywords: Nonylphenol, genotoxicity, micronucleus.

Farklı dozajlarda uygulanan nonylphenol'ün kemik iliği üzerine genotoksik etkisinin değerlendirilmesi

ÖZ

Nonilfenoller; endokrin bozucu toksik bileşiklerden olup yaygın olarak kullanılmaktadır. Bu sebeple çalışmamızda farklı dozlarda uygulanan Nonilfenoller'in, fare kemik iliği hücreleri üzerine genotoksik etkisinin araştırılması amaçlanmıştır. Gruplar; kontrol grubu, sadece sham uygulanan grup, düşük doz, orta doz ve yüksek doz nonilfenol uygulanan grup olacak şekilde sınıflandırıldı. Ötenazi sonrası, femur kemik iliği hücrelerinde Polikromatik eritrosit/Normokromatik eritrosit oranı ile mikroçekirdekli polikromatik eritrosit sayısı belirlenerek DNA hasarını tespit etmek için analizleri yapıldı. Farklı dozlarda nonilfenol uygulanan gruplardan özellikle yüksek doz nonilfenol uygulanan grupta Polikromatik eritrosit/Normokromatik eritrosit oranı kontrole düşük bulunurken, bu azalma istatistiksel olarak anlamlı değildi. Mikroçekirdekli polikromatik eritrosit değerlerine bakıldığında ise özellikle orta ve yüksek doz gruplarında kontrole göre istatistiksel olarak anlamlı derecede bir artış olduğu gözlendi. Yüksek doz nonilfenol toksik etki göstermekte olup, genotoksik ajanlarla etkileşerek kanser gelişimi gibi uzun vadeli genotoksik etkiye sahip olabilir.

Anahtar Kelimeler: Nonilfenol, genotoksisite, mikronükleus.

1. INTRODUCTION

Short-term, low-dose exposure to xenobiotics may not cause any permanent effects on DNA, but chronic exposure to xenobiotics can cause mutations and future cancer.[1] Nonylphenol (NP) is one of the xenobiotic compounds frequently encountered in many environments directly or indirectly.[2] NP is a degradation product of plastic compounds used in the manufacture of dentistry, food packaging, textiles, pesticides, detergents,

DOI: http://dx.doi.org/10.32571/ijct.1186924 **E-ISSN: 2602-277X**

paints, and cosmetics.[3] NP is of great interest as a hazardous pollutant due to its long-term persistence in the environment and multiple toxic effects.[4] Trace consumption of NPs in food and water is thought to be the main source of human exposure.[5] It has been stated that NP has a DNA damaging effect due to its biotransformation to reactive intermediates that can cause changes in DNA.[6] Most of the previous studies have focused on the toxicity of 4-NP and its effects on the developmental process and reproductive system, especially in aquatic ecosystems, were evaluated.[7,8] Little information is available about its genotoxic effect on bone marrow. The micronucleus (MN) test, which is one of the popular tests preferred in the evaluation of environmental genotoxicity, is an indicator of cytogenetic damage.[9] MN is produced from fragments of chromosomes or whole chromosomes that are delayed in cell division due to centromere deficiency, damage to the centromere, or defects in cytokinesis. In actively dividing cells, the MN number reflects the effect of clastogenic or aneugenic compounds.[10] The MN test, which is easy to apply, is used to determine the damage of these agents. An increase in the number of MN in cells is a marker of genomic instability in somatic cells.[9]

When hematopoietic cells divide, the application of various chemicals results in chromosome damage or the suppression of mitosis.[11] Bone marrow (BM) is the main hematopoietic organ in adult rodents. Erythrocytes are used in the micronucleus test, which is studied with mouse bone marrow. After transforming into polychromatic erythrocytes (PCE), erythroblasts lose their nuclei approximately 6 hours after mitosis. In this way, it is easier to determine the formation of MN.[12]An increase in the amount of immature PCE containing MN (MNPCE) is a sign of chromosomal or cytogenetic damage caused by anaphase delay.[11] The significant decrease observed in the polychromatic erythrocyte/normochromatic erythrocyte (PCE/NCE) ratio indicates that the applied chemical exerts a cytotoxic effect on the division and maturation of nucleated cells.[13] This study aimed to investigate the genotoxic effect of nonylphenol applied at different doses on rat BM cells.

2. MATERIALS AND METHODS

An ethics committee approval (20/077) was obtained from the Erciyes University Animal Experiments Local Ethics Committee for the realization of this study. In the study, 50 male Wistar-albino rats, 8-10 weeks old, were reared in the Erciyes University Experimental and Clinical Research Center. The rats weighed between 200 and 250 g. The rats were housed in plastic cages and fed with normal pellets under standard laboratory conditions throughout the study.

2.1. Chemicals and working groups

In the study, Nonylphenol (cat no:84852-15-3, Sigma-Aldrich) were obtained from the project and used. Groups were created as following; 50 Wistar-albino adult male rats were divided into 5 groups with 10 rats in each group. Doses were determined for all applications and administered at the same time of the day. Anesthesia was administered intraperitoneally 24 hours after the last administration with ketamine hydrochloride (50 mg kg^{-1}) and 2% xylazine hydrochloride (10 mg kg^{-1}). After removing the femoral bone of each rat, the BM was placed in an eppendorf tube.

Control group: No intervention was administered.

Sham group: 150 µL of corn oil was given via gavage for 15 days.

Low Dose Nonylphenol group: 25 µL dose of nonylphenol dissolved in 125 µL corn oil was given for 15 days via gavage.

Medium Dose Nonylphenol group: 50 µL dose of nonylphenol dissolved in 100 µL corn oil was given for 15 days via gavage.

High Dose Nonylphenol group: 75 µL dose of nonylphenol dissolved in 75 µL of corn oil was given via gavage for 15 days.

2.2. Micronucleus test

Rats' femurs were removed by cervical dislocation. The supernatant was discarded by centrifugation at 2000 rpm for 7 minutes. The remainder was suspended in 0.5 mL fetal calf serum and spread on slides. After fixing with methanol, it was painted with 20% Giemsa dye for 30 minutes and left to dry at room temperature. Each rat was coded from the BM to prepare four preparations, and the prepared preparations were covered with entellan. For genotoxic activity, 1000 PCEs were randomly counted from the preparation prepared for each rat at X100 magnification in all groups under the microscope (Olympus BX51, Tokyo, Japan). Their percentages were calculated by determining the MNPCE numbers in them. In addition, the PCE/NCE ratio was determined by counting 2000 erythrocytes to show cytotoxicity.[14]

2.3. Statistical analysis

Statistical analyses of the data were performed using the Graphpad PRISM (Graphpad Software Inc., Version 8.0d) software program. The conformity of the data to the normal distribution was determined by the Shapiro-Wilk and Kolmogorov-Smirnov tests. Percent vitality values according to doses were compared with one sample t-test. A one-way Anova test was used to compare normally distributed data in multiple comparisons, and Kruskal-

Wallis tests were used to compare non-normally distributed data. Post-hoc comparisons of the variables that were significant as a result of group comparisons were made with the Bonferroni test for the one-way Anova test and Dunn's test for the Kruskal-Wallis test. $p < 0.05$ was considered statistically significant.

3. RESULTS AND DISCUSSION

3.1. Micronucleus frequency in control and experimental groups

For the MN test, a total of 1.000 PCEs were counted in the BM preparations of each animal, and the percentage of PCEs with MN in them was determined (MNPCE) (Figure 1). In total, 10.000 cells were counted per group (10 rats per group). The change in the frequency of MN depending on the dose is given in Figure 2. In addition, PCE/NCE ratios were calculated by counting 2.000 erythrocytes from each rat sample, that is, 20.000 erythrocytes (PCE and NCE) for each group. Table 1 displays the MNPCE and PCE/NCE ratios determined for the control and experimental groups.

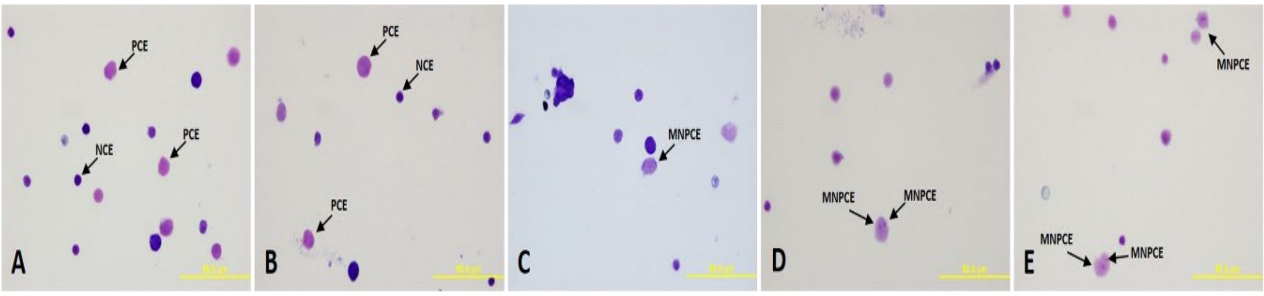

Figure 1. Polychromatic erythrocytes (PCE), normochromatic erythrocytes (NCE), and micronucleated polychromatic erythrocytes (MNPCE) in rat BM (Giemsa staining X40, Olympus BX51). A) Control group, B) Sham group, C) Low-dose group, D) Medium-dose group, and E) High-dose group.

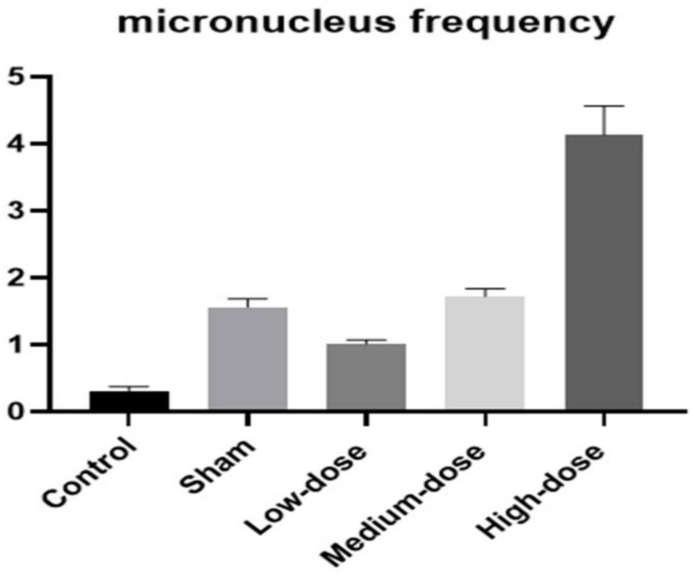

Figure 2. Change of micronucleus frequency according to groups.

Table 1. PCE/NCE ratio and MNPCE frequencies between different groups.

Groups (n=10)	**Control group (mean±SD)**	**Sham group (mean±SD)**	**Low-dose group (mean±SD)**	**Medium-dose group (mean±SD)**	**High-dose group (mean±SD)**	**p**
PCE/NCE	(0.99 ± 0.37)^{ac}	(1.44 ± 0.34)^{ab}	(1.61 ± 0.26)^{b}	(1.92 ± 0.51)^{b}	(0.65 ± 0.32)^{c}	< 0.0001
MNPCE, %	(0.31 ± 0.20)^{a}	(1.56 ± 0.38)^{b}	(1.01 ± 0.19)^{ab}	(1.72 ± 0.36)^{b}	(4.13 ± 1.38)^{c}	< 0,0001

DOI: http://dx.doi.org/10.32571/ijct.1186924 E-ISSN: 2602-277X

3.2. PCE/NCE ratios in control and experimental groups

When the PCE/NCE ratios were considered, it was found that the high-dose NP group was lower than the control group. However, this change was not statistically significant ($p = 0.4595$). When the MNPCE values were examined, a statistically significant increase was observed in the medium and high dose groups compared to the control (respectively $p = 0.0002$, $p < 0.0001$). At the same time, a statistically significant increase was observed when the high-dose NP-administered group was compared with the low-and medium-dose NP-administered groups ($p < 0.0001$).

Genotoxic agents are substances that disrupt genetic material by causing adverse effects on cell DNA. Genotoxic effects cause mutation. Mutations can manifest themselves with various idiosyncratic and allergic reactions, as well as with carcinogenic effects. For this reason, it is of great importance to investigate and reveal mutating agents in terms of health. Some pharmaceutical and chemical substances, cytotoxic agents used in cancer treatment, radioactive drugs, or wastes containing such substances can cause genotoxic effects. While such genotoxic substances can be directly effective, some of them are activated by metabolic reactions and cause genotoxicity.[15]

Identifying mutagenic and toxic substances is particularly important because of their potential to cause cancer and cause adverse changes in future generations. From this point of view, the risk associated with the DNA-damaging effect caused by NP needs scientific studies to deepen its knowledge. In a previous study, mice were subchronically exposed to X-rays (0.05 Gy and 0.10 Gy), nonylphenol (NP) (25 mg kg^{-1} and 50 mg kg^{-1}), or a combination of both. As a result of the study, it was stated that NP increased the DNA damage both when used alone and in combination with X-rays.[5] Dobrzynska[5] investigated the effects of NP and ionizing radiation on DNA damage in mouse (male and female) somatic cells, separately or in combination, using the Comet Assay Method. The induction of DNA damage by NP differs according to tissue and gender. Although NP alone is not mutagenic in female mice, it has been shown to increase DNA damage in some organs with combined administration, whereas in male mice the damage has been shown to be reduced after exposure. At the same time, there are different studies in which the frequency of MN increases after exposure to 4-NP.[16,17] In this study, unlike other studies, the effect of NP on DNA damage in the BM was evaluated depending on the dose by administering three different low, medium, and high doses of NP.

4. CONCLUSIONS

According to our results, the increases in NP cause significant increases in MNPCE in cells. Due to the activation of the chemical in the bone marrow, the erythrocytes in the division phase could not perform the correct division. As the nonylphenol dose increases, genomic instability increases, preventing cells from adopting the correct structures. Therefore, the genomic instability occurring in erythrocytes, and mature erythrocyte formation cannot be observed. The low number of NCEs in the microscopic field is important proof that the transition of cells to the mature erythrocyte is less. Additionally, it is also conceivable that NPs have negative effects on specific transcription control mechanisms that are affected during the mitosis stage. As a result of our findings, the toxicity of NP increases depending on the dose increases, especially high-dose NP. From this point of view, it shows that when NP interacts with other genotoxic agents, it may cause an increase in long-term genotoxic effects such as cancer development, and it shows that care should be taken about the use of NP in daily life. We believe that these findings will shed light on further studies to find new agents to be used against the genotoxicity of NP.

ACKNOWLEDGEMENTS

This study (project no: TCD-2021-11459) was supported by Erciyes University Scientific Research Projects Coordination Unit.

Ethics Committee Approval

Erciyes University Ethics Committee (2020/077).

Conflict of interests

I declares that there is no a conflict of interest with any person, institute, company, etc.

REFERENCES

1. Ozdemir, F.; Kayaaltı, Z.; Dilek, K. A. *Marmara Pharm. J.* **2015**, 19(3), 246-251.

2. Zemheri, F.; Cevdet, U. *Marmara Üniv. Fen Bilim. Derg.* **2018**, 30(1), 71-76.

3. Urriola-Muñoz, P.; Li, X.; Maretzky, T.; McIlwain, D.R.; Mak, T.W.; Reyes, J.G.; Blobel, C.P.; Moreno, D. *J. Cell. Physiol.* **2018**, 233(3), 2247-2256.

4. Abou Khalil, N. S.; Abd-Elkareem, M.; Sayed, A. H. *Aquac. Nutr.* **2017**, 23(6), 1467-1474.

5. Dobrzyńska, M. M. *Mutat. Res. Genet. Toxicol. Environ. Mutagen.* **2014**, 772, 14-19.

6. Vazquez-Duhalt, R.; Marquez-Rocha, F.; Ponce, E.; Licea, A.F.; Vaiana, M.T. *Appl. Ecol. Environ. Res.* **2005**, 4:1-25.

7. Wu, F.; Lin, L.; Qiu, J.W.; Chen, H.; Weng, S.; Luan, T. *Aquat. Toxicol.* **2014**, 155, 43-51.

DOI: http://dx.doi.org/10.32571/ijct.1186924 **E-ISSN: 2602-277X**

8. Shirdel, I.; Mohammad, R.K. *Comp. Biochem. Physiol. C Toxicol. Pharmacol.* **2016**, 183-184, 28-35.

9. Fenech, M.; Chang, W. P.; Kirsch-Volders, M.; Holland, N.; Bonassi, S.; Zeiger, E. *Mut. Res.* **2003**, 534, 65-75.

10. Baršienė, J.; Dedonytė, V.; Rybakovas, A.; Andreikėnaitė, L.; Andersen, O. K. *Aquat. Toxicol.* **2006**, 78, 99-104.

11. Lambert, I.B.; Singer, T.M.; Boucher, S.E.; Douglas, G.R. *Mutat. Res.* **2005**, 590, 1-280.

12. Mavourni, K.H.; Blakey, D.H.; Cimino, M.C.; Salamone, M.F.; Heddle, J.A. *Mutat. Res.* **1990**, 239, 29-80.

13. Celik, A.; Mazmanci, B.; Camlica, Y.; Askin, A.; Comelekoglu, U. *Mutat. Res.* **2003**, 539, 91-97.

14. Bara, M.; Bitgen, N.; Kalkan, K.T.; Goktepe, O.; Varol, S.; Yay, A.H. *Dicle Tip Derg.* **2022**, 49(1), 36-44.

15. Aksu, P.; Doğan, A.; Gül, S.; Kanıcı, A. *Kafkas Univ. Vet. Fak. Derg.* **2013**, 19(6), 955-961.

16. Mekkawy, I. A.; Mahmoud, U. M.; Sayed, A.H. *Tissue and Cell.* **2011**, 43, 223-229.

17. Sharma, M.; Chadha, P. *Drug Chem. Toxicol.* **2017**, 40(3), 320-325.

DOI: http://dx.doi.org/10.32571/ijct.1265612 **E-ISSN: 2602-277X**

International Journal of Chemistry and Technology

http://dergipark.org.tr/ijct

Research Article

Evaluation of grain and forage yield and forage quality traits in some hybrid maize genotypes cultivated as second crop under the Eastern Mediterranean conditions

İbrahim ERTEKİN[1*] Ömer KONUŞKAN[1] İbrahim ATIŞ[1]

[1] *Department of Field Crops, Faculty of Agriculture, Hatay Mustafa Kemal University, Hatay, 31060, Türkiye*

Received: 16 March 2023; Revised: 26 June 2023; Accepted: 27 June 2023

*Corresponding author e-mail: ibrahim.ertkn@hotmail.com

Citation: Ertekin, İ.; Konuşkan, Ö.; Atış, İ. *Int. J. Chem. Technol.* **2023**, 7 (1), 113-118.

ABSTRACT

This research was conducted in order to guide researchers by determining grain, forage yield and yield-related traits and forage quality of different parts of the whole plant in some maize cultivars in Eastern Mediterranean ecological conditions. In this study, it was assessed grain and forage yield and fodder quality of four maize cultivars (PR91G98, SY Castaneda, SY Gladius, and SY Tuscani) cultivated under the Estern Mediterranean conditions. To determine forage quality, ear, stem and leaves of the whole plant maize were analyzed separately. To evaluate grain and forage yield, parameters like plant height, stem diameter, hay yield, dry matter yield, green leaf yield, green stem yield, ear weight, green ear yield were investigated while features such as crude protein, crude ash, organic matter, NDF, ADF, digestibility of dry matter, dry matter intake and relative feed value were examined to determine forage quality. The results of this study revealed that ear is very important for forage yield and quality. The greatest hay and grain yield were produced by PR31G98 maize cultivar. It was observed SY Tuscani had higher NDF and ADF values than other maize varieties. With this study, the importance of nutrient content according to silage yield and plant parts in second crop corn cultivation was determined. In addition, research results showed important source data for farmers and researchers regarding forage and grain yield of maize farming and production area is continually increasing.

Keywords: Maize, fodder, quality, cultivar.

Doğu Akdeniz koşullarında ikinci ürün olarak yetiştirilen bazı hibrit mısır genotiplerinde tane ve yem verimi ile yem kalite özelliklerinin değerlendirilmesi

ÖZ

Bu araştırma Doğu Akdeniz ekolojik koşullarında II. ürün koşullarında bazı mısır çeşitlerinin hem silaj olarak hem de tane ürünü olarak değerlendirilmesi ile elde edilen ürünün bitkisel ve kalite özelliklerini belirleyerek çiftçiler ve gelecekteki araştırmalara yardımcı olmak amacıyla yürütülmüştür. Araştırmada ikinci ürün koşullarında 4 mısır genotipinin (PR91G98, SY Castaneda, SY Gladius, ve SY Tuscani) yeşil yem ve tane özellikleri yanında silaj kalitesi değerlendirilmiştir. Araştırma sonuçları, tane ürünü için en iyi mısır çeşidinin PR31G98 olduğunu gösterirken yem kalitesi için ise çeşitler arasında önemli bir fark olmadığını göstermiştir. İncelenen koçan, sap ve yaprağın yem kalitesinde önemli farklılıkların olduğu belirlenmiştir. En yüksek kuru ot ve tane verimi PR31G98 mısır çeşidinden elde edilmiştir. SY Tuscani'nin diğer mısır çeşitlerine göre NDF ve ADF değerlerinin daha yüksek olduğu görülmüştür. Sürekli yeni mısır genotiplerinin geliştirilmesi nedeniyle, yeni çeşitlerin agronomik uygulamalara tepkisinin belirlenmesi önemlidir. Özellikle yeşil yem amacı ile yetiştiricilikte bitkinin içerisindeki koçanın kaliteye etkisinin daha önemli olduğu yapılan çalışmada tespit edilmiştir. Çalışma tane ve silajlık mısır tarımında alternatif bir yaklaşım olan yeşil yem veya taneye bırakmanın sonuçlarını ortaya koyarak Akdeniz iklim kuşağı için uygulamaya yönelik veriler ortaya koymuştur. Araştırma sonuçları, üretim alanları sürekli artan mısır için çiftçilere ve araştırıcılara önemli kaynak veriler ortaya koymaktadır.

Anahtar Kelimeler: Mısır, kaba yem, kalite, çeşit.

1. INTRODUCTION

Worldwide, maize (*Zea mays* L.) is a member of family Gramineae (Poiaceae) and is the most important grain and forage crop in our country and all over the world due to its high adaptability and high grain and forage yield.[1,2] Maize is grown in Major ecological zones of the country, making it available to be used as livestock feed.[3,4] While corn has a significant role in human nutrition and agriculture-based industry with its grain, in the last 30 years, a significant part of its production has become an important feeding used in animals and provided source of energy for livestock animals.[5] The sowing area of grain and silage maize has enlarged constantly in the last decade and reached 1.2 million ha in 2020 respectively.[6] The production of maize could have been attributed to a combination of genetic improvement (50 %) and improved crop management practices (50 %).[7] Maize genotypes interact with crop management practices in producing yield, and hence, understanding the dynamics between plant genetics and agronomic management will enhance the occasion to maximize yield potential of a hybrid using a corresponding recommended agricultural management system.[8,9]

One of the major problems to be solved in the development of our country's livestock is to meet the need for high quality, cheap and abundant roughage regularly. Therefore, in order to meet the quality roughage requirement of livestock enterprises, it is essential to improve pastures, to enlarge the production areas of forage crops, to bring cheap and alternative roughage sources to animal production, and to transfer quality roughage production techniques to producers.[10,11] Maize has higher potential yield (t DM/ha/cut) than all the grasses, legumes and crops used as forage material. The proximate and mineral compositions of maize depend on cultural practice of the forage material. It was determined as the ranges of 18-19 and 35-37 % for acid detergent fiber (ADF) and neutral detergent fiber (NDF) contents, respectively in maize forage.[3] Roth and Henrichs[12] conducted experiment on maize silage and they found the ranges of 7.2-10.0, 23.6-33.2 and 41.0-54.1% for crude protein (CP), acid detergent fiber (ADF) and neutral detergent fiber (NDF) contents, respectively and the same was observed by McDonald et al.[13] in maize plant with values of 23.3, 5.7 and 10.0% for crude fiber (CF), ether extract (EE) and ash, respectively and noted these findings. Öner et al.[14] reported crude protein, ADF and NDF ratios of silage maize under Samsun conditions as between 3.85% and 5.85%, 31% and 41% and 49% and 60%, respectively.

The research studies on maize genotypes should be performed to achieve height grain and hay yield quality, which are appropriate for the region in the Eastern Mediterranean conditions. Therefore, the purpose of this study was to assess the grain yield and forage quality responses of maize in the second crops under the Eastern Mediterranean condition.

2. MATERIALS AND METHODS

The experiment was conducted under the Mediterranean condition (in Amik lowland) in the second crop growing seasons in 2020. The soil was clay loam having pH 7.7, low in available phosphorus (7.40 kg ha^{-1}) and organic matter content (1.95%). Some climatic data which occurred in the experimental area during the growth period are given in Table 1. The study was arranged in randomized complete block design with three replications. Maize hybrids were PR91G98, SY Castaneda, SY Gladius, and SY Tuscani. The seeds were sown on June 21, 2020, maintaining 5 m long 4 rows with 70 cm row distance.

Fertilizers were applied as basal during the sowing (350 kg N, P_2O_5 and K_2O ha^{-1} (15-15-15). At V6 stage of maize, 400 kg ha^{-1} urea was applied as top dress (on July 10, 2020). The plots were irrigated once every 10-14 days when consuming nearly half of the available soil water. The control of weed and insect was performed when it was necessary. The regular agronomic practices for the maize crop were carried out according to the recommendations.

Months	Year and LYM	Precipitation (mm)	Temperature (°C)	Humidity (%)
June	2020	0.4	25.2	67.4
	LYM	32.0	24.8	-
July	2020	0.0	29.5	68.3
	LYM	16.0	27.2	-
August	2020	0.0	29.6	64.7
	LYM	18.2	27.8	-
September	2020	0.0	29.6	65.6
	LYM	41.1	25.7	-

LYM: Long years mean

For hay and dry matter, center two rows of each plot were harvested for about 35 days. The plant heights and stem diameters of ten plants selected randomly were measured before harvest. The plants were cut approximately 5 cm above ground. Three of these sample plants were divided into leaves, stem and ear; all plant fractions were dried in an oven to constant weight at 65°C for their dry matter ratio.

The other three samples were chopped in to 2 3 cm by a shredder (Bosch AXT 25D shredder, Germany) and a 300 g sub-sample taken from the chopped samples was dried in a forced-draft oven to constant weight at 65°C for dry matter (DM) content. The dried samples were ground in a mill to pass a 1 mm screen for chemical analysis.[15] Another 250 g sub-sample taken from the chopped samples was dried at 105°C and used for calculation of dry matter content.

Crude protein, NDF, ADF, and ADL were determined for all samples. Nitrogen concentrations were determined by the Kjeldahl procedure and crude protein concentration was calculated by the formula of N concentration × 6.25. NDF, ADF and ADL were analyzed according to the sequential method of Van Soest *et al.*[16] by adding α-amylase with sodium sulfite and using the ANKOM filter bag system with A220 fiber analyzer (ANKOM Technology, Fairport, NY), and expressed as exclusive residual ash.

Relative feed value (RFV) computed by using ADF (related dry matter digestibility) and NDF (related intake potential) was used as an index indicating forage quality. Relative feed value (RFV) was identified and formulated by Van Dyke and Anderson [17] as below:

DDM = 88.9 – (0.77×ADF%) DMI= (120/NDF%)

RFV= DDM% × DMI% × 0.775

Where DDM was digestible dry matter as % of dry matter, and DMI was dry matter intake as a % of body weight.

All data were performed for analysis of variance procedures using the JMP, and the TUKEY pairwise test was used to determine the statistical differences among the average values ($p \leq 0.05$).

3. RESULTS AND DISCUSSION

The statistical analysis of the evaluated characteristics for the plant height, stem diameter, hay yield, dry matter yield and grain yield is given in Table 2, and for ear weight, green leaf yield, green steam yield, green ear yield it is presented in Table 3.

Table 2. Plant height (cm), stem diameter (mm), forage yield (kg da^{-1}), dry matter yield (kg da^{-1}) and grain yield (kg da^{-1}) traits of maize varieties1

		Plant height (cm)	**Stem diameter (mm)**	**Hay yield (kg da^{-1})**	**Dry matter yield (kg da^{-1})**	**Grain yield (kg da^{-1})**
	Genotypes					
Cv.1	SYCastaneda	205.67±0.67^{ab}	17.17±0.17^{ab}	4264.63±73.04	1671.94±104.44	686.35±76.88^{b}
Cv.2	SY Cladius	211.67±1.67^{b}	16.50±0.29^{b}	4427.68±98.23	1882.01±102.86	833.33±46.91^{ab}
Cv.3	PR91G98	208.33±1.45^{ab}	17.83±0.44^{ab}	4499.08±67.65	1661.66±208.53	1006.03±88.84^{a}
Cv.4	SY Tuscani	220.00±1.67^{a}	18.00±0.29^{a}	4358.22±61.51	1653.95±106.66	889.37±22.96^{ab}
	Mean	211.42	17.38	4387.40	1717.39	853.77
	Significance	*	*	ns	ns	*

		Ear weight (g)	**Green leaf yield (kg da^{-1})**	**Green stem yield (kg da^{-1})**	**Green ear yield (kg da^{-1})**
	Genotypes				
Cv.1	SYCastaneda	144.13±16.15	664.00±73.04	1549.52±197.89	2051.148.22
Cv.2	SY Cladius	172.00±12.85	670.22±98.23	1694.60±293.10	2062.86±79.10
Cv.3	PR91G98	176.60±24.64	607.33±67.65	1877.14±235.10	2014.60±286.95
Cv.4	SY Tuscani	186.77±4.82	647.11±61.51	1731.43±99.05	1979.68±117.63
	Mean	169.88	647.17	1713.17	2027.06
	Significance	ns	ns	ns	ns

ns: not significant, *: Significant at statistic level of 5%, a-c Data shown with different superscripts in the same column were different from each other.

The differences among the genotype means were significant ($P < 0.05$) for plant height and stem diameter. The highest plant height and stem diameter were obtained from SY Tuscani. In terms of plant height and stem diameter, genotypes had statistically similar values to those of Tuscani, PR91G98 and Castenada except for Gladius. Among the varieties, the highest hay yield was 4499 kg da^{-1} in PR91G98 and also Cladius, while the highest dry matter yield was determined as 1882 kg da^{-1}. Grain yield for four genotypes ranged from 1006 kg da^{-1} to 686 kg da^{-1}. The PR91G98 genotype had higher grain yield values than the others. The plant height values and stem diameter determined for the examined maize genotypes were within the values found out in previous studies.[5,18,19] Although the plant traits of maize depend on the genotype, environmental conditions also have a significant effect on the plant traits of maize.

Although the plant height of maize depends on the genotype, the environmental conditions also have a significant impact on the plant height of the maize. Güney et al.[20] reported that the average plant height of maize genotypes varied depending on the years and this characteristic was affected by ecological conditions. Silage yields of different silage corn seeds under Hatay conditions were determined as 55.9-69.5 kg ha^{-1} in different maize varieties.[5]

Although the plant parts, crude protein, organic matter, NDF, ADF, DDM, DMI, RFV were not statistically significant for the genotypes, the plant parts were statistically important for all traits (Table 4). Genotype and plant part interactions were statistically significant for NDF, ADF, DDM, DMI, and RFV (Table 4). Crude protein of forages is one of the main criteria for forage quality. Forage quality was significantly influenced by harvest dates,[21] and ADF and NDF concentrations are important forage quality characteristics.[22] These results are in agreement with the work done by Roth and Henrics et al.[12] who reported that crude protein (CP), acid detergent fibre (ADF) and neutral detergent fibre (NDF) contents of maize silage ranged between 7.2-10.0, 23.6-33.2 and 41.0-54.1%, respectively.

Table 3. Means of ratio of plant part, crude protein (CP), crude ash (CA), and organic matter (OM) parameters.

		Ratio of Plant Part (%)	**CP (% KM)**	**CA (% KM)**	**OM (% KM)**
	Genotypes (G)				
Cv.1	SY Castaneda	33.33±5.60	7.11±1.36	6.26±1.59	93.74±1.59
Cv.2	SY Cladius	33.33±6.08	8.02±1.32	6.84±1.63	93.16±1.63
Cv.3	PR91G98	33.33±4.10	6.96±1.20	5.65±1.31	94.35±1.31
Cv.4	SY Tuscani	33.33±4.20	6.62±1.13	5.60±1.32	94.40±1.32
	Mean	33.33	7.18	6.09	93.91
	Significance	ns	ns	ns	ns
	Plant pars (P)				
	Ear	52.49±1.52 ^{a}	7.13±0.14 ^{b}	1.81±0.06 ^{c}	98.19±0.06 ^{a}
	Stem	26.96±1.11 ^{b}	2.94±0.18 ^{c}	4.90±0.32 ^{b}	95.10±0.32 ^{b}
	Leaves	20.55±0.78 ^{c}	11.46±0.40 ^{a}	11.55±0.41 ^{a}	88.45±0.41 ^{c}
	Mean	33.33	7.18	6.09	93.91
	Significance	**	**	**	**
	Significance (GXP)	ns	ns	ns	ns

ns: not significant, **: Significant at statistic level of 1%, a-c Data shown with different superscripts in the same column were different from each other.

Table 4. Means of neutral detergent fiber (NDF), acid detergent fiber (ADF), digestible of dry matter (DDM), dry matter intake (DMI), and relative feed value features.

		NDF (% KM)	**ADF (% KM)**	**DDM (%)**	**DMI (%)**	**RFV**
	Genotypes (G)					
Cv.1	SYCastaneda	49.60±7.75	25.30±4.88	69.19±3.80	3.36±0.78	197.82±55.82
Cv.2	SY Cladius	47.92±8.18	24.76±5.05	69.61±3.93	3.77±0.95	225.78±67.65
Cv.3	PR91G98	49.21±6.57	24.17±3.98	70.07±3.10	3.03±0.56	175.11±40.20
Cv.4	SY Tuscani	50.92±7.32	26.23±4.72	68.47±3.67	3.07±0.63	176.60±45.13
	Mean	49.41	25.11	69.34	3.31	193.83
	Significance	ns	ns	ns	ns	ns
	Plant parts (P)					
	Ear	20.10±1.05 ^{c}	7.17±0.45 ^{c}	83.32±0.35 ^{a}	6.16±0.34 ^{a}	398.79±23.44 ^{a}
	Stem	67.83±0.97 ^{a}	38.20±0.74 ^{a}	59.15±0.58 ^{c}	1.77±0.03 ^{b}	81.40±1.97 ^{b}
	Leaves	60.30±0.73 ^{b}	29.98±0.29 ^{b}	65.55±0.23 ^{b}	1.99±0.02 ^{b}	101.30±1.53 ^{b}
	Mean	49.41	25.11	69.34	3.31	193.83
	Significance	**	**	**	**	**
	Significance (GXP)	**	**	**	**	**

ns: not significant, Significant at statistic level of 1%, a-c Data shown with different superscripts in the same column were different from each other.

For the first order of interaction (V×PP), the data in Figure 1 clarified that the NDF was significantly affected by the (V×PP) interaction. The highest NDF was recorded in stems, while the smallest ones were recorded in ears. For the second order interaction (G×PP), data in Figure 2 stated that the ADF was significantly affected by the (V×PP) interaction. The greatest ADF was recorded in stems, while the lowest ones were recorded in ears.

Regarding to the interaction between maize hybrids and parts of the plant, the data in Figure 3 stated that the DDM was significantly affected by the (G×PP) interaction. The maximum DDM was recorded in ears of all genotypes, while the minimum ones were recorded in stems. As can be seen in Figure 4, DMI was significantly affected by the (V×PP) interaction. Regarding the interactions among the maize hybrids and parts of the plant, the data in Figure 5 stated that the RFV was significantly influenced by the (V×PP) interaction. According to the results, the RFV of maize variety changed significantly according to parts of the plant. The RFV in ears of Tuscani and Cladius was the same groups and other genotypes were the same group in terms of RFV property, too. The results indicated that the RFV of all maize ear, stem and leaves showed significant differences depending on part of the plants (P<0.05).

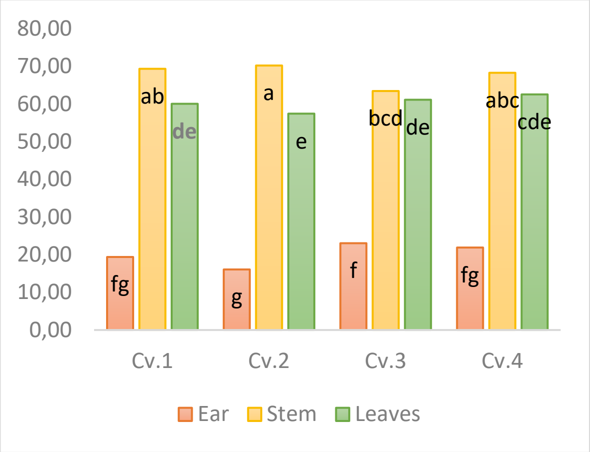

Figure 1. Genotype × part of the plant interaction of NDF

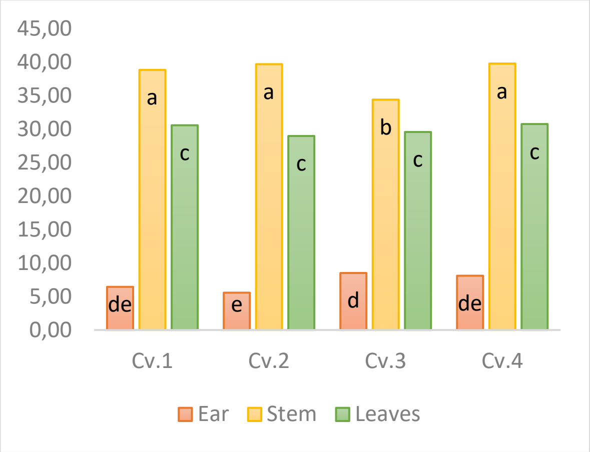

Figure 2. Genotype × part of the plant interaction of ADF.

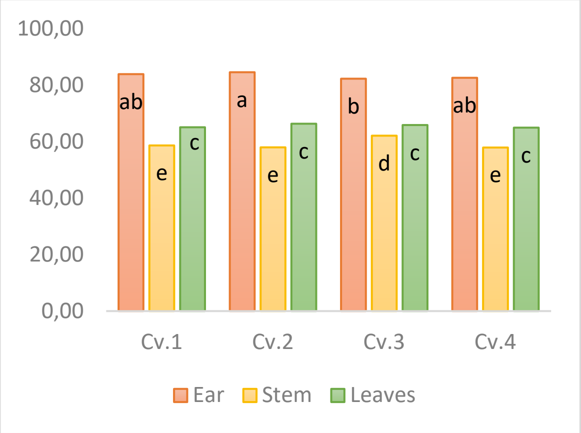

Figure 3. Genotype × part of the plant interaction of DDM.

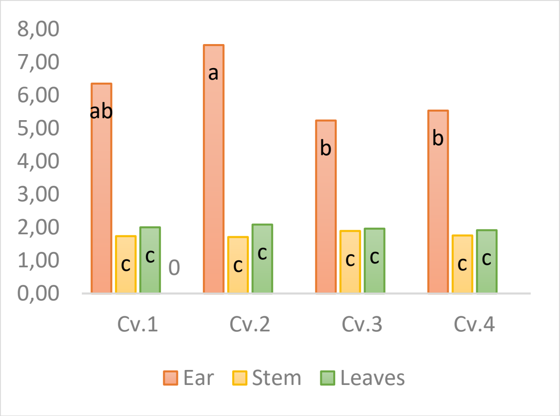

Figure 4. Genotype × part of the plant interaction of DMI.

Figure 5. Genotype × part of the plant interaction of RFV.

4. CONCLUSIONS

The new production area and hybrids revealed a significant effect on yield attributes and herbage yield of forage maize. The differences among the four maize genotypes and plant parts were generally signficant in terms of all investigated traits. Especially parts of the plant (ear, stem and leaves) were important in maize cultivars for NDF, ADF, DDM, DMI, RFV. PR91G98 hybrid maize variety resulted in more productivity for parameters. Farmers and maize growers should be encouraged to use part of the plant that performs better adaptability in the specific Hatay ecological conditions. Among the investigated hybrid genotypes for grain yield, PR91G98 hybrid maize variety realized more yield. In conclusion, we deduced that the grain yield, stem diameter and plant height determined for forage yield were more essential than plant parts.

Conflict of interests

I declares that there is no a conflict of interest with any person, institute, company, etc.

REFERENCES

1. Konuskan, O.; Konuskan-Bozdogan, D.; Lavei, C.M. Rev. Chim. **2017**, 68(9), 2073-2075.

DOI: http://dx.doi.org/10.32571/ijct.1265612 **E-ISSN: 2602-277X**

2. Wasaya, A.; Affan, M.; Ahmad Yasir, T.; Atique-ur-Rehman Mubeen, K.; Rehman Hu Ali, M.; Nawaz, F.; Galal, A.; Iqbal, M.A.; Islam, M.S.; El-Sharnouby, M.; Rahman, M.H.; EL Sabagh, A. Atmosphere. **2021**, 12(6), 663.

3. Konuskan, O.; Kilinc, C. Fresenius Environ. Bull. **2019**, 28 (4), 2795-2801.

4. Saboor, A.; Ali, M.A.; Ahmed, N.; Skalicky, M.; Danish, S.; Fahad, S.; Hassan, F.; Hassan, M.M.; Brestic, M.; EL Sabagh, A.; Datta, R. Agriculture. **2021**; 11(4), 310.

5. Yilmaz, S.; Gozubenli, H.; Konuskan, O.; Atis, I. Asian J. Plant Sci. **2007**, 6(3), 538-541.
6. Anonymous. TUİK Bitkisel Üretim İstatistikleri. Retrieved March 25, 2020, from http://www.tuik.gov.tr/PreTablo.do?alt_id=1001.

7. Duvick, D.N. Adv. Agron. **2005**, 86, 83-145.
8. Mastrodomenico, A.T.; Hendrix, C.C.; Below, F.E. Agriculture. **2018**, 8(1), 3.

9. EL Sabagh, A.; Hossain, A.; Iqbal, M.A.; Barutçular, C.; Islam, M.S.; Çig, F.; et al. in Plant Stress Physiology, ed. A. Hossain, 2020, (London: IntechOpen)

10. Serin, Y.; Tan, M. Atatürk Üniversitesi Ziraat Fakültesi Yayınları, **2001**, No: 206.

11. Yolcu, H.; Tan, M. Tar. Bil. Derg. **2008**, 14 (3), 303-312.

12. Roth, G.W.; Heinrichs, A.J. Agronomy fact-18. Published by Information and Communication Technology in the College of Agricultural Sciences, Pennsylvania State University, 2001, Retrieved from http://www.cas.psu.edu

13. McDonald, P.; Edwards, R.A.; Greenhalgh, J.F.D.; Morgan, C.A. Longman Publishers, **1998**, pp. 431-438

14. Öner, F.; Aydın, İ.; Sezer, İ.; Gülümser, A.; Özata, E.; Algan, D. 2011. IX. Tarla Bitkileri Kongresi, 2011, 12–5. Eylül 2011. Bursa

15. Ertekin, İ.; Atış, İ.; Yılmaz, Ş.; Can, E.; Kızılşimşek, M. KSU J. Agric. Nat. **2019**, 22(5), 781-786.

16. Van Soest, P.J.; Robertson, J.B.; Lewis, B.A. J. Dairy Sci. **1991**, 74 (10), 3583-3597.

17. Van Dyke, N.J.; Anderson, P.M. Alabama Cooperative Extension, Circular, 2002, ANR-890.

18. Atış, İ.; Konuşkan, Ö.; Gözübenli, H.; Yılmaz, Ş.; Can, E.; Çeliktaş, N.. Turkey 10. Field Crops Congress, 10-13 September 2013, Konya, Volume 3, p: 649-653.

19. Konuskan, Ö.; Atış, İ.; Gözübenli, H. MKÜ. Ziraat Fak. Derg. **2015**, 20(2), 1-6.

20. Güney, E.; Tan, M.; Dumlu-Gül, Z.; Gül, İ. Atatürk Üniv. Zir. Fak. Derg. **2010**, 41 (2), 105-111.

21. Atis, I.; Konuskan, O.; Duru, M.; Gozubenli, H.; Yilmaz, S. Int. J. Agric. Biol. **2012**, 14, 879–886.

22. Yilmaz, S.; Özel, A.; Erayman, M.; Atak, M. Turk. J. Agric. For. **2015**, 39, 135-143.